KU LEUVEN

ARENBERG DOCTORAL SCHOOL
FACULTY OF ENGINEERING SCIENCE

THE NUMERICAL SOLUTION OF LARGE SCALE DYNAMIC SOIL–STRUCTURE INTERACTION PROBLEMS

Pieter COULIER

Dissertation presented in partial
fulfillment of the requirements for
the degree of Doctor
in Engineering

May 2014

THE NUMERICAL SOLUTION OF LARGE SCALE DYNAMIC SOIL–STRUCTURE INTERACTION PROBLEMS

Pieter COULIER

Jury:
Prof. dr. ir. J. Berlamont, chair
Prof. dr. ir. G. Degrande, supervisor
Prof. dr. ir. G. Lombaert, co–supervisor
Prof. dr. ir. W. Desmet
Prof. dr. ir. D. Roose
Prof. dr. ir. M. Bonnet
(ENSTA ParisTech)
Prof. dr. ir. H. Hunt
(University of Cambridge)

Dissertation presented in partial fulfillment of the requirements for the degree of Doctor in Engineering

May 2014

D/2014/7515/55
ISBN 978-94-6018-831-2

Voorwoord

"Continuous effort – not strength nor intelligence –
is the key to unlocking our potential."
Sir Winston Churchill (1874–1965)

Met het schrijven van dit voorwoord komt mijn doctoraatsonderzoek na drieëneenhalf jaar ten einde. Het eindresultaat, dit proefschrift, had nooit gerealiseerd kunnen worden zonder de steun van een aantal cruciale personen, die ik graag expliciet wil bedanken.

In de eerste plaats wens ik mijn promotoren Geert Degrande en Geert Lombaert te bedanken voor de kans die ze me boden om dit doctoraat aan te vatten. Ik dank hen voor het aansturen van het onderzoek, de inspirerende suggesties, en het nauwgezet nalezen van publicaties. Bovendien gunden ze me veel vrijheid in mijn onderzoek, wat ik steeds erg gewaardeerd heb. Dit resulteerde in een productieve, maar bovenal een aangename samenwerking. Verder heb ik hen meerdere malen mogen vergezellen op (buitenlandse) congressen, vergaderingen, en workshops, wat steeds verrijkende ervaringen waren.

I wish to express my gratitude to Hugh Hunt of the University of Cambridge, whose enthusiastic guidance of my master's thesis in 2009–2010 encouraged me to embark on this journey. I am not only grateful for his willingness to be a member of the supervisory committee and the jury of my doctorate, but also for having welcomed me once more in Cambridge for a research stay in 2013. His valuable advice and enriching ideas have broadened my view, and it has always been a great pleasure to work with him.

Wim Desmet bedank ik voor het opvolgen van dit doctoraat als lid van de begeleidingscommissie en de jury. Ook de overige juryleden, Marc Bonnet en Dirk Roose, bedank ik voor hun waardevolle opmerkingen. Jean Berlamont dank ik voor het vervullen van de voorzitterstaak.

Het Fonds Wetenschappelijk Onderzoek – Vlaanderen (FWO) dank ik voor het ondersteunen van mijn onderzoek door middel van een vierjarig aspirantenmandaat, alsook voor het financieren van mijn verblijf in Cambridge en mijn deelname aan enkele internationale congressen.

De voorbije jaren heb ik met plezier aan de afdeling Bouwmechanica gewerkt. Op inhoudelijk vlak kon ik in het bijzonder rekenen op Stijn François, die steeds bereid was om te overleggen en mijn praktische vragen te beantwoorden. Daarnaast heb ik vaak samengewerkt met Hans Verbraken, met wie ik het zowel tijdens als na de werkuren goed kon vinden. De (nachtelijke) meetcampagnes in Lincent, Hasselt, en Loon–Plage zullen me nog lang bijblijven, net als de talloze hevig bevochten pingpongwedstrijden, niet in het minst omwille van het positieve winstsaldo. Het is me een raadsel hoe we die wedstrijden steeds zonder kleerscheuren wisten door te komen. Een speciale vermelding is er voor Ellen Simoen, met wie ik drie jaar een bureau (waar er altijd wel iets te beleven viel) heb gedeeld. Jeroen Hillewaere dank ik voor de hulp bij het omslagontwerp van dit proefschrift en voor het aangename gezelschap tijdens onze rondreis door Brazilië aansluitend op WCCM 2012. Graag bedank ik ook Eliz–Mari, Miche, Bram, Mattias, Saartje, Edwin, Kristof, Katrien, Arne, Jonas, Amin, Leqia, Ali, en alle andere collega's en buitenlandse bezoekers die voor een aangename en stimulerende werkomgeving zorgden. Verder heb ik de interesse in mijn onderzoek van Guido De Roeck, hoofd van de afdeling Bouwmechanica, steeds ten zeerste geapprecieerd. Danielle Jennes en Ann Zwarts verdienen een pluim voor de feilloze administratieve ondersteuning.

I would like to express my appreciation to all colleagues and friends who made my research stay in Cambridge so enjoyable. I am particularly grateful to Alice, Hilary, Francesco, Elke, and Sergii for the useful work–related discussions, but even more for the many pleasant moments outside of the office.

Tot slot wens ik ook iedereen te bedanken die minder direct bij dit doctoraat betrokken was. Mijn dank gaat uit naar familie en vrienden voor de getoonde interesse in mijn onderzoek – ook al was het ongetwijfeld niet altijd even duidelijk waar ik me precies mee bezig hield – en voor het voorzien van de nodige afleiding en ontspanning. Het grootste woord van dank richt ik tot mijn ouders, zussen, en grootouders voor de wijze raad en de onvoorwaardelijke steun.

Pieter Coulier
April 2014

Summary

In the analysis of the dynamic behaviour of many civil engineering structures, it is essential to account for the interaction between the structure and its environment. Despite the advance of high performance computers, the numerical solution of large scale dynamic soil–structure interaction (SSI) problems remains very challenging and in many cases beyond current computer capabilities.

This dissertation addresses the development and application of fast, stable, and accurate numerical techniques for the solution of dynamic SSI problems, focusing on linear problems formulated in the frequency domain. A domain decomposition approach is employed, where finite elements for the structure(s) are coupled to boundary elements for the soil, accounting for the soil's stratification. Innovative methodologies are presented for improving the efficiency and applicability of existing three–dimensional and two–and–a–half–dimensional formulations, allowing for the solution of large scale dynamic SSI problems. The computational performance of the proposed procedures is assessed and their suitability is illustrated through numerical examples.

The novel techniques are subsequently employed for the efficient solution of several challenging dynamic SSI problems related to railway induced ground vibrations. The vibration reduction efficiency of mitigation measures on the propagation path in the soil, including an open trench and a stiff wave barrier, is studied in detail, providing fundamental insight in the underlying physical mechanisms; trenches and barriers of infinite and finite length are analyzed. The wave propagation in a dense urban environment characterized by multiple closely–spaced buildings is considered as well, taking the dynamic through–soil coupling of all structures into account.

Samenvatting

Bij het analyseren van het dynamisch gedrag van bouwkundige constructies is het vaak van essentieel belang om de interactie tussen de structuur en zijn omgeving in rekening te brengen. Ondanks de opkomst van rekenkrachtige en performante computers blijft het numeriek oplossen van grootschalige dynamische grond–structuurinteractieproblemen echter heel uitdagend en vanuit rekentechnisch oogpunt dikwijls onhaalbaar.

Dit proefschrift focust op de ontwikkeling en toepassing van efficiënte, stabiele, en nauwkeurige technieken voor het oplossen van dynamische grond–structuurinteractieproblemen, met een nadruk op lineaire problemen geformuleerd in het frequentiedomein. Een substructuurmethode wordt aangewend, waarbij eindige elementen voor één of meerdere structuren gekoppeld worden met randelementen voor de ondergrond. De gelaagdheid van de grond wordt hierbij expliciet in rekening gebracht. Innovatieve methoden die de efficiëntie en de toepasbaarheid van bestaande driedimensionale en tweeëneenhalfdimensionale formuleringen verbeteren worden voorgesteld; deze technieken maken het oplossen van grootschalige dynamische grond–structuurinteractieproblemen mogelijk. De rekentechnische performantie van de vooropgestelde procedures wordt nagegaan en hun toepasbaarheid wordt geïllustreerd aan de hand van numerieke voorbeelden.

De nieuwe technieken worden vervolgens aangewend om een aantal uitdagende dynamische grond–structuurinteractieproblemen op een efficiënte manier op te lossen. Deze toepassingen hebben allen betrekking op het voorspellen van trillingen in de bebouwde ongeving veroorzaakt door treinverkeer. De efficiëntie van trillingsbeperkende maatregelen op het golfvoortplantingspad in de grond wordt eerst in detail bestudeerd, wat een fundamenteel inzicht in de onderliggende fysische mechanismen oplevert; zowel open sleuven als stijve wanden worden geanalyseerd. Daarnaast wordt ook de golfvoortplanting in een dichtbebouwde stedelijke omgeving onderzocht, waarbij de dynamische interactie tussen nabijgelegen gebouwen in rekening wordt gebracht.

Contents

PART I

EXECUTIVE SUMMARY

Chapter 1

Introduction

1.1 Problem outline

In civil engineering, and more particularly in structural mechanics, computational tools are used to understand and predict the dynamic behaviour of structures (bridges, buildings, wind turbines, ...) or their individual components (cables, floors, propeller blades, ...) in several limit states. A major complexity lies in the fact that many structures, if not all, are in direct contact with the underlying or surrounding soil domain. The dynamic interaction between the structures and the soil often plays a crucial role in structural mechanics and should be accounted for in numerical models [18, 35, 157]. An efficient solution of dynamic soil–structure interaction (SSI) problems is indispensable, for example, for the assessment of damage to buildings caused by earthquakes [32], the evaluation of annoyance in the built environment due to vibrations originating from road and railway traffic [97], or the design of offshore structures subjected to wind and wave loadings [45].

Of particular interest in this dissertation are railway induced vibrations [145]. These vibrations are generated at the wheel–rail interface, propagate as elastic waves in the surrounding soil and excite surrounding buildings, where they may cause disturbance of sensitive equipment, annoyance to people, and structural damage (primarily in the frequency range between 1 and 80 Hz) [98]. These vibrations are a problem of considerable societal and economic importance, given the large number of new railway lines that are presently planned or under construction to meet increasing demands for passenger and freight transport in densely populated areas. Increasing public sensitivity to noise and vibration

calls for efficient mitigation measures in both existing and new built situations, however; the high cost of such interventions necessitates to support their design by numerical prediction models [98].

The accurate prediction of railway induced ground vibrations involves the numerical solution of three–dimensional (3D) dynamic SSI problems at both the source (railway tunnel or track) and the receiver (building where vibrations are perceived or should be avoided). This is a challenging task, as multiple structures interact through wave propagation in the soil. The semi–infinite extent of the soil as well as its stratification need to be taken into account in numerical models; the latter is especially important if soft top layers are present. The advance of high performance computers has stimulated the development of fast and efficient numerical methods for dynamic SSI problems, which is the subject of ongoing research worldwide.

1.2 State of the art

Numerous techniques have been developed over the past decades for the solution of dynamic SSI problems, especially in the field of earthquake engineering [18]. For simple geometries, (semi–)analytical solutions can be found [62, 157], whereas numerical approximation techniques are required for more complex systems. A domain decomposition approach is often introduced in numerical models, allowing for the application of different techniques for the soil and the structure [35]. These models can either be formulated in the time or in the frequency domain.

Various methods exist for the simulation of elastodynamic wave propagation in the soil. The finite element (FE) method discretizes the domain of interest in a number of elements and approximates the field variables within these elements by means of simple functions (often low order polynomials). This approach offers the flexibility to model complex geometries and enables the incorporation of tailored constitutive laws. The size of the elements should be sufficiently small compared to the wavelength in order to limit the numerical dispersion, implying that a large amount of elements is required for an accurate solution, especially at high frequencies [112]. The FE method has been adopted, among others, by Bielak et al. [20] and Taborda and Bielak [139] for large scale earthquake simulations involving millions of elements, using an octree–based approach. The use of higher order approximations for the field variables results in the spectral element (SE) method. This method provides a very effective and powerful approach for solving 3D elastodynamic wave propagation problems, as demonstrated for example in [47, 90, 131].

The discontinuous Galerkin (DG) method can be employed in finite and spectral element formulations to analyze non–conforming discretizations, which is especially appealing if strong heterogeneities and discontinuities appear. An application of DG in conjunction with spectral elements for elastodynamic wave propagation has recently been presented by Mazzieri et al. [105]. The aforementioned methods can all be used for high performance parallel computing. Other methods are the finite difference (FD) method [59, 127] and the discrete element (DE) method [147].

Domain discretization methods suffer from a fundamental problem when modelling wave propagation in a domain of (semi–)infinite extent, as the discretization should ideally extend to infinity but has to be truncated in practice. This necessitates the introduction of appropriate techniques to minimize spurious reflections due to the artificial boundaries. Infinite elements [19, 163], absorbing boundary conditions (ABCs) [117], or perfectly matched layers (PMLs) [10, 31, 48] can be employed to account for the decay of waves towards infinity.

The boundary element (BE) method provides a valuable alternative for the methods outlined above. This method is based on the discretization of a boundary integral equation that inherently satisfies the radiation conditions in the soil [25]. Moreover, it leads to a reduction of the spatial problem dimension as only the boundaries of the domain have to be discretized (i.e. surface instead of volume discretization). A major drawback of classical BE formulations is that they result in dense and unsymmetric matrices, which leads to high computational costs. Several fast BE methods have therefore been developed to improve the computational efficiency, including the fast multipole method (FMM) [123], the panel clustering technique [75], and methods based on hierarchical matrices ($\mathscr{H}$–matrices) [74]. In the FMM, the Green's functions are reformulated using a multipole expansion, which has proven to be very efficient if analytical expressions of the Green's functions are available [113]. Existing fast multipole formulations for elastodynamics are therefore usually based on closed form full space fundamental solutions [28, 29, 58, 71]; an extended formulation for a homogeneous halfspace has recently been presented by Chaillat et al. [27]. A considerable amount of boundary elements is thus required for the discretization of the layer interfaces (and possibly also for the free surface if a full space formulation is used), hence limiting the actual problem size that can be treated. A complementary class of fast BE methods is based on $\mathscr{H}$–matrices in combination with efficient algorithms such as adaptive cross approximation. These methods essentially are algebraic tools to approximate the BE matrices [13, 122], providing an alternative to tackle problems for which analytical expressions of the Green's functions are not available.

Each of these methods for the soil can subsequently be coupled to a numerical model for the structure(s); the FE method is commonly applied in structural dynamics. This has led to the development of methodologies such as coupled FE–BE [164] or FE–PML [31] approaches.

Apart from 3D models, a two–and–a-half–dimensional (2.5D) approach can be employed for problems with an invariant geometry in the longitudinal direction. Many of the aforementioned numerical techniques have been formulated in a 2.5D framework, see e.g. Gavrić [60, 61] for 2.5D FE models, Stamos and Beskos [137] for 2.5D BE models, Sheng et al. [134] for a 2.5D FE–BE formulation, Yang et al. [159,161] for a 2.5D finite–infinite element approach, or François et al. [55] for a 2.5D PML technique. Dedicated numerical techniques have also been developed for problems with a periodic lay–out [36, 78].

1.3 Objectives and achievements

Although substantial progress has been made in recent years regarding the development of efficient prediction models, the numerical solution of large 3D dynamic SSI problems remains very challenging and in many cases beyond current computer capabilities. A compromise between accuracy and computational efficiency is therefore often required. This dissertation aims at developing and applying fast, stable, and accurate numerical methods in order to cope with ever larger and more complex dynamic SSI problems.

Within the frame of the present work, 3D and 2.5D coupled FE–BE methods are developed and employed. The scope of this dissertation is limited to linear problems that can be treated in the frequency domain. Special attention is paid to the soil stratification, as accounting for the latter is considered crucial for an accurate solution of many dynamic SSI problems.

The original methodological contributions of this work are listed below:

- A fast BE method based on $\mathscr{H}$–matrices, taking into account the layered nature of the soil, is developed. The incorporation of Green's functions of a layered halfspace avoids meshing of the free surface and the layer interfaces. The method leads to a significant reduction of the required memory and CPU time with respect to classical BE formulations, which allows for an increase of the problem size by at least one order of magnitude.

- Innovative techniques for the coupling of FE and fast $\mathscr{H}$-BE methods are presented. In particular, the convergence behaviour of iterative coupling

approaches is investigated in detail, as the application of such schemes in the frequency domain is not trivial. Relaxation procedures are introduced to ensure and accelerate the convergence. The resulting FE–$\mathscr{H}$-BE methods allow for the solution of large 3D dynamic SSI problems.

- A spatial windowing technique, originating from vibro–acoustics [150], is proposed to extend the applicability of existing 2.5D FE–BE methods for elastodynamic transmission and radiation problems. This method enables the application of a 2.5D approach to structures that are not longitudinally invariant, hence providing a very efficient alternative to full 3D computations. The suitability of this approach is demonstrated and its limitations are pointed out.

The developed methods are applicable to a large variety of dynamic SSI problems. Within the frame of the present work, several applications related to the prediction of railway induced vibrations are investigated. The original contributions to this field are the following:

- Vibration mitigation measures on the propagation path in the soil are studied. In particular, the effectiveness of an open trench and a stiff wave barrier are investigated in detail and the underlying physical mechanisms are revealed; trenches and barriers of infinite and finite length are considered. Furthermore, rules of thumb to assess the vibration reduction efficiency in a preliminary design stage are formulated based on extensive FE–BE calculations.

- The influence of source–receiver interaction on the numerical prediction of railway induced vibrations is assessed. It is investigated under which conditions the dynamic SSI at the source (railway tunnel or track) can be uncoupled with reasonable accuracy from the dynamic SSI at the receiver (building).

- A first step is set towards the simulation of wave propagation in an urban environment in the frequency range of interest for railway induced vibrations. Two case studies are presented in which the dynamic interaction between multiple buildings is rigorously taken into account.

The original contributions outlined above are the topic of five key publications, forming the cornerstones of this dissertation.

1.4 Organization of the text

This dissertation is divided into two main parts. The first part, including the current chapter, gives an overview of the research context and provides a concise summary of the most important contributions.

Chapter 1 introduces the dissertation by situating the subject of dynamic SSI and outlining the state of the art. The original contributions are highlighted and the organization of the text is clarified.

Chapter 2 deals with coupled FE–BE methods for the solution of dynamic SSI problems, which is the main numerical methodology employed throughout this work.

Chapter 3 summarizes two innovative approaches for the solution of large scale 3D dynamic SSI problems. First, a fast 3D BE method based on $\mathscr{H}$–matrices is reviewed and appropriate FE–$\mathscr{H}$-BE coupling procedures are discussed. Second, a technique is presented to extend the applicability of 2.5D models for dynamic SSI to structures of finite length, while still exploiting the computational efficiency of a 2.5D approach.

Chapter 4 focuses on applications involving dynamic SSI. The first application is related to the mitigation of ground–borne vibrations by means of mitigation measures on the propagation path in the soil, while the other applications involve dynamic through–soil coupling of multiple structures.

Chapter 5 summarizes the most important conclusions and gives recommendations for further research.

The second part of this dissertation consists of five key publications, presenting the main achievements and original contributions of the present work. Each of these publications is self–contained and includes a state of the art, the theoretical background of the problem, and illustrative numerical examples. All papers have been published in international peer reviewed journals.

Paper A [40] has been published in *Engineering Analysis with Boundary Elements* and presents the application of $\mathscr{H}$–matrices to BE methods for elastodynamics based on Green's functions of a horizontally layered halfspace.

Paper B [41] discusses the coupling of finite element and fast boundary element methods for the solution of dynamic SSI problems. Three coupling methodologies are proposed and their computational performance is assessed through numerical examples, allowing for the formulation of guidelines concerning the choice of an appropriate coupling strategy for a specific dynamic SSI problem. This paper has been published in the *International Journal for*

Numerical Methods in Engineering.

Paper C [39] presents a spatial windowing technique that allows accounting for the effect of finite dimensions in 2.5D models for dynamic SSI. This technique enables the application of 2.5D models even if the assumption of longitudinal invariance is not fulfilled, hence maintaining the associated computational efficiency. This paper has been published in *Soil Dynamics and Earthquake Engineering*.

Paper D [38] has been published in *Soil Dynamics and Earthquake Engineering* and investigates the efficiency of subgrade stiffening as a mitigation measure for railway induced vibrations. The physical mechanism that leads to a reduction of vibration levels is revealed and explained in detail.

Paper E [42] studies the influence of source–receiver interaction on the numerical prediction of railway induced vibrations. The common assumption in seismic engineering that source–receiver interaction can be disregarded if the distance between source and receiver is sufficiently large is assessed. This paper has been published in the *Journal of Sound and Vibration*.

Chapter 2

Coupled FE–BE methods for dynamic SSI problems

The numerical solution of 3D dynamic SSI problems is a challenging task [18]. A domain decomposition approach is often introduced in numerical models, allowing for the application of different numerical techniques for the soil and the structure [8, 9]. Coupled FE–BE methods are employed throughout this dissertation, in which the FE method is used to model structures with complex geometries while the BE method is utilized to simulate wave propagation in the soil, accounting for the radiation of waves towards infinity. All methods are formulated in the frequency domain.

Coupled FE–BE methods for dynamic SSI are well–established and belong to the state of the art [153, 164]. This chapter briefly reviews the main features of this methodology, hence providing a solid basis for the novel developments and applications in chapters 3 and 4. Section 2.1 introduces the governing equations of elastodynamic wave propagation. The BE and FE method are subsequently considered in sections 2.2 and 2.3, respectively, while the FE–BE coupling is addressed in section 2.4. Both 3D and 2.5D formulations are discussed.

2.1 Wave propagation in the soil

2.1.1 Governing equations

Consider a Green elastic medium in a Cartesian frame of reference. The displacement vector at position $\mathbf{x} = (x, y, z)$ at time t is denoted as $\mathbf{u}(\mathbf{x}, t)$. In this dissertation, steady–state harmonic motion at a radial frequency ω is of concern. The time t and the radial frequency ω are related through the following Fourier transformation pair:

$$\hat{f}(\omega) = \mathscr{F}[f(t), \omega] = \int_{-\infty}^{+\infty} f(t) \exp(-i\omega t)\, \mathrm{d}t \tag{2.1}$$

$$f(t) = \mathscr{F}^{-1}\left[\hat{f}(\omega), t\right] = \frac{1}{2\pi} \int_{-\infty}^{+\infty} \hat{f}(\omega) \exp(i\omega t)\, \mathrm{d}\omega \tag{2.2}$$

where a hat above a variable denotes its representation in the frequency domain.

For small strains, the Green–Lagrange strain tensor reduces to the symmetric small strain tensor $\hat{\boldsymbol{\epsilon}}(\mathbf{x}, \omega)$:

$$\hat{\boldsymbol{\epsilon}}(\mathbf{x}, \omega) = \frac{1}{2}\left[\nabla \hat{\mathbf{u}}(\mathbf{x}, \omega) + (\nabla \hat{\mathbf{u}}(\mathbf{x}, \omega))^{\mathrm{T}}\right] \tag{2.3}$$

The small strain tensor $\hat{\boldsymbol{\epsilon}}(\mathbf{x}, \omega)$ is related to the Cauchy stress tensor $\hat{\boldsymbol{\sigma}}(\mathbf{x}, \omega)$ through Hooke's law:

$$\hat{\boldsymbol{\sigma}}(\mathbf{x}, \omega) = \mathsf{C} : \hat{\boldsymbol{\epsilon}}(\mathbf{x}, \omega) \tag{2.4}$$

where C is a fourth order elasticity tensor. In case of a linear elastic isotropic material, the latter is characterized by only two independent elastic moduli, i.e. the first and second Lamé parameters λ and μ:

$$\mathsf{C} = \lambda\, \mathbf{I} \otimes \mathbf{I} + 2\mu\, \mathsf{I} \tag{2.5}$$

In equation (2.5), $\mathbf{I}$ is the second order identity tensor, while I is the symmetric part of the fourth order identity tensor. The Lamé parameters can be related to the Young's modulus $E = \mu(3\lambda + 2\mu)/(\lambda + \mu)$ and Poisson's ratio $\nu = \lambda/(2(\lambda + \mu))$.

With a body force $\rho\hat{\mathbf{b}}(\mathbf{x}, \omega)$ acting on the medium, conservation of momentum can be expressed as:

$$\nabla \cdot \hat{\boldsymbol{\sigma}}(\mathbf{x}, \omega) + \rho\hat{\mathbf{b}}(\mathbf{x}, \omega) = -\rho\omega^2 \hat{\mathbf{u}}(\mathbf{x}, \omega) \tag{2.6}$$

where ρ is the mass density of the medium. Combining equations (2.3)–(2.6) provides the linearized dynamic equilibrium equation in terms of the displacement vector $\hat{\mathbf{u}}(\mathbf{x}, \omega)$ only [46]:

$$(\lambda + \mu) \nabla\nabla \cdot \hat{\mathbf{u}}(\mathbf{x}, \omega) + \mu\nabla^2 \hat{\mathbf{u}}(\mathbf{x}, \omega) + \rho\hat{\mathbf{b}}(\mathbf{x}, \omega) = -\rho\omega^2 \hat{\mathbf{u}}(\mathbf{x}, \omega) \tag{2.7}$$

Equation (2.7) is known as the Navier equation of elasticity. The homogeneous Navier equation (i.e. in the absence of body forces $\rho\hat{\mathbf{b}}(\mathbf{x}, \omega)$) is commonly solved in elastodynamics by introducing the Helmholtz decomposition of the displacement vector into an irrotational and a rotational part [2]. This results in two uncoupled equations describing the propagation of dilatational (primary, P) and shear (secondary, S) waves, respectively, where particles move parallel to or perpendicular on the wave propagation direction. These waves are body waves; the corresponding wave velocities are $C_\mathrm{p} = \sqrt{(\lambda + 2\mu)/\rho}$ and $C_\mathrm{s} = \sqrt{\mu/\rho}$.

Within the frame of the present work, the soil is modelled as a horizontally layered elastic halfspace (figure 2.1). The presence of a free surface gives rise to surface waves such as Rayleigh [118] and Love [101] waves; the latter only arise in a heterogeneous halfspace. Stoneley waves are waves propagating along the interface between two soil layers [138].

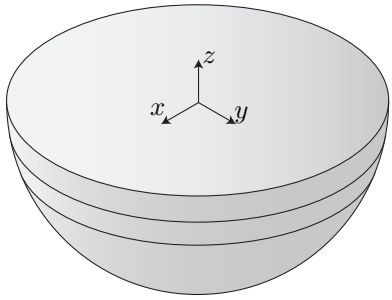

Figure 2.1: A horizontally layered halfspace.

As waves propagate through a medium, energy is spread over an increasing area, resulting in an amplitude attenuation with distance. This phenomenon is referred to as geometric or radiation damping. The amplitude of propagating body waves decays as $\mathcal{O}(r^{-1})$ within the medium and as $\mathcal{O}(r^{-2})$ at the free surface (where r indicates the distance travelled from the source). Rayleigh and Love waves, on the other hand, are confined to the surface and their amplitudes only decay as $\mathcal{O}(r^{-1/2})$; surface waves consequently dominate the free field response in the far field. The dissipation of energy in the soil, caused by several mechanisms such as friction between individual particles, is denoted

as material damping. In soil dynamics, material damping is often assumed to be rate independent and can be modelled in the frequency domain using hysteretic material damping ratios [91]. Application of the correspondence principle [120] results in complex elastic moduli $(\lambda + 2\mu)^{\dagger} = (\lambda + 2\mu)(1 + 2\beta_{\mathrm{p}} i)$ and $\mu^{\dagger} = \mu(1 + 2\beta_{\mathrm{s}} i)$, where β_{p} and β_{s} represent hysteretic material damping ratios in volumetric and deviatoric deformation, respectively. A first order Taylor expansion for small values of β_{p} and β_{s} yields complex wave velocities $C_{\mathrm{p}}^{\dagger} \simeq C_{\mathrm{p}}(1 + \beta_{\mathrm{p}} i)$ and $C_{\mathrm{s}}^{\dagger} \simeq C_{\mathrm{s}}(1 + \beta_{\mathrm{s}} i)$.

2.1.2 Green's functions of a layered halfspace: the direct stiffness method

The elastodynamic state of a medium due to a concentrated harmonic load is referred to as the Green's function or fundamental solution of the medium [154]. The load is applied at a source point $\mathbf{x}'$ in a direction $\mathbf{e}_i$ and is written as a body force $\rho\hat{\mathbf{b}}(\mathbf{x}, \omega)$:

$$\rho\hat{\mathbf{b}}(\mathbf{x}, \omega) = \delta(\mathbf{x} - \mathbf{x}')\,\mathbf{e}_i \tag{2.8}$$

The resulting displacements at a receiver $\mathbf{x}$ in a direction $\mathbf{e}_j$ are denoted as the Green's displacements $\hat{u}_{ij}^{\mathrm{G}}(\mathbf{x}', \mathbf{x}, \omega)$, while the tractions on a plane characterized by a unit outward normal vector $\mathbf{n}$ are written as $\hat{t}_{ij}^{\mathrm{G}\mathbf{n}}(\mathbf{x}', \mathbf{x}, \omega)$. Green's functions are an indispensable ingredient of boundary integral formulations, as will be elucidated in section 2.2.

The Green's functions of a medium depend on the geometry, the boundary conditions, and the constitutive behaviour. For the particular configuration of a homogeneous full space, closed form analytical expressions can be found in the literature [43, 86]. This is not the case for a horizontally layered halfspace, however, which implies that the Green's functions have to be computed numerically. Within the frame of the present work, the direct stiffness method [87] is employed for their computation by means of the MATLAB toolbox EDT [130]. This method provides element stiffness matrices for homogeneous layers and a homogeneous halfspace, formulated in the frequency–wavenumber domain. The stiffness matrix of a horizontally layered halfspace is obtained from the assembly of the element stiffness matrices. Solving the corresponding set of equations provides the Green's functions in the frequency–wavenumber domain. An inverse transformation from the wavenumber to the spatial domain is subsequently performed to obtain the Green's functions in the frequency–spatial domain. This is obtained by a numerical transformation algorithm, developed by Talman [144] and improved by Schevenels et al. [129, 130].

The global system size in the direct stiffness method grows for an increasing number of soil layers and the time required to compute the Green's functions for a stratified halfspace increases correspondingly [115]. In cases with a very large number of layers, other numerical methods such as the Haskell–Thomson transfer matrix approach [77, 146] may provide a more efficient alternative. Nonetheless, the direct stiffness method has some appealing advantages compared to the latter method, such as the fact that stiffness matrices are symmetric, involve half as many degrees of freedom as transfer matrices, and remain robust and stable for thick layers and/or high frequencies if limiting expressions are implemented; transfer matrices, on the other hand, contain terms of exponential growth that require special consideration and treatment [6, 44, 102]. A more elaborate comparison of the direct stiffness and the propagator matrix method is given by Kausel [86].

2.2 The boundary element method in elastodynamics

The boundary element method is well suited to model wave propagation in a stratified halfspace, as the radiation of waves towards infinity is inherently taken into account. Moreover, a reduction of the spatial problem dimension is obtained due to the fact that only the boundaries of the domain have to be discretized. This section aims at introducing the main theoretical and numerical aspects of the method; the reader is referred to the literature for a comprehensive overview of boundary element methods in elastodynamics [22, 43, 103]. The structure of this section is inspired by [51].

2.2.1 The dynamic reciprocity theorem

The dynamic reciprocity theorem forms the basis of all boundary integral equations in elastodynamics. This theorem relates two elastodynamic states of a medium and is an extension of the classical reciprocity theorem of Betti–Rayleigh in elastostatics [154].

Let displacements $\hat{\mathbf{u}}_1(\mathbf{x}, \omega)$, tractions $\hat{\mathbf{t}}_1^{\mathbf{n}}(\mathbf{x}, \omega)$, and body forces $\rho\hat{\mathbf{b}}_1(\mathbf{x}, \omega)$ be associated with a first elastodynamic state of a domain Ω with boundary Σ; a second state is defined analogously. The dynamic reciprocity theorem specifies the relationship between this pair of elastodynamic states and reads as follows

in the frequency domain:

$$\int_\Sigma \hat{\mathbf{t}}_1^{\mathbf{n}}(\mathbf{x},\omega)\cdot\hat{\mathbf{u}}_2(\mathbf{x},\omega)\,\mathrm{d}S + \int_\Omega \rho\hat{\mathbf{b}}_1(\mathbf{x},\omega)\cdot\hat{\mathbf{u}}_2(\mathbf{x},\omega)\,\mathrm{d}V = \int_\Sigma \hat{\mathbf{t}}_2^{\mathbf{n}}(\mathbf{x},\omega)\cdot\hat{\mathbf{u}}_1(\mathbf{x},\omega)\,\mathrm{d}S + \int_\Omega \rho\hat{\mathbf{b}}_2(\mathbf{x},\omega)\cdot\hat{\mathbf{u}}_1(\mathbf{x},\omega)\,\mathrm{d}V \quad (2.9)$$

2.2.2 Boundary integral equation

Equation (2.9) can be employed to formulate an integral equation relating the field variables of an unknown elastodynamic state to a known fundamental state of the domain Ω. The known state is characterized by the Green's displacements $\hat{u}_{ij}^{\mathrm{G}}(\mathbf{x}',\mathbf{x},\omega)$ and tractions $\hat{t}_{ij}^{\mathrm{G}\mathbf{n}}(\mathbf{x}',\mathbf{x},\omega)$ as induced by the body force defined in equation (2.8), while displacements $\hat{\mathbf{u}}(\mathbf{x},\omega)$ and tractions $\hat{\mathbf{t}}^{\mathbf{n}}(\mathbf{x},\omega)$ are associated with the unknown state. In the absence of body forces $\rho\hat{\mathbf{b}}(\mathbf{x},\omega)$ in this state, equation (2.9) becomes a boundary integral equation relating the displacement $\hat{u}_i(\mathbf{x}',\omega)$ in a point $\mathbf{x}'$ to the elastodynamic state on the boundary Σ [154]:

$$\kappa\hat{u}_i(\mathbf{x}',\omega) = \int_\Sigma \left(\hat{u}_{ij}^{\mathrm{G}}(\mathbf{x}',\mathbf{x},\omega)\hat{t}_j^{\mathbf{n}}(\mathbf{x},\omega) - \hat{t}_{ij}^{\mathrm{G}\mathbf{n}}(\mathbf{x}',\mathbf{x},\omega)\hat{u}_j(\mathbf{x},\omega)\right)\mathrm{d}S \quad (2.10)$$

In equation (2.10), $\kappa = 1$ when the point $\mathbf{x}'$ is located inside the domain Ω and $\kappa = 0$ if the point $\mathbf{x}'$ is located outside the domain Ω. The boundary integral equation (2.10) does not hold for points $\mathbf{x}'$ located on the boundary Σ due to the singular behaviour of the Green's functions. A classical limiting procedure [22, 43] results in Somigliana's identity, involving the evaluation of Cauchy principal value (CPV) integrals of the strongly singular Green's tractions. Dedicated techniques have been developed for the evaluation of these integrals [73]. The evaluation of CPV integrals is avoided in this dissertation, however, through the use of a regularized boundary integral equation [7, 22, 121]. The regularization procedure is based on the fact that the singularities of the static and dynamic Green's functions at the source point are similar. In case of an unbounded domain Ω, the regularized boundary integral equation, which is valid for points $\mathbf{x}'$ located on the boundary Σ, reads as follows [22]:

$$\hat{u}_i(\mathbf{x}',\omega) - \int_\Sigma \hat{u}_{ij}^{\mathrm{G}}(\mathbf{x}',\mathbf{x},\omega)\hat{t}_j^{\mathbf{n}}(\mathbf{x},\omega)\,\mathrm{d}S + \int_\Sigma \left(\hat{t}_{ij}^{\mathrm{G}\mathbf{n}}(\mathbf{x}',\mathbf{x},\omega)\hat{u}_j(\mathbf{x},\omega) - t_{ij}^{\mathrm{G}\mathbf{ns}}(\mathbf{x}',\mathbf{x})\hat{u}_j(\mathbf{x}',\omega)\right)\mathrm{d}S = 0 \quad (2.11)$$

where $t_{ij}^{\mathrm{Gns}}(\mathbf{x}', \mathbf{x})$ denotes the static Green's tractions. The integral free term $\hat{u}_i(\mathbf{x}', \omega)$ in equation (2.11) vanishes for a bounded domain Ω.

2.2.3 Boundary element discretization

The regularized boundary integral equation (2.11) can in general not be solved analytically. A spatial discretization of the boundary Σ with an appropriate number of boundary elements is therefore introduced, forming the support for n_{i} interpolation functions $M_k(\mathbf{x})$. The displacement vector $\hat{u}_j(\mathbf{x}, \omega)$ and traction vector $\hat{t}_j^{\mathbf{n}}(\mathbf{x}, \omega)$ in equation (2.11) are discretized as [22]:

$$\hat{u}_j(\mathbf{x}, \omega) \simeq \sum_{k=1}^{n_{\mathrm{i}}} M_k(\mathbf{x}) \hat{u}_j^k(\omega) \tag{2.12}$$

$$\hat{t}_j^{\mathbf{n}}(\mathbf{x}, \omega) \simeq \sum_{k=1}^{n_{\mathrm{i}}} M_k(\mathbf{x}) \hat{t}_j^{\mathbf{n}k}(\omega) \tag{2.13}$$

where $\hat{u}_j^k(\omega)$ and $\hat{t}_j^{\mathbf{n}k}(\omega)$ correspond to the j^{th} component of the displacement vector $\hat{\mathbf{u}}(\mathbf{x}_k, \omega)$ and the traction vector $\hat{\mathbf{t}}^{\mathbf{n}}(\mathbf{x}_k, \omega)$ at an interpolation node $\mathbf{x}_k$, respectively. The same interpolation functions $M_k(\mathbf{x})$ are employed for the discretization of the displacements and tractions in equations (2.12) and (2.13). Although it is possible to use different interpolation functions, this is a convenient choice as it results in a square system of equations. It is common to choose the interpolation nodes $\mathbf{x}_k$ at the center of the boundary elements and to use piecewise constant interpolation functions for both displacements and tractions. An alternative is the isoparametrical approach where the interpolation nodes correspond to the geometrical nodes of the boundary element mesh; this strategy is especially appealing if the boundary elements are coupled to finite elements (as will be discussed in section 2.4).

Introducing equations (2.12) and (2.13) into equation (2.11) results in a discretized boundary integral equation. In a collocation approach, this equation is enforced at a finite number of collocation points $\mathbf{x}' = \mathbf{x}_l$ on Σ:

$$\begin{aligned} \hat{u}_i(\mathbf{x}_l, \omega) - \int_\Sigma \sum_{k=1}^{n_{\mathrm{i}}} \left(M_k(\mathbf{x}) \hat{u}_{ij}^{\mathrm{G}}(\mathbf{x}_l, \mathbf{x}, \omega) \hat{t}_j^{\mathbf{n}k}(\omega) \right) \mathrm{d}S \\ + \int_\Sigma \left(\sum_{k=1}^{n_{\mathrm{i}}} \left(M_k(\mathbf{x}) \hat{t}_{ij}^{\mathrm{G}\mathbf{n}}(\mathbf{x}_l, \mathbf{x}, \omega) \hat{u}_j^k(\omega) \right) - t_{ij}^{\mathrm{G}\mathbf{n}\mathrm{s}}(\mathbf{x}_l, \mathbf{x}) \hat{u}_j^l(\omega) \right) \mathrm{d}S = 0 \end{aligned} \tag{2.14}$$

Collocation in conjunction with constant or isoparametrical shape functions $M_k(\mathbf{x})$ is referred to as an element or nodal collocated boundary element approach, respectively. The collocation points $\mathbf{x}_l$ are usually chosen to coincide with the interpolation nodes $\mathbf{x}_k$, as this choice leads to as many equations as unknowns. The resulting algebraic system of equations reads as:

$$\left[\widehat{\mathbf{T}}(\omega) + \mathbf{I}\right] \underline{\hat{\mathbf{u}}}(\omega) = \widehat{\mathbf{U}}(\omega)\underline{\hat{\mathbf{t}}}(\omega) \tag{2.15}$$

where the vectors $\underline{\hat{\mathbf{u}}}(\omega)$ and $\underline{\hat{\mathbf{t}}}(\omega)$ collect the displacements and tractions at the collocations points, respectively. The system matrices $\widehat{\mathbf{U}}(\omega)$ and $\widehat{\mathbf{T}}(\omega)$ follow from equation (2.14) and require integration of the Green's functions over Σ. The boundary integrals are at most weakly singular (as a regularized boundary integral equation is used) and are evaluated using classical Gaussian integration. $\mathbf{I}$ represents a unit matrix, corresponding to the integral free term in equation (2.14); this term vanishes for a bounded domain. The incorporation of Green's functions of a layered halfspace in equation (2.14) is beneficial, as this avoids the necessity to discretize the free surface and the layer interfaces.

Depending on whether a Neumann, Dirichlet or mixed Neumann–Dirichlet problem is considered, equation (2.15) is solved for unknown displacements, tractions, or both. Once the displacements $\underline{\hat{\mathbf{u}}}(\omega)$ and tractions $\underline{\hat{\mathbf{t}}}(\omega)$ on Σ are known, the displacements at a receiver $\mathbf{x}_\mathrm{r}$ in the domain Ω can be computed through the discretized version of the integral representation theorem (2.10):

$$\underline{\hat{\mathbf{u}}}_\mathrm{r}(\omega) = \widehat{\mathbf{U}}_\mathrm{r}(\omega)\underline{\hat{\mathbf{t}}}(\omega) - \widehat{\mathbf{T}}_\mathrm{r}(\omega)\underline{\hat{\mathbf{u}}}(\omega) \tag{2.16}$$

where $\widehat{\mathbf{U}}_\mathrm{r}(\omega)$ and $\widehat{\mathbf{T}}_\mathrm{r}(\omega)$ are boundary element transfer matrices, requiring integration of the Green's functions.

The boundary element method may suffer from the occurrence of fictitious eigenfrequencies if applied to external wave propagation problems. This is the case when the excitation frequency coincides with an eigenfrequency of the corresponding interior domain with Dirichlet boundary conditions on Σ. The Combined Helmholtz Integral Equation Formulation (CHIEF) [128], which is based on enforcing the integral representation theorem (2.10) in a number of randomly distributed points in the interior domain, is used in this dissertation to overcome this problem.

The system matrices $\widehat{\mathbf{U}}(\omega)$ and $\widehat{\mathbf{T}}(\omega)$ in equation (2.15) are fully populated and unsymmetric; the unsymmetry is caused by the application of point collocation. Symmetric matrices can alternatively be obtained if a Galerkin approach is followed, where the discretized equation (2.14) is weighted over the boundary elements [22, 23]. The Galerkin approach is known to be more accurate than than the collocation method, but has as main disadvantage that it

involves a double integration of the Green's functions, which is computationally expensive [23]. Within the frame of the present work, only collocation boundary element formulations are therefore employed.

2.2.4 Two–and–a–half–dimensional formulation

The dense matrices $\widehat{\mathbf{U}}(\omega)$ and $\widehat{\mathbf{T}}(\omega)$ lead to stringent memory and CPU requirements, hindering the applicability of the BE method to large scale 3D problems. In order to obtain a substantial reduction of the computational effort, the geometry of the problem is in some cases assumed to be periodic or invariant in the longitudinal direction, e.g. for roads, railway tracks, tunnels, dams, vibration isolation screens, lifelines, and alluvial valleys [140, 142] (figure 2.3). For a periodic lay–out, a Floquet transform can be employed to formulate the governing equations in a reference cell [33, 36]. In the case of a longitudinally invariant geometry, a forward Fourier transform from the longitudinal coordinate y to the wavenumber k_y allows representing the 3D response on a 2D mesh, resulting in a two–and–a–half–dimensional (2.5D) approach in the frequency–wavenumber domain [137, 141]. The substantial reduction of the number of degrees of freedom (and the associated matrix dimensions) makes this approach computationally very efficient. The Fourier transformation pair relating y and k_y is defined as follows:

$$\tilde{f}(k_y) = \mathscr{F}\left[f(y), k_y\right] = \int_{-\infty}^{+\infty} f(y) \exp\left(ik_y y\right) \, \mathrm{d}y \tag{2.17}$$

$$f(y) = \mathscr{F}^{-1}\left[\tilde{f}(k_y), y\right] = \frac{1}{2\pi} \int_{-\infty}^{+\infty} \tilde{f}(k_y) \exp\left(-ik_y y\right) \, \mathrm{d}k_y \tag{2.18}$$

where a tilde above a variable denotes its representation in the frequency–wavenumber domain.

The 2.5D boundary element method is based on a 2.5D boundary integral equation. The latter can be derived from the 2.5D reciprocity theorem [134] or from the 3D integral representation theorem (2.10) [56] and reads as follows:

$$\begin{aligned} \kappa\tilde{u}_i(x', k_y, z', \omega) = &\int_S \tilde{u}_{ij}^{\mathrm{G}}(x', 0, z', x, -k_y, z, \omega)\tilde{t}_j^{\mathbf{n}}(x, k_y, z, \omega) \, \mathrm{d}S \\ &- \int_S \tilde{t}_{ij}^{\mathrm{G}\mathbf{n}}(x', 0, z', x, -k_y, z, \omega)\tilde{u}_j(x, k_y, z, \omega) \, \mathrm{d}S \end{aligned} \tag{2.19}$$

where S is the intersection of the boundary Σ with the plane $y = 0$. A regularization procedure proposed by François et al. [56] is employed in this

dissertation to obtain a regularized 2.5D boundary integral equation, which is discretized by means of two–dimensional boundary elements. Application of point collocation finally provides an algebraic system of equations relating the displacements $\underline{\tilde{\mathbf{u}}}(k_y,\omega)$ and tractions $\underline{\tilde{\mathbf{t}}}(k_y,\omega)$ at the collocation points:

$$\left[\widetilde{\mathbf{T}}(k_y,\omega)+\mathbf{I}\right]\underline{\tilde{\mathbf{u}}}(k_y,\omega)=\widetilde{\mathbf{U}}(k_y,\omega)\underline{\tilde{\mathbf{t}}}(k_y,\omega) \tag{2.20}$$

where $\widetilde{\mathbf{U}}(k_y,\omega)$ and $\widetilde{\mathbf{T}}(k_y,\omega)$ are wavenumber dependent BE matrices. As in 3D boundary element formulations, Green's functions of a full space [141] or a layered halfspace [130] can be incorporated in the 2.5D approach. Upon solution of equation (2.20), the radiated wavefield $\underline{\tilde{\mathbf{u}}}_{\mathrm{r}}(k_y,\omega)$ can be computed by means of the discretized 2.5D representation theorem in the frequency–wavenumber domain:

$$\underline{\tilde{\mathbf{u}}}_{\mathrm{r}}(k_y,\omega)=\widetilde{\mathbf{U}}_{\mathrm{r}}(k_y,\omega)\underline{\tilde{\mathbf{t}}}(k_y,\omega)-\widetilde{\mathbf{T}}_{\mathrm{r}}(k_y,\omega)\underline{\tilde{\mathbf{u}}}(k_y,\omega) \tag{2.21}$$

The application of a 2.5D formulation in the frequency–wavenumber domain implies that the equations have to be assembled and solved for each wavenumber k_y. The response in the frequency–spatial domain can finally be found by means of an inverse Fourier transform from the wavenumber k_y to the longitudinal coordinate y, using an efficient Filon quadrature scheme [49].

The MATLAB toolbox BEMFUN [54] developed by François et al. is employed throughout this dissertation for evaluating 3D and 2.5D boundary element models. All the aspects outlined in section 2.2 are incorporated in this toolbox, such as the computation of the boundary element system and transfer matrices, the CHIEF method for mitigating the occurrence of fictitious eigenfrequencies, etcetera.

2.3 The finite element method in structural dynamics

2.3.1 Principle of virtual work

Consider a domain Ω with boundary $\Gamma=\Gamma_u\cup\Gamma_\sigma$; Dirichlet and Neumann boundary conditions are imposed on Γ_u and Γ_σ, respectively. The dynamic equilibrium of Ω can be expressed in a weak variational form based on the principle of virtual work. For any virtual displacement field $\hat{\mathbf{v}}(\mathbf{x},\omega)$ imposed on Ω that satisfies the Dirichlet boundary conditions on Γ_u, the sum of the

virtual work of the internal and inertial forces is equal to the virtual work of the external loads $\rho\hat{\mathbf{b}}(\mathbf{x},\omega)$ on Ω and $\hat{\bar{\mathbf{t}}}^{\mathbf{n}}(\mathbf{x},\omega)$ on Γ_σ:

$$\int_\Omega \hat{\boldsymbol{\epsilon}}(\hat{\mathbf{v}}(\mathbf{x},\omega)) : \hat{\boldsymbol{\sigma}}(\hat{\mathbf{u}}(\mathbf{x},\omega))\,\mathrm{d}V - \omega^2 \int_\Omega \hat{\mathbf{v}}(\mathbf{x},\omega)\cdot\rho\hat{\mathbf{u}}(\mathbf{x},\omega)\,\mathrm{d}V = \int_\Omega \hat{\mathbf{v}}(\mathbf{x},\omega)\cdot\rho\hat{\mathbf{b}}(\mathbf{x},\omega)\,\mathrm{d}V + \int_{\Gamma_\sigma} \hat{\mathbf{v}}(\mathbf{x},\omega)\cdot\hat{\bar{\mathbf{t}}}^{\mathbf{n}}(\mathbf{x},\omega)\,\mathrm{d}S \quad (2.22)$$

The strain–displacement relation (2.3) and the constitutive equation (2.4) are subsequently introduced in equation (2.22) together with the finite element discretization $\hat{\mathbf{u}}(\mathbf{x},\omega) \simeq \mathbf{N}(\mathbf{x})\hat{\underline{\mathbf{u}}}(\omega)$, where $\mathbf{N}(\mathbf{x})$ represents the globally defined shape functions and $\hat{\underline{\mathbf{u}}}(\omega)$ collects the degrees of freedom at all nodal points. Application of a standard Galerkin procedure provides the following set of finite element equations [165]:

$$\left[\mathbf{K} - \omega^2\mathbf{M}\right]\hat{\underline{\mathbf{u}}}(\omega) = \hat{\underline{\mathbf{f}}}(\omega) \quad (2.23)$$

where $\mathbf{K}$ and $\mathbf{M}$ are the structural stiffness and mass matrices, respectively. The bracketed term on the left hand side of equation (2.23) is identified as the dynamic stiffness matrix $\widehat{\mathbf{K}}(\omega) = \mathbf{K} - \omega^2\mathbf{M}$ of the structure. The effect of material damping can be included through addition of $i\omega\mathbf{C}$ to $\widehat{\mathbf{K}}(\omega)$; $\mathbf{C}$ represents the damping matrix. The force vector $\hat{\underline{\mathbf{f}}}(\omega)$ results from the body forces $\rho\hat{\mathbf{b}}(\mathbf{x},\omega)$ on Ω and the tractions $\hat{\bar{\mathbf{t}}}^{\mathbf{n}}(\mathbf{x},\omega)$ on Γ_σ. Adequate numerical solvers that account for the sparsity and symmetry of the system can be employed to solve equation (2.23).

2.3.2 Two–and–a–half–dimensional formulation

As for the boundary element method (subsection 2.2.4), a 2.5D strategy can also be applied for finite element calculations in case of longitudinally invariant structures. The wavenumber dependent counterpart of equation (2.23) reads as [56]:

$$\left[\mathbf{K}_0 - ik_y\mathbf{K}_1 - k_y^2\mathbf{K}_2 + ik_y^3\mathbf{K}_3 + k_y^4\mathbf{K}_4 - \omega^2\mathbf{M}\right]\tilde{\underline{\mathbf{u}}}(k_y,\omega) = \tilde{\underline{\mathbf{f}}}(k_y,\omega) \quad (2.24)$$

The stiffness matrices $\mathbf{K}_0$ to $\mathbf{K}_4$ as well as the mass matrix $\mathbf{M}$ are independent of the wavenumber k_y and the frequency ω and are therefore only assembled once [56].

2.4 Coupling of FE and BE models

The coupling of finite elements and boundary elements allows for the efficient solution of dynamic soil–structure interaction problems, using the subdomain formulation developed by Aubry and Clouteau [8, 9, 34]. It is assumed in the following that finite elements are used to model the structural domain Ω_b, while boundary elements are employed to model wave propagation in the surrounding soil domain Ω_s; subscripts 'b' and 's' are introduced to differentiate between the structure and the soil. The domain Ω_b represents a generalized structure, comprising the actual structure and part of the soil domain, as depicted in figure 2.2. Within the frame of the present work, only conforming interface discretizations are employed, where the coupling conditions (continuity of displacements and equilibrium of tractions at the soil–structure interface Σ) are imposed in a strong sense:

$$\hat{\mathbf{u}}_\mathrm{b}(\mathbf{x},\omega) - \hat{\mathbf{u}}_\mathrm{s}(\mathbf{x},\omega) = \mathbf{0} \qquad \text{on } \Sigma \tag{2.25}$$

$$\hat{\mathbf{t}}_\mathrm{b}^{\mathbf{n}_\mathrm{b}}(\mathbf{x},\omega) + \hat{\mathbf{t}}_\mathrm{s}^{\mathbf{n}_\mathrm{s}}(\mathbf{x},\omega) = \mathbf{0} \qquad \text{on } \Sigma \tag{2.26}$$

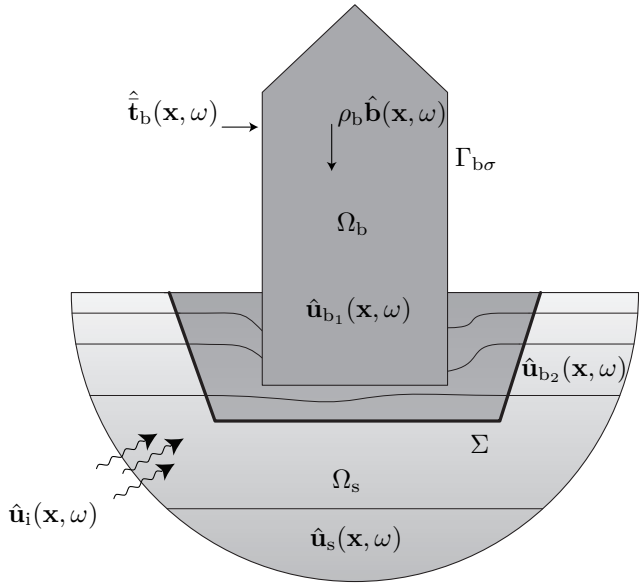

Figure 2.2: Geometry of the subdomains: structural domain Ω_b and soil domain Ω_s [51].

The wavefield in the soil $\hat{\mathbf{u}}_\mathrm{s}(\mathbf{x},\omega)$ is decomposed into the incident wavefield $\hat{\mathbf{u}}_\mathrm{i}(\mathbf{x},\omega)$, the locally diffracted wavefield $\hat{\mathbf{u}}_\mathrm{d0}(\mathbf{x},\omega)$, and the scattered wavefield $\hat{\mathbf{u}}_\mathrm{sc}(\mathbf{x},\omega)$ [8, 9, 34]. The latter corresponds to the displacement field radiated by structural displacements on Σ, while $\hat{\mathbf{u}}_\mathrm{d0}(\mathbf{x},\omega)$ is defined so that the combined wavefield $\hat{\mathbf{u}}_\mathrm{i}(\mathbf{x},\omega) + \hat{\mathbf{u}}_\mathrm{d0}(\mathbf{x},\omega)$ vanishes on Σ. In a classical direct coupling strategy [153], the coupling conditions (2.25)–(2.26) are straightforwardly introduced into the virtual work equation (2.22) of the structural domain Ω_b, accounting for the decomposition of the wavefield in the soil. This results in a global coupled system of equations:

$$\left[\widehat{\mathbf{K}}_\mathrm{b}(\omega) + \widehat{\mathbf{K}}^\mathrm{s}_\mathrm{b}(\omega)\right] \underline{\hat{\mathbf{u}}}_\mathrm{b}(\omega) = \underline{\hat{\mathbf{f}}}_\mathrm{b}(\omega) + \underline{\hat{\mathbf{f}}}^\mathrm{s}_\mathrm{b}(\omega) \tag{2.27}$$

where $\widehat{\mathbf{K}}^\mathrm{s}_\mathrm{b}(\omega)$ represents the dynamic soil stiffness matrix. The additional force vector $\underline{\hat{\mathbf{f}}}^\mathrm{s}_\mathrm{b}(\omega)$ is due to the incident wavefield $\hat{\mathbf{u}}_\mathrm{i}(\mathbf{x},\omega)$ impinging on Σ [8, 9]. A subdivision of equation (2.27) into block matrices according to internal degrees of freedom $\underline{\hat{\mathbf{u}}}_{\mathrm{b}_1}(\omega)$ in the structural domain Ω_b and degrees of freedom $\underline{\hat{\mathbf{u}}}_{\mathrm{b}_2}(\omega)$ on the soil–structure interface Σ yields:

$$\left(\begin{bmatrix} \widehat{\mathbf{K}}_{\mathrm{b}_1\mathrm{b}_1}(\omega) & \widehat{\mathbf{K}}_{\mathrm{b}_1\mathrm{b}_2}(\omega) \\ \widehat{\mathbf{K}}_{\mathrm{b}_2\mathrm{b}_1}(\omega) & \widehat{\mathbf{K}}_{\mathrm{b}_2\mathrm{b}_2}(\omega) \end{bmatrix} + \begin{bmatrix} \mathbf{0} & \mathbf{0} \\ \mathbf{0} & \widehat{\mathbf{K}}^\mathrm{s}_{\mathrm{b}_2\mathrm{b}_2}(\omega) \end{bmatrix} \right) \begin{Bmatrix} \underline{\hat{\mathbf{u}}}_{\mathrm{b}_1}(\omega) \\ \underline{\hat{\mathbf{u}}}_{\mathrm{b}_2}(\omega) \end{Bmatrix} = \begin{Bmatrix} \underline{\hat{\mathbf{f}}}_{\mathrm{b}_1}(\omega) \\ \underline{\hat{\mathbf{f}}}_{\mathrm{b}_2}(\omega) \end{Bmatrix} + \begin{Bmatrix} \underline{\mathbf{0}} \\ \underline{\hat{\mathbf{f}}}^\mathrm{s}_{\mathrm{b}_2}(\omega) \end{Bmatrix} \tag{2.28}$$

The dynamic soil stiffness matrix $\widehat{\mathbf{K}}^\mathrm{s}_{\mathrm{b}_2\mathrm{b}_2}(\omega)$ is calculated as:

$$\begin{aligned} \widehat{\mathbf{K}}^\mathrm{s}_{\mathrm{b}_2\mathrm{b}_2}(\omega) &= \int_\Sigma \mathbf{N}^\mathrm{T}_{\mathrm{b}_2}(\mathbf{x}) \mathbf{N}_{\mathrm{b}_2}(\mathbf{x}) \underline{\hat{\mathbf{t}}}(\mathbf{N}_{\mathrm{b}_2}(\mathbf{x}))(\omega)\, \mathrm{d}S \\ &= \mathbf{T}_\mathrm{q}\, \underline{\hat{\mathbf{t}}}(\mathbf{N}_{\mathrm{b}_2}(\mathbf{x}))(\omega) \end{aligned} \tag{2.29}$$

where $\mathbf{N}_{\mathrm{b}_2}(\mathbf{x})$ indicates the FE shape functions on the soil–structure interface Σ, conforming with the BE interpolation functions. The matrix $\widehat{\mathbf{K}}^\mathrm{s}_{\mathrm{b}_2\mathrm{b}_2}(\omega)$ is dense and unsymmetric; its computation requires the evaluation of tractions $\underline{\hat{\mathbf{t}}}(\mathbf{N}_{\mathrm{b}_2}(\mathbf{x}))(\omega)$ by means of the BE method, which requires the solution of equation (2.15) for all shape functions $\mathbf{N}_{\mathrm{b}_2}(\mathbf{x})$ on Σ. Addition of this matrix to $\widehat{\mathbf{K}}_\mathrm{b}(\omega)$ strongly affects the sparsity of the system, reducing the efficiency of sparse FE solvers. The frequency independent matrix $\mathbf{T}_\mathrm{q} = \int_\Sigma \mathbf{N}^\mathrm{T}_{\mathrm{b}_2}(\mathbf{x}) \mathbf{N}_{\mathrm{b}_2}(\mathbf{x})\, \mathrm{d}S$ links the FE and BE discretizations. The force vector

$\underline{\hat{\mathbf{f}}}^{\mathrm{s}}_{\mathrm{b}_2}(\omega)$ is defined as:

$$\begin{aligned}\underline{\hat{\mathbf{f}}}^{\mathrm{s}}_{\mathrm{b}_2}(\omega) &= -\int_{\Sigma} \mathbf{N}^{\mathrm{T}}_{\mathrm{b}_2}(\mathbf{x})\mathbf{N}_{\mathrm{b}_2}(\mathbf{x})\underline{\hat{\mathbf{t}}}\left(\hat{\mathbf{u}}_{\mathrm{i}}(\mathbf{x},\omega)+\hat{\mathbf{u}}_{\mathrm{d}0}(\mathbf{x},\omega)\right)\,\mathrm{d}S \\ &= -\mathbf{T}_{\mathrm{q}}\,\underline{\hat{\mathbf{t}}}\left(\hat{\mathbf{u}}_{\mathrm{i}}(\mathbf{x},\omega)+\hat{\mathbf{u}}_{\mathrm{d}0}(\mathbf{x},\omega)\right) \end{aligned} \tag{2.30}$$

The computational effort in this direct coupling strategy can be limited by considering a reduced kinematic basis for the displacement vector $\underline{\hat{\mathbf{u}}}_{\mathrm{b}_2}(\omega)$ on the interface Σ through the introduction of a modal decomposition $\underline{\hat{\mathbf{u}}}_{\mathrm{b}_2}(\omega) \simeq \boldsymbol{\Psi}_{\mathrm{b}_2}\underline{\hat{\boldsymbol{\alpha}}}(\omega)$, where $\boldsymbol{\Psi}_{\mathrm{b}_2}$ and $\underline{\hat{\boldsymbol{\alpha}}}(\omega)$ collect the mode shapes and the modal coordinates, respectively [33]. This allows rewriting equation (2.28) in terms of modal coordinates $\underline{\hat{\boldsymbol{\alpha}}}(\omega)$, and only a modal soil stiffness matrix $\boldsymbol{\Psi}^{\mathrm{T}}_{\mathrm{b}_2}\widehat{\mathbf{K}}^{\mathrm{s}}_{\mathrm{b}_2\mathrm{b}_2}(\omega)\boldsymbol{\Psi}_{\mathrm{b}_2}$ with dimensions $(n_{\mathrm{m}_2} \times n_{\mathrm{m}_2})$ has to be computed:

$$\boldsymbol{\Psi}^{\mathrm{T}}_{\mathrm{b}_2}\widehat{\mathbf{K}}^{\mathrm{s}}_{\mathrm{b}_2\mathrm{b}_2}(\omega)\boldsymbol{\Psi}_{\mathrm{b}_2} = \int_{\Sigma} \left(\mathbf{N}_{\mathrm{b}_2}(\mathbf{x})\boldsymbol{\Psi}_{\mathrm{b}_2}\right)^{\mathrm{T}} \mathbf{N}_{\mathrm{b}_2}(\mathbf{x})\underline{\hat{\mathbf{t}}}(\mathbf{N}_{\mathrm{b}_2}(\mathbf{x})\boldsymbol{\Psi}_{\mathrm{b}_2})(\omega)\,\mathrm{d}S \tag{2.31}$$

As a result, equation (2.15) is only solved n_{m_2} times for tractions $\underline{\hat{\mathbf{t}}}(\mathbf{N}_{\mathrm{b}_2}(\mathbf{x})\boldsymbol{\Psi}_{\mathrm{b}_2})(\omega)$; the number of modes n_{m_2} is generally much lower than the number of degrees of freedom n_{dof_2} on the interface Σ. As the modal soil stiffness matrix is calculated directly through equation (8), it is not required to use a conforming FE–BE discretization on Σ in this approach [51]. Although a substantial reduction in computation time can be achieved compared to the use of a full kinematic basis, the resulting modal soil stiffness matrix $\boldsymbol{\Psi}^{\mathrm{T}}_{\mathrm{b}_2}\widehat{\mathbf{K}}^{\mathrm{s}}_{\mathrm{b}_2\mathrm{b}_2}(\omega)\boldsymbol{\Psi}_{\mathrm{b}_2}$ remains dense and unsymmetric. Furthermore, an appropriate choice of the modes $\boldsymbol{\Psi}_{\mathrm{b}_2}$ is required for obtaining accurate results.

Solving equation (2.28) provides the displacement vectors $\underline{\hat{\mathbf{u}}}_{\mathrm{b}_1}(\omega)$ and $\underline{\hat{\mathbf{u}}}_{\mathrm{b}_2}(\omega)$; the latter corresponds to the soil displacement vector $\underline{\hat{\mathbf{u}}}_{\mathrm{s}}(\omega)$ on the soil–structure interface Σ due to continuity. The BE equations allow to retrieve the soil tractions $\underline{\hat{\mathbf{t}}}_{\mathrm{s}}(\omega) = \widehat{\mathbf{U}}^{-1}(\omega)\left(\widehat{\mathbf{T}}(\omega)+\mathbf{I}\right)\underline{\hat{\mathbf{u}}}_{\mathrm{s}}(\omega)$. The displacements $\underline{\hat{\mathbf{u}}}_{\mathrm{s}}(\omega)$ and tractions $\underline{\hat{\mathbf{t}}}_{\mathrm{s}}(\omega)$ on Σ are subsequently used to evaluate the scattered wavefield $\underline{\hat{\mathbf{u}}}_{\mathrm{sc}}(\omega)$ in the soil through the discretized boundary integral equation (2.10).

Equation (2.27) provides a straightforward solution to the dynamic SSI problem in case a single structure Ω_{b} is considered. If N structures Ω_j are present $(j = 1 \ldots N)$, however, equation (2.27) is generalized and becomes:

$$\widehat{\mathbf{K}}_j(\omega)\underline{\hat{\mathbf{u}}}_j(\omega) + \sum_{k=1}^{N} \widehat{\mathbf{K}}^{\mathrm{s}}_{jk}(\omega)\underline{\hat{\mathbf{u}}}_k(\omega) = \underline{\hat{\mathbf{f}}}_j(\omega) + \underline{\hat{\mathbf{f}}}^{\mathrm{s}}_j(\omega) \quad \text{for} \quad j = 1 \ldots N \tag{2.32}$$

where the dynamic soil stiffness matrices $\widehat{\mathbf{K}}^{\mathrm{s}}_{jk}(\omega)$ represent through–soil coupling of Ω_j and Ω_k for $j \neq k$. The BE method is employed for the computation of all these matrices.

Finite elements and boundary elements can also be coupled in the frame of a 2.5D approach in the frequency–wavenumber domain [56, 114] (figure 2.3). The resulting coupled FE–BE equation reads as equation (2.32), where each variable should be replaced by its wavenumber dependent counterpart.

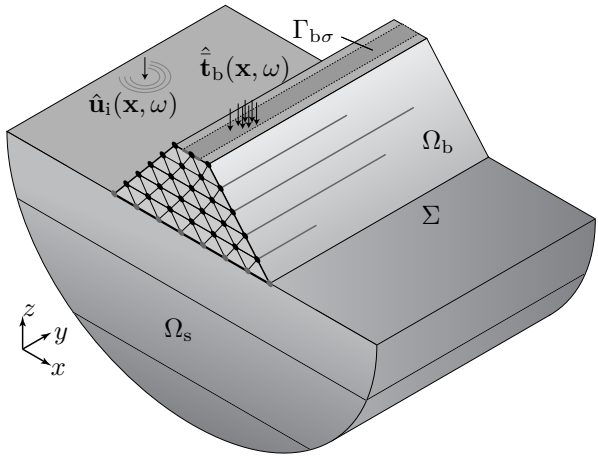

Figure 2.3: The 2.5D dynamic SSI problem.

2.5 Conclusion

In this chapter, the solution of dynamic SSI problems by means of a subdomain formulation is discussed, where boundary elements for the soil are coupled to finite elements for the structure. This well–established coupled FE–BE methodology will be employed throughout the next chapters of this dissertation.

First, the governing equations of wave propagation in the soil as well as the computation of Green's functions of stratified soils using the direct stiffness method have been reviewed. Next, the boundary element method has been introduced, where a regularized boundary integral equation is discretized to obtain an algebraic set of equations, relating displacements and tractions on the boundary of a domain. This method has as advantage that the radiation of waves in the soil is inherently accounted for and that it leads to a reduction

of the spatial problem dimension (i.e. surface instead of volume discretization). The benefits of the BE method are partially negated, however, by the fact that dense matrices arise from the formulation, which limits its applicability to problems of moderate size. The application of a 2.5D approach provides a computationally efficient alternative but remains restricted to longitudinally invariant geometries. The finite element method for modelling the structural domain was subsequently briefly discussed. Finally, the coupling of finite and boundary elements has been addressed, presenting a classical direct coupling strategy that requires the computation of dynamic soil stiffness matrices.

Chapter 3

Fast methods for large scale dynamic SSI problems

As discussed in chapter 2, the numerical solution of large 3D dynamic SSI problems (involving structures with an arbitrary geometry) with a coupled FE–BE methodology remains a challenging task, especially due to the high computational cost associated with BE models. The use of a 2.5D approach is computationally much more efficient but is only applicable to structures with a longitudinally invariant geometry.

This chapter gives a concise overview of innovative numerical methodologies that have been developed within the frame of the present work to overcome the current limitations of 3D and 2.5D FE–BE methods. First, the development of a fast 3D boundary element method that allows incorporating Green's functions of a horizontally layered halfspace is discussed. This method is based on the application of hierarchical matrices ($\mathscr{H}$–matrices) and forms the subject of paper A in Part II of the dissertation. The application of $\mathscr{H}$–matrices affects the efficiency of the FE–BE coupling approach outlined in section 2.4, however. Various FE–$\mathscr{H}$-BE coupling algorithms are therefore presented and their computational performance is assessed through numerical examples (Paper B). Finally, the applicability of 2.5D FE–BE methods for dynamic SSI is extended by means of a technique that accounts for the structures' finite length, while maintaining the computational efficiency of the 2.5D approach (Paper C).

3.1 3D FE–$\mathscr{H}$-BE methods

The boundary element matrices $\widehat{\mathbf{T}}(\omega)$ and $\widehat{\mathbf{U}}(\omega)$ in equation (2.15) relate the displacements $\underline{\hat{\mathbf{u}}}(\omega)$ and tractions $\underline{\hat{\mathbf{t}}}(\omega)$ at the collocations points of the boundary element mesh. These matrices are dense and unsymmetric; their storage requires a quadratic amount of memory ($\mathcal{O}(N_{\mathrm{DOF}}^2)$) with respect to the number of degrees of freedom N_{DOF}. Furthermore, solving equation (2.15) by means of a direct numerical solver such as an LU–decomposition requires a cubic amount of numerical operations ($\mathcal{O}(N_{\mathrm{DOF}}^3)$). The application of the classical boundary element method is for that reason presently limited to problems of moderate size [122].

It is therefore the aim to find approximations of $\widehat{\mathbf{T}}(\omega)$ and $\widehat{\mathbf{U}}(\omega)$ that lead to a reduction of the required memory, while maintaining the desired accuracy. It is unfortunately not possible to find such approximations for the global matrices because of the singular behaviour of the Green's functions along the main diagonal [122]. Nonetheless, some matrix blocks of $\widehat{\mathbf{T}}(\omega)$ and $\widehat{\mathbf{U}}(\omega)$ have low ranks and can be efficiently approximated. This results in so–called $\mathscr{H}$–matrices consisting of collections of block matrices of various sizes. Their application provides an elegant way to treat dense matrices with almost linear complexity [68], as will be elaborated in the following.

3.1.1 Application of $\mathscr{H}$–matrices for the approximation of BE collocation matrices

Hierarchical clustering

The assembly of a $\mathscr{H}$–matrix requires several steps. First, a hierarchical cluster tree is constructed based on the boundary element mesh. At the lowest level (i.e. level 0), the cluster consists of the complete BE mesh. Each cluster is recursively partitioned into two sons. Several techniques are available in order to obtain a suitable cluster tree (e.g. nested dissection [63, 69], cardinality balanced clustering [13], ...). In this work, a clustering strategy based on principal component analysis (PCA) is employed, as this approach is known to provide geometrically well–balanced cluster trees that do not depend on the actual numbering of the collocation points [13, 122]. This technique requires the computation of the covariance matrix $\mathbf{C}$ of each cluster, which is defined as:

$$\mathbf{C} = \sum_{l=1}^{n_{\mathrm{c}}} (\mathbf{x}_l - \mathbf{x}_{\mathrm{c}}) (\mathbf{x}_l - \mathbf{x}_{\mathrm{c}})^{\mathrm{T}} \in \mathbb{R}^{3\times 3} \tag{3.1}$$

where $\mathbf{x}_l$ are the collocation points, while $\mathbf{x}_\mathrm{c}$ represents the geometrical center of the cluster under consideration (containing n_c collocation points). The eigendecomposition of this symmetric matrix reads as:

$$\mathbf{C} = \mathbf{\Phi}\mathbf{\Lambda}\mathbf{\Phi}^\mathrm{T} \tag{3.2}$$

where the diagonal matrix $\mathbf{\Lambda}$ collects the eigenvalues in decreasing order, while $\mathbf{\Phi}$ contains the corresponding orthogonal eigenvectors. The eigenvector $\boldsymbol{\varphi}_1$ corresponding to the largest eigenvalue λ_1 gives the main direction of the cluster. A separation plane through $\mathbf{x}_\mathrm{c}$ and orthogonal to $\boldsymbol{\varphi}_1$ divides the cluster in two (more or less equal) sons: collocation points satisfying $(\mathbf{x}_l - \mathbf{x}_\mathrm{c})^\mathrm{T}\boldsymbol{\varphi}_1 \geq 0$ are attributed to the first son, while the other are attributed to the second. This procedure is recursively applied to every son until the clusters contain less or equal than a prescribed number of collocation points N_min.

For illustrative purposes, the clustering of a unit sphere discretized by means of $N = 3072$ eight node quadrilateral boundary elements with element collocation is visualized in figure 3.1. A minimum number of collocation points $N_\mathrm{min} = 24$ is specified, resulting in $\log_2(3072/24) = 7$ cluster levels.

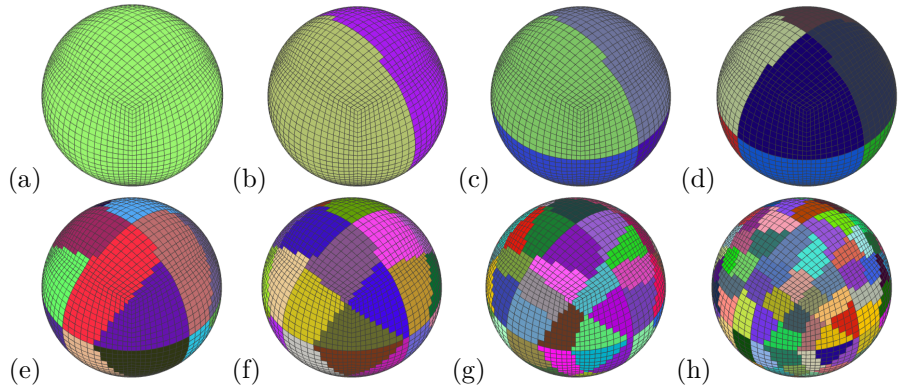

Figure 3.1: Hierarchical clustering of a unit sphere by means of PCA, resulting in (a) 2^0 clusters at level 0, (b) 2^1 clusters at level 1, (c) 2^2 clusters at level 2, (d) 2^3 clusters at level 3, (e) 2^4 clusters at level 4, (f) 2^5 clusters at level 5, (g) 2^6 clusters at level 6 and (h) 2^7 clusters at level 7.

The second step in the assembly of a $\mathscr{H}$–matrix consists of identifying cluster pairs (X, Y) which are geometrically well–separated, i.e. so–called admissible cluster pairs. The interactions between such pairs can be regarded as 'far field' interactions. The following geometric admissibility criterion is employed [11,

122]:

$$\min\{\mathrm{diam(X)}, \mathrm{diam(Y)}\} < \eta \mathrm{dist(X,Y)} \qquad 0 < \eta < 1 \tag{3.3}$$

where diam(X) denotes the maximal extent of cluster X and dist(X, Y) is the minimal distance between clusters X and Y:

$$\mathrm{diam(X)} = \max_{\substack{1 \le i \le n_\mathrm{X}-1 \\ i+1 \le j \le n_\mathrm{X}}} ||\mathbf{x}_{\mathrm{X}_i} - \mathbf{x}_{\mathrm{X}_j}|| \tag{3.4}$$

$$\mathrm{dist(X,Y)} = \min_{\substack{1 \le i \le n_\mathrm{X} \\ 1 \le j \le n_\mathrm{Y}}} ||\mathbf{x}_{\mathrm{X}_i} - \mathbf{x}_{\mathrm{Y}_j}|| \tag{3.5}$$

The parameter η in equation (3.3) controls the number of admissible pairs [24]. Throughout this work, a value $\eta = 0.95$ has been adopted. Cluster pairs not satisfying equation (3.3) are referred to as inadmissible pairs and involve 'near field' interactions. Admissible pairs can be composed of clusters of different levels; inadmissible pairs, on the other hand, always consist of clusters of the lowest level. Examples of an admissible pair (consisting of clusters of levels 4 and 5) and an inadmissible pair (with both clusters belonging to level 7) corresponding to the hierarchical cluster tree presented in figure 3.1 are shown in figure 3.2.

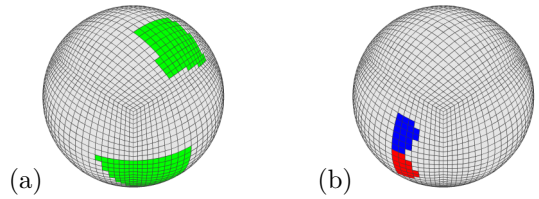

Figure 3.2: (a) Admissible and (b) inadmissible cluster pair (X, Y) corresponding to the hierarchical clustering shown in figure 3.1.

The identification of admissible and inadmissible cluster pairs in the boundary element mesh allows representing the BE matrices $\widehat{\mathbf{U}}(\omega)$ and $\widehat{\mathbf{T}}(\omega)$ as a collection of block matrices of various sizes [122]. This is illustrated in figure 3.3 for the case of the unit sphere, where the blocks corresponding to admissible and inadmissible cluster pairs are depicted in green and red, respectively. Note that the BE degrees of freedom have been reordered in this matrix in accordance with the clustering depicted in figure 3.1.

For an admissible cluster pair (X, Y) (with m and n degrees of freedom in clusters X and Y, respectively), the Green's functions are sufficiently

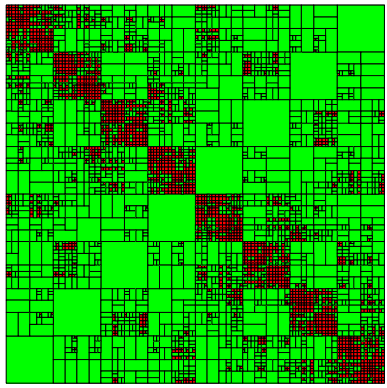

Figure 3.3: Hierarchical matrix decomposition corresponding to a BE model of a unit sphere. The green blocks (corresponding to admissible cluster pairs) are approximated by means of ACA, while the red blocks (corresponding to inadmissible cluster pairs) are computed exactly.

smooth such that the corresponding block BE matrices $\widehat{\mathbf{T}}_{(X,Y)}(\omega) \in \mathbb{C}^{m\times n}$ and $\widehat{\mathbf{U}}_{(X,Y)}(\omega) \in \mathbb{C}^{m\times n}$ can be approximated by low rank approximations. For example, the block matrix $\widehat{\mathbf{T}}_{(X,Y)}(\omega)$ is replaced by its approximation $\widetilde{\widehat{\mathbf{T}}}_{(X,Y)}(\omega)$ of rank k:

$$\widehat{\mathbf{T}}_{(X,Y)}(\omega) \simeq \widetilde{\widehat{\mathbf{T}}}_{(X,Y)}(\omega) = \left(\widehat{\mathbf{V}}_{\mathbf{T}_{(X,Y)}}(\omega)\right)\left(\widehat{\mathbf{W}}_{\mathbf{T}_{(X,Y)}}(\omega)\right)^{\star} \tag{3.6}$$

with $\widehat{\mathbf{V}}_{\mathbf{T}_{(X,Y)}}(\omega) \in \mathbb{C}^{m\times k}$ and $\widehat{\mathbf{W}}_{\mathbf{T}_{(X,Y)}}(\omega) \in \mathbb{C}^{n\times k}$ and where $\star$ indicates the complex conjugate. The computation of the matrices $\widehat{\mathbf{V}}_{\mathbf{T}_{(X,Y)}}(\omega)$ and $\widehat{\mathbf{W}}_{\mathbf{T}_{(X,Y)}}(\omega)$ is addressed further on in the text. For $k(m+n) < mn$, $\widetilde{\widehat{\mathbf{T}}}_{(X,Y)}(\omega)$ is called a low rank approximation of $\widehat{\mathbf{T}}_{(X,Y)}(\omega)$ as the memory is reduced from $\mathcal{O}(mn)$ to $\mathcal{O}(k(m+n))$ by storing $\widehat{\mathbf{V}}_{\mathbf{T}_{(X,Y)}}(\omega)$ and $\widehat{\mathbf{W}}_{\mathbf{T}_{(X,Y)}}(\omega)$ instead of $\widehat{\mathbf{T}}_{(X,Y)}(\omega)$, which is linear in m and n. The outer–product representation (3.6) is consequently preferred. The rank k in equation (3.6) is determined such that the approximation $\widetilde{\widehat{\mathbf{T}}}_{(X,Y)}(\omega)$ is accurate up to a prescribed relative accuracy ε:

$$||\widehat{\mathbf{T}}_{(X,Y)}(\omega) - \widetilde{\widehat{\mathbf{T}}}_{(X,Y)}(\omega)||_{\mathrm{F}} \leq \varepsilon||\widehat{\mathbf{T}}_{(X,Y)}(\omega)||_{\mathrm{F}} \tag{3.7}$$

where $||\diamond||_{\mathrm{F}}$ indicates the Frobenius norm of the matrix $\diamond$.

For inadmissible cluster pairs (X, Y), the Green's functions show a singular behaviour which does not allow for the construction of a low rank approximation of the corresponding block matrices. These blocks are therefore computed exactly and stored entrywise.

Low rank approximations

Several techniques can be employed to find a suitable low rank approximation of the matrix blocks $\widehat{\mathbf{T}}_{(X,Y)}(\omega)$ and $\widehat{\mathbf{U}}_{(X,Y)}(\omega)$ corresponding to an admissible cluster pair (X, Y). These blocks are denoted in the following as $\mathbf{A}$. The best possible approximation of rank k of a matrix $\mathbf{A} \in \mathbb{C}^{m\times n}$ (minimizing the error norm) is given by its partial singular value decomposition (SVD) $\mathbf{A}_k$ [66]:

$$\mathbf{A} \simeq \mathbf{A}_k = \mathbf{U}_k \mathbf{\Sigma}_k \mathbf{V}_k^\star \tag{3.8}$$

The diagonal matrix $\mathbf{\Sigma}_k \in \mathbb{R}^{k\times k}$ is composed of the first k singular values $\sigma_i \in \mathbb{R}_+$ of $\mathbf{A}$ (appearing in decreasing order), while the matrices $\mathbf{U}_k \in \mathbb{C}^{m\times k}$ and $\mathbf{V}_k \in \mathbb{C}^{n\times k}$ contain the corresponding left and right singular vectors, respectively. Note that equation (3.8) can be transformed into the outer–product representation of equation (3.6) by multiplying $\mathbf{U}_k$ or $\mathbf{V}_k^\star$ with $\mathbf{\Sigma}_k$. It can be shown that the error of the approximation (3.8) is given by [66]:

$$||\mathbf{A} - \mathbf{A}_k|| = ||\mathbf{\Sigma} - \mathbf{\Sigma}_k|| \tag{3.9}$$

where $\mathbf{\Sigma}$ collects all singular values. If the spectral norm is used, then $||\mathbf{A}-\mathbf{A}_k||_2 = \sigma_{k+1}$, while the error is $||\mathbf{A}-\mathbf{A}_k||_{\mathrm{F}} = \sqrt{\sum_{l=k+1}^{\min(m,n)} \sigma_l^2}$ in terms of the Frobenius norm. Equation (3.9) can also be used to determine the lowest required rank k if a relative accuracy ε is prescribed for $\mathbf{A}_k$:

$$||\mathbf{A} - \mathbf{A}_k|| \leq \varepsilon ||A|| \tag{3.10}$$

If the accuracy is prescribed with respect to the spectral norm, the rank k is given by:

$$k(\varepsilon) = \min\{k \in \mathbb{N} : \sigma_{k+1} \leq \varepsilon \sigma_1\} \tag{3.11}$$

while equation (3.10) becomes:

$$k(\varepsilon) = \min\left\{ k \in \mathbb{N} : \sum_{l=k+1}^{\min(m,n)} \sigma_l^2 \leq \varepsilon^2 \sum_{l=1}^{\min(m,n)} \sigma_l^2 \right\} \tag{3.12}$$

if the Frobenius norm is employed. In many cases, only the first few singular values σ_i and corresponding singular vectors are required to obtain an accurate approximation of $\mathbf{A}$ (and thus a low rank $k \ll m, n$).

Unfortunately, the calculation of the complete SVD of a dense matrix $\mathbf{A}$ requires $\mathcal{O}(n^3)$ arithmetical operations, making it unattractive for large scale computations. Moreover, the matrix $\mathbf{A}$ has to be known before its SVD can be computed. The adaptive cross–approximation (ACA) algorithm [15, 122] provides a more efficient way for the calculation of a low rank approximant $\mathbf{A}_k$ of $\mathbf{A}$ and is therefore employed. This algorithm adaptively calculates some of the rows and columns of the original matrix to obtain an outer–product approximation (3.6) from few of the original matrix entries. It is not necessary to assemble the complete matrix beforehand; the required matrix entries can be computed on demand [13]. The algorithm stops if the prescribed accuracy ε is attained, but a criterion such as in equation (3.7) can not be employed as the original matrix is never generated completely. An intrinsic stopping criterion based on the variation of the Frobenius norm in consecutive approximations is therefore used. The amount of numerical operations required in the ACA algorithm is $\mathcal{O}(k^2(m+n))$ [122]. Once a low rank approximation of $\mathbf{A}$ is computed by means of ACA (in the outer–product form (3.6)), an additional compression can be performed to reduce the memory storage even further. As it is relatively inexpensive to compute the SVD of a low rank matrix (in contrast to the SVD of a dense matrix), a memory reduction is obtained by discarding the smallest singular values and corresponding singular vectors of $\mathbf{A}_k$, hence reducing the rank while maintaining the desired approximation accuracy. Details on this recompression technique are provided in paper A and in the literature [14, 67, 68].

It is emphasized that ACA is a purely algebraic approximation technique based on the matrix entries only. This is in contrast with other approaches such as the fast multipole method [113, 123] or the panel clustering technique [75], where the underlying Green's functions (rather than the matrices) are approximated. The use of ACA consequently avoids the need for (semi–)analytical expressions of the Green's functions (although it is also applicable in that case), enabling its application to a large variety of boundary element formulations. The main novelty in the present work is the incorporation of Green's functions of layered soils (computed by means of the direct stiffness method), which is an approach that has not been attempted yet.

Solving the $\mathscr{H}$-BE equations

Following the procedure outlined above leads to an approximation of the BE matrices $\widehat{\mathbf{T}}(\omega)$ and $\widehat{\mathbf{U}}(\omega)$ by their hierarchical representations $\widehat{\mathbf{T}}_{\mathscr{H}}(\omega)$ and $\widehat{\mathbf{U}}_{\mathscr{H}}(\omega)$, respectively, in which matrix blocks corresponding to admissible cluster pairs are approximated by ACA while the other blocks are computed

exactly. The BE equation (2.15) is thus replaced by:

$$\left[\widehat{\mathbf{T}}_{\mathscr{H}}(\omega) + \mathbf{I}\right] \hat{\underline{\mathbf{u}}}(\omega) = \widehat{\mathbf{U}}_{\mathscr{H}}(\omega)\hat{\underline{\mathbf{t}}}(\omega) \tag{3.13}$$

Equation (3.13) can be rewritten as:

$$\widehat{\mathbf{A}}_{\mathscr{H}}(\omega)\hat{\underline{\mathbf{x}}}(\omega) = \hat{\underline{\mathbf{b}}}(\omega) \tag{3.14}$$

where the vector of unknowns $\hat{\underline{\mathbf{x}}}(\omega)$ contains displacements, tractions or both, depending on whether a Neumann, Dirichlet or mixed Neumann–Dirichlet problem is considered. In order to solve equation (3.14), iterative Krylov subspace methods such as the generalized minimal residual method (GMRES) [126] are well suited. The matrix–vector multiplication forms the core of iterative solvers, and the complexity of this operation is only $\mathcal{O}(N_{\mathrm{DOF}} \log N_{\mathrm{DOF}})$ for $\mathscr{H}$–matrices [13]. Iterations are performed until the relative residual norm $||\hat{\underline{\mathbf{b}}}(\omega) - \widehat{\mathbf{A}}_{\mathscr{H}}(\omega)\hat{\underline{\mathbf{x}}}(\omega)||/||\hat{\underline{\mathbf{b}}}(\omega)||$ reaches a specified tolerance (e.g. 10^{-6}).

It is often desirable to accelerate the convergence of an iterative solver through the incorporation of a suitable preconditioner. A right preconditioner $\widehat{\mathbf{M}}(\omega)$ is used in this work in order to lower the condition number of the coefficient matrix $\widehat{\mathbf{A}}_{\mathscr{H}}(\omega)$:

$$\widehat{\mathbf{A}}_{\mathscr{H}}(\omega)\widehat{\mathbf{M}}^{-1}(\omega)\hat{\underline{\mathbf{y}}}(\omega) = \hat{\underline{\mathbf{b}}}(\omega) \tag{3.15}$$

with $\widehat{\mathbf{M}}(\omega)\hat{\underline{\mathbf{x}}}(\omega) = \hat{\underline{\mathbf{y}}}(\omega)$. An example of an efficient preconditioner is the approximate $\mathscr{H}$–LU decomposition [12]; its computation requires, however, additional arithmetic operations. A much simpler strategy is therefore applied, following the approach recently adopted by Chaillat et al. [30] for the acceleration of the fast multipole method for elastodynamics. A block diagonal preconditioner $\widehat{\mathbf{M}}(\omega) = \mathrm{blkdiag}\left(\widehat{\mathbf{A}}_{\mathscr{H}}(\omega)\right)$ is employed, where the size of the diagonal blocks is determined by the lowest hierarchical cluster level. An inner GMRES solver with a moderate tolerance (e.g. 10^{-2}) is applied to solve the preconditioning linear systems, resulting in a nested inner–outer iteration scheme. The flexible GMRES (FGMRES) algorithm [125] is employed for the outer iteration, as the preconditioner varies in each step. Since $\widehat{\mathbf{M}}(\omega)$ is already computed and stored, the proposed approach is very cheap in terms of computational resources.

Numerical example

Within the frame of the present work, $\mathscr{H}$–matrix algebra has been implemented in the MATLAB toolbox BEMFUN [54]. The core of this toolbox is

implemented in C++ using the MATLAB MEX interface in order to achieve a seamless integration with MATLAB as well as a high numerical efficiency. Verification examples are presented and discussed extensively in paper A; these examples involve Green's functions of a full space, a homogeneous halfspace, and a horizontally layered halfspace.

In the following, the example of a massless rigid square surface foundation with side d on a layered halfspace is considered to illustrate the accuracy and efficiency of the methodology. The geometric and dynamic characteristics of the foundation and the halfspace are detailed in paper A. The vertical soil impedance $\hat{K}^{\mathrm{s}}_{zz}(\omega)$ of the foundation is defined as [62]:

$$\hat{K}^{\mathrm{s}}_{zz}(\omega) = \int_{\Sigma} \boldsymbol{\psi}_{zz} \cdot \hat{\mathbf{t}}^{\mathbf{n}_{\mathrm{s}}}_{\mathrm{s}} \left(\hat{\mathbf{u}}_{\mathrm{sc}}(\boldsymbol{\psi}_{zz})\right) \mathrm{d}S = \hat{K}^{\mathrm{s}}_{zz0} \left(k_{zz}(a_0) + i a_0 c_{zz}(a_0)\right) \quad (3.16)$$

where $\boldsymbol{\psi}_{zz}$ represents the vertical rigid body translation of the foundation. K^{s}_{zz0} indicates the static stiffness, while $k_{zz}(a_0)$ and $c_{zz}(a_0)$ are dimensionless stiffness and damping coefficients, respectively, as a function of the dimensionless frequency $a_0 = \omega B / C_{\mathrm{s}}$ (with $B = d/2$ and C_{s} the shear wave velocity of the top soil layer).

The soil–foundation interface is discretized with 30×30 equally sized quadrilateral boundary elements with element collocation; this allows for the calculation of the tractions $\hat{\mathbf{t}}^{\mathbf{n}_{\mathrm{s}}}_{\mathrm{s}} \left(\hat{\mathbf{u}}_{\mathrm{sc}}(\boldsymbol{\psi}_{zz})\right)$ due to imposed displacements $\boldsymbol{\psi}_{zz}$ by means of equation (3.13). Green's functions of a layered halfspace are incorporated in the $\mathscr{H}$-BE formulation [87, 130], avoiding the necessity to discretize the free surface and the layer interfaces. Consequently, the BE matrix $\widehat{\mathbf{T}}_{\mathscr{H}}(\omega)$ is zero for the surface foundation under concern.

Figure 3.4 shows the coefficients $k_{zz}(a_0)$ and $c_{zz}(a_0)$ in a dimensionless frequency range between 0 and 10, for the threshold ε used in the ACA algorithm (cf. equation (3.7)) varying logarithmically from 10^{-1} to 10^{-4}. These coefficients are compared to results obtained with a classical BE approach (i.e. without application of hierarchical matrix algebra), and a good agreement is found if ε is smaller than 10^{-2}. The accuracy of the proposed methodology is also assessed in figure 3.5a, showing the relative error $||\hat{K}^{\mathrm{s}}_{zz,\mathscr{H}}(a_0) - \hat{K}^{\mathrm{s}}_{zz,\mathrm{c}}(a_0)||/||\hat{K}^{\mathrm{s}}_{zz,\mathrm{c}}(a_0)||$, where $\hat{K}^{\mathrm{s}}_{zz,\mathscr{H}}(a_0)$ and $\hat{K}^{\mathrm{s}}_{zz,\mathrm{c}}(a_0)$ represent the vertical soil impedance computed with the hierarchical and the classical BE method, respectively. The relative error decreases considerably for reduced values of ε. Furthermore, a decrease of almost one order of magnitude is observed for increasing dimensionless frequencies in case $\varepsilon = 10^{-1}$ and $\varepsilon = 10^{-2}$, while the relative error is less dependent on the frequency for the other cases.

The RAM that is required for the storage of $\widehat{\mathbf{U}}_{\mathscr{H}}(\omega)$ (with respect to the dense matrix $\widehat{\mathbf{U}}(\omega)$ in the classical approach) is shown in figure 3.5b. As

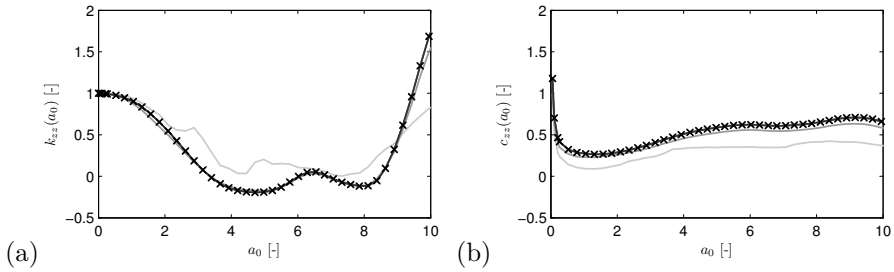

Figure 3.4: Dimensionless (a) stiffness coefficient $k_{zz}(a_0)$ and (b) damping coefficient $c_{zz}(a_0)$ of a massless rigid square surface foundation on a layered halfspace in function of the dimensionless frequency a_0. The solution obtained with the hierarchical BE method (solid lines) for the threshold ε used in the ACA algorithm varying from 10^{-1} (light grey line) to 10^{-4} (dark grey line) is compared to the solution obtained with the classical BE method (black crosses).

expected, the efficiency decreases for reduced values of ε, as well as for an increasing dimensionless frequency a_0. Such trends have also been observed in hierarchical BE methods for anisotropic elastodynamic problems [17, 110]. Figures 3.4 and 3.5 clearly indicate that the overall computational precision and the RAM usage strongly depend on the value of the threshold ε. A trade–off between accuracy and efficiency should hence be made when applying the proposed methodology.

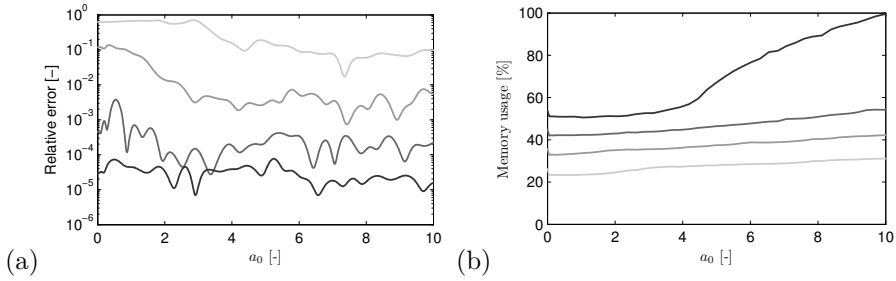

Figure 3.5: (a) Relative error $||\hat{K}^{\mathrm{s}}_{zz,\mathscr{H}}(a_0) - \hat{K}^{\mathrm{s}}_{zz,\mathrm{c}}(a_0)||/||\hat{K}^{\mathrm{s}}_{zz,\mathrm{c}}(a_0)||$ and (b) memory usage with respect to the classical BE method for the threshold ε used in the ACA algorithm varying from 10^{-1} (light grey line) to 10^{-4} (dark grey line).

The efficiency of the application of $\mathscr{H}$–matrices is further investigated at a particular dimensionless frequency $a_0 = \pi$, for an increasing number of boundary elements. Figure 3.6a compares the memory required to store the BE matrices $\widehat{\mathbf{U}}(\omega)$ and $\widehat{\mathbf{U}}_{\mathscr{H}}(\omega)$ on a double logarithmic plot, in which the slope of the curve corresponds to the power relating the number of degrees of freedom and the required memory. As expected, a quadratic trend $\mathcal{O}(N_{\mathrm{DOF}}^2)$ can be observed for the classical BE method. Calculations are limited to a model with 43200 degrees of freedom, as the storage of the complex floating point entries of $\widehat{\mathbf{U}}(\omega)$ in double precision requires $2 \times N_{\mathrm{DOF}}^2 \times 8$ bytes $= 27.8$ GB of RAM, which is the limit of the hardware employed. For the hierarchical BE method, however, the memory requirement is of the order $\mathcal{O}(N_{\mathrm{DOF}} \log_{10}^3 N_{\mathrm{DOF}})$, allowing for the extension of the model size up to 399675 degrees of freedom with 28 GB of RAM available. Applying the recompression procedure mentioned before even allows considering up to 468075 degrees of freedom with the same amount of memory. In comparison, 2380 GB and 3265 GB of RAM would, respectively, be required in order to handle such models with the classical BE method.

Figure 3.6b shows the CPU time required to calculate $\hat{K}_{zz}^{\mathrm{s}}(a_0 = \pi)$, including both the time to assemble the matrices $\widehat{\mathbf{U}}(\omega)$ or $\widehat{\mathbf{U}}_{\mathscr{H}}(\omega)$ and to solve the corresponding BE equations; no preconditioner has been incorporated. For relatively small models ($\mathcal{O}(10^3)$), the classical BE method turns out to be a little faster, but the hierarchical approach is considerably more efficient from a moderate model size on. The relative contribution of the assembly and solution time to the total CPU time is different for both approaches: for large models, the total solution time of the classical BE method is dominated by the time required to solve equation (2.15) (which increases in a cubic way $\mathcal{O}(N_{\mathrm{DOF}}^3)$), while the contribution of the solution time is negligible compared to the assembly time for the hierarchical BE method. This is reviewed in detail in paper A.

3.1.2 FE–$\mathscr{H}$-BE coupling procedures

The application of $\mathscr{H}$–matrices enables the evaluation of much larger BE models than with the classical approach, but it also deteriorates the efficiency of the direct FE–BE coupling strategy outlined in section 2.4, as will be elucidated in the following. More efficient FE–$\mathscr{H}$-BE coupling methodologies have therefore been developed in the frame of the present work. Paper B presents three coupling approaches (direct, iterative, and monolithic) and compares their computational performance through numerical examples. The main features of these techniques are summarized below; the reader is referred to paper B for a comprehensive overview and discussion.

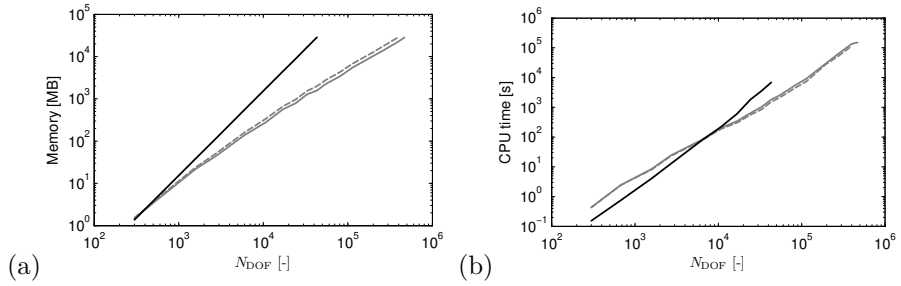

Figure 3.6: (a) RAM and (b) total CPU time required for an increasing number of degrees of freedom with the classical (black lines) and the hierarchical BE method with (solid grey lines) and without (dashed grey lines) recompression.

Direct FE–$\mathscr{H}$-BE coupling

The classical direct coupling strategy outlined in section 2.4 provides a straightforward solution to the dynamic SSI problem. This approach requires the assembly of the dense and unsymmetric dynamic soil stiffness matrix $\widehat{\mathbf{K}}^{\mathrm{s}}_{\mathrm{b_2 b_2}}(\omega)$, however, and thus the evaluation of tractions $\underline{\hat{\mathbf{t}}}(\mathbf{N}_{\mathrm{b_2}}(\mathbf{x}))(\omega)$ for all shape functions $\mathbf{N}_{\mathrm{b_2}}(\mathbf{x})$ on Σ through the solution of equation (3.15). As the implemented FGMRES algorithm is only able to handle one right hand side at a time, this coupling strategy becomes computationally very expensive for large problems. The introduction of a modal decomposition can reduce the computational cost, but does not eliminate the main disadvantages associated with this direct coupling approach; it remains inefficient for large problems.

Iterative FE–$\mathscr{H}$-BE coupling

Iterative coupling procedures provide a valuable alternative to the conventional direct strategy. The governing equations are solved separately for each subdomain, while the boundary conditions (2.25)–(2.26) at the soil–structure interface are updated until convergence is achieved. This methodology avoids the assembly and solution of a global system of coupled equations; it hence allows for the use of dedicated FE and $\mathscr{H}$-BE solvers in both subdomains. Iterative schemes are often used for dynamic SSI problems in the time domain to allow different time discretization schemes in the FE and BE subdomains [53, 151, 152]. Their application in the frequency domain has only received limited attention in the literature so far [70], however, as it is not easy to

achieve convergence with these algorithms [135]. Frequency domain iterative algorithms described in the literature mainly involve acoustic–acoustic [136] and acoustic–elastodynamic [135] coupling; the iterative coupling of FE and fast multipole BE models for visco–elastodynamics in the frequency domain is discussed by Grasso [70].

Four different iterative algorithms for the coupling of FE and $\mathscr{H}$-BE models are presented in paper B and are briefly reviewed in the following.

Sequential Neumann–Dirichlet algorithm
Figure 3.7 illustrates a sequential Neumann–Dirichlet procedure. At iteration step k, an estimation $\underline{\hat{\mathbf{q}}}^k(\omega)$ of the dynamic SSI forces is applied to the FE subdomain Ω_b on the soil–structure interface Σ. Solving the corresponding FE equations provides the internal and interface displacements $\underline{\hat{\mathbf{u}}}^k_{\mathrm{b}_1}(\omega)$ and $\underline{\hat{\mathbf{u}}}^k_{\mathrm{b}_2}(\omega)$. The latter are subsequently imposed as Dirichlet boundary conditions on the BE subdomain, which allows solving the preconditioned equation (3.15) for the interface tractions $\underline{\hat{\mathbf{t}}}^k(\omega)$ using the FGMRES solver. These tractions are used to calculate equivalent nodal forces $\underline{\tilde{\hat{\mathbf{q}}}}^{k+1}(\omega) = -\mathbf{T}_\mathrm{q}\,\underline{\hat{\mathbf{t}}}^k(\omega)$, where $\mathbf{T}_\mathrm{q}$ is defined in equation (2.29) and where a tilde above a variable indicates an unrelaxed quantity. The interaction forces are finally relaxed using an iteration dependent relaxation parameter λ^k to obtain a new estimate $\underline{\hat{\mathbf{q}}}^{k+1}(\omega)$:

$$\underline{\hat{\mathbf{q}}}^{k+1}(\omega) = \lambda^k \underline{\tilde{\hat{\mathbf{q}}}}^{k+1}(\omega) + (1-\lambda^k)\underline{\hat{\mathbf{q}}}^k(\omega) \tag{3.17}$$

Once the relaxed interaction forces $\underline{\hat{\mathbf{q}}}^{k+1}(\omega)$ are computed, a subsequent step in the iterative procedure is performed until convergence is obtained.

The choice of a suitable relaxation parameter λ^k in equation (3.17) is of great importance in order to ensure and/or speed up the convergence of the iterative algorithm. Within the frame of the present work, Aitken's Δ^2–method [3] is employed for the determination of an iteration dependent relaxation parameter λ^k. This method provides a simple but efficient procedure to determine λ^k, based on the results of two subsequent iterations. It is often applied in the iterative solution of fluid–structure interaction problems [93,111] and has already been adopted for transient elastodynamic problems [53], but not yet for elastodynamic problems formulated in the frequency domain.

The methodology is illustrated in figure 3.8 for a general iteration process involving a variable x and a function $f(x)$; the aim is to determine the solution $\overline{x} = f(\overline{x})$ through subsequent evaluations of $f(x)$. An unrelaxed estimation $\tilde{x}^{k+1} = f(x^k)$ is computed in step k of the iterative procedure. The estimation $\tilde{x}^{k+1}$ is combined with the result of the previous iteration step $k-1$, which allows for the determination of the new approximation x^{k+1} as the intersection of the linearized function $\tilde{f}^k(x)$ through the points $\left\{x^{k-1}, \tilde{x}^k = f(x^{k-1})\right\}^\mathrm{T}$ and

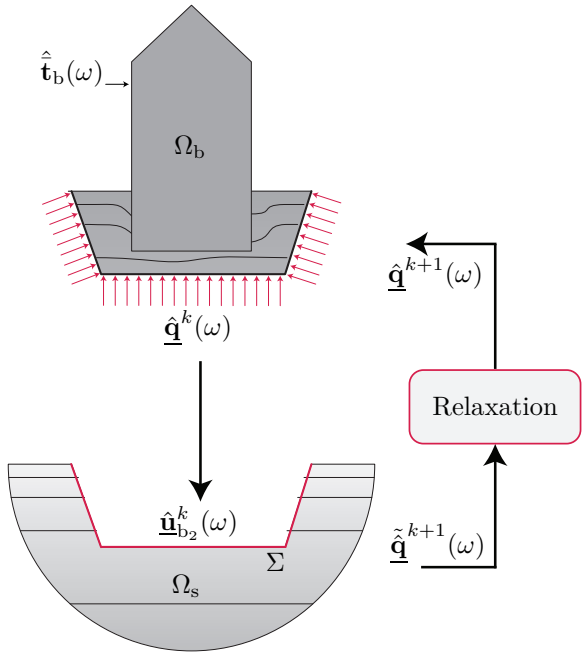

Figure 3.7: Sequential Neumann–Dirichlet procedure.

$\left\{x^k, \tilde{x}^{k+1} = f(x^k)\right\}^{\mathrm{T}}$, and the function $y = x$, respectively. This corresponds to a single step of the secant method [93].

The relaxation parameter λ^k can be expressed as:

$$\lambda^k = \frac{x^k - x^{k-1}}{x^k - \tilde{x}^{k+1} - x^{k-1} + \tilde{x}^k} \tag{3.18}$$

$$= \lambda^{k-1} \frac{\tilde{x}^k - x^{k-1}}{x^k - \tilde{x}^{k+1} - x^{k-1} + \tilde{x}^k} \tag{3.19}$$

$$= -\lambda^{k-1} \frac{r^{k-1}}{r^k - r^{k-1}} \tag{3.20}$$

with the residual r^k defined as $r^k = x^k - \tilde{x}^{k+1}$. For the vectorized interaction forces $\hat{\underline{\mathbf{q}}}(\omega)$ in equation (3.17), the relaxation parameter λ^k is obtained following the approach presented by Irons and Tuck [81], in which the vectors are

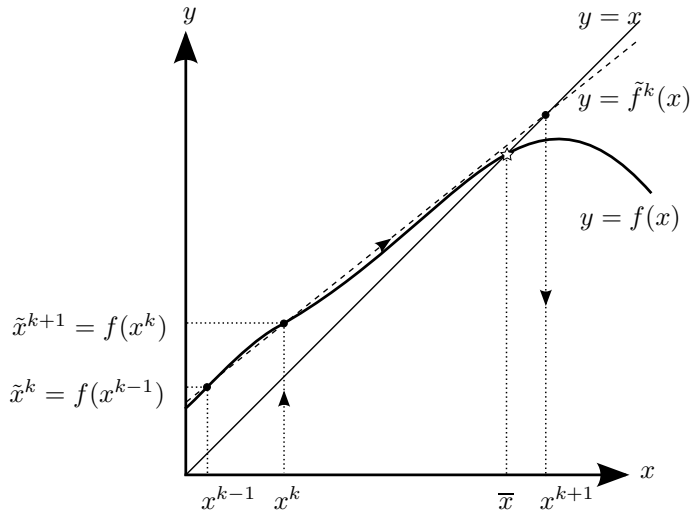

Figure 3.8: Aitken's Δ^2 interface relaxation technique employed in sequential iterative algorithms, involving the functions $y = x$ (thin solid line), $y = f(x)$ (thick solid line) and $y = \tilde{f}^k(x)$ (dashed line). The target solution $\overline{x} = f(\overline{x})$ is indicated with a star.

projected in the direction $\underline{\hat{\mathbf{r}}}^k(\omega) - \underline{\hat{\mathbf{r}}}^{k-1}(\omega) = \underline{\hat{\mathbf{q}}}^k(\omega) - \underline{\tilde{\hat{\mathbf{q}}}}^{k+1}(\omega) - \underline{\hat{\mathbf{q}}}^{k-1}(\omega) + \underline{\tilde{\hat{\mathbf{q}}}}^k(\omega)$:

$$\lambda^k = -\lambda^{k-1} \frac{\left(\underline{\hat{\mathbf{r}}}^k(\omega) - \underline{\hat{\mathbf{r}}}^{k-1}(\omega)\right)^{\mathrm{T}} \underline{\hat{\mathbf{r}}}^{k-1}(\omega)}{||\underline{\hat{\mathbf{r}}}^k(\omega) - \underline{\hat{\mathbf{r}}}^{k-1}(\omega)||^2} \tag{3.21}$$

with $\lambda^0 = 1$. Equation (3.21) can be evaluated at low computational cost, providing a simple and robust way to calculate an iteration dependent relaxation parameter, hence avoiding the need for an empirical trial–and–error process [152].

An additional reduction of the computation time is achieved by providing an initial guess to the FGMRES solver that is employed to solve equation (3.15); the relaxed tractions $-\mathbf{T}_{\mathrm{q}}^{-1}\, \underline{\hat{\mathbf{q}}}^k(\omega)$ obtained in iteration $k-1$ are used as an initial guess for the determination of tractions $\underline{\hat{\mathbf{t}}}^k(\omega)$ in iteration k. Using a start vector in the first Neumann–Dirichlet iteration corresponding to the converged solution of the previous frequency step is also advantageous, provided that the frequency bin is sufficiently small. A major disadvantage of the proposed algorithm is its inability to determine the static solution, as application of Neumann boundary conditions to the unconstrained structural domain Ω_{b}

results in singular FE equations. The convergence behaviour at low frequencies is hence expected to be poor; the frequency sweep is therefore performed from high to low frequencies. Singularity of the FE equations is also encountered if the structure is excited at one of its natural frequencies; incorporation of structural damping remediates this issue.

Sequential Dirichlet–Neumann algorithm
An alternative sequential Dirichlet–Neumann scheme is obtained if the type of boundary conditions applied to each subdomain is reversed, as visualized in figure 3.9. At iteration step k, Dirichlet boundary conditions $\underline{\hat{\mathbf{u}}}_{\mathrm{b}_2}^{k}(\omega)$ are imposed on the interface Σ of the FE subdomain, providing the interaction forces $\underline{\hat{\mathbf{q}}}^{k}(\omega)$ through the solution of the FE equations. The corresponding interface tractions $\underline{\hat{\mathbf{t}}}^{k}(\omega) = -\mathbf{T}_{\mathrm{q}}^{-1}\,\underline{\hat{\mathbf{q}}}^{k}(\omega)$ are applied to the BE subdomain, and unrelaxed interface displacements $\underline{\tilde{\hat{\mathbf{u}}}}_{\mathrm{b}_2}^{k+1}(\omega)$ are obtained by solving the preconditioned system of equations (3.15) using the FGMRES solver. Aitken's Δ^2–method is finally employed for the determination of an optimized relaxation parameter λ^k (with equation (3.21) now based on interface displacements instead of interaction forces), allowing for the computation of relaxed interface displacements $\underline{\hat{\mathbf{u}}}_{\mathrm{b}_2}^{k+1}(\omega)$. This iterative procedure is repeated until convergence is achieved.

Parallel Neumann–Neumann algorithm
A parallel Neumann–Neumann iterative scheme (figure 3.10) is obtained if the interaction forces $\underline{\hat{\mathbf{q}}}^{k}(\omega)$ and corresponding interface tractions $\underline{\hat{\mathbf{t}}}^{k}(\omega) = -\mathbf{T}_{\mathrm{q}}^{-1}\,\underline{\hat{\mathbf{q}}}^{k}(\omega)$ are simultaneously imposed as Neumann boundary conditions on the interface Σ of the FE and BE subdomain, respectively. This provides (incompatible) interface displacements $\underline{\hat{\mathbf{u}}}_{\mathrm{b}_2,\mathrm{FE}}^{k}(\omega)$ and $\underline{\hat{\mathbf{u}}}_{\mathrm{b}_2,\mathrm{BE}}^{k}(\omega)$. The discrepancy of interface displacements $\Delta\underline{\hat{\mathbf{u}}}_{\mathrm{b}_2}^{k}(\omega) = \underline{\hat{\mathbf{u}}}_{\mathrm{b}_2,\mathrm{BE}}^{k}(\omega) - \underline{\hat{\mathbf{u}}}_{\mathrm{b}_2,\mathrm{FE}}^{k}(\omega)$ is subsequently employed to calculate an increment of interaction forces $\Delta\underline{\hat{\mathbf{q}}}^{k}(\omega)$. The displacement discrepancy $\Delta\underline{\hat{\mathbf{u}}}_{\mathrm{b}_2}^{k}(\omega)$ is imposed on the FE as well as on the BE subdomain to compute this increment; this yields unrelaxed interaction forces $\underline{\tilde{\hat{\mathbf{q}}}}_{\mathrm{FE}}^{k+1}(\omega) = \underline{\hat{\mathbf{q}}}^{k}(\omega) + \Delta\underline{\hat{\mathbf{q}}}_{\mathrm{FE}}^{k}(\omega)$ and $\underline{\tilde{\hat{\mathbf{q}}}}_{\mathrm{BE}}^{k+1}(\omega) = \underline{\hat{\mathbf{q}}}^{k}(\omega) + \Delta\underline{\hat{\mathbf{q}}}_{\mathrm{BE}}^{k}(\omega)$. A novel and robust relaxation procedure (presented in paper B) is then applied for the determination of relaxed interaction forces $\underline{\hat{\mathbf{q}}}^{k+1}(\omega)$, where $\underline{\tilde{\hat{\mathbf{q}}}}_{\mathrm{FE}}^{k+1}(\omega)$ and $\underline{\tilde{\hat{\mathbf{q}}}}_{\mathrm{BE}}^{k+1}(\omega)$ are simultaneously taken into account.

The novel relaxation procedure is illustrated in figure 3.11 for a general iteration process involving two functions $f(x)$ and $g(x)$, with solution $\overline{x} = f(\overline{x}) = g(\overline{x})$. The proposed approach is based on a simultaneous application of Aitken relaxation to $f(x)$ and $g(x)$. At iteration step k, two estimations $\tilde{x}_f^{k+1} = f(x^k)$ and $\tilde{x}_g^{k+1} = g(x^k)$ are calculated. These estimations are combined with the

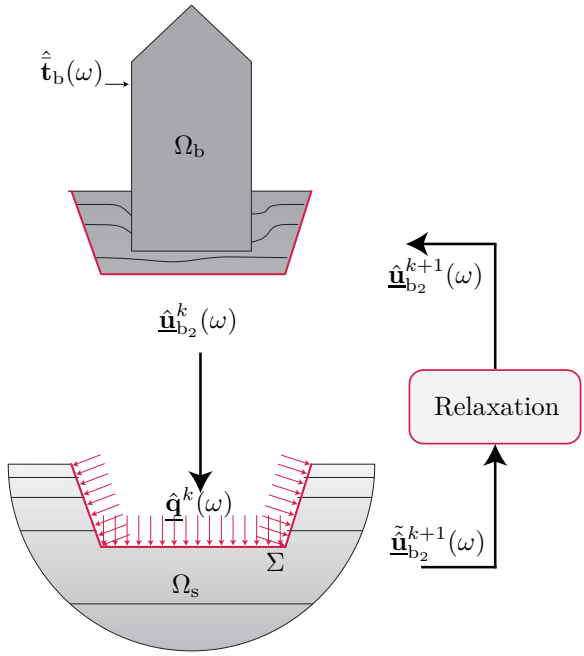

Figure 3.9: Sequential Dirichlet–Neumann procedure.

data points $\{x^{k-1}, \tilde{x}_f^k = f(x^{k-1})\}^{\mathrm{T}}$ and $\{x^{k-1}, \tilde{x}_g^k = g(x^{k-1})\}^{\mathrm{T}}$ obtained in the previous iteration step $k-1$ to define linear approximations $\tilde{f}^k(x)$ and $\tilde{g}^k(x)$ of the functions $f(x)$ and $g(x)$, respectively. The ordinate of the intersection of these linearized functions $\tilde{f}^k(x)$ and $\tilde{g}^k(x)$ provides a new approximation x^{k+1} of the solution $\overline{x}$:

$$x^{k+1} = \frac{r_g^k}{r_g^k - r_f^k}\,\tilde{x}_f^{k+1} - \frac{r_f^k}{r_g^k - r_f^k}\,\tilde{x}_g^{k+1} \tag{3.22}$$

with $r_f^k = \tilde{x}_f^{k+1} - \tilde{x}_f^k$ and $r_g^k = \tilde{x}_g^{k+1} - \tilde{x}_g^k$; these residual vectors are defined differently compared to equation (3.20). For the vectorized interaction forces $\hat{\underline{\mathbf{q}}}(\omega)$, a projection in the direction $\hat{\underline{\mathbf{r}}}^k_{\mathrm{BE}}(\omega) - \hat{\underline{\mathbf{r}}}^k_{\mathrm{FE}}(\omega) = \tilde{\hat{\underline{\mathbf{q}}}}^{k+1}_{\mathrm{BE}}(\omega) - \tilde{\hat{\underline{\mathbf{q}}}}^{k}_{\mathrm{BE}}(\omega) -$

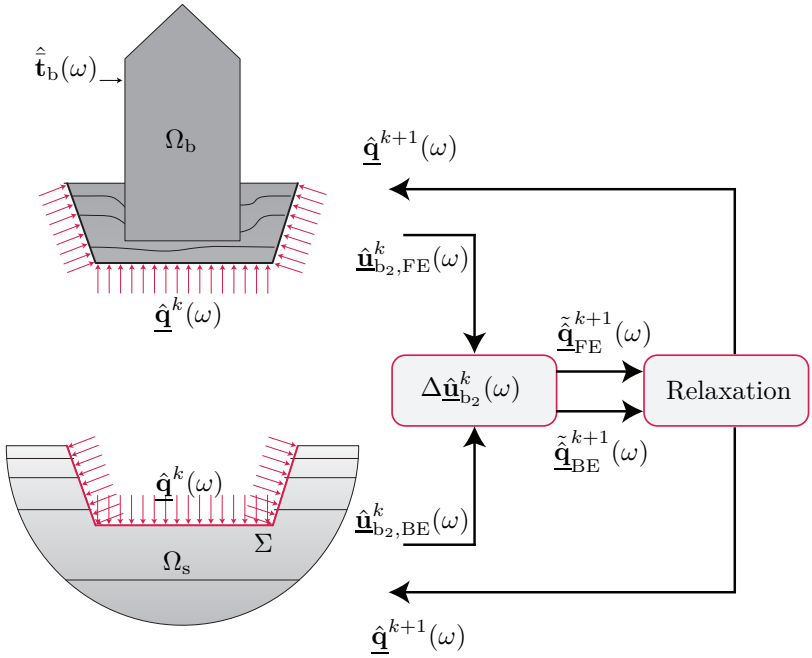

Figure 3.10: Parallel Neumann–Neumann procedure.

$\tilde{\hat{\underline{\mathbf{q}}}}^{k+1}_{\mathrm{FE}}(\omega) + \tilde{\hat{\underline{\mathbf{q}}}}^{k}_{\mathrm{FE}}(\omega)$ is introduced in equation (3.22):

$$\hat{\underline{\mathbf{q}}}^{k+1}(\omega) = \frac{\left(\hat{\underline{\mathbf{r}}}^{k}_{\mathrm{BE}}(\omega) - \hat{\underline{\mathbf{r}}}^{k}_{\mathrm{FE}}(\omega)\right)^{\mathrm{T}} \hat{\underline{\mathbf{r}}}^{k}_{\mathrm{BE}}(\omega)}{||\hat{\underline{\mathbf{r}}}^{k}_{\mathrm{BE}}(\omega) - \hat{\underline{\mathbf{r}}}^{k}_{\mathrm{FE}}(\omega)||^2} \tilde{\hat{\underline{\mathbf{q}}}}^{k+1}_{\mathrm{FE}}(\omega) - \frac{\left(\hat{\underline{\mathbf{r}}}^{k}_{\mathrm{BE}}(\omega) - \hat{\underline{\mathbf{r}}}^{k}_{\mathrm{FE}}(\omega)\right)^{\mathrm{T}} \hat{\underline{\mathbf{r}}}^{k}_{\mathrm{FE}}(\omega)}{||\hat{\underline{\mathbf{r}}}^{k}_{\mathrm{BE}}(\omega) - \hat{\underline{\mathbf{r}}}^{k}_{\mathrm{FE}}(\omega)||^2} \tilde{\hat{\underline{\mathbf{q}}}}^{k+1}_{\mathrm{BE}}(\omega) \quad (3.23)$$

Equation (3.23) clearly indicates that $\tilde{\hat{\underline{\mathbf{q}}}}^{k+1}_{\mathrm{FE}}(\omega)$ and $\tilde{\hat{\underline{\mathbf{q}}}}^{k+1}_{\mathrm{BE}}(\omega)$ are simultaneously accounted for in the determination of a new estimate $\hat{\underline{\mathbf{q}}}^{k+1}(\omega)$, with iteration dependent weighting factors based on data of two subsequent iterations; these weighting factors can be calculated at low computational cost.

Parallel Dirichlet–Dirichlet algorithm
Figure 3.12 depicts an alternative parallel Dirichlet–Dirichlet strategy. Imposing Dirichlet boundary conditions $\hat{\underline{\mathbf{u}}}^{k}_{\mathrm{b}_2}(\omega)$ on the interface Σ of the FE and BE

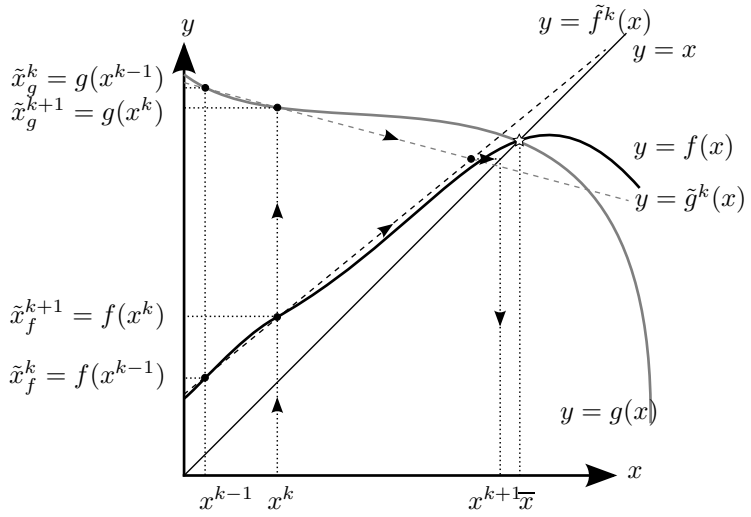

Figure 3.11: Interface relaxation technique employed in parallel iterative algorithms, involving the functions $y = f(x)$ (black solid line), $y = g(x)$ (grey solid line), $y = \tilde{f}^k(x)$ (black dashed line), $y = \tilde{g}^k(x)$ (grey dashed line), and $y = x$ (thin solid line). The target solution $\overline{x} = f(\overline{x}) = g(\overline{x})$ is indicated with a star.

subdomain allows for the computation of interaction forces $\underline{\hat{\mathbf{q}}}^k_{\mathrm{FE}}(\omega)$ and $\underline{\hat{\mathbf{q}}}^k_{\mathrm{BE}}(\omega)$, respectively. The resulting force discrepancy $\Delta\underline{\hat{\mathbf{q}}}^k(\omega) = \underline{\hat{\mathbf{q}}}^k_{\mathrm{BE}}(\omega) - \underline{\hat{\mathbf{q}}}^k_{\mathrm{FE}}(\omega)$ is employed to calculate interface displacement increments $\Delta\underline{\hat{\mathbf{u}}}^k_{\mathrm{b_2,FE}}(\omega)$ and $\Delta\underline{\hat{\mathbf{u}}}^k_{\mathrm{b_2,BE}}(\omega)$, and unrelaxed displacements $\underline{\tilde{\hat{\mathbf{u}}}}^{k+1}_{\mathrm{b_2,FE}}(\omega) = \underline{\hat{\mathbf{u}}}^k_{\mathrm{b_2,FE}}(\omega) + \Delta\underline{\hat{\mathbf{u}}}^k_{\mathrm{b_2,FE}}(\omega)$ and $\underline{\tilde{\hat{\mathbf{u}}}}^{k+1}_{\mathrm{b_2,BE}}(\omega) = \underline{\hat{\mathbf{u}}}^k_{\mathrm{b_2,BE}}(\omega) + \Delta\underline{\hat{\mathbf{u}}}^k_{\mathrm{b_2,BE}}(\omega)$ can subsequently be obtained. The relaxed interface displacements $\underline{\hat{\mathbf{u}}}^{k+1}_{\mathrm{b_2}}(\omega)$ are finally computed by means of the relaxation procedure illustrated in figure 3.11; equation (3.23) is in that case based on interface displacements instead of interaction forces. The procedure is repeated until convergence is achieved.

Monolithic FE–$\mathscr{H}$-BE coupling

The coupling of FE and $\mathscr{H}$-BE models can also performed by means of a monolithic approach, in which the governing equations of both subdomains are solved simultaneously, while the assembly of a dynamic soil stiffness matrix is avoided. This approach fundamentally differs from the conventional direct coupling approach outlined in subsection 2.4. Combining equations (2.23)

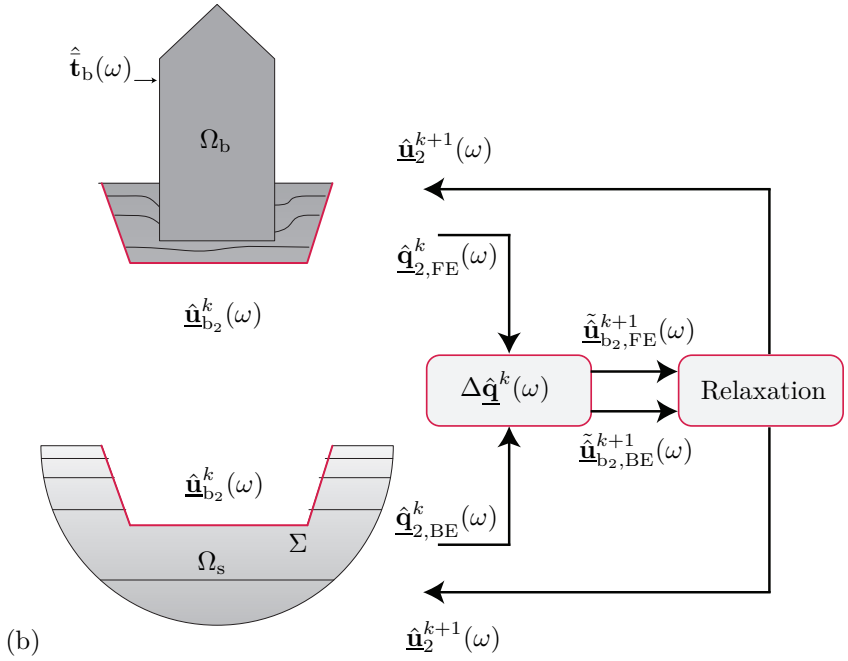

Figure 3.12: Parallel Dirichlet–Dirichlet procedure.

and (3.13) and accounting for continuity of displacements and equilibrium of tractions at the soil–structure interface Σ yields:

$$\begin{bmatrix} \widehat{\mathbf{K}}_{\mathrm{b}_1\mathrm{b}_1}(\omega) & \widehat{\mathbf{K}}_{\mathrm{b}_1\mathrm{b}_2}(\omega) & \mathbf{0} \\ \widehat{\mathbf{K}}_{\mathrm{b}_2\mathrm{b}_1}(\omega) & \widehat{\mathbf{K}}_{\mathrm{b}_2\mathrm{b}_2}(\omega) & \mathbf{T}_{\mathrm{q}} \\ \mathbf{0} & \widehat{\mathbf{T}}_{\mathscr{H}}(\omega)+\mathbf{I} & -\widehat{\mathbf{U}}_{\mathscr{H}}(\omega) \end{bmatrix} \begin{Bmatrix} \hat{\underline{\mathbf{u}}}_{\mathrm{b}_1}(\omega) \\ \hat{\underline{\mathbf{u}}}_{\mathrm{b}_2}(\omega) \\ \hat{\underline{\mathbf{t}}}(\omega) \end{Bmatrix} = \begin{Bmatrix} \hat{\underline{\mathbf{f}}}_{\mathrm{b}_1}(\omega) \\ \hat{\underline{\mathbf{f}}}_{\mathrm{b}_2}(\omega) \\ \underline{\mathbf{0}} \end{Bmatrix} + \begin{Bmatrix} \underline{\mathbf{0}} \\ \hat{\underline{\mathbf{f}}}_{\mathrm{b}_2}^{\mathrm{s}}(\omega) \\ \underline{\mathbf{0}} \end{Bmatrix} \tag{3.24}$$

The system size in this monolithic approach is significantly larger than in the classical direct coupling strategy of section 2.4. The coefficient matrix is never assembled explicitly, however, as equation (3.24) is solved by means of an iterative GMRES solver. This requires an efficient evaluation of the matrix–vector product, indicating that the monolithic formulation (3.24) is only advantageous if a fast BE method (in casu a formulation based on $\mathscr{H}$–matrices) is employed. A monolithic approach is rarely used in elastodynamics [70]; the monolithic coupling of FE and fast multipole BE models presented by

Margonari et al. [104] remains restricted to elastostatics. This strategy is more often applied for solving strongly coupled fluid–structure interaction problems [79, 109], as discretization methods commonly used for the fluid and the structure lead to sparse matrices.

The coefficient matrix in equation (3.24) is likely to be ill–conditioned, as the matrix entries arising from the FE and BE discretizations differ by several orders of magnitude. Convergence of the iterative solver will therefore be slow, and the incorporation of a suitable preconditioner is indispensable. A simple right preconditioner is presented in paper B.

Numerical example

The numerical implementation of the proposed FE–$\mathscr{H}$-BE coupling algorithms has been verified and their computational performance has been assessed in paper B. As an illustration, the example of a 3D spherical cavity embedded in a layered space and loaded by an internal pressure $\hat{p}(\omega)$ is considered here. The cavity has an inner radius r_i, while the layered space consists of a spherical layer with outer radius r_o and a homogeneous full space (figure 3.13a).

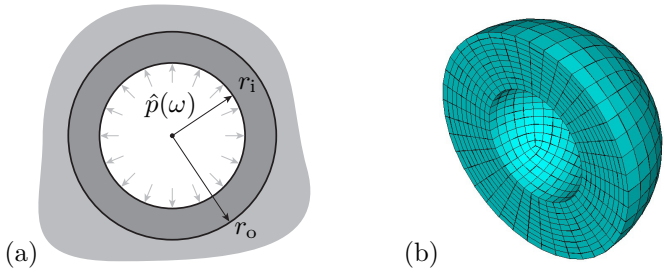

Figure 3.13: (a) 3D spherical cavity with inner radius r_i embedded in a layered space, consisting of a spherical layer with outer radius r_o and a homogeneous full space, and subjected to an internal pressure $\hat{p}(\omega)$. Half of the FE discretization of the spherical layer is shown in (b).

The full space is characterized by a dilatational wave velocity C_p, a density ρ, and a material damping ratio β_p in volumetric deformation. The dilatational wave velocity in the spherical layer is defined as αC_p, where the following values are considered for the ratio α: (i) $\alpha = 1/2$, (ii) $\alpha = 1$ and (iii) $\alpha = 2$. The same material damping ratio and density as in the full space are used. The geometric and dynamic characteristics are specified in paper B. The spherical layer is discretized by means of 6000 eight–node solid finite elements, which

are coupled to a conforming BE mesh consisting of 600 four–node quadrilateral elements on the soil–structure interface (figure 3.13b). A nodal collocation scheme is used for the latter to facilitate the FE–BE coupling, resulting in 19866 FE and 1806 BE degrees of freedom. Analytical full space fundamental solutions [86] are employed in the $\mathscr{H}$-BE formulation.

Each of the FE–$\mathscr{H}$-BE coupling strategies outlined above is employed to calculate the response in the frequency range between 0 Hz and 100 Hz, with a frequency step of 1 Hz. A maximum of 200 iterations is prescribed for the iterative coupling algorithms. Figure 3.14 shows the real and imaginary part of the radial displacement at $r = r_o$, for the three values of the wave velocity ratio α. All methods yield accurate results in very good agreement with the analytical solution [29] for all values of the ratio α, with exception of the sequential Neumann–Dirichlet algorithm, which is unable to retrieve the correct solution within the prescribed number of iterations at [12,31–38,41–42,46,49–62,64–80,82–100] Hz for a wave velocity ratio $\alpha = 1/2$. At these particular frequencies, the relative residual norm of the interface displacements and interaction forces still exceeds the specified accuracy of 10^{-4}.

The computational performance of the methods strongly differs from one another. Figure 3.15 shows the CPU time required in each algorithm as a function of the frequency, for the three wave velocity ratios considered. It is observed that the computation time in the direct coupling approach significantly exceeds the computational effort of the alternative procedures, rendering the conventional method the least efficient. The computation time remains quasi independent of the wave velocity ratio, but increases with frequency. This is caused by an increase of the time required for the assembly and solution of the $\mathscr{H}$-BE equations at higher frequencies [40]; a similar trend is also observed for the other coupling methodologies.

The computational efficiency of the iterative coupling schemes, on the other hand, shows a much stronger dependency on the wave velocity ratio α. This is in particular the case for the sequential variants: the CPU time in the Neumann–Dirichlet algorithm strongly decreases for increasing values of α, while the reverse is observed for the Dirichlet–Neumann approach. This indicates that Neumann boundary conditions should be applied to the most stiff subdomain in order to achieve the fastest convergence. The efficiency of the parallel iterative algorithms depends less strongly on α due to the novel relaxation procedure introduced in equation (3.23), as the contribution of each subdomain to the relaxed interaction forces or displacements is balanced in every step of the iterative procedure. Finally, figure 3.15 illustrates that the monolithic coupling scheme is also relatively insensitive to the value of α, but the overall computational performance of this methodology remains relatively poor compared to the iterative algorithms. The implementation of a more

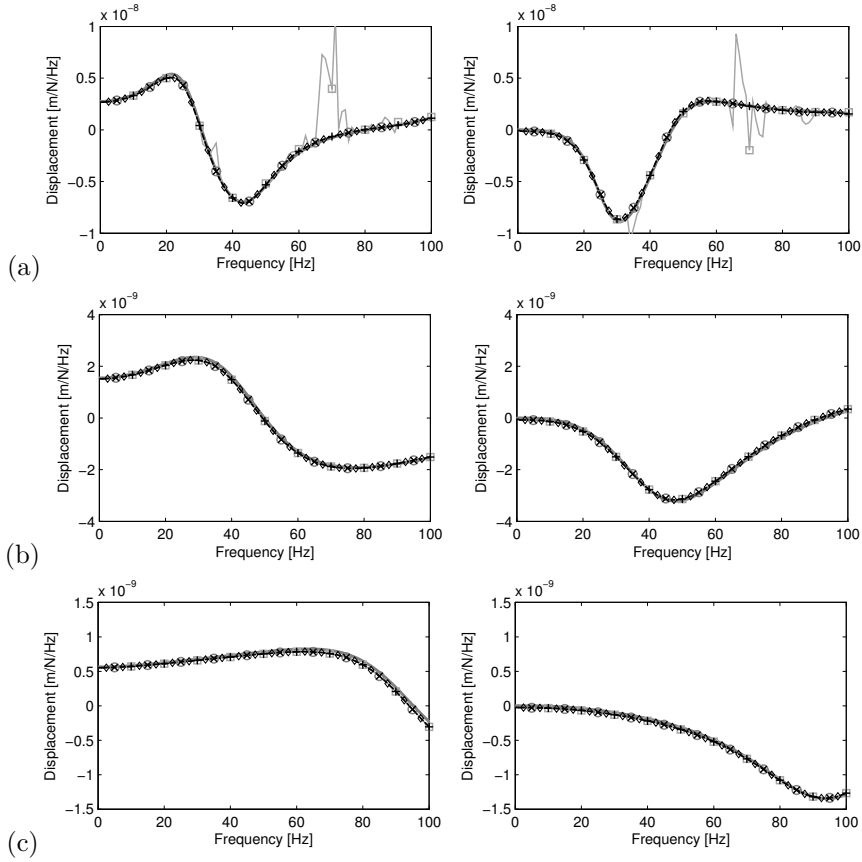

Figure 3.14: Real (left) and imaginary (right) part of the radial displacement at $r = r_o$ due to a unit harmonic pressure applied to a spherical cavity embedded in a layered space, for (a) $\alpha = 1/2$, (b) $\alpha = 1$ and (c) $\alpha = 2$. The solutions of the classical direct coupling approach (dashed black line), the iterative Neumann–Dirichlet (grey squares), Dirichlet–Neumann (black plus signs), Neumann–Neumann (grey circles) and Dirichlet–Dirichlet (black crosses) algorithms, and the monolithic coupling procedure (black rhombuses) are compared to the analytical solution (solid grey line) [29]. The markers are only drawn at a limited number of frequencies.

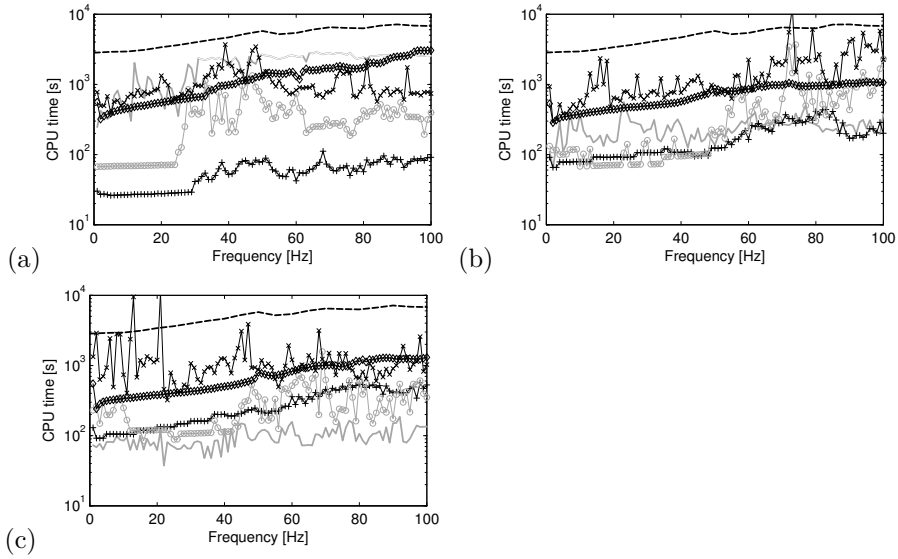

Figure 3.15: CPU time required in the classical direct coupling approach (dashed black line), the iterative Neumann–Dirichlet (solid grey line), Dirichlet–Neumann (black plus signs), Neumann–Neumann (grey circles) and Dirichlet–Dirichlet (black crosses) algorithms, and the monolithic coupling procedure (black rhombuses), for a spherical cavity embedded in a layered space with (a) $\alpha = 1/2$, (b) $\alpha = 1$ and (c) $\alpha = 2$. The lines are only drawn if convergence is achieved.

rigorous preconditioner than the one applied here could result in an improved convergence behaviour.

A more detailed investigation of the computational performance of the coupling procedures, and especially of the iterative algorithms, is provided in paper B. In particular, it is demonstrated that the application of Aitken's Δ^2–method is crucial to ensure convergence in the sequential iterative algorithms; no convergence could be obtained with these algorithms in any of the numerical examples in case a fixed value was attributed to the relaxation parameter λ^k, in the entire frequency range of interest. Furthermore, the robustness of the novel relaxation technique for parallel iterative algorithms is illustrated.

3.2 2.5D FE–BE methods with spatial windowing

The coupled FE–$\mathscr{H}$-BE methodology summarized in section 3.1 provides an efficient solution to large 3D dynamic SSI problems. Nevertheless, the associated computation times remain relatively high, in particular for structures with large dimensions. The use of a 2.5D strategy is a computationally efficient alternative but is in its current formulation restricted to structures with an invariant longitudinal geometry. A spatial windowing technique has therefore been developed in the frame of the present work; this technique accounts for the finite length of structures, while maintaining the efficiency of a 2.5D approach in the wavenumber domain. The method is presented in paper C for the case of a single structure and is summarized in the following. Furthermore, an extension to multiple structures is introduced.

The spatial windowing technique originates from vibro–acoustics [150], where it is used e.g. for the calculation of the transmission loss of sandwich composite panels [65] or for the investigation of the vibro–acoustic response of finite multilayered structures [119] and orthogonally stiffened plates [94]. This technique is not well suited for acoustic applications at low frequencies (i.e. when individual modes of the structure dominate the response), as it is unable to account for reflected waves at the boundaries to reproduce the resonant behaviour of the modes [94]. At higher frequencies, however, the response shifts from the resonant to the non–resonant mass–law regime and application of the spatial windowing technique leads to results in good agreement with experiments [94, 119, 150]. Its application to dynamic SSI problems fundamentally differs from acoustic problems, however, as the resonant behaviour of individual modes is strongly affected by the dynamic interaction between the structure and the soil.

Single structure

Consider a 2.5D dynamic SSI problem involving the soil domain Ω_s and a single invariant structure Ω_b (e.g. only the wave barrier $\Omega_\mathrm{b} = \Omega_j$ or only the building $\Omega_\mathrm{b} = \Omega_k$ in figure 3.16a). A plane wave $\hat{u}(y,\omega) = \frac{1}{2\pi}\hat{u}_0(\omega)\exp\left(-ik_{y0}y\right)$ with fixed longitudinal wavenumber k_{y0} travels along Ω_b. Its wavenumber spectrum

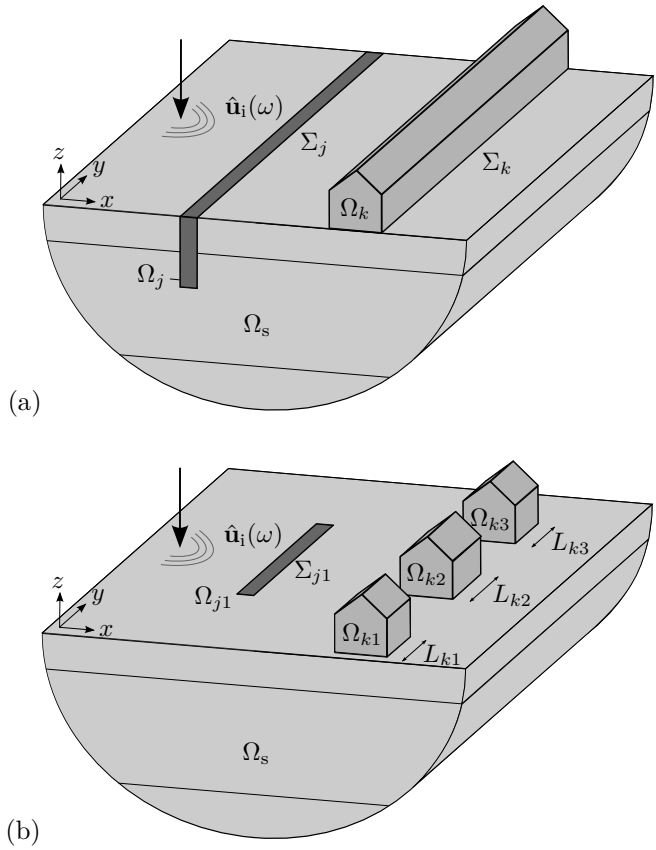

Figure 3.16: The 2.5D dynamic SSI problem (a) before and (b) after application of the spatial windowing technique (with $n_j = 1$ and $n_k = 3$).

is a Dirac delta function at $k_y = k_{y0}$ (figure 3.17a):

$$\tilde{u}(k_y, \omega) = \int_{-\infty}^{+\infty} \frac{1}{2\pi} \hat{u}_0(\omega) \exp\left(-ik_{y0}y\right) \exp\left(ik_y y\right) \, \mathrm{d}y \tag{3.25}$$

$$= \hat{u}_0(\omega) \delta\left(k_y - k_{y0}\right) \tag{3.26}$$

If the structure Ω_b is not invariant but rather consists of a collection of n_b substructures $\Omega'_\mathrm{b} = \bigcup_{l=1}^{n_\mathrm{b}} \Omega_{\mathrm{b}l}$, with each domain $\Omega_{\mathrm{b}l}$ having a finite length $L_{\mathrm{b}l}$ and ranging from $y_{\mathrm{b}l_1}$ to $y_{\mathrm{b}l_2} = y_{\mathrm{b}l_1} + L_{\mathrm{b}l}$ (figure 3.16b), then waves will only

be radiated into the soil domain Ω_s along the soil–structure interface $\Sigma'_\mathrm{b} = \bigcup_{l=1}^{n_\mathrm{b}} \Sigma_{\mathrm{b}l}$. The wavenumber spectrum is consequently determined by restricting the integration in the forward Fourier transform (3.25) to $y \in \bigcup_{l=1}^{n_\mathrm{b}} [y_{\mathrm{b}l_1}, y_{\mathrm{b}l_2}]$:

$$\tilde{u}_\mathrm{sw}(k_y,\omega) = \sum_{l=1}^{n_\mathrm{b}} \int_{y_{\mathrm{b}l_1}}^{y_{\mathrm{b}l_2}} \frac{1}{2\pi}\hat{u}_0(\omega)\exp\left(-ik_{y0}y\right)\exp\left(ik_y y\right)\,\mathrm{d}y \tag{3.27}$$

$$= \sum_{l=1}^{n_\mathrm{b}} \frac{1}{2\pi}\hat{u}_0(\omega)\frac{\exp\left[i\left(k_y-k_{y0}\right)y_{\mathrm{b}l_2}\right]}{i\left(k_y-k_{y0}\right)}\left(1-\exp\left[-i\left(k_y-k_{y0}\right)L_{\mathrm{b}l}\right]\right) \tag{3.28}$$

with $\lim_{k_y\to k_{y0}} \tilde{u}_\mathrm{sw}(k_y,\omega) = \sum_{l=1}^{n_\mathrm{b}} \frac{1}{2\pi}\hat{u}_0(\omega)L_{\mathrm{b}l}$. The subscript 'sw' refers to a spatially windowed quantity. Equation (3.28) reveals that spatial windowing results in a distribution of the energy over the entire wavenumber range [150], while it was concentrated at $k_y = k_{y0}$ for the longitudinally invariant structure. This is illustrated in figure 3.17b (for $n_\mathrm{b} = 1$).

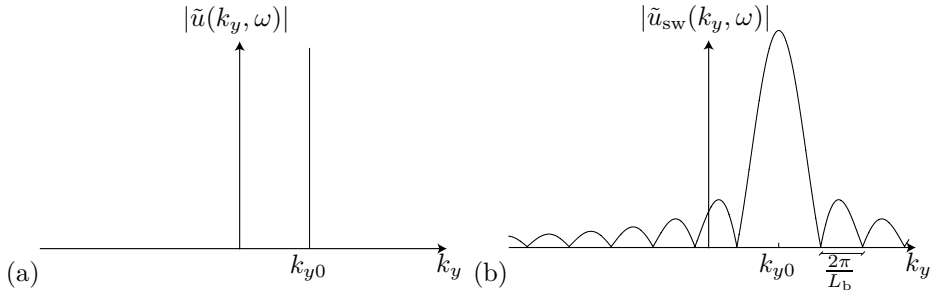

Figure 3.17: Wavenumber spectrum of a plane wave with wavenumber k_{y0} propagating in an infinite structure (a) before and (b) after application of the spatial windowing technique (for $n_\mathrm{b} = 1$).

Application of the spatial windowing technique in the framework of the 2.5D FE–BE methodology outlined in subsection 2.4 implies that each wavenumber component of the displacement vector $\underline{\tilde{\mathbf{u}}}_\mathrm{s}(k_y,\omega)$ is distributed over the entire wavenumber domain according to equation (3.28). As in equation (3.27), the spatially windowed wavenumber spectrum $\underline{\tilde{\mathbf{u}}}_{\mathrm{s,sw}}(k_y,\omega)$ is determined by

restricting the integration in the Fourier integral to $y \in \bigcup_{l=1}^{n_\mathrm{b}} [y_{\mathrm{b}l_1}, y_{\mathrm{b}l_2}]$:

$$\underline{\tilde{\mathbf{u}}}_{\mathrm{s,sw}}(k_y,\omega) = \sum_{l=1}^{n_\mathrm{b}} \int_{y_{\mathrm{b}l_1}}^{y_{\mathrm{b}l_2}} \underline{\hat{\mathbf{u}}}_{\mathrm{s}}(y,\omega) \exp\left(ik_y y\right)\, \mathrm{d}y \tag{3.29}$$

Introducing the inverse Fourier transform (2.18) into equation (3.29) yields:

$$\begin{aligned}&\underline{\tilde{\mathbf{u}}}_{\mathrm{s,sw}}(k_y,\omega)\\ &= \sum_{l=1}^{n_\mathrm{b}} \int_{y_{\mathrm{b}l_1}}^{y_{\mathrm{b}l_2}} \left[\frac{1}{2\pi}\int_{-\infty}^{+\infty} \underline{\tilde{\mathbf{u}}}_{\mathrm{s}}(\varkappa,\omega) \exp\left(-i\varkappa y\right)\, \mathrm{d}\varkappa\right] \exp\left(ik_y y\right)\, \mathrm{d}y\end{aligned} \tag{3.30}$$

Using Fubini's theorem, the order of integration can be changed and equation (3.30) is rewritten as:

$$\underline{\tilde{\mathbf{u}}}_{\mathrm{s,sw}}(k_y,\omega) = \int_{-\infty}^{+\infty} \underline{\tilde{\mathbf{u}}}_{\mathrm{s}}(\varkappa,\omega) \left[\sum_{l=1}^{n_\mathrm{b}} \int_{y_{\mathrm{b}l_1}}^{y_{\mathrm{b}l_2}} \frac{1}{2\pi} \exp\left(i\left(k_y-\varkappa\right)y\right)\, \mathrm{d}y\right]\, \mathrm{d}\varkappa \tag{3.31}$$

Equation (3.31) is identified as the convolution of the original displacement vector $\underline{\tilde{\mathbf{u}}}_{\mathrm{s}}(k_y,\omega)$ and the function $\tilde{w}_{\mathrm{b}}\left(k_y\right)$:

$$\underline{\tilde{\mathbf{u}}}_{\mathrm{s,sw}}(k_y,\omega) = \int_{-\infty}^{+\infty} \underline{\tilde{\mathbf{u}}}_{\mathrm{s}}(\varkappa,\omega)\tilde{w}_{\mathrm{b}}(k_y-\varkappa)\, \mathrm{d}\varkappa \tag{3.32}$$

$$= \underline{\tilde{\mathbf{u}}}_{\mathrm{s}}(k_y,\omega) * \tilde{w}_{\mathrm{b}}\left(k_y\right) \tag{3.33}$$

where $*$ indicates convolution, while the windowing function $\tilde{w}_{\mathrm{b}}\left(k_y\right)$ is defined as:

$$\tilde{w}_{\mathrm{b}}\left(k_y\right) = \sum_{l=1}^{n_\mathrm{b}} \int_{y_{\mathrm{b}l_1}}^{y_{\mathrm{b}l_2}} \frac{1}{2\pi} \exp\left(ik_y y\right)\, \mathrm{d}y \tag{3.34}$$

$$= \sum_{l=1}^{n_\mathrm{b}} \frac{1}{2\pi} \frac{\exp\left(ik_y y_{\mathrm{b}l_2}\right)}{ik_y} \left(1-\exp\left[-ik_y L_{\mathrm{b}l}\right]\right) \tag{3.35}$$

Spatially windowed interface tractions $\underline{\tilde{\mathbf{t}}}_{\mathrm{s,sw}}(k_y,\omega)$ are defined analogously:

$$\underline{\tilde{\mathbf{t}}}_{\mathrm{s,sw}}(k_y,\omega) = \underline{\tilde{\mathbf{t}}}_{\mathrm{s}}(k_y,\omega) * \tilde{w}_{\mathrm{b}}\left(k_y\right) \tag{3.36}$$

Equations (3.33) and (3.36) indicate that the spatial windowing technique only entails postprocessing of the original 2.5D results, hence providing an efficient

way to account for the structures' finite length. A major limitation of the technique is, however, its inability to account for the modal behaviour of the structures; only the diffraction due to the structures' finite length is considered.

The radiated wavefield in the soil $\underline{\tilde{\mathbf{u}}}_{\mathrm{r,sw}}(k_y,\omega)$ can finally be computed by means of the discretized 2.5D representation formula (2.21), substituting $\underline{\tilde{\mathbf{u}}}_{\mathrm{s}}(k_y,\omega)$ and $\underline{\tilde{\mathbf{t}}}_{\mathrm{s}}(k_y,\omega)$ by their spatially windowed equivalents $\underline{\tilde{\mathbf{u}}}_{\mathrm{s,sw}}(k_y,\omega)$ and $\underline{\tilde{\mathbf{t}}}_{\mathrm{s,sw}}(k_y,\omega)$, respectively.

It is demonstrated in the following that the calculation of the radiated wavefield with the 2.5D integral representation theorem, incorporating spatially windowed displacements and tractions, is equivalent to a 3D formulation. Consider to this end the continuous 2.5D wavenumber domain integral representation theorem (2.19), which relates the displacements $\tilde{u}_{\mathrm{sw},i}(x',k_y,z',\omega)$ in the soil domain to the displacements $\tilde{u}_{\mathrm{sw},j}(x,k_y,z,\omega)$ and tractions $\tilde{t}^{\mathbf{n}}_{\mathrm{sw},j}(x,k_y,z,\omega)$ on the boundary S (after application of spatial windowing):

$$\begin{aligned}\kappa\tilde{u}_{\mathrm{sw},i}(x',k_y,z',\omega) = &\int_S \tilde{u}^{\mathrm{G}}_{ij}(x',0,z',x,-k_y,z,\omega)\tilde{t}^{\mathbf{n}}_{\mathrm{sw},j}(x,k_y,z,\omega)\,\mathrm{d}S \\ &- \int_S \tilde{t}^{\mathrm{G}\mathbf{n}}_{ij}(x',0,z',x,-k_y,z,\omega)\tilde{u}_{\mathrm{sw},j}(x,k_y,z,\omega)\,\mathrm{d}S\end{aligned} \tag{3.37}$$

The displacements $\hat{u}_{\mathrm{sw},i}(x',y',z',\omega)$ in the frequency–spatial domain are found through the inverse Fourier transform (2.18) from the wavenumber k_y to the longitudinal coordinate y':

$$\begin{aligned}&\kappa\hat{u}_{\mathrm{sw},i}(x',y',z',\omega) \\ &= \frac{1}{2\pi}\int_{-\infty}^{+\infty} \kappa\tilde{u}_{\mathrm{sw},i}(x',k_y,z',\omega)\exp\left(-ik_y y'\right)\,\mathrm{d}k_y \\ &= \frac{1}{2\pi}\int_{-\infty}^{+\infty} \left[\int_S \tilde{u}^{\mathrm{G}}_{ij}(x',0,z',x,-k_y,z,\omega)\tilde{t}^{\mathbf{n}}_{\mathrm{sw},j}(x,k_y,z,\omega)\,\mathrm{d}S\right. \\ &\left. - \int_S \tilde{t}^{\mathrm{G}\mathbf{n}}_{ij}(x',0,z',x,-k_y,z,\omega)\tilde{u}_{\mathrm{sw},j}(x,k_y,z,\omega)\,\mathrm{d}S\right]\exp\left(-ik_y y'\right)\,\mathrm{d}k_y\end{aligned} \tag{3.38}$$

The spatially windowed tractions and displacements are subsequently expressed as a convolution of the original 2.5D variables and the windowing function

$\tilde{w}_{\mathrm{b}}(k_y)$, respectively, according to equations (3.33) and (3.36):

$$\begin{aligned}
&\kappa\hat{u}_{\mathrm{sw},i}(x',y',z',\omega)\\
&= \frac{1}{2\pi}\int_{-\infty}^{+\infty}\left[\int_S \tilde{u}_{ij}^{\mathrm{G}}(x',0,z',x,-k_y,z,\omega)\left[\tilde{t}_j^{\mathbf{n}}(x,k_y,z,\omega)*\tilde{w}_{\mathrm{b}}(k_y)\right]\mathrm{d}S\right.\\
&\left.-\int_S \tilde{t}_{ij}^{\mathrm{G}\mathbf{n}}(x',0,z',x,-k_y,z,\omega)\left[\tilde{u}_j(x,k_y,z,\omega)*\tilde{w}_{\mathrm{b}}(k_y)\right]\mathrm{d}S\right]\\
&\times\exp\left(-ik_y y'\right)\mathrm{d}k_y
\end{aligned}\tag{3.39}$$

The convolutions in equation (3.39) are elaborated and equation (3.34) is introduced for $\tilde{w}_{\mathrm{b}}(k_y)$:

$$\begin{aligned}
&\kappa\hat{u}_{\mathrm{sw},i}(x',y',z',\omega)\\
&= \frac{1}{2\pi}\int_{-\infty}^{+\infty}\left[\int_S \tilde{u}_{ij}^{\mathrm{G}}(x',0,z',x,-k_y,z,\omega)\right.\\
&\left.\times\left[\int_{-\infty}^{+\infty}\tilde{t}_j^{\mathbf{n}}(x,\varkappa,z,\omega)\left[\sum_{l=1}^{n_{\mathrm{b}}}\int_{y_{\mathrm{b}l_1}}^{y_{\mathrm{b}l_2}}\frac{1}{2\pi}\exp\left(i\left(k_y-\varkappa\right)y\right)\mathrm{d}y\right]\mathrm{d}\varkappa\right]\mathrm{d}S\right]\\
&\times\exp\left(-ik_y y'\right)\mathrm{d}k_y\\
&-\frac{1}{2\pi}\int_{-\infty}^{+\infty}\left[\int_S \tilde{t}_{ij}^{\mathrm{G}\mathbf{n}}(x',0,z',x,-k_y,z,\omega)\right.\\
&\left.\times\left[\int_{-\infty}^{+\infty}\tilde{u}_j(x,\varkappa,z,\omega)\left[\sum_{l=1}^{n_{\mathrm{b}}}\int_{y_{\mathrm{b}l_1}}^{y_{\mathrm{b}l_2}}\frac{1}{2\pi}\exp\left(i\left(k_y-\varkappa\right)y\right)\mathrm{d}y\right]\mathrm{d}\varkappa\right]\mathrm{d}S\right]\\
&\times\exp\left(-ik_y y'\right)\mathrm{d}k_y
\end{aligned}\tag{3.40}$$

Fubini's theorem allows changing the order of integration. Equation (3.40) is consequently rewritten as:

$$\begin{aligned}
&\kappa\hat{u}_{\mathrm{sw},i}(x',y',z',\omega)\\
&=\int_S\left[\sum_{l=1}^{n_\mathrm{b}}\int_{y_{\mathrm{b}l_1}}^{y_{\mathrm{b}l_2}}\left[\frac{1}{2\pi}\int_{-\infty}^{+\infty}\tilde{u}_{ij}^{\mathrm{G}}(x',0,z',x,-k_y,z,\omega)\exp\left(ik_y\left(y-y'\right)\right)\mathrm{d}k_y\right]\right.\\
&\left.\times\left[\frac{1}{2\pi}\int_{-\infty}^{+\infty}\tilde{t}_j^{\mathbf{n}}(x,\varkappa,z,\omega)\exp\left(-i\varkappa y\right)\mathrm{d}\varkappa\right]\,\mathrm{d}y\right]\,\mathrm{d}S\\
&-\int_S\left[\sum_{l=1}^{n_\mathrm{b}}\int_{y_{\mathrm{b}l_1}}^{y_{\mathrm{b}l_2}}\left[\frac{1}{2\pi}\int_{-\infty}^{+\infty}\tilde{t}_{ij}^{\mathrm{G}\mathbf{n}}(x',0,z',x,-k_y,z,\omega)\exp\left(ik_y\left(y-y'\right)\right)\mathrm{d}k_y\right]\right.\\
&\left.\times\left[\frac{1}{2\pi}\int_{-\infty}^{+\infty}\tilde{u}_j(x,\varkappa,z,\omega)\exp\left(-i\varkappa y\right)\mathrm{d}\varkappa\right]\,\mathrm{d}y\right]\,\mathrm{d}S
\end{aligned}\tag{3.41}$$

The bracketed integrals over k_y and $\varkappa$ in equation (3.41) are identified as inverse Fourier transforms from the wavenumber domain to the spatial domain. Following expression is hence obtained:

$$\begin{aligned}
&\kappa\hat{u}_{\mathrm{sw},i}(x',y',z',\omega)\\
&=\int_S\left[\sum_{l=1}^{n_\mathrm{b}}\int_{y_{\mathrm{b}l_1}}^{y_{\mathrm{b}l_2}}\hat{u}_{ij}^{\mathrm{G}}(x',0,z',x,y-y',z,\omega)\hat{t}_j^{\mathbf{n}}(x,y,z,\omega)\,\mathrm{d}y\right]\,\mathrm{d}S\\
&-\int_S\left[\sum_{l=1}^{n_\mathrm{b}}\int_{y_{\mathrm{b}l_1}}^{y_{\mathrm{b}l_2}}\hat{t}_{ij}^{\mathrm{G}\mathbf{n}}(x',0,z',x,y-y',z,\omega)\hat{u}_j(x,y,z,\omega)\,\mathrm{d}y\right]\,\mathrm{d}S
\end{aligned}\tag{3.42}$$

It is furthermore assumed that the soil is invariant in the horizontal direction [56]. As a result, the Green's functions only depend on the relative horizontal distance between source and receiver, and the source and receiver positions can therefore be shifted from 0 and $y-y'$ to y' and y, respectively. This yields the following equation:

$$\begin{aligned}
&\kappa\hat{u}_{\mathrm{sw},i}(x',y',z',\omega)\\
&=\int_S\left[\sum_{l=1}^{n_\mathrm{b}}\int_{y_{\mathrm{b}l_1}}^{y_{\mathrm{b}l_2}}\hat{u}_{ij}^{\mathrm{G}}(x',y',z',x,y,z,\omega)\hat{t}_j^{\mathbf{n}}(x,y,z,\omega)\,\mathrm{d}y\right]\,\mathrm{d}S\\
&-\int_S\left[\sum_{l=1}^{n_\mathrm{b}}\int_{y_{\mathrm{b}l_1}}^{y_{\mathrm{b}l_2}}\hat{t}_{ij}^{\mathrm{G}\mathbf{n}}(x',y',z',x,y,z,\omega)\hat{u}_j(x,y,z,\omega)\,\mathrm{d}y\right]\,\mathrm{d}S
\end{aligned}\tag{3.43}$$

Equation (3.43) agrees with the 3D integral representation formula (2.10) (with the boundary Σ written as $\Sigma = \bigcup_{l=1}^{n_\mathrm{b}} \Sigma_{\mathrm{b}l}$). This demonstrates that the calculation of the radiated wavefield in the soil by means of a 2.5D formulation with spatial windowing is equivalent to a 3D formulation.

Multiple structures

The spatial windowing technique can also be extended to 2.5D dynamic SSI problems where multiple structures interact (e.g. if the wave barrier and building in figure 3.16 are considered simultaneously). If N structures Ω_j are considered, the soil displacement vector $\underline{\tilde{\mathbf{u}}}_{\mathrm{s}j}(k_y,\omega)$ at each soil–structure interface Σ_j becomes:

$$\underline{\tilde{\mathbf{u}}}_{\mathrm{s}j,\mathrm{sw}}(k_y,\omega) = \underline{\tilde{\mathbf{u}}}_{\mathrm{s}j}(k_y,\omega) * \tilde{w}_j\,(k_y) \quad \text{for} \quad j = 1\ldots N \tag{3.44}$$

where the windowing function $\tilde{w}_j\,(k_y)$ characterizes the presence of n_j finite substructures along Ω_j and is defined as in equation (3.35). The dynamic through soil–coupling of structures Ω_j and Ω_k implies that the displacement vector $\underline{\tilde{\mathbf{u}}}_{\mathrm{s}j,\mathrm{sw}}(k_y,\omega)$ is also affected by the application of spatial windowing to all other structures Ω_k, which is not accounted for, however, if equation (3.44) is applied independently to each subdomain Ω_j. It is thus required to re–calculate the displacements $\underline{\tilde{\mathbf{u}}}_{\mathrm{s}j}(k_y,\omega)$, accounting for the spatially windowed displacements $\underline{\tilde{\mathbf{u}}}_{\mathrm{s}k,\mathrm{sw}}(k_y,\omega)$ at Σ_k, by means of the BE equation (2.20). Equation (2.20) is elaborated as:

$$\sum_{k=1}^{N} \left(\widetilde{\mathbf{T}}_{jk}(k_y,\omega) + \mathbf{I}_{jk}\right) \underline{\tilde{\mathbf{u}}}_{\mathrm{s}k}(k_y,\omega) = \sum_{k=1}^{N} \widetilde{\mathbf{U}}_{jk}(k_y,\omega)\underline{\tilde{\mathbf{t}}}_{\mathrm{s}k}(k_y,\omega) \quad \text{for} \quad j = 1\ldots N \tag{3.45}$$

The term on the left hand side of equation (3.45) can subsequently be expanded as follows:

$$\left(\widetilde{\mathbf{T}}_{jj}(k_y,\omega) + \mathbf{I}_{jj}\right) \underline{\tilde{\mathbf{u}}}_{\mathrm{s}j}(k_y,\omega) + \sum_{k\neq j}^{N} \widetilde{\mathbf{T}}_{jk}(k_y,\omega)\underline{\tilde{\mathbf{u}}}_{\mathrm{s}k}(k_y,\omega) = \sum_{k=1}^{N} \widetilde{\mathbf{U}}_{jk}(k_y,\omega)\underline{\tilde{\mathbf{t}}}_{\mathrm{s}k}(k_y,\omega) \quad \text{for} \quad j = 1\ldots N \tag{3.46}$$

This allows expressing the displacements $\underline{\tilde{\mathbf{u}}}_{\mathrm{s}j}(k_y,\omega)$, replacing the displacements $\underline{\tilde{\mathbf{u}}}_{\mathrm{s}k}(k_y,\omega)$ by their spatially windowed equivalents $\underline{\tilde{\mathbf{u}}}_{\mathrm{s}k,\mathrm{sw}}(k_y,\omega)$:

$$\underline{\tilde{\mathbf{u}}}_{\mathrm{s}j}(k_y,\omega) = \left(\widetilde{\mathbf{T}}_{jj}(k_y,\omega) + \mathbf{I}_{jj}\right)^{-1} \left[\sum_{k=1}^{N} \widetilde{\mathbf{U}}_{jk}(k_y,\omega)\underline{\tilde{\mathbf{t}}}_{\mathrm{s}k}(k_y,\omega) - \sum_{k\neq j}^{N} \widetilde{\mathbf{T}}_{jk}(k_y,\omega)\underline{\tilde{\mathbf{u}}}_{\mathrm{s}k,\mathrm{sw}}(k_y,\omega)\right] \quad \text{for} \quad j = 1\ldots N \tag{3.47}$$

The resulting displacements $\underline{\tilde{\mathbf{u}}}_{\mathrm{s}j}(k_y,\omega)$ $(j = 1\ldots N)$ are subsequently spatially windowed using equation (3.44), which allows for another evaluation of equation (3.47). An iterative procedure is thus performed until convergence is achieved, incorporating Aitken's Δ^2–method to accelerate convergence.

Numerical example

Various numerical examples are presented and discussed in paper C to illustrate the spatial windowing technique and to investigate its applicability; full 3D FE–$\mathscr{H}$-BE calculations are performed for validation. In all of these examples, a single finite structure is studied. An example of the application of spatial windowing to multiple structures will be discussed in section 4.3.

The first set of examples considered in paper C involves elongated structures with a length that is relatively large compared to the other dimensions (i.e. barriers for the mitigation of vibration transmission in the soil); the application of a 2.5D approach with spatial windowing hence seems to be appropriate for these cases. These examples will be reviewed in section 4.1. The applicability of the proposed technique is also illustrated for short structures that can not at all be regarded as invariant. It is demonstrated in paper C that the proposed technique is appropriate as long as the modal behaviour of the finite structure(s) does not dominate the response, which is the case in many dynamic SSI problems due to the radiation damping in the soil. A numerical example of a short structure is recapitulated in the following to illustrate the validity of the methodology.

Consider a flexible square surface foundation on a horizontally layered halfspace which is loaded by a unit harmonic vertical point load at its center. The geometric and dynamic characteristics of the foundation and the halfspace are specified in paper C. Within the frequency range of interest, the foundation has bending eigenmodes at 40 Hz and 62 Hz that can be excited by the loading under consideration. The spatial windowing technique is employed to compute

the response of the foundation and the wavefield in the soil based on a 2.5D calculation.

Figure 3.18 shows the real part of the vertical displacement $\hat{u}_z(\mathbf{x}, \omega)$ of the foundation and the soil at 25 Hz and 100 Hz. Results obtained with the original 2.5D FE–BE model (for an infinitely long flexible foundation), the 2.5D FE–BE model with spatial windowing, and a 3D FE–$\mathscr{H}$-BE model are compared. At 25 Hz, a reasonable agreement between the results of the three models is observed, as the wavelength in the soil remains large compared to the dimensions of the foundation. At higher frequencies, however, the wavefield in the soil is more strongly affected by the presence of the foundation. Application of the spatial windowing technique modifies the original 2.5D results considerably; this results in a good agreement with the 3D calculations.

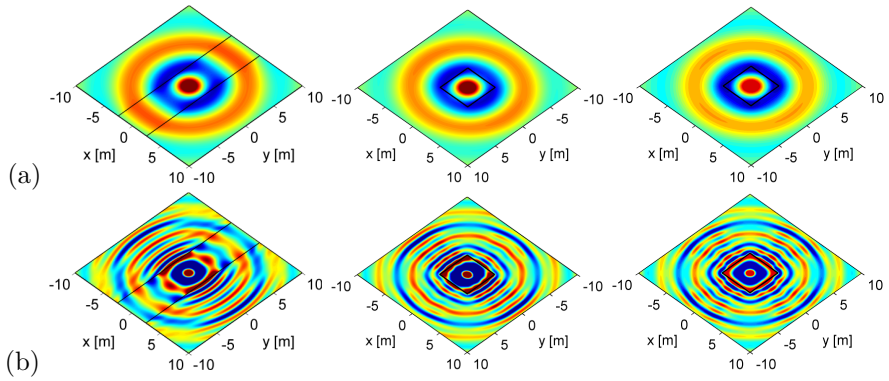

Figure 3.18: Real part of the vertical displacement $\hat{u}_z(\mathbf{x}, \omega)$ of the flexible foundation and the soil at (a) 25 Hz and (b) 100 Hz. The results are calculated by means of a 2.5D FE–BE model (left), a 2.5D FE–BE model with spatial windowing (middle), and a 3D FE–$\mathscr{H}$-BE model (right).

Figure 3.19 shows the free field mobility along the line $y = 0$ m at several distances from the foundation in the frequency range between 0 Hz and 100 Hz. Below 25 Hz, the three numerical methodologies yield the same result, as the wavelength in the soil remains large compared to the dimensions of the foundation, while significant discrepancies between the 2.5D and 3D model are observed at higher frequencies (as expected). These deviations are more pronounced in the near field and are almost negligible in the far field. The mobilities obtained after application of spatial windowing are in good correspondence with the 3D results, although the agreement at $x = 8$ m remains relatively poor.

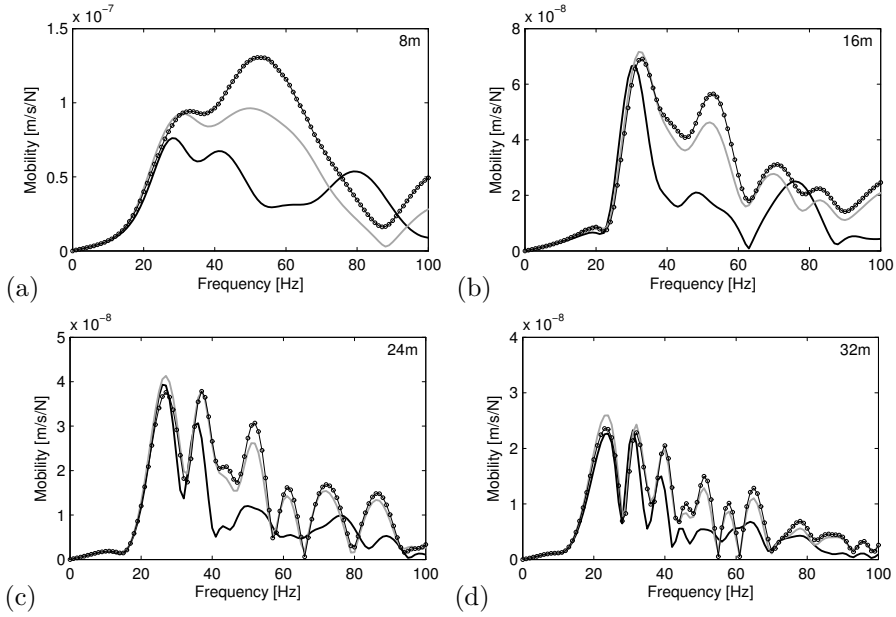

Figure 3.19: Free field mobility along the line $y = 0\,\mathrm{m}$ at (a) 8 m, (b) 16 m, (c) 24 m, and (d) 32 m from the center of the foundation. The results are calculated by means of a 2.5D FE–BE model (black line), a 2.5D FE–BE model with spatial windowing (circles), and a 3D FE–$\mathscr{H}$-BE model (grey line).

The natural frequencies of the foundation at 40 Hz and 62 Hz are not apparent in figure 3.19 due to the strong dynamic SSI and the associated radiation damping in the soil. This is also illustrated in figure 3.20, which shows the modulus and phase of the vertical displacement $\hat{u}_z(\omega)$ at the center of the foundation. The peak at 20 Hz corresponds to resonance of the foundation on the layered halfspace; it is not a natural frequency of the foundation. The response is thus not dominated by the modal behaviour of the foundation, explaining the suitability of the spatial windowing technique in the case under consideration.

The limitations of the spatial windowing technique are further explored by replacing the layered halfspace by a single layer on bedrock. The characteristics of this layer are chosen such that the surface waves in the soil remain evanescent in the whole frequency range under consideration (see paper C). The modulus and phase of the vertical displacement $\hat{u}_z(\omega)$ at the center of the foundation are shown in figure 3.21. As there are no propagative surface waves in the soil,

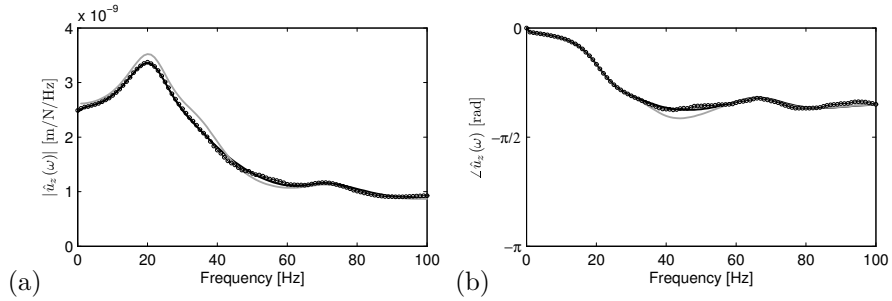

Figure 3.20: (a) Modulus and (b) phase of the vertical displacement $\hat{u}_z(\omega)$ at the center of a flexible foundation on a layered halfspace. The results are calculated by means of a 2.5D FE–BE model (black line), a 2.5D FE–BE model with spatial windowing (circles), and a 3D FE–$\mathscr{H}$-BE model (grey line).

the radiation damping is very limited, and the eigenmodes of the foundation consequently prevail in the response of the 3D coupled soil–foundation system. The resonance peaks near 40 Hz and 62 Hz can clearly be distinguished in figure 3.21. The 2.5D approach with spatial windowing gives a reasonable correspondence with these results below 40 Hz, but large discrepancies are observed at higher frequencies. This example illustrates the shortcoming of the technique in case of low radiation damping in the soil, as it is unable to account for the dominant modal behaviour of the structure.

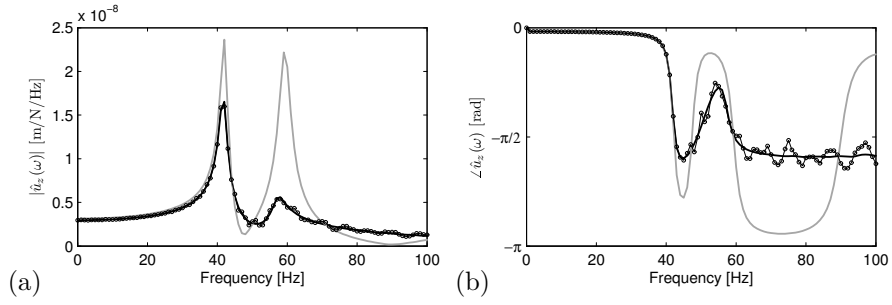

Figure 3.21: (a) Modulus and (b) phase of the vertical displacement $\hat{u}_z(\omega)$ at the center of a flexible foundation on a single layer on bedrock. The results are calculated by means of a 2.5D FE–BE model (black line), a 2.5D FE–BE model with spatial windowing (circles), and a 3D FE–$\mathscr{H}$-BE model (grey line).

3.3 Conclusion

In this chapter, innovative methods for the efficient solution of dynamic SSI problems have been presented. These methods form the subject of papers A, B, and C in Part II of the dissertation. Their application to large scale problems will subsequently be considered in chapter 4.

First, the use of $\mathscr{H}$–matrices for the approximation of dense BE collocation matrices has been discussed. These matrices consist of collections of block matrices of various sizes, in which the ACA algorithm is employed to compute low rank approximations of blocks corresponding to admissible cluster pairs. A major advantage of ACA is its purely algebraic character, avoiding the need for (semi–)analytical expressions of the Green's functions employed in the BE formulation as compared to e.g. the fast multipole method; this enables the incorporation of numerically computed Green's functions of layered soils. The resulting set of $\mathscr{H}$-BE equations is subsequently solved with an iterative (F)GMRES solver. The application of $\mathscr{H}$–matrices enables the evaluation of much larger 3D models compared to classical BE methods, as has been illustrated through a numerical example.

Direct, iterative and monolithic FE–$\mathscr{H}$-BE coupling strategies have been considered next. The computational performance of each algorithm has been assessed, revealing that the direct approach is the least efficient as the assembly of a dynamic soil stiffness matrix requires the solution of a large amount of $\mathscr{H}$-BE equations. Iterative coupling procedures are more efficient, provided that suitable boundary conditions are applied to each subdomain. It is demonstrated that sequential iterative algorithms should be preferred if there exists a strong stiffness contrast between the FE and $\mathscr{H}$-BE subdomain, with Neumann boundary conditions to be imposed on the most stiff subdomain. The application of Aitken's Δ^2–method for the determination of a proper interface relaxation parameter ensures and speeds up the convergence of these sequential algorithms. Parallel iterative algorithms provide a valuable alternative for cases where an a priori estimation of the flexibility of each subdomain is not obvious and an appropriate novel relaxation procedure has been proposed for these algorithms. An efficient combination of FE and $\mathscr{H}$–BE models can also be achieved by means of a monolithic coupling scheme, although the convergence in the examples considered turns out to be relatively slow.

Finally, the applicability of 2.5D FE–BE methods for dynamic SSI problems has been extended by means of a spatial windowing technique, hence providing an efficient alternative to full 3D computations. This technique results in a redistribution of the wavenumber spectrum over the entire wavenumber domain using a windowing function that characterizes the presence of one or more finite

substructures. The diffraction occurring at the structures' edges is accounted for, but the appearance of structural modes resulting from reflections of waves at the structures' boundaries is not. These modes have only a limited influence on the structural response in most of the applications due to dynamic SSI and the associated radiation damping in the soil; the proposed methodology is then even appropriate for short structures. If eigenmodes prevail in the response, however, the spatial windowing technique reaches its limits of suitability.

Chapter 4

Applications

The numerical techniques presented in chapters 2 and 3 allow for the rigorous solution of a large variety of dynamic SSI problems. This chapter gives an overview of three applications considered in the publications of part II.

All applications are related to railway induced ground vibrations, which can lead to disturbance of sensitive equipment and hindrance to people in buildings in close proximity of railway lines ($1 - 80\,\mathrm{Hz}$). Section 4.1 investigates the mitigation of vibrations by means of measures on the propagation path between source (railway tunnel or track) and receiver (building). The importance of dynamic through–soil coupling of source and receiver in numerical prediction models for railway induced vibrations is subsequently studied in section 4.2. Finally, the interaction between multiple neighbouring buildings in an urban environment is addressed in section 4.3.

4.1 Vibration mitigation measures on the propagation path in the soil

During the last decades, a lot of research has been performed to develop efficient and cost–effective vibration countermeasures for reducing the levels of railway induced building vibration [82, 88]. Measures can either be taken at the source [100], on the propagation path between source and receiver [85], or at the receiver [143]. An advantage of interventions on the propagation path is that no modifications of the track are required, while multiple buildings can

be shielded simultaneously from vibration. Furthermore, this type of measures can relatively easily be implemented in existing situations. Typical examples are vibration isolation screens [158], buried wall barriers [5], and wave impeding blocks [134].

Within the frame of the present work, two types of mitigation measures have been studied: an open trench and a stiff wave barrier. In both cases, 2.5D computations (without and with spatial windowing) as well as full 3D calculations have been performed.

4.1.1 Open trench

Open trenches aim to reflect the impinging waves and are expected to be effective if their depth d becomes comparable to the penetration depth of the Rayleigh waves in the soil [158]. The efficiency of a trench in a homogeneous halfspace has been investigated in detail in paper C; the main findings are summarized in the following.

A trench with width $w = 2\,\mathrm{m}$ and depth $d = 2\,\mathrm{m}$ is considered, positioned at $x = 4\,\mathrm{m}$ and aligned along the y–axis of the coordinate system. The halfspace is characterized by a shear wave velocity $C_\mathrm{s} = 200\,\mathrm{m/s}$, a dilatational wave velocity $C_\mathrm{p} = 400\,\mathrm{m/s}$, a density $\rho = 2000\,\mathrm{kg/m^3}$, and material damping ratios $\beta_\mathrm{s} = \beta_\mathrm{p} = 0.025$ in deviatoric and volumetric deformation. Figure 4.1a shows the real part of the vertical displacement $\hat{u}_z(\mathbf{x}, \omega)$ in the soil due to a harmonic point load at 30 Hz at the surface of the halfspace. The propagation of Rayleigh waves with a wavelength $\lambda_\mathrm{R}(f) = 6.2\,\mathrm{m}$ can clearly be observed. The wavefield in the soil in case an infinitely long trench is excavated is shown in figure 4.1b; this is obtained with a 2.5D BE calculation. The dimensionless trench depth $\bar{d} = d/\lambda_\mathrm{R}(f)$ equals $\bar{d} = 0.32$ at the frequency under consideration. A significant reduction of vibration levels is achieved behind the trench. The vibration reduction efficiency is quantified through the vertical insertion loss $\widehat{\mathrm{IL}}_z(\mathbf{x}, \omega)$:

$$\widehat{\mathrm{IL}}_z(\mathbf{x}, \omega) = 20 \log_{10} \frac{|\hat{u}_z^\mathrm{ref}(\mathbf{x}, \omega)|}{|\hat{u}_z(\mathbf{x}, \omega)|} \tag{4.1}$$

which compares the vertical displacement $\hat{u}_z^\mathrm{ref}(\mathbf{x}, \omega)$ in the reference case (without a trench) to the vertical displacement $\hat{u}_z(\mathbf{x}, \omega)$ in case a trench is included. Positive values of the insertion loss indicate a reduction of the vertical free field vibrations. Insertion loss values of 6 dB and more are obtained in figure 4.1b due to the reflection of waves by the trench; this corresponds to a reduction of vibration levels by a factor of two and more.

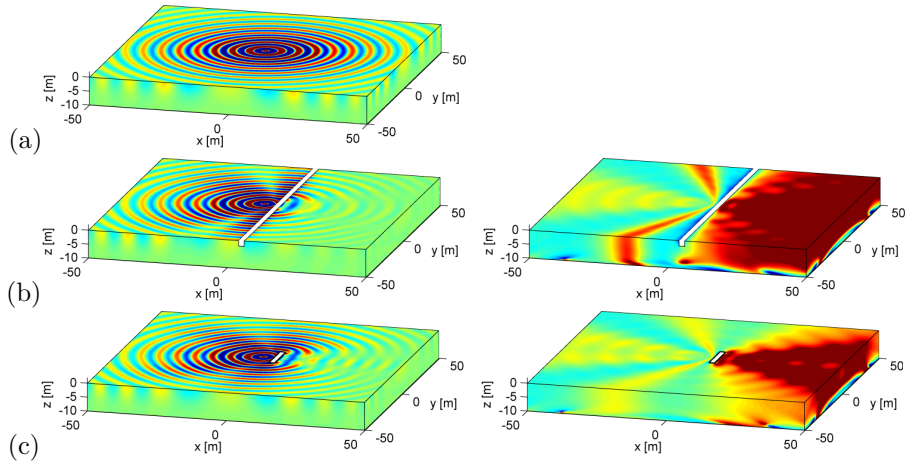

Figure 4.1: Real part of the vertical displacement $\hat{u}_z(\mathbf{x}, \omega)$ at 30 Hz (a) without trench, (b) with an infinitely long open trench, and (c) with an open trench of 15 m (left hand side). The corresponding insertion loss $\widehat{\mathrm{IL}}_z(\mathbf{x}, \omega)$ is shown at the right hand side.

Figure 4.1c shows the vertical wavefield in the soil and the corresponding insertion loss in case the trench has only a length of 15 m. These results are obtained by applying the spatial windowing technique (outlined in section 3.2) to the original 2.5D results. The results obtained with this approach have furthermore been compared in paper C to full 3D $\mathscr{H}$-BE computations and an excellent agreement was found. Due to its limited length, the trench is only able to reflect the part of the wavefield that impinges on the trench, leading to a reduction of the area where vibration levels are effectively reduced (compared to the calculation based on the assumption of longitudinal invariance). This indicates that it is important to account for a trench's finite length when designing this type of vibration mitigation measure.

The effectiveness of the trench can also be interpreted in the frequency–wavenumber domain. Figure 4.2a shows the insertion loss $\widetilde{\mathrm{IL}}_z(x = 8\,\mathrm{m}, \bar{k}_y, z = 0\,\mathrm{m}, \omega)$ for an infinitely long trench, which is defined as in equation (4.1) but now for the frequency–wavenumber domain representation of the vertical free field displacement. The dimensionless wavenumber $\bar{k}_y$ is defined as $\bar{k}_y = k_y C_\mathrm{s}/\omega$, where C_s is the shear wave velocity of the halfspace. The insertion loss is only shown in a range $0 \leq \bar{k}_y \leq \bar{k}_\mathrm{R}$, with $\bar{k}_\mathrm{R} = C_\mathrm{s}/C_\mathrm{R}$ the dimensionless wavenumber corresponding to a Rayleigh wave propagating in the y–direction. For wavenumbers $\bar{k}_y > \bar{k}_\mathrm{R}$, waves do not propagate in the x–direction, as

the lateral wavenumber $\bar{k}_x = -i\sqrt{\bar{k}_y^2 - \bar{k}_\mathrm{R}^2}$ becomes imaginary, resulting in evanescent waves. The dispersion curve of a Rayleigh wave propagating in the y–direction is a horizontal line due to its non–dispersive character in a homogeneous halfspace. It is observed in figure 4.2a that no significant reduction of vibration levels can be achieved below 20 Hz, as the dimensionless trench depth $\bar{d}$ is only 0.20 at this frequency; a significant part of the energy passes underneath the trench. The insertion loss increases up to 4 to 6 dB in the frequency range between 20 Hz and 45 Hz, while it tends to 10 dB and more above 45 Hz. This frequency corresponds to a dimensionless trench depth $\bar{d} = 0.50$, confirming the rule of thumb formulated in [158].

Figure 4.2b shows the insertion loss $\widetilde{\mathrm{IL}}_z(x = 8\,\mathrm{m}, \bar{k}_y, z = 0\,\mathrm{m}, \omega)$ for a trench of 15 m. As only part of the wavefield impinges on the trench, the insertion loss in the $(\omega, \bar{k}_y)$–domain remains limited for $\bar{k}_y > \bar{k}_\mathrm{R} \sin\theta_x$, where the angle θ_x is measured from the x–axis to the line connecting the point of excitation and one edge of the trench (as indicated on figure 3 of paper C).

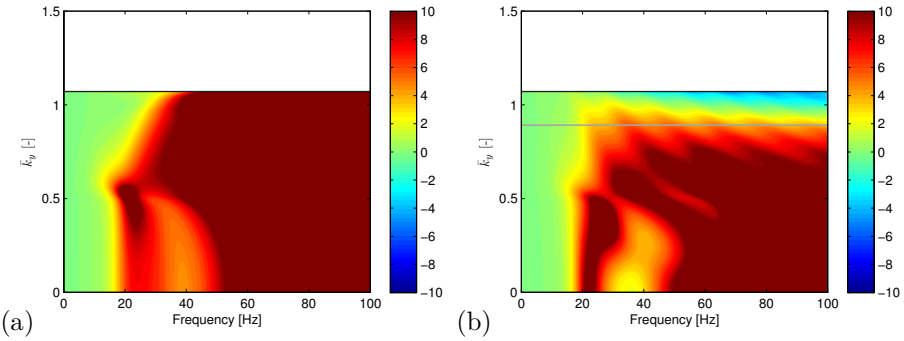

Figure 4.2: Vertical insertion loss $\widetilde{\mathrm{IL}}_z(x = 8\,\mathrm{m}, \bar{k}_y, z = 0\,\mathrm{m}, \omega)$ for (a) an infinitely long open trench and (b) an open trench of 15 m, calculated by means of a 2.5D BE model (with spatial windowing). Superimposed are the dispersion curve of a Rayleigh wave in the y–direction (black line) and the curve $\bar{k}_y = \bar{k}_\mathrm{R} \sin\theta_x$ (grey line).

4.1.2 Stiff wave barrier

For stability reasons, the construction of an open trench in the soil is limited to shallow depths. Furthermore, an open trench can easily get inundated due to surface water run–off or groundwater infiltration, posing concerns on efficiency, durability, and safety. The use of either soft or stiff in–fill materials

(compared to the original soil) allows for an increase of depth and results in a more durable solution. If a soft in–fill material is used, the behaviour of a filled trench resembles that of an open trench [57]. The use of a stiff in–fill material, however, fundamentally alters the physical mechanism that leads to a reduction of vibration levels. This mechanism has been revealed in paper D for the case of an infinitely long barrier using a 2.5D approach; the vibration reduction efficiency for a barrier of finite length has been investigated in papers B and C. The main features are elucidated below.

The case study of an open trench discussed in subsection 4.1.1 is reconsidered, introducing an in–fill material with a shear wave velocity $C_\mathrm{s} = 550\,\mathrm{m/s}$ and a dilatational wave velocity $C_\mathrm{p} = 950\,\mathrm{m/s}$; the density and material damping ratios are the same as those in the halfspace. Figure 4.3a shows the real part of the vertical displacement $\hat{u}_z(\mathbf{x},\omega)$ in the soil due to a harmonic point load at 30 Hz at the surface of the halfspace. The wavefield in case an infinitely long stiff barrier is embedded in the halfspace is shown in figure 4.3b, together with the corresponding insertion loss $\widehat{\mathrm{IL}}_z(\mathbf{x},\omega)$. Almost no reduction of vibration levels is achieved in a sharply delimited central area behind the barrier, while the insertion loss reaches up to 10 dB and more outside this area. This pattern strongly differs from the insertion loss for an open trench in figure 4.1b.

Figure 4.3c shows the vertical wavefield in the soil and the corresponding insertion loss if the length L_y of the barrier is limited to 15 m. It is clear that this finite barrier does not succeed in creating a similar wave impeding effect as in the case where the barrier is assumed to be of infinite length.

The observations in figure 4.3 are best explained by considering the insertion loss $\widetilde{\mathrm{IL}}_z(x = 8\,\mathrm{m}, \bar{k}_y, z = 0\,\mathrm{m}, \omega)$ in the frequency–wavenumber domain. Figure 4.4a shows the insertion loss in the range $0 \leq \bar{k}_y \leq \bar{k}_\mathrm{R}$ for an infinitely long barrier in a halfspace. Superimposed on figure 4.4a is the dispersion curve $\bar{k}_y = \bar{k}_\mathrm{b}(\omega)$ of a free bending wave in an infinitely long Timoshenko beam with the same properties as the stiff wave barrier [76]. The region where a substantial insertion loss is obtained in the $\left(\omega, \bar{k}_y\right)$–domain is clearly bounded by the Rayleigh wave dispersion curve $\bar{k}_y = \bar{k}_\mathrm{R}$ and the free bending wave dispersion curve $\bar{k}_y = \bar{k}_\mathrm{b}(\omega)$. The transmission of propagating plane waves with a wavenumber $\bar{k}_y$ larger than $\bar{k}_\mathrm{b}(\omega)$ (i.e. with a trace wavelength λ_y smaller than $\lambda_\mathrm{b}(\omega)$) is impeded by the barrier, as the admittance of a beam of infinite length is then dominated by its bending stiffness and decreases proportionally to $\bar{k}_y^{-4}$ at a given radial frequency ω [76]. The intersection of the Rayleigh wave and the free bending wave dispersion curves hence determines the critical

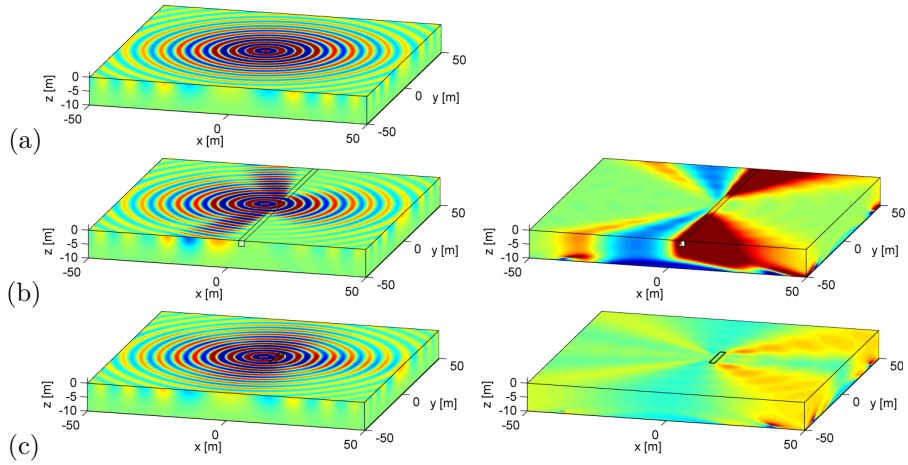

Figure 4.3: Real part of the vertical displacement $\hat{u}_z(\mathbf{x},\omega)$ at 30 Hz (a) without barrier, (b) with an infinitely long barrier, and (c) with a barrier of 15 m (left hand side). The corresponding insertion loss $\widehat{\mathrm{IL}}_z(\mathbf{x},\omega)$ is shown at the right hand side.

frequency f_c from which the stiff barrier becomes effective:

$$f_\mathrm{c} = \frac{C_\mathrm{R}^2}{2\pi}\sqrt{\frac{\rho A}{EI}}\sqrt{\frac{E\mu\kappa}{(E-\rho C_\mathrm{R}^2)(\mu\kappa-\rho C_\mathrm{R}^2)}} \tag{4.2}$$

where E is the Young's modulus, μ the shear modulus, and ρ the density of the in–fill material, while A is the cross sectional area, I the area moment of inertia, and κ the shear coefficient of the barrier. The critical frequency equals 12 Hz in the present case, explaining why large insertion loss values are obtained at 30 Hz in figure 4.3b. In the spatial domain, a reduction of vibration levels is only achieved in an area delimited by a critical angle $\theta_\mathrm{c}(\omega) = \sin^{-1}\left(\bar{k}_\mathrm{b}(\omega)/\bar{k}_\mathrm{R}\right)$, defined as:

$$\theta_\mathrm{c}(\omega) = \sin^{-1}\left(C_\mathrm{R}\sqrt{\rho\frac{E+\mu\kappa+\sqrt{(E-\mu\kappa)^2+\frac{4E(\mu\kappa)^2A}{\rho I\omega^2}}}{2E\mu\kappa}}\right) \tag{4.3}$$

This angle can clearly be distinguished in figure 4.3b. Equations (4.2) and (4.3) are of great practical importance, as they provide simple rules of thumb to assess the expected vibration reduction efficiency of a stiff wave barrier in a preliminary design stage.

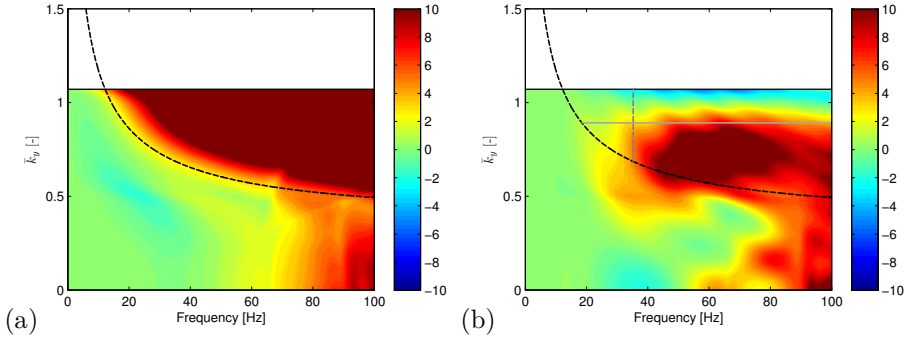

Figure 4.4: Vertical insertion loss $\widetilde{\mathrm{IL}}_z(x = 8\,\mathrm{m}, \bar{k}_y, z = 0\,\mathrm{m}, \omega)$ for (a) an infinitely long barrier and (b) a barrier of 15 m, calculated by means of a 2.5D FE–BE model (with spatial windowing). Superimposed are the dispersion curve of a Rayleigh wave in the y–direction (solid black line), the free bending wave dispersion curve in an infinitely long beam (dashed black line), the curve $\bar{k}_y = \bar{k}_\mathrm{R} \sin\theta_x$ (solid grey line), and the curve $L_y = 2\lambda_\mathrm{b}(\omega)$ (dashed grey line).

Figure 4.4b shows the insertion loss $\widetilde{\mathrm{IL}}_z(x = 8\,\mathrm{m}, \bar{k}_y, z = 0\,\mathrm{m}, \omega)$ for a barrier of 15 m, as obtained with the spatial windowing technique. Large insertion loss values are only observed in a part of the region indicated on figure 4.4a. Two phenomena evoke this reduction of performance. First, a finite barrier is only able to impede the transmission of the part of the wavefield that impinges on it, and no reduction of vibration levels is obtained for $\bar{k}_y > \bar{k}_\mathrm{R} \sin\theta_x$. This is similar to the behaviour of a finite trench discussed in subsection 4.1.1. Second, the results indicate that the barrier should be approximately twice as long as the free bending wavelength $\lambda_\mathrm{b}(\omega)$ in order to develop a similar behaviour as a barrier of infinite length and thus to hinder the transmission of plane waves with a longitudinal wavelength smaller than $\lambda_\mathrm{b}(\omega)$. These two additional conditions are visualized in figure 4.4b by means of a horizontal and vertical line, respectively, clearly delimiting a reduced area of significant insertion loss in the $(\omega, \bar{k}_y)$–domain. Both phenomena result in an upward shift of the critical frequency with respect to the case of an infinite barrier, yielding a critical frequency of 35.2 Hz for a barrier with a length of 15 m.

Two case studies involving a layered halfspace have been discussed as well in paper D, highlighting how the mitigation effectiveness of a stiff wave barrier critically depends on the soil characteristics of the site where it is applied. The validity of equations (4.2) and (4.3) has been verified, demonstrating their usefulness as a design tool even in the case of a stratified soil. Furthermore,

the vibration reduction efficiency during the passage of a train has been investigated.

4.2 The influence of source–receiver interaction

A large number of numerical models have been developed over the past years for the prediction of railway induced vibrations [4, 50, 99, 132, 133, 160]. Computational restrictions as well as the lack of knowledge on appropriate model parameters necessitate the introduction of simplifying assumptions in these models, however. These assumptions are related to the track geometry [56,134], the constitutive behaviour of the soil [37,83,84], the dynamic interaction between neighbouring structures [92], etcetera. The prediction uncertainty related to such simplifications often remains unquantified [80].

In the majority of the numerical models, it is assumed that the dynamic through–soil coupling of source and receiver can be disregarded, resulting in an uncoupled analysis at reduced computational cost [106]. This implies that the dynamic soil stiffness matrices $\widehat{\mathbf{K}}^{\mathrm{s}}_{jk}(\omega)$ $(j \neq k)$ in the FE–BE equation (2.32) are not accounted for. Such an uncoupled approach is well established in seismic engineering, where the distance between source and receiver is sufficiently large compared to the wavelength of waves in the soil, especially in case of far fault ground motions [21, 162]. This assumption might not be valid when predicting railway induced vibrations, given the much smaller separation distance.

Paper E presents a numerical study that quantifies and assesses the influence of source–receiver interaction. A 2.5D FE–BE methodology is employed to analyze such interaction effects in two case studies, i.e. for a building with a railway tunnel at depth and for a building with a ballasted track at the surface of a homogeneous halfspace, respectively, for three different soil types. It is demonstrated that the response of the tunnel and the track are unlikely to be affected by the presence of the building. The train–track interaction (resulting in dynamic forces exerted by a running train on the track) can consequently be analyzed with reasonable accuracy using an uncoupled strategy in which through–soil coupling is disregarded. If the transfer functions from source to receiver are considered, however, significant local variations are induced by source–receiver interaction. This is illustrated in figure 4.5, showing the real part of the vertical displacement $\hat{u}_z(\mathbf{x}, \omega)$ of a railway tunnel, a four storey portal frame, and a homogeneous halfspace due to a vertical harmonic load applied to the tunnel invert at 25 Hz. The through–soil coupling of tunnel and building is disregarded in figure 4.5a, while it has been accounted for in figure 4.5b. Source–receiver interaction is quantified in figure 4.5c through the

vertical vibration insertion gain $\widehat{\mathrm{IG}}_z(\mathbf{x},\omega)$, providing a pointwise comparison of the vibration levels obtained with the uncoupled and coupled approach, respectively. Large local differences between both approaches are observed, resulting in insertion gain values in the soil and the building reaching up to 10 dB and more.

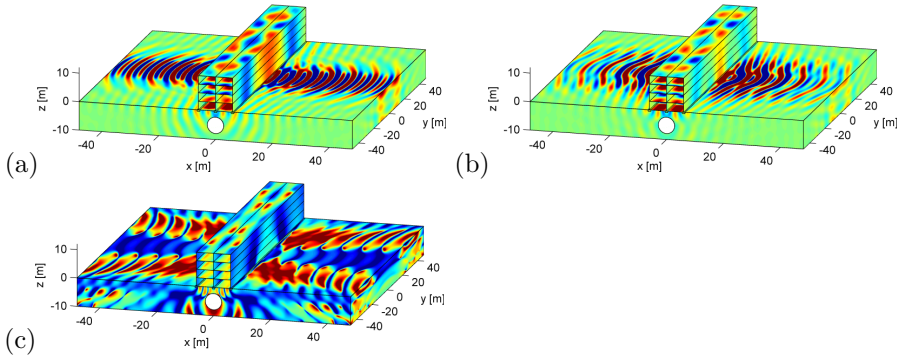

Figure 4.5: Real part of the vertical displacement $\hat{u}_z(\mathbf{x},\omega)$ of a railway tunnel, a four storey portal frame, and a homogeneous halfspace due to a vertical harmonic load applied to the tunnel invert at 25 Hz, as obtained with (a) an uncoupled and (b) a coupled approach. The pointwise vibration insertion gain $\widehat{\mathrm{IG}}_z(\mathbf{x},\omega)$ is shown in (c).

The insertion gain $\widehat{\mathrm{IG}}_z(\mathbf{x},\omega)$, as considered in figure 4.5c, highly depends on the location $\mathbf{x}$. These small scale variations are inconvenient when assessing global (dis)similarities between numerical methodologies (i.e. a coupled vs. an uncoupled approach). A global quantifier which eliminates this dependency on $\mathbf{x}$ has therefore been considered as well in paper E. Power flow provides a way to characterize the global significance of source–receiver interaction, using the mean vibrational energy entering the building as a measure for all internal structural vibrations and re–radiated noise [143]. A change of the amount of power flowing into the building due to through–soil coupling is thus of main interest for the evaluation of source–receiver interaction.

The power flow approach has been employed to assess the intuitive idea that source–receiver interaction can be disregarded if the distance between source and receiver is sufficiently large compared to the wavelength of waves in the soil, as often assumed in seismic engineering [21, 162]. Figure 4.6 shows the power flow insertion gain $\widehat{\mathrm{PFIG}}(\omega)$ (comparing the total mean power flowing into the building obtained with the uncoupled and coupled approach) in the frequency range from 0 Hz to 80 Hz for a railway tunnel at a depth D_t below a building;

this depth varies from 5 m to 25 m. Superimposed is a line corresponding to the frequencies at which the distance between source and receiver equals the dilatational wavelength λ_p in the soil. The $\widehat{\mathrm{PFIG}}(\omega)$ tends to 0 dB above this line, indicating that the uncoupled approach indeed yields the same result as the coupled approach if the source–receiver distance is larger than the dilatational wavelength λ_p. An increasing deviation up to ± 2 dB between the coupled and uncoupled approach can be observed below the line, as the separation distance is then smaller than the wavelength λ_p. The uncoupling does, however, not systematically result in an under– or overestimation of the total mean power entering the building. Although the different regions in the contour plots are not very sharply delimited, this result nevertheless suggests that the rule of thumb commonly applied in seismic engineering also applies to the prediction of railway induced vibrations.

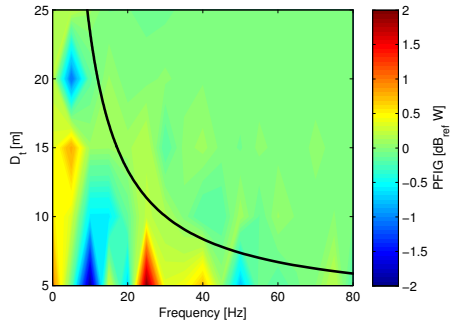

Figure 4.6: Power flow insertion gain $\widehat{\mathrm{PFIG}}(\omega)$ for a building and a railway tunnel at depth D_t.

Similar conclusions have been obtained when considering the interaction between a building and a railway track at grade, although the source–receiver interaction effects depend in that case on the ratio of the separation distance and the Rayleigh wavelength in the soil (instead of the dilatational wavelength). The reader is referred to paper E for a more detailed discussion.

4.3 Wave propagation in an urban environment

Most numerical prediction models do not only neglect source–receiver interaction but also disregard the dynamic through–soil coupling of neighbouring buildings at the receiver side. Only the building of interest is usually analyzed or, if several buildings are considered, the dynamic SSI at each building is

assumed to be uncoupled from the dynamic SSI at the other buildings. This assumption might not be valid in dense urban areas (where vibration annoyance is mostly experienced), necessitating the solution of strongly coupled dynamic SSI problems, which is computationally very demanding.

Characterizing the influence of building clusters in dense urban areas has been the topic of recent investigations, particularly in the field of earthquake engineering. The study of this so–called city–site effect has been initiated, among others, by Wirgin and Bard [155]. Tsogka and Wirgin [148, 149] and Groby et al. [72] have considered a 2D model of an idealized city consisting of ten buildings, without [148, 149] and with [72] internal energy dissipation. A simplified 2D approach was followed by Kham et al. [89] for the identification of the main governing phenomena in city–site interaction. An analytical procedure has been proposed by Boutin and Roussillon [26] for the case of periodically distributed oscillators on the free surface of a halfspace, as well as by Ghergu and Ionescu [64]; Lombaert and Clouteau [95, 96] have considered the case of randomly distributed elastodynamic scatterers. Mazzieri et al. [105] have simulated the 3D seismic response of the central business district of Christchurch (NZ) using a discontinuous Galerkin spectral approximation.

The aforementioned studies are all limited to low frequencies ($< 10\,\mathrm{Hz}$); the higher frequency range of interest makes the prediction of railway induced vibrations in an urban environment very challenging. The innovative numerical techniques outlined in chapter 3 are well suited to tackle this problem. Two relevant case studies have been considered within the frame of the present work and are reviewed in the following.

A first case study, presented in paper A, considers a set of 12 identical masonry buildings on top of a layered halfspace. Each $12\,\mathrm{m} \times 6\,\mathrm{m} \times 8\,\mathrm{m}$ building consists of two stories that are subdivided into four rooms [52]. The FE–$\mathscr{H}$-BE methodology is employed to compute the response of the buildings due to a harmonic point load at the surface of the halfspace. Figure 4.7a shows the wavefield in the soil at 10 Hz. The wavefield remains almost cylindrical at this frequency, but the buildings close to the source of excitation shield the surrounding ones from the incident waves (i.e. the displacements at the soil–structure interfaces are reduced compared to the incident wavefield). At 50 Hz, the Rayleigh wavelength is only $\lambda_{\mathrm{R}}(f) = 2.9\,\mathrm{m}$ and thus of the same order of magnitude as the dimensions of the foundations and the distance between the buildings. As observed in figure 4.7b, the dynamic interaction between the buildings and the halfspace significantly affects the wavefield in that case.

The influence of dynamic through–soil coupling on the structural response at 50 Hz is illustrated in figure 4.8. Figure 4.8a shows the vertical displacement $\hat{u}_z(\mathbf{x}, \omega)$ of all buildings in case the presence of the surrounding buildings

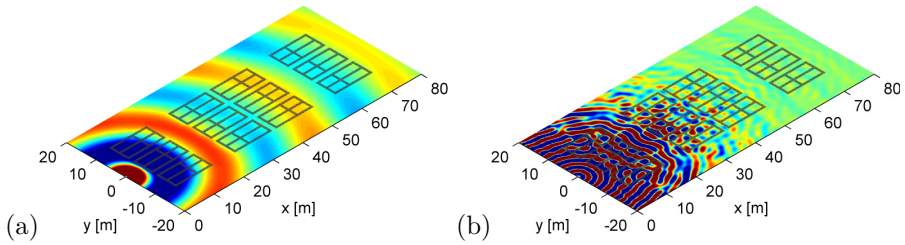

Figure 4.7: Real part of the vertical soil displacement $\hat{u}_z(\mathbf{x}, \omega)$ at (a) 10 Hz and (b) 50 Hz.

is disregarded for each building, while figure 4.8b illustrates the structural response in case the presence of all 12 buildings is simultaneously taken into account. It is observed that the response of the three buildings closest to the source remains almost unaffected, while the response of the buildings further away from the source is considerably altered by the presence of the surrounding buildings. A detailed investigation of the influence of through–soil coupling on the response along the soil–structure interface of a specific building is provided in paper A.

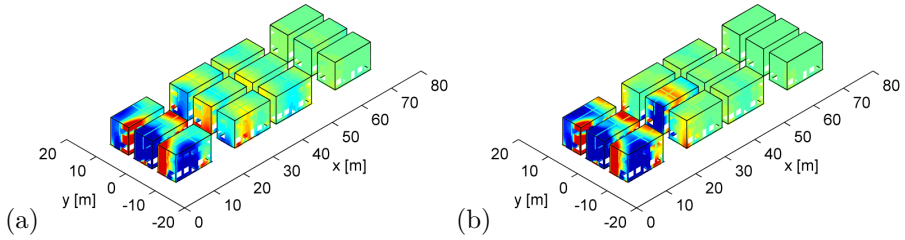

Figure 4.8: Real part of the vertical structural displacement $\hat{u}_z(\mathbf{x}, \omega)$ at 50 Hz in case dynamic through–soil coupling of the buildings is (a) disregarded and (b) taken into account.

The second (yet unpublished) case study consists of a realistic setting of 90 non-equally spaced, non-equally sized buildings in a city quarter of 250×500 m; this case is investigated by means of the spatial windowing technique introduced in section 3.2. The initial 2.5D model is composed of eight homogeneous solid building blocks on concrete foundations on top of a homogeneous halfspace. The foundations have a thickness $t = 0.25$ m, a Young's modulus $E = 33$ GPa, a Poisson's ratio $\nu = 0.20$, a density $\rho = 2500\,\mathrm{kg/m^3}$, and a hysteretic damping ratio $\beta = 0.03$, while the homogenized superstructures have a shear wave

velocity $C_\mathrm{s} = 300\,\mathrm{m/s}$, a dilatational wave velocity $C_\mathrm{p} = 490\,\mathrm{m/s}$, a density $\rho = 325\,\mathrm{kg/m^3}$, and a hysteretic damping ratio $\beta = 0.03$. Similar values for homogeneous building blocks have been used in recent studies of the seismic city–site effect [72, 89, 139, 149, 155]. The halfspace is characterized by a shear wave velocity $C_\mathrm{s} = 200\,\mathrm{m/s}$, a dilatational wave velocity $C_\mathrm{p} = 400\,\mathrm{m/s}$, a density $\rho = 2000\,\mathrm{kg/m^3}$, and material damping ratios $\beta_\mathrm{s} = \beta_\mathrm{p} = 0.025$ in deviatoric and volumetric deformation.

The geometric characteristics of the eight 2.5D buildings are summarized in table 4.1. The length of the individual 3D buildings and the interbuilding spacings (in the longitudinal direction) are subsequently generated from uniform distributions $\mathcal{U} \in [15\,\mathrm{m}, 45\,\mathrm{m}]$ and $\mathcal{U} \in [5\,\mathrm{m}, 25\,\mathrm{m}]$, respectively. The buildings' longitudinal positions define the windowing functions $\tilde{w}_j(k_y)$ in equation (3.44). The resulting lay–out of the city quarter is shown in figure 4.9.

Building	w [m]	h [m]	x_0 [m]
Ω_1	15	35	20.0
Ω_2	10	15	47.5
Ω_3	15	35	75.0
Ω_4	20	45	112.5
Ω_5	20	45	152.5
Ω_6	15	35	190.0
Ω_7	10	15	217.5
Ω_8	10	15	242.5

Table 4.1: Width w, height h, and foundation center x_0 of eight 2.5D buildings.

Figures 4.10a and 4.10b show the vertical displacement $\hat{u}_z(\mathbf{x}, \omega)$ of the soil and buildings due to a harmonic point load at the surface of the halfspace at 5 Hz and 25 Hz, respectively. The importance of the city–site effect is quantified in figure 4.11. This figure compares the mean power flowing through the soil–foundation interface of six particular buildings in the city quarter to the case where through–soil coupling of the surrounding buildings is neglected. The influence of through–soil coupling on the structural response is negligible for the building situated in front of the source of excitation (figure 4.11a), while a much larger impact is observed for the other buildings. This is especially the case above 50 Hz, as accounting for the presence of all buildings results in a significant increase of the amount of power flowing into the buildings. This demonstrates the importance of the city–site effect.

A final note is related to the computation of the power flow into each building. The spatial windowing technique presented in section 3.2 does not conserve energy and is as such not suited to perform power flow calculations. Even if

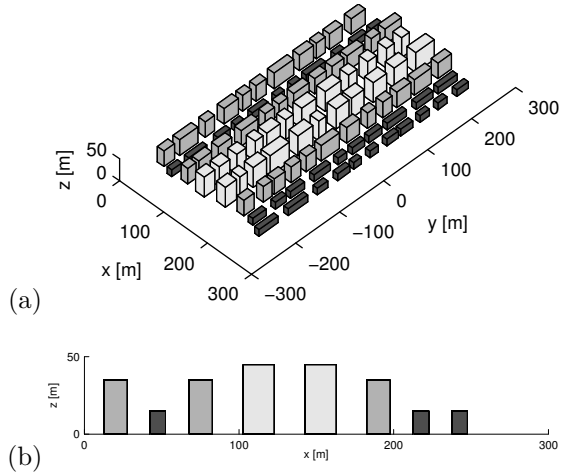

Figure 4.9: (a) Isometric and (b) side view of the city quarter.

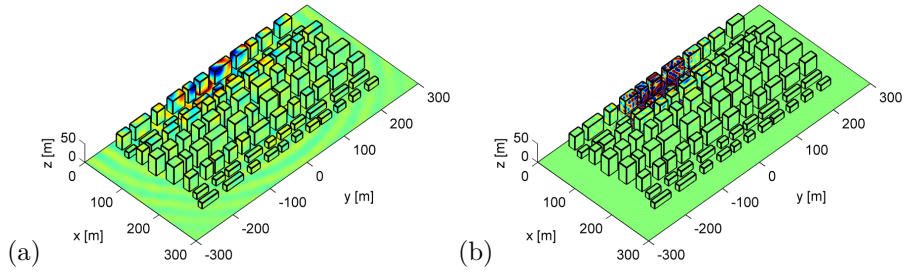

Figure 4.10: Real part of the vertical displacement $\hat{u}_z(\mathbf{x}, \omega)$ of the soil and buildings at (a) 5 Hz and (b) 25 Hz.

the damping ratio β in the buildings equals zero, a certain amount of power flow through the soil–foundation interface of each building is retrieved, which is non–physical. The results in figure 4.11 are obtained by subtracting the mean power flow as obtained with a damped ($\beta = 0.03$) and an undamped calculation ($\beta = 0$), hence necessitating the solution of two problems. A comparison with 3D FE–$\mathscr{H}$-BE calculations has demonstrated that this approach provides an accurate estimation of the energy dissipated within each building.

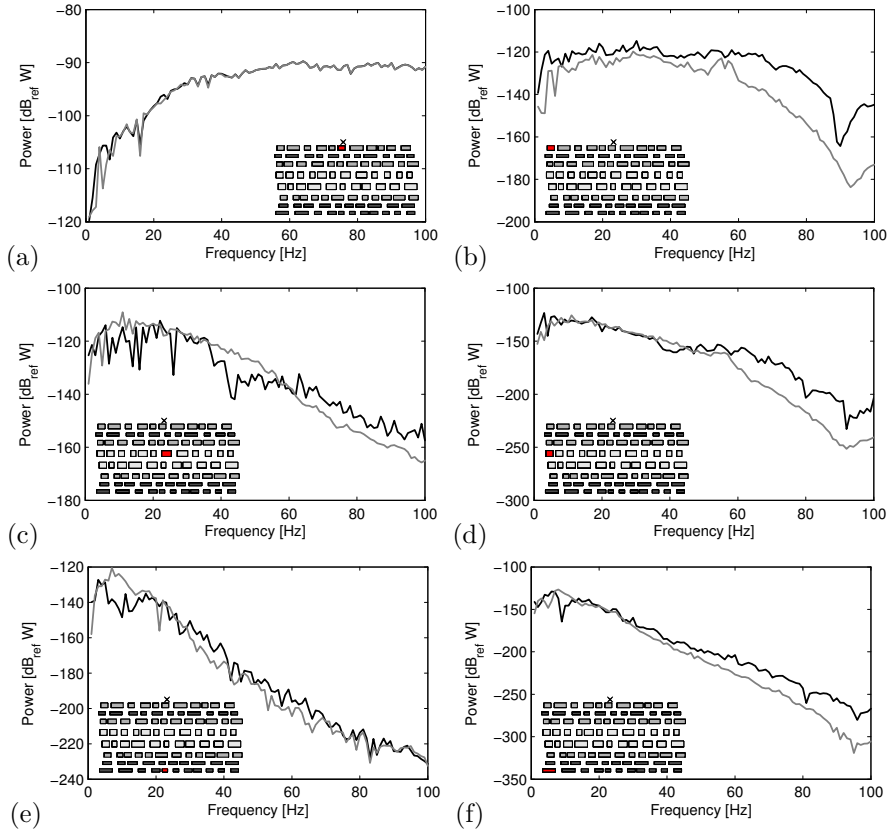

Figure 4.11: Mean power flow trough the soil–foundation interface of six buildings, disregarding (grey line) or accounting for (black line) the presence of the surrounding buildings.

4.4 Conclusion

The numerical techniques presented in chapters 2 and 3 have been employed for the solution of several challenging dynamic SSI problems related to railway induced vibrations. In this chapter, three applications were reviewed.

First, the mitigation of ground–borne vibrations by means of measures on the propagation path in the soil has been addressed. The effectiveness of an open trench and a stiff wave barrier was investigated and the underlying physical mechanisms were elucidated. It is demonstrated that an open trench is able to reflect the impinging waves if its depth is sufficiently large compared to the penetration depth of the Rayleigh waves in the soil. The efficiency of a stiff barrier, on the other hand, is determined by the interaction of Rayleigh waves in the soil and bending waves in the barrier; a large stiffness contrast between the soil and the barrier is required to achieve a significant reduction of vibration levels.

Next, the importance of source–receiver interaction has been discussed. A pointwise comparison of the transfer functions from source to receiver indicates that significant local variations up to 10 dB are induced by the through–soil coupling. The use of a power flow approach allows for a global assessment, revealing that source–receiver interaction mainly occurs if their separation distance is small compared to a characteristic wavelength in the soil. This observation is in line with the rule of thumb commonly applied in seismic engineering.

Finally, two case studies of wave propagation in an urban environment have been considered, using a 3D FE–$\mathscr{H}$-BE approach and a 2.5D FE–BE strategy with spatial windowing, respectively. It is demonstrated that the dynamic interaction between neighbouring buildings can significantly alter the structural response, especially at higher frequencies.

Chapter 5

Conclusions and recommendations for further research

5.1 Conclusions

This dissertation addresses the numerical solution of large scale dynamic SSI problems, focusing on linear problems formulated in the frequency domain. This is a challenging task, as the through–soil coupling of multiple structures and the radiation of waves towards infinity have to be accounted for. A domain decomposition approach is therefore followed in the frame of the present work, using finite elements for the structures that are coupled to boundary elements for the soil. Methodological developments on coupled FE–BE methods as well as applications related to the prediction of railway induced vibrations are presented in five key publications.

First, an innovative fast 3D BE method based on $\mathscr{H}$–matrices has been proposed, accounting for the stratification of the soil (paper A). Application of the ACA algorithm provides low rank approximations for matrix blocks corresponding to admissible cluster pairs, resulting in an improved computational efficiency compared to classical BE methods. The algebraic character of ACA allows incorporating Green's functions of a layered soil that are numerically computed by means of the direct stiffness method. This is advantageous, as there is in that case no need to discretize the free surface and the layer interfaces.

The coupling of FE and $\mathscr{H}$-BE models has subsequently been studied in detail (paper B). It is demonstrated that a direct coupling approach, necessitating the computation of a dynamic soil stiffness matrix through the solution of multiple $\mathscr{H}$-BE equations, is not efficient. This is caused by the inability of the implemented FGMRES solver to simultaneously handle multiple right hand sides. Iterative coupling schemes have been considered as well, where the governing equations of each subdomain are solved separately, while the boundary conditions at the soil–structure interface are updated until convergence is achieved. Application of such algorithms to dynamic SSI problems in the frequency domain is not trivial, as convergence can hardly be achieved if no relaxation is incorporated. Aitken's Δ^2-method is therefore employed in sequential iterative schemes for the calculation of an optimized interface relaxation parameter. Numerical examples show that the efficiency of these algorithms strongly depends on the boundary conditions applied to each subdomain; the fastest convergence is observed if Neumann boundary conditions are imposed on the stiffest subdomain. Parallel iterative algorithms provide a valuable alternative for cases where an a priori estimation of the flexibility of each subdomain is not obvious, and an appropriate novel relaxation technique has been proposed for these algorithms. A monolithic coupling approach has also been introduced, in which the governing equations are solved simultaneously while the assembly of a dynamic soil stiffness matrix is avoided. The incorporation of a preconditioner is indispensable, however, in order to obtain an efficient solution strategy.

Finally, a methodology has been developed for alleviating the restriction that 2.5D FE–BE models are only applicable to structures with a longitudinally invariant geometry (paper C). The proposed spatial windowing technique originates from vibro–acoustics [150] and is based on a redistribution of the wavenumber spectrum over the entire wavenumber domain by means of windowing functions that characterize the presence of one or more finite substructures. This technique enables the solution of challenging 3D dynamic SSI problems while maintaining the computational efficiency of a 2.5D approach. It is demonstrated that the proposed technique is accurate as long as the modal behaviour of the structures does not dominate the response.

Coupled FE–BE models have been used throughout this dissertation to examine three applications related to railway induced vibrations. Vibration mitigation measures on the propagation path in the soil, including an open trench and a stiff wave barrier, have been analyzed first (papers B, C, and D). While the former aims at reflecting the impinging waves, the latter impedes the propagation of waves with a trace wavelength λ_y smaller than the free bending wavelength $\lambda_\mathrm{b}(\omega)$. This leads to the existence of a critical frequency from which a stiff barrier starts to be effective, as well as a critical angle delimiting the

area where vibration levels are reduced [39]. Analytical expressions for these quantities are of practical use in a preliminary design stage.

The influence of source–receiver interaction has been quantified next (paper E). It is found that the train–track interaction at the source is not affected by the presence of the receiver; through–soil coupling of source and receiver can thus be disregarded for the calculation of the dynamic axle loads. If the transfer functions are considered, on the other hand, local variations up to 10 dB in terms of insertion gain are observed, showing a large spatial and directional variability. Power flow has subsequently been used for a global assessment, revealing that source–receiver interaction mainly occurs if the distance between source and receiver is small compared to a characteristic wavelength in the soil.

Two case studies of wave propagation in an urban environment have finally demonstrated that the dynamic interaction between closely spaced buildings affects the structural response, especially at higher frequencies.

5.2 Recommendations for further research

Based on the main conclusions of this work, recommendations for further research are specified. Suggestions that pertain to the development of numerical techniques for dynamic SSI are listed below:

- The assembly of $\mathscr{H}$–matrices relies on the efficient approximation of matrix blocks corresponding to admissible cluster pairs. In the present work, the ACA algorithm is employed for this purpose, but the efficiency of this algorithm deteriorates at high frequencies (see e.g. figures 3.5 and 3.15). This is caused by the oscillatory behaviour of the Green's functions; a similar reduction of the efficiency at high frequencies is also observed in other fast BE approaches such as the FMM. Recently, so–called directional variants of ACA [16] and the FMM [108] have been developed for Helmholtz boundary value problems, where the (analytical) Green's functions are multiplied with a plane wave in a specific direction to obtain a frequency independent formulation. The problem becomes more complicated in elastodynamics, however, as two elastic wave velocities have to be taken into account. It is worth developing a directional variant of ACA for elastodynamics that remains efficient over the whole frequency range.
- Throughout this dissertation, only conforming FE–BE interface discretizations have been considered, where the coupling conditions (2.25)–(2.26) are imposed in a strong sense. The use of non–conforming FE–BE

interfaces [124] provides a more flexible solution strategy and therefore deserves further attention. Such non–conforming discretizations arise if the nodes of the FE and BE mesh do not match and/or if different approximation orders are used for the shape functions across the interface. Mortar methods [116, 156] can provide an efficient solution in that case, where Lagrange multipliers are introduced to establish the coupling between the FE and BE domain.

- $\mathscr{H}$–matrices are also appropriate for BE calculations in the time domain. For example, Messner and Schanz [107] present a fast time domain elastodynamic BE formulation using full space Green's functions. Although not attempted yet, it is believed that time domain Green's functions of a layered halfspace can be straightforwardly incorporated.

- The FE–BE coupling procedures developed in the frame of the present work can also be employed in the time domain for the solution of transient non–linear dynamic SSI problems. More specifically, the iterative coupling schemes are very appealing since they allow for different time steps in the finite and boundary element model; both subdomains commonly impose different conditions on the time integration step for reasons of stability and accuracy. The presented relaxation techniques are expected to be applicable in the time domain.

Recommendations related to the prediction of railway induced vibrations are summarized in the following:

- The developed numerical methods pave the way for the solution of various inverse problems involving dynamic SSI, as an efficient solution of the latter is often only feasible if a fast and reliable forward model is available. Inverse models employ measurements to obtain a better understanding of the system behaviour and to infer system parameters, which can e.g. be used for quantifying and reducing uncertainty in the prediction of ground–borne vibrations.

- The availability of fast methods is not only beneficial for inverse modelling, but also facilitates the solution of optimization problems. For example, vibration mitigation measures on the propagation path in the soil are usually designed by trial and error because of the high computational cost, but the presented spatial windowing technique allows for an efficient optimization of the longitudinal geometry.

- The spatial windowing technique is also believed to be well suited for including parametric excitation in 2.5D models of conventional ballasted

railway tracks. This type of excitation is due to the periodic support of rails on sleepers, spatial variations of the track stiffness, the presence of switches or crossings at localized positions, ... The incorporation of this type of excitation is expected to significantly improve the accuracy of ground–borne vibration predictions.

- It is crucial to validate the vibration reduction efficiency of the proposed mitigation measures on the transmission path in the soil experimentally. Within the frame of the EU FP7 project RIVAS (Railway Induced Vibration Abatement Solutions) [1], a continuous stiff wave barrier of 1 m × 7.5 m × 55 m has been created close to an existing railway track at a site in El Realengo (Spain), using overlapping jet grout columns (figure 5.1a). Track – free field transfer functions and train passages before and after installation of the barrier have been measured. Processing of these results will allow for a comprehensive comparison of simulations and measurements.

(a)  (b) 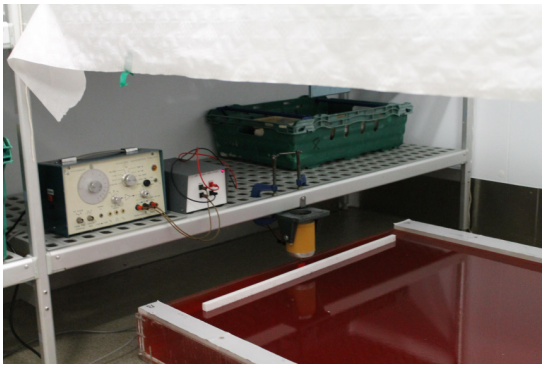

Figure 5.1: (a) Stiff wave barrier in the soil in El Realengo and (b) polystyrene beam in a tank filled with (strawberry) jelly.

Apart from field measurements, lab experiments at reduced scale are also valuable for demonstrating the existence of the critical frequency and critical angle. An attempt has already been undertaken during a research stay at the University of Cambridge, using a polystyrene beam as wave barrier in a tank filled with (strawberry) jelly, as shown in figure 5.1b. The reflections of a laser on the surface of the jelly at a limited number of points were employed for visualizing surface waves generated by a harmonic shaker, but this approach turned out to be too simplistic. The use of a sophisticated laser vibrometer is expected to provide a more

accurate and detailed visualization of the wavefield that can be used for validating the theory outlined in paper D.

Finally, it is emphasized that the developed numerical techniques also enable the study of other dynamic SSI problems, such as the prediction of damage due to earthquakes induced by the extraction of natural and shale gas in densely populated areas, the design of nuclear waste storage facilities in deep soil layers, or the characterization of the dynamic behaviour of foundations for offshore wind turbines and oil platforms.

Bibliography

[1] http://www.rivas-project.eu, 2011.

[2] J.D. Achenbach. *Wave propagation in elastic solids*, volume 16 of *North-Holland Series in Applied Mathematics and Mechanics*. North-Holland, Amsterdam, The Netherlands, 1973.

[3] A.C. Aitken. Studies in practical mathematics II: The evaluation of the latent roots and latent vectors of a matrix. *Proceedings of the Royal Society of Edinburgh*, 57:269–304, 1937.

[4] L. Andersen and C.J.C. Jones. Coupled boundary and finite element analysis of vibration from railway tunnels – a comparison of two- and three-dimensional models. *Journal of Sound and Vibration*, 293(3-5):611–625, 2006.

[5] L. Andersen and S.R.K. Nielsen. Reduction of ground vibration by means of barriers or soil improvement along a railway track. *Soil Dynamics and Earthquake Engineering*, 25:701–716, 2005.

[6] R.J. Apsel and J.E. Luco. On the Green's functions for a layered half-space. Part II. *Bulletin of the Seismological Society of America*, 73(4):931–951, 1983.

[7] D. Aubry and D. Clouteau. A regularized boundary element method for stratified media. In G. Cohen, L. Halpern, and P. Joly, editors, *Proceedings of the First International Conference on Mathematical and Numerical Aspects of Wave Propagation Phenomena*, pages 660–668, Strasbourg, France, April 1991. SIAM, Philadephia.

[8] D. Aubry and D. Clouteau. A subdomain approach to dynamic soil-structure interaction. In V. Davidovici and R.W. Clough, editors, *Recent advances in Earthquake Engineering and Structural Dynamics*, pages 251–272. Ouest Editions/AFPS, Nantes, 1992.

[9] D. Aubry, D. Clouteau, and G. Bonnet. Modelling of wave propagation due to fixed or mobile dynamic sources. In N. Chouw and G. Schmid, editors, *Workshop Wave '94, Wave propagation and Reduction of Vibrations*, pages 109–121, Ruhr Universität Bochum, Germany, December 1994.

[10] U. Basu and A.K. Chopra. Perfectly matched layers for time-harmonic elastodynamics of unbounded domains: theory and finite-element implementation. *Computer Methods in Applied Mechanics and Engineering*, 192(11-12):1337–1375, 2003.

[11] M. Bebendorf. Approximation of boundary element matrices. *Numerische Mathematik*, 86:565–589, 2000.

[12] M. Bebendorf. Hierarchical *LU* decomposition based preconditioners for BEM. *Computing*, 74:225–247, 2005.

[13] M. Bebendorf. *Hierarchical Matrices: A Means to Efficiently Solve Elliptic Boundary Value Problems*. Springer Publishing Company, 1st edition, 2008.

[14] M. Bebendorf and S. Kunis. Recompression techniques for adaptive cross approximation. *Journal of Integral Equations and Applications*, 21(3):331–357, 2009.

[15] M. Bebendorf and S. Rjasanow. Adaptive low–rank approximation of collocation matrices. *Computing*, 70:1–24, 2003.

[16] M. Bebendorf and R. Venn. Frequency–independent approximation of integral formulations of Helmholtz boundary value problems. In N. Heuer and C. Jerez-Hanckes, editors, *Proceedings of the Symposium of the International Association for Boundary Element Methods IABEM 2013*, page 19, Santiago, Chile, January 2013.

[17] I. Benedetti and M.H. Aliabadi. A fast hierarchical dual boundary element method for three-dimensional elastodynamic crack problems. *International Journal for Numerical Methods in Engineering*, 84(9):1038–1067, 2010.

[18] D.E. Beskos, T. Krauthammer, and I. Vardoulakis, editors. *Dynamic soil-structure interaction*. A.A. Balkema, 1984.

[19] P. Bettess. Infinite elements. *International Journal for Numerical Methods in Engineering*, 11:53–64, 1977.

[20] J. Bielak, O. Ghattas, and E.J. Kim. Parallel octree-based finite element method for large-scale earthquake ground motion simulation. *Computer Modelling in Engineering and Sciences*, 10(2):99–112, 2005.

[21] J. Bielak, K. Loukakis, Y. Hisada, and C. Yoshimura. Domain reduction method for three-dimensional earthquake modeling in localized regions, Part I: Theory. *Bulletin of the Seismological Society of America*, 93(2):817–824, 2003.

[22] M. Bonnet. *Boundary integral equation methods for solids and fluids*. John Wiley and Sons, Chichester, United Kingdom, 1995.

[23] M. Bonnet, G. Maier, and C. Polizzotto. Symmetric Galerkin boundary element method. *Applied Mechanics Reviews*, 51:669–704, 1998.

[24] S. Börm, L. Grasedyck, and W. Hackbusch. Introduction to hierarchical matrices with applications. *Engineering Analysis with Boundary Elements*, 27(5):405–422, 2003.

[25] M. Bouchon and F.J. Sánchez-Sesma. Boundary integral equations and boundary elements methods in elastodynamics. *Advances in Geophysics*, 48:157–189, 2007.

[26] C. Boutin and P. Roussillon. Wave propagation in presence of oscillators on the free surface. *International Journal of Engineering Science*, 44:180–204, 2006.

[27] S. Chaillat and M. Bonnet. A new fast multipole formulation for the elastodynamic half-space Green's tensor. *Journal of Computational Physics*, 258:787–808, 2014.

[28] S. Chaillat, M. Bonnet, and J.-F. Semblat. A multi-level fast multipole BEM for 3-D elastodynamics in the frequency domain. *Computer Methods in Applied Mechanics and Engineering*, 197(49–50):4233–4249, 2008.

[29] S. Chaillat, M. Bonnet, and J.-F. Semblat. A new fast multi-domain BEM to model seismic wave propagation and amplification in 3D geological structures. *Geophysical Journal International*, 177:509–531, 2009.

[30] S. Chaillat, J.-F. Semblat, and M. Bonnet. A preconditioned 3-D multi-region fast multipole solver for seismic wave propagation in complex geometries. *Communications in Computational Physics*, 11(2):594–609, 2012.

[31] W.C. Chew and Q.H. Liu. Perfectly matched layers for elastodynamics: A new absorbing boundary condition. *Journal of Computational Acoustics*, 4(4):341–359, 1996.

[32] A.K. Chopra. *Dynamics of structures: theory and applications to earthquake engineering*. Prentice-Hall, Englewood Cliffs, New Jersey, 1995.

[33] D. Clouteau, M. Arnst, T.M. Al-Hussaini, and G. Degrande. Freefield vibrations due to dynamic loading on a tunnel embedded in a stratified medium. *Journal of Sound and Vibration*, 283(1–2):173–199, 2005.

[34] D. Clouteau and D. Aubry. Computational soil-structure interaction. In W.S. Hall and G. Oliveto, editors, *Boundary Element Methods for Soil-Structure Interaction*, pages 61–125. Kluwer Academic Publishers, 2003.

[35] D. Clouteau, R. Cottereau, and G. Lombaert. Dynamics of structures coupled with elastic media. A review of numerical models and methods. *Journal of Sound and Vibration*, 332:2415–2436, 2013.

[36] D. Clouteau, M.L. Elhabre, and D. Aubry. Periodic BEM and FEM-BEM coupling: application to seismic behaviour of very long structures. *Computational Mechanics*, 25:567–577, 2000.

[37] P.A. Costa, R. Calçada, A.S. Cardoso, and A. Bodare. Influence of soil non-linearity on the dynamic response of high-speed railway tracks. *Soil Dynamics and Earthquake Engineering*, 30(4):221–235, 2010.

[38] P. Coulier, A. Dijckmans, S. François, G. Degrande, and G. Lombaert. A spatial windowing technique to account for finite dimensions in 2.5D dynamic soil–structure interaction problems. *Soil Dynamics and Earthquake Engineering*, 59:51–67, 2014.

[39] P. Coulier, S. François, G. Degrande, and G. Lombaert. Subgrade stiffening next to the track as a wave impeding barrier for railway induced vibrations. *Soil Dynamics and Earthquake Engineering*, 48:119–131, 2013.

[40] P. Coulier, S. François, G. Lombaert, and G. Degrande. Application of hierarchical matrices to boundary element methods for elastodynamics based on Green's functions for a horizontally layered halfspace. *Engineering Analysis with Boundary Elements*, 37(12):1745–1758, 2013.

[41] P. Coulier, S. François, G. Lombaert, and G. Degrande. Coupled finite element – hierarchical boundary element methods for dynamic soil–structure interaction in the frequency domain. *International Journal for Numerical Methods in Engineering*, 97(7):505–530, 2014.

[42] P. Coulier, G. Lombaert, and G. Degrande. The influence of source–receiver interaction on the numerical prediction of railway induced vibrations. *Journal of Sound and Vibration*, 333(12):2520–2538, 2014.

[43] J. Domínguez. *Boundary elements in dynamics*. Computational Mechanics Publications and Elsevier Applied Science, Southampton, United Kingdom, 1993.

[44] J.W. Dunkin. Computation of modal solutions in layered, elastic media at high frequencies. *Bulletin of the Seismological Society of America*, 55(2):335–358, 1965.

[45] A.A. Elshafey, M.R. Haddara, and H. Marzouk. Identification of the excitation and reaction forces on offshore platforms using the random decrement technique. *Ocean Engineering*, 36:521–528, 2009.

[46] A.C. Eringen and E.S. Suhubi. *Elastodynamics, Volume 2, Linear theory*. Academic Press, New York, USA, 1975.

[47] E. Faccioli, F. Maggio, R. Paolucci, and A. Quarteroni. 2D and 3D elastic wave propagation by a pseudo-spectral domain decomposition method. *Journal of Seismology*, 1(3):237–251, 1997.

[48] G. Festa and S. Nielsen. PML absorbing boundaries. *Bulletin of the Seismological Society of America*, 93(2):891–903, 2003.

[49] L.N.G. Filon. On a quadrature formula for trigonometric integrals. *Proceedings of the Royal Society of Edinburgh*, 49:38–47, 1929.

[50] J.A. Forrest and H.E.M. Hunt. A three-dimensional tunnel model for calculation of train-induced ground vibration. *Journal of Sound and Vibration*, 294:678–705, 2006.

[51] S. François. *Nonlinear modelling of the response of structures due to ground vibrations*. PhD thesis, Department of Civil Engineering, KU Leuven, 2008.

[52] S. François, C. Karg, W. Haegeman, and G. Degrande. A numerical model for foundation settlements due to deformation accumulation in granular soils under repeated small amplitude dynamic loading. *International Journal for Numerical and Analytical Methods in Geomechanics*, 34(3):273–296, 2010.

[53] S. François, H.R. Masoumi, and G. Degrande. An iterative coupled boundary-finite element method for the dynamic response of structures. In P. Sas and M. De Munck, editors, *Proceedings of ISMA2006*

International Conference on Noise and Vibration Engineering, pages 1701–1716, Leuven, Belgium, September 2006.

[54] S. François, M. Schevenels, and G. Degrande. BEMFUN: MATLAB toolbox for boundary elements in elastodynamics. Version 2.1 Build 16. User's guide BWM-2009-26, Department of Civil Engineering, KU Leuven, December 2009.

[55] S. François, M. Schevenels, G. Lombaert, and G. Degrande. A 2.5D displacement based PML for elastodynamic wave propagation. *International Journal for Numerical Methods in Engineering*, 90(7):819–837, 2012.

[56] S. François, M. Schevenels, G. Lombaert, P. Galvín, and G. Degrande. A 2.5D coupled FE-BE methodology for the dynamic interaction between longitudinally invariant structures and a layered halfspace. *Computer Methods in Applied Mechanics and Engineering*, 199(23-24):1536–1548, 2010.

[57] S. François, M. Schevenels, B. Thyssen, J. Borgions, and G. Degrande. Design and efficiency of a vibration isolating screen in the soil. *Soil Dynamics and Earthquake Engineering*, 39:113–127, 2012.

[58] H. Fujiwara. The fast multipole method for solving integral equations of three-dimensional topography and basin problems. *Geophysical Journal International*, 140(1):198–210, 2000.

[59] M. Fuyuki and Y. Matsumoto. Finite difference analysis of Rayleigh wave scattering at a trench. *Bulletin of the Seismological Society of America*, 70: 2051–2069, 1980.

[60] L. Gavrić. Finite element computation of dispersion properties of thin-walled waveguides. *Journal of Sound and Vibration*, 173(1):113–124, 1994.

[61] L. Gavrić. Computation of propagative waves in free rail using finite element technique. *Journal of Sound and Vibration*, 183(3):531–543, 1995.

[62] G. Gazetas. Analysis of machine foundation vibrations: state of the art. *Soil Dynamics and Earthquake Engineering*, 2(1):2–42, 1983.

[63] A. George. Nested dissection of a regular finite element mesh. *SIAM Journal on Numerical Analysis*, 10:345–363, 1973.

[64] M. Ghergu and I.R. Ionescu. Structure-soil-structure coupling in seismic excitation and "city effect". *International Journal of Engineering Science*, 47(3):342–354, 2009.

[65] S. Ghinet and N. Atalla. The transmission loss of curved laminates and sandwich composite panels. *Journal of the Acoustical Society of America*, 118(2):774–790, 2005.

[66] G.H. Golub and C.F. Van Loan. *Matrix computations*. John Hopkins University Press, Baltimore, MD, 3d edition, 1996.

[67] L. Grasedyck. Adaptive recompression of $\mathscr{H}$-matrices for BEM. *Computing*, 74(3):205–223, 2005.

[68] L. Grasedyck and W. Hackbusch. Construction and arithmetics of $\mathscr{H}$-matrices. *Computing*, 70:295–334, 2003.

[69] L. Grasedyck, R. Kriemann, and S. Le Borne. Domain decomposition based $\mathscr{H}$-*LU* preconditioning. *Numerische Mathematik*, 112(4):565–600, 2009.

[70] E. Grasso. *Modelling visco-elastic seismic wave propagation: a fast-multipole boundary element method and its coupling with finite elements*. PhD thesis, Université Paris-Est, 2012.

[71] E. Grasso, S. Chaillat, M. Bonnet, and J.-F. Semblat. Application of the multi-level time-harmonic fast multipole BEM to 3-D visco-elastodynamics. *Engineering Analysis with Boundary Elements*, 36(5):744–758, 2012.

[72] J.-P. Groby, C. Tsogka, and A. Wirgin. Simulation of seismic response in a city-like environment. *Soil Dynamics and Earthquake Engineering*, 25:487–504, 2005.

[73] M. Guiggiani and P. Casalini. Direct computation of Cauchy principal value integrals in advanced boundary elements. *International Journal for Numerical Methods in Engineering*, 24:1711–1720, 1987.

[74] W. Hackbusch. A sparse matrix arithmetic based on $\mathscr{H}$-matrices. Part I: Introduction to $\mathscr{H}$-matrices. *Computing*, 62(2):89–108, 1999.

[75] W. Hackbusch and Z.P. Nowak. On the fast matrix multiplication in the boundary element method by panel clustering. *Numerische Mathematik*, 54:463–491, 1989.

[76] P. Hagedorn and A. DasGupta. *Vibrations and Waves in Continuous Mechanical Systems*. John Wiley & Sons, Chichester, United Kingdom, 2007.

[77] N.A. Haskell. The dispersion of surface waves on multilayered media. *Bulletin of the Seismological Society of America*, 73:17–43, 1953.

[78] J. Huang and Z. Shi. Application of periodic theory to rows of piles for horizontal vibration attenuation. *International Journal of Geomechanics*, 13(2):132–142, 2013.

[79] B. Hübner, E. Walhorn, and D. Dinkler. A monolithic approach to fluid-structure interaction using space-time finite elements. *Computer Methods in Applied Mechanics and Engineering*, 193(23–26):2087–2104, 2004.

[80] H.E.M. Hunt and M.F.M. Hussein. Vibration from railways: can we achieve better than +/-10 dB prediction accuracy? In *14th International Congress on Sound and Vibration*, Cairns, Australia, July 2007.

[81] B.M. Irons and R.C. Tuck. A version of the Aitken accelerator for computer iteration. *International Journal for Numerical Methods in Engineering*, 1(3):275–277, 1969.

[82] C.J.C. Jones. Use of numerical-models to determine the effectiveness of anti-vibration systems for railways. *Proceedings of the Institution of Civil Engineers-Transport*, 105(1):43–51, 1994.

[83] S. Jones and H.E.M. Hunt. The effect of inclined soil layers on surface vibration from underground railways using the thin layer method. *ASCE Journal of Engineering Mechanics*, 137(12):887–900, 2011.

[84] S. Jones and H.E.M. Hunt. Predicting surface vibration from underground railways through inhomogeneous soil. *Journal of Sound and Vibration*, 331(9):2055–2069, 2012.

[85] A. Karlström and A. Boström. Efficiency of trenches along railways for trains moving at sub- or supersonic speeds. *Soil Dynamics and Earthquake Engineering*, 27:625–641, 2007.

[86] E. Kausel. *Fundamental solutions in elastodynamics: a compendium*. Cambridge University Press, New York, 2006.

[87] E. Kausel and J.M. Roësset. Stiffness matrices for layered soils. *Bulletin of the Seismological Society of America*, 71(6):1743–1761, 1981.

[88] A.M. Kaynia, C. Madshus, and P. Zackrisson. Ground vibration from high speed trains: prediction and countermeasure. *Journal of Geotechnical and Geoenvironmental Engineering, Proceedings of the ASCE*, 126(6):531–537, 2000.

[89] M. Kham, J.-F. Semblat, P.-Y. Bard, and P. Dangla. Seismic city-site interaction: main governing phemomena through simplified numerical models. *Bulletin of the Seismological Society of America*, 96(5):1934–1951, 2006.

[90] D. Komatitsch and J.P. Vilotte. The spectral element method: An efficient tool to simulate the seismic response of 2D and 3D geological structures. *Bulletin of the Seismological Society of America*, 88(2):368–392, 1998.

[91] S.L. Kramer. *Geotechnical earthquake engineering*. Prentice-Hall, Upper Saddle River, New Jersey, 1996.

[92] K.A. Kuo, H.E.M. Hunt, and M.F.M. Hussein. The effect of a twin tunnel on the propagation of ground-borne vibration from an underground railway. *Journal of Sound and Vibration*, 330(25):6203–6222, 2011.

[93] U. Küttler and W.A. Wall. Fixed-point fluid-structure interaction solvers with dynamic relaxation. *Computational Mechanics*, 43(1):61–72, 2008.

[94] J. Legault, A. Mejdi, and N. Atalla. Vibro-acoustic response of orthogonally stiffened panels: the effects of finite dimensions. *Journal of Sound and Vibration*, 330(24):5928–5948, 2011.

[95] G. Lombaert and D. Clouteau. The resonant multiple wave scattering in the seismic response of a city. *Waves in Random and Complex Media*, 16(3):205–230, 2006.

[96] G. Lombaert and D. Clouteau. Elastodynamic wave scattering by finite-sized resonant scatterers at the surface of a horizontally layered halfspace. *Journal of the Acoustical Society of America*, 125(4):2041–2052, 2009.

[97] G. Lombaert, G. Degrande, and D. Clouteau. Numerical modelling of free field traffic induced vibrations. *Soil Dynamics and Earthquake Engineering*, 19(7):473–488, 2000.

[98] G. Lombaert, G. Degrande, S. François, and D.J. Thompson. Ground-borne vibration due to railway traffic. In J. Nielsen, D. Anderson, P. de Vos, P.-E. Gautier, M. Iida, J. Nelson, T. Tielkes, D. Thompson, and D. Towers, editors, *Proceedings of the 11th International Workshop on Railway Noise IWRN11*, pages 266–301, Uddevalla, Sweden, September 2013. Invited state of the art paper.

[99] G. Lombaert, G. Degrande, J. Kogut, and S. François. The experimental validation of a numerical model for the prediction of railway induced vibrations. *Journal of Sound and Vibration*, 297(3-5):512–535, 2006.

[100] G. Lombaert, G. Degrande, B. Vanhauwere, B. Vandeborght, and S. François. The control of ground borne vibrations from railway traffic by means of continuous floating slabs. *Journal of Sound and Vibration*, 297(3-5):946–961, 2006.

[101] A.E.H. Love. *Some problems of geodynamics*. Dover, New York, U.S.A., 1967.

[102] J.E. Luco and R.J. Apsel. On the Green's functions for a layered half-space. Part I. *Bulletin of the Seismological Society of America*, 4:909–929, 1983.

[103] G.D. Manolis and D.E. Beskos. *Boundary element methods in Elastodynamics*. Unwin Hyman Ltd, London, UK, 1988.

[104] M. Margonari and M. Bonnet. Fast multipole method applied to elastostatic BEM-FEM coupling. *Computers and Structures*, 83(10–11):700–717, 2004.

[105] I. Mazzieri, M. Stupazzini, R. Guidotti, and C. Smerzini. SPEED: SPectral Elements in Elastodynamics with Discontinuous Galerkin: a non-conforming approach for 3D multi-scale problems. *International Journal for Numerical Methods in Engineering*, 95(12):991–1010, 2013.

[106] L. Menglin, W. Huaifeng, C. Xi, and Z. Yongmei. Structure-soil-structure interaction: Literature review. *Soil Dynamics and Earthquake Engineering*, 31(12):1724–1731, 2011.

[107] M. Messner and M. Schanz. An accelerated symmetric time-domain boundary element formulation for elasticity. *Engineering Analysis with Boundary Elements*, 34(11):944–955, 2010.

[108] M. Messner, M. Schanz, and E. Darve. Fast directional multilevel summation for oscillatory kernels based on Chebyshev interpolation. *Journal of Computational Physics*, 231(4):1175–1196, 2012.

[109] C. Michler, S.J. Hulshoff, E.H. van Brummelen, and R. de Borst. A monolithic approach to fluid-structure interaction. *Computers and Fluids*, 33:839–848, 2004.

[110] A. Milazzo, I. Benedetti, and M.H. Aliabadi. Hierarchical fast BEM for anisotropic time-harmonic 3-D elastodynamics. *Computers and Structures*, 96–97:9–24, 2012.

[111] D.P. Mok, W.A. Wall, and E. Ramm. Accelerated iterative substructuring schemes for instationary fluid-structure interaction. In

K.J. Bathe, editor, *Computational Fluid and Solid Mechanics*, pages 1325–1328. Elsevier, 2001.

[112] R. Mullen and T. Belytschko. Dispersion analysis of finite element discretisations of the two-dimensional wave equation. *International Journal for Numerical Methods in Engineering*, 18:11–29, 1982.

[113] N. Nishimura. Fast multipole accelerated boundary integral equation methods. *Applied Mechanics Reviews*, 22:175–181, 2002.

[114] Z. Ozdemir, P. Coulier, M.A. Lak, S. François, G. Lombaert, and G. Degrande. Numerical evaluation of the dynamic response of pipelines to vibrations induced by the operation of a pavement breaker. *Soil Dynamics and Earthquake Engineering*, 44:153–167, 2013.

[115] E. Pan. Static Green's functions in multilayered half spaces. *Applied Mathematical Modelling*, 21(8):509–521, 1997.

[116] M.A. Puso. A 3D mortar method for solid mechanics. *International Journal for Numerical Methods in Engineering*, 59(3):315–336, 2004.

[117] D. Rabinovich, D. Givoli, J. Bielak, and T. Hagstrom. A finite element scheme with a high order absorbing boundary condition for elastodynamics. *Computer Methods in Applied Mechanics and Engineering*, 200(23-24):2048–2066, 2011.

[118] J.W.S. Rayleigh. On waves propagated along the plane surface of an elastic solid. *Proceedings of the London Mathematical Society*, 17:4–11, 1887.

[119] D. Rhazi and N. Atalla. Transfer matrix modeling of the vibroacoustic response of multi–materials structures under mechanical excitation. *Journal of Sound and Vibration*, 329(13):2532–2546, 2010.

[120] F.J. Rizzo and D.J. Shippy. An application of the correspondence principle of linear viscoelasticity theory. *SIAM Journal on Applied Mathematics*, 21(2):321–330, 1971.

[121] F.J. Rizzo, D.J. Shippy, and M. Rezayat. A boundary integral equation method for radiation and scattering. *International Journal for Numerical Methods in Engineering*, 21:115–129, 1985.

[122] S. Rjasanow and O. Steinbach. *The Fast Solution of Boundary Integral Equations (Mathematical and Analytical Techniques with Applications to Engineering)*. Springer-Verlag New York, 2007.

[123] V. Rokhlin. Rapid solution of integral equations of classical potential theory. *Journal of Computational Physics*, 60:187–207, 1985.

[124] T. Rüberg and M. Schanz. Coupling finite and boundary element methods for static and dynamic elastic problems with non-conforming interfaces. *Computer Methods in Applied Mechanics and Engineering*, 198(3–4):449–458, 2008.

[125] Y. Saad. A flexible inner-outer preconditioned GMRES algorithm. *SIAM Journal on Scientific and Statistical Computing*, 14(2):461–469, 1993.

[126] Y. Saad and M.H. Schultz. GMRES: a generalized minimal residual algorithm for solving nonsymmetric linear systems. *SIAM Journal on Scientific and Statistical Computing*, 7(3):856–869, 1986.

[127] E.H. Saenger, N. Gold, and S.A. Shapiro. Modeling the propagation of elastic waves using a modified finite-difference grid. *Wave Motion*, 31(1):77–92, 2000.

[128] H.A. Schenck. Improved integral formulation for acoustic radiation problems. *Journal of the Acoustical Society of America*, 44:41–58, 1968.

[129] M. Schevenels. *The impact of uncertain dynamic soil characteristics on the prediction of ground vibrations*. PhD thesis, Department of Civil Engineering, KU Leuven, 2007.

[130] M. Schevenels, S. François, and G. Degrande. EDT: An ElastoDynamics Toolbox for MATLAB. *Computers & Geosciences*, 35(8):1752–1754, 2009.

[131] G. Seriani. 3-D large-scale wave propagation modeling by spectral element method on Cray T3E multiprocessor. *Computer Methods in Applied Mechanics and Engineering*, 164(1-2):235–247, 1998.

[132] M. Shamalta and A.V. Metrikine. Analytical study of the dynamic response of an embedded railway track to a moving load. *Archive of Applied Mechanics*, 73:131–146, 2003.

[133] X. Sheng, C.J.C. Jones, and D.J. Thompson. A theoretical model for ground vibration from trains generated by vertical track irregularities. *Journal of Sound and Vibration*, 272(3-5):937–965, 2004.

[134] X. Sheng, C.J.C. Jones, and D.J. Thompson. Modelling ground vibrations from railways using wavenumber finite- and boundary-element methods. *Proceedings of the Royal Society A - Mathematical, Physical and Engineering Sciences*, 461:2043–2070, 2005.

[135] D. Soares Jr. and L. Godinho. An optimized BEM–FEM iterative coupling algorithm for acoustic–elastodynamic interaction analyses in the frequency domain. *Computers and Structures*, 106–107:68–80, 2012.

[136] D. Soares Jr., L. Godinho, A. Pereira, and C. Dors. Frequency domain analysis of acoustic wave propagation in heterogeneous media considering iterative coupling procedures between the method of fundamental solutions and Kansa's method. *International Journal for Numerical Methods in Engineering*, 89(7):914–938, 2012.

[137] A.A. Stamos and D.E. Beskos. 3-D seismic response analysis of long lined tunnels in half-space. *Soil Dynamics and Earthquake Engineering*, 15:111–118, 1996.

[138] R. Stoneley. Elastic waves at the surface of separation of two solids. *Philosophical Transactions of the Royal Society A - Mathematical, Physical and Engineering Sciences*, 106(738):416–428, 1924.

[139] R. Taborda and J. Bielak. Large-scale earthquake simulation: Computational seismology and complex engineering systems. *Computing in Science and Engineering*, 13(4):14–27, 2011.

[140] A.J.B. Tadeu, J.M.P. Antonio, and L. Godhino. Green's function for two-and-a-half dimensional elastodynamic problems in a half-space. *Computational Mechanics*, 27(6):484–491, 2001.

[141] A.J.B. Tadeu, J.M.P. Antonio, and E. Kausel. 3D scattering of waves by a cylindrical irregular cavity of infinite length in a homogeneous elastic medium. *Computer Methods in Applied Mechanics and Engineering*, 191:3015–3033, 2002.

[142] A.J.B. Tadeu and E. Kausel. Green's functions for two-and-a-half-dimensional elastodynamic problems. *ASCE Journal of Engineering Mechanics*, 126(10):1093–1096, 2000.

[143] J.P. Talbot and H.E.M. Hunt. A generic model for evaluating the performance of base-isolated buildings. *Journal of Low Frequency Noise, Vibration and Active Control*, 22(3):149–160, 2003.

[144] J.D. Talman. Numerical Fourier and Bessel transforms in logarithmic variables. *Journal of Computational Physics*, 29(1):35–48, 1978.

[145] D.J. Thompson. *Railway noise and vibration: mechanisms, modelling, and means of control*. Elsevier, Oxford, 2009.

[146] W.T. Thomson. Transmission of elastic waves through a stratified solid medium. *Journal of Applied Physics*, 21:89–93, 1950.

[147] A. Toomey and C.J. Bean. Numerical simulation of seismic waves using a discrete particle scheme. *Geophysical Journal International*, 141(3):595–604, 2000.

[148] C. Tsogka and A. Wirgin. Seismic response of a set of blocks partially imbedded in soft soil. *Comptes Rendus Mécanique*, 331:217–224, 2003.

[149] C. Tsogka and A. Wirgin. Simulation of seismic response in an idealized city. *Soil Dynamics and Earthquake Engineering*, 23:391–402, 2003.

[150] M. Villot, C. Guigou, and L. Gagliardini. Predicting the acoustical radiation of finite size multi-layered structures by applying spatial windowing on infinite structures. *Journal of Sound and Vibration*, 245(3):433–455, 2001.

[151] O. Von Estorff and M. Firuziaan. Coupled BEM/FEM approach for nonlinear soil/structure interaction. *Engineering Analysis with Boundary Elements*, 24:605–621, 2000.

[152] O. Von Estorff and C. Hagen. Iterative coupling of FEM and BEM in 3D transient elastodynamics. *Engineering Analysis with Boundary Elements*, 29:775–787, 2005.

[153] O. Von Estorff and E. Kausel. Coupling of boundary and finite elements for soil-structure interaction. *Earthquake Engineering and Structural Dynamics*, 18:1065–1075, 1989.

[154] L.T. Wheeler and E. Sternberg. Some theorems in classical elastodynamics. *Archive for Rational Mechanics and Analysis*, 31:51–90, 1968.

[155] A. Wirgin and P.-Y. Bard. Effects of buildings on the duration and amplitude of ground motion in Mexico City. *Bulletin of the Seismological Society of America*, 86(3):914–920, 1996.

[156] B.I. Wohlmuth. *Discretization Methods and Iterative Solvers Based on Domain Decomposition*. Springer Publishing Company, 1st edition, 2001.

[157] J.P. Wolf. *Dynamic soil-structure interaction*. Prentice-Hall, Englewood Cliffs, New Jersey, 1985.

[158] R.D. Woods. Screening of surface waves in soils. *Journal of the Soil Mechanics and Foundation Division, Proceedings of the ASCE*, 94(SM4):951–979, 1968.

[159] Y.B. Yang and H.H. Hung. A 2.5D finite-infinite element approach for modelling visco-elastic bodies subjected to moving loads. *International Journal for Numerical Methods in Engineering*, 51:1317–1336, 2001.

[160] Y.B. Yang and H.H. Hung. Soil vibrations caused by underground moving trains. *Journal of Geotechnical and Geoenvironmental Engineering, Proceedings of the ASCE*, 134(11):1633–1644, 2008.

[161] Y.B. Yang, H.H. Hung, and D.W. Chang. Train-induced wave propagation in layered soils using finite/infinite element simulation. *Soil Dynamics and Earthquake Engineering*, 23:263–278, 2003.

[162] C. Yoshimura, J. Bielak, Y. Hisada, and A. Fernández. Domain reduction method for three-dimensional earthquake modeling in localized regions, Part II: Verification and applications. *Bulletin of the Seismological Society of America*, 93(2):825–840, 2003.

[163] C. Zhang and C. Zhao. Coupling method of finite and infinite elements for strip foundation wave problems. *Earthquake Engineering and Structural Dynamics*, 15:839–851, 1987.

[164] O.C. Zienkiewicz, D.W. Kelly, and P. Bettes. The coupling of the finite element method and boundary solution procedures. *International Journal for Numerical Methods in Engineering*, 11:355–375, 1977.

[165] O.C. Zienkiewicz and R.L. Taylor. *The finite element method, Volume 1: the basis*. Butterworth-Heinemann, Oxford, United Kingdom, fifth edition, 2000.

PART II

KEY PUBLICATIONS

Paper A

Application of hierarchical matrices to boundary element methods for elastodynamics based on Green's functions for a horizontally layered halfspace

Published in Engineering Analysis with Boundary Elements 37 (2013) 1745–1758
http://dx.doi.org/10.1016/j.enganabound.2013.09.009

Application of hierarchical matrices to boundary element methods for elastodynamics based on Green's functions for a horizontally layered halfspace

P. Coulier, S. François, G. Lombaert, G. Degrande
KU Leuven, Department of Civil Engineering,
Kasteelpark Arenberg 40, B-3001 Leuven, Belgium

Abstract

This paper presents the application of hierarchical matrices to boundary element methods for elastodynamics based on Green's functions for a horizontally layered halfspace. These Green's functions are computed by means of the direct stiffness method; their application avoids meshing of the free surface and the layer interfaces. The effectiveness of the methodology is demonstrated through numerical examples, indicating that a significant reduction of memory and CPU time can be achieved with respect to the classical boundary element method. This allows increasing the problem size by one order of magnitude. The proposed methodology therefore offers perspectives to study large scale problems involving three–dimensional elastodynamic wave propagation in a layered halfspace, with possible applications in seismology and dynamic soil–structure interaction.

Keywords: boundary element method; elastodynamics; $\mathscr{H}$–matrices; halfspace Green's functions; railway induced vibrations.

1 Introduction

The boundary element (BE) method is well–suited to model three–dimensional (3D) elastodynamic wave propagation in a stratified halfspace, as the radiation of waves towards infinity is inherently taken into account. Moreover, a reduction of the spatial problem dimension is obtained due to the fact that only the boundaries of the domain have to be discretized. The BE method is therefore often employed to model a variety of problems, such as seismic site effects [1], railway induced vibrations [2] and other applications involving dynamic soil–structure interaction [3]. Accounting for the soil stratification is important in many of these applications, especially in presence of soft top layers. Although it is common to use closed form full space Green's functions in the BE formulation, numerically computed Green's functions for a horizontally layered halfspace can be incorporated as well in order to avoid meshing of the free surface and the layer interfaces, as will be done throughout this paper.

The advantages of the BE method are partially negated, however, by the fact that dense, fully populated unsymmetric matrices arise from the formulation, resulting in stringent memory and CPU requirements. This hinders the applicability of the BE method to large scale problems. Several fast BE methods have been developed in the past decade to improve the computational efficiency, including the fast multipole method (FMM) [4], the panel clustering technique [5] and methods based on hierarchical matrices [6]. In the FMM, the Green's functions are reformulated using a multipole expansion, which has proven to be very efficient if analytical expressions of the Green's functions are available [7]. Existing FMM formulations for (visco–)elastodynamics are therefore based on closed form full space fundamental solutions [8–10], while innovative methods based on Green's functions for a homogeneous halfspace are currently under development [11]. The latter approach has the main disadvantage, however, that a considerable amount of boundary elements is required for the discretization of the free surface and the layer interfaces, limiting the actual problem size that can be treated. A complementary class of fast BE methods is based on hierarchical matrices in combination with efficient algorithms such as adaptive cross approximation. These methods essentially are algebraic tools to approximate the BE matrices [12,13], providing an alternative to tackle problems for which analytical expressions of the Green's functions are not available.

Hierarchical matrices have been employed to solve elliptic Helmholtz [14], Laplace [15] and elastostatic Lamé problems [16, 17]. Only a few authors, however, have considered the use of hierarchical matrices for elastodynamics. Messner et al. [18] present an accelerated time domain elastodynamic boundary

element formulation in which the time dependent problem is transformed into a system of decoupled Laplace domain problems using the convolution quadrature method. Full space elastodynamic fundamental solutions are employed in this approach, necessitating the discretization of the free surface to model wave propagation in a halfspace. Benedetti et al. [19] consider hierarchical matrices to solve elastodynamic crack problems using a dual boundary element method formulated in the Laplace domain, while Milazzo et al. [20] apply the concept to anisotropic elastodynamics in the frequency domain.

The aim of this paper is to demonstrate that hierarchical matrices are also suited to model 3D visco–elastodynamic wave propagation in a stratified halfspace, incorporating Green's functions for a horizontally layered halfspace. As the methodology is formulated in the frequency domain, material damping is accounted for through the correspondence principle [21] and visco–elastodynamic problems can easily be treated. The text is organized as follows. The basic concepts of the classical BE method are summarized in section 2, while the application of hierarchical matrices is discussed in section 3. The computation of the Green's functions for a horizontally layered halfspace is also briefly addressed. The numerical implementation of the proposed methodology is validated in section 4 and the computational performance is assessed in terms of memory and CPU requirements. The applicability of the novel approach is finally illustrated in section 5 by means of a case study in which dynamic through–soil coupling of closely spaced buildings under the influence of an incident wavefield is investigated.

2 The boundary element method for elastodynamics based on Green's functions for a horizontally layered halfspace

2.1 Boundary integral equation

Consider a domain $\Omega \in \mathbb{R}^3$ with boundary Σ, characterized by a unit outward normal vector $\mathbf{n}$. The classical boundary integral equation relates the displacement $\hat{u}_i(\mathbf{x}', \omega)$ in a point $\mathbf{x}'$ to the elastodynamic state on the boundary Σ in the frequency domain [22]:

$$\kappa \hat{u}_i(\mathbf{x}', \omega) = \int_\Sigma \left(\hat{u}_{ij}^{\mathrm{G}}(\mathbf{x}', \mathbf{x}, \omega) \hat{t}_j^{\mathbf{n}}(\mathbf{x}, \omega) - \hat{t}_{ij}^{\mathrm{G}\mathbf{n}}(\mathbf{x}', \mathbf{x}, \omega) \hat{u}_j(\mathbf{x}, \omega) \right) \mathrm{d}S \qquad (1)$$

where the presence of body forces is neglected. A hat above a variable denotes its representation in the frequency domain. The Green's displacements $\hat{u}_{ij}^{\mathrm{G}}(\mathbf{x}', \mathbf{x}, \omega)$ and tractions $\hat{t}_{ij}^{\mathbf{Gn}}(\mathbf{x}', \mathbf{x}, \omega)$ correspond to the fundamental solutions at a receiver $\mathbf{x}$ in a direction $\mathbf{e}_j$ due to a unit time harmonic point load at a source $\mathbf{x}'$ in a direction $\mathbf{e}_i$. Throughout this paper, Green's functions for a homogeneous full space as well as a horizontally layered halfspace will be employed; the use of the latter avoids the discretization of the free surface and the layer interfaces. No closed form expressions are available for these Green's functions for layered soils, however, which implies that they have to be computed numerically. This will briefly be addressed in subsection 2.3.

In equation (1), $\kappa = 1$ when the point $\mathbf{x}'$ is located inside the domain Ω and $\kappa = 0$ if the point $\mathbf{x}'$ is located outside the domain Ω. The boundary integral equation (1) does not hold for points $\mathbf{x}'$ located on the boundary Σ due to the singular behaviour of the Green's functions. A classical limiting procedure [23, 24] results in Somigliana's identity, involving the evaluation of Cauchy principal value (CPV) integrals of the strongly singular Green's tractions. In this paper, however, a regularized boundary integral equation is employed, in which the evaluation of CPV integrals is avoided [24–26]. The regularization procedure is based on the fact that the singularity of the static and dynamic Green's functions at the source point is similar. In case of an unbounded domain Ω, the regularized boundary integral equation, which is valid for points $\mathbf{x}'$ located on the boundary Σ, reads as follows [24]:

$$\hat{u}_i(\mathbf{x}', \omega) - \int_\Sigma \hat{u}_{ij}^{\mathrm{G}}(\mathbf{x}', \mathbf{x}, \omega) \hat{t}_j^{\mathbf{n}}(\mathbf{x}, \omega) \, \mathrm{d}S + \int_\Sigma \left(\hat{t}_{ij}^{\mathbf{Gn}}(\mathbf{x}', \mathbf{x}, \omega) \hat{u}_j(\mathbf{x}, \omega) - t_{ij}^{\mathbf{Gns}}(\mathbf{x}', \mathbf{x}) \hat{u}_j(\mathbf{x}', \omega) \right) \mathrm{d}S = 0 \quad (2)$$

where $t_{ij}^{\mathbf{Gns}}$ denotes the static Green's tractions. The integral free term $\hat{u}_i(\mathbf{x}', \omega)$ in equation (2) vanishes for a bounded domain Ω. The boundary integrals in equation (2) are at most weakly singular and are evaluated using classical Gaussian integration.

2.2 Boundary element discretization

The regularized boundary integral equation (2) is solved numerically by discretizing the boundary Σ with an appropriate number of boundary elements, resulting in a boundary element system of equations. For an unbounded domain Ω, the displacements $\underline{\hat{\mathbf{u}}}(\omega)$ and tractions $\underline{\hat{\mathbf{t}}}(\omega)$ at the collocation points

are related as follows:

$$\left[\widehat{\mathbf{T}}(\omega) + \mathbf{I}\right] \underline{\hat{\mathbf{u}}}(\omega) = \widehat{\mathbf{U}}(\omega)\underline{\hat{\mathbf{t}}}(\omega) \tag{3}$$

The system matrices $\widehat{\mathbf{U}}(\omega)$ and $\widehat{\mathbf{T}}(\omega)$ are fully populated unsymmetric matrices, while $\mathbf{I}$ represents a unit matrix, corresponding to the integral free term in the boundary integral equation. The latter vanishes for a bounded domain. The computation of the system matrices $\widehat{\mathbf{U}}(\omega)$ and $\widehat{\mathbf{T}}(\omega)$ requires integration of the Green's functions $\hat{u}_{ij}^{\mathrm{G}}(\mathbf{x}', \mathbf{x}, \omega)$ and $\hat{t}_{ij}^{\mathrm{G}\mathbf{n}}(\mathbf{x}', \mathbf{x}, \omega)$ over the boundary Σ, respectively.

A quadratic amount of memory ($\mathcal{O}(N_{\mathrm{DOF}}^2)$) is required to store the system matrices $\widehat{\mathbf{U}}(\omega)$ and $\widehat{\mathbf{T}}(\omega)$, where N_{DOF} represents the number of degrees of freedom in the BE model. Furthermore, solving equation (3) by means of direct numerical solvers such as LU–decomposition requires a cubic amount of numerical operations ($\mathcal{O}(N_{\mathrm{DOF}}^3)$). The application of the classical boundary element method is therefore presently limited to problems involving up to $\mathcal{O}(10^4)$ degrees of freedom [12].

2.3 Green's functions for layered soils: the direct stiffness method

As mentioned in subsection 2.1, Green's functions $\hat{u}_{ij}^{\mathrm{G}}(\mathbf{x}', \mathbf{x}, \omega)$ and $\hat{t}_{ij}^{\mathrm{G}\mathbf{n}}(\mathbf{x}', \mathbf{x}, \omega)$ for a horizontally layered halfspace are employed in the boundary element formulation. These Green's functions are computed with the direct stiffness method [27] using the MATLAB toolbox EDT 2.2 [28]. The direct stiffness method provides element stiffness matrices for homogeneous layers and a homogeneous halfspace, formulated in the frequency–wavenumber domain. The stiffness matrix of a horizontally layered halfspace is obtained from the assembly of the element stiffness matrices. Solving the corresponding set of equations provides the Green's functions in the frequency–wavenumber domain. An inverse transformation from the wavenumber to the spatial domain is subsequently performed to obtain the Green's functions in the frequency–spatial domain. This is obtained by a numerical transformation algorithm, developed by Talman [29] and improved by Schevenels et al. [28, 30]. The calculation of these Green's functions is computationally expensive, however, in particular when a large number of source/receiver depths is considered.

The global system size in the direct stiffness method grows for an increasing number of soil layers and the time required to compute the Green's functions for a stratified halfspace increases correspondingly [31]. In cases with a very large number of layers, other numerical methods such as the propagator

matrix method [32,33] may provide a more efficient alternative; these Green's functions can be incorporated straightforwardly in the boundary element formulation. Nonetheless, the direct stiffness method has some appealing advantages compared to the latter method, such as the fact that stiffness matrices are symmetric, involve half as many degrees of freedom as propagator matrices, and remain robust and stable for thick layers and/or high frequencies if limiting expressions are implemented; propagator matrices, on the other hand, contain terms of exponential growth that require special consideration and treatment [34–36]. The direct stiffness method is therefore employed throughout this paper; a more elaborate comparison of the direct stiffness and the propagator matrix method is given by Kausel [37].

3 Application of hierarchical matrices

The applicability of the classical boundary element method is limited due to stringent memory and CPU requirements. The use of hierarchical matrices ($\mathscr{H}$–matrices) provides an elegant way to treat fully populated matrices with almost linear complexity [38]. In this section, the basic principles of the boundary element method based on $\mathscr{H}$–matrices are briefly summarized. The reader is referred to the literature [6,13,38,39] for a detailed description of the methodology.

3.1 Hierarchical matrix assembly

A $\mathscr{H}$–matrix is a data–sparse representation of a matrix, consisting of a collection of block matrices of various sizes. The construction of a $\mathscr{H}$–matrix requires several steps. First, a hierarchical cluster tree is constructed based on the boundary element mesh. At the lowest level (i.e. level 0), the cluster consists of the complete BE mesh. Each cluster is recursively partitioned into two (more or less equal) sons. Several techniques are available in order to obtain a suitable cluster tree (e.g. nested dissection [40, 41], cardinality balanced clustering [13], ...). In the following, a clustering strategy based on principal component analysis (PCA) is employed [12]. In PCA, the eigenvectors of the covariance matrix of a cluster are first calculated. The eigenvector corresponding to the largest eigenvalue gives the main direction of the cluster considered. A separation plane orthogonal to the aforementioned eigenvector is drawn through the center of the cluster, dividing it in two (more or less equal) sons. This procedure can be recursively applied to every son, until the clusters contain less or equal than a prescribed number $N_{\min}$ of elements (or nodes).

Second, admissible cluster pairs (X, Y) are identified, i.e. cluster subdomains which satisfy a geometric admissibility criterion such that the corresponding fundamental solutions are smooth [12, 42]:

$$\min\{\mathrm{diam(X)}, \mathrm{diam(Y)}\} < \eta \mathrm{dist(X, Y)} \qquad 0 < \eta < 1 \tag{4}$$

where diam(X) denotes the maximal extent of cluster X and dist(X, Y) is the minimal distance between clusters X and Y. The parameters $N_{\min}$ and η affect the number of admissible blocks and the quality of the approximation of the admissible pairs [20, 39]. A trade–off between accuracy and efficiency should be made when selecting these parameters.

The identification of admissible and inadmissible cluster pairs finally allows for the approximation of the BE matrices $\widehat{\mathbf{T}}(\omega)$ and $\widehat{\mathbf{U}}(\omega)$ by their hierarchical representations $\widehat{\mathbf{T}}_{\mathscr{H}}(\omega)$ and $\widehat{\mathbf{U}}_{\mathscr{H}}(\omega)$, respectively. For an admissible cluster pair (X, Y), the fundamental solutions are sufficiently smooth such that the corresponding block BE matrices $\widehat{\mathbf{T}}_{(X,Y)}(\omega) \in \mathbb{C}^{m\times n}$ and $\widehat{\mathbf{U}}_{(X,Y)}(\omega) \in \mathbb{C}^{m\times n}$ can be approximated by low rank approximations. m and n denote the number of degrees of freedom in clusters X and Y, respectively. For example, the block matrix $\widehat{\mathbf{T}}_{(X,Y)}(\omega)$ is approximated by $\widetilde{\widehat{\mathbf{T}}}_{(X,Y)}(\omega)$:

$$\widehat{\mathbf{T}}_{(X,Y)}(\omega) \simeq \widetilde{\widehat{\mathbf{T}}}_{(X,Y)}(\omega) = \left(\widehat{\mathbf{V}}_{\mathbf{T}_{(X,Y)}}(\omega)\right)\left(\widehat{\mathbf{W}}_{\mathbf{T}_{(X,Y)}}(\omega)\right)^{\star} \tag{5}$$

with $\widehat{\mathbf{V}}_{\mathbf{T}_{(X,Y)}}(\omega) \in \mathbb{C}^{m\times k}$ and $\widehat{\mathbf{W}}_{\mathbf{T}_{(X,Y)}}(\omega) \in \mathbb{C}^{n\times k}$ and where $\star$ indicates the complex conjugate. k is the rank of the representation. For $k(m+n) < mn$, $\widetilde{\widehat{\mathbf{T}}}_{(X,Y)}(\omega)$ is called a low rank approximation of $\widehat{\mathbf{T}}_{(X,Y)}(\omega)$, as the memory storage can be reduced from $\mathcal{O}(mn)$ to $\mathcal{O}(k(m+n))$ by storing $\widehat{\mathbf{V}}_{\mathbf{T}_{(X,Y)}}(\omega)$ and $\widehat{\mathbf{W}}_{\mathbf{T}_{(X,Y)}}(\omega)$ instead of $\widehat{\mathbf{T}}_{(X,Y)}(\omega)$, which is linear in m and n. The rank k is determined such that the approximation $\widetilde{\widehat{\mathbf{T}}}_{(X,Y)}(\omega)$ is accurate up to a prescribed relative accuracy ε:

$$||\widehat{\mathbf{T}}_{(X,Y)}(\omega) - \widetilde{\widehat{\mathbf{T}}}_{(X,Y)}(\omega)||_{\mathrm{F}} \leq \varepsilon ||\widehat{\mathbf{T}}_{(X,Y)}(\omega)||_{\mathrm{F}} \tag{6}$$

where $||\diamond||_{\mathrm{F}}$ indicates the Frobenius norm of the matrix $\diamond$. The partially pivoted adaptive cross approximation (ACA) algorithm [12,43] is employed to compute the matrices $\widehat{\mathbf{V}}_{\mathbf{T}_{(X,Y)}}(\omega)$ and $\widehat{\mathbf{W}}_{\mathbf{T}_{(X,Y)}}(\omega)$ for the low rank approximation defined in equation (5). This is an algebraic approximation technique; the algorithm adaptively calculates some of the rows and columns of the original block matrix to obtain an approximation from few of the original matrix entries. The algorithm stops if the prescribed accuracy ε is attained; the stopping criterion defined in equation (6) can however not be employed, as

the original matrix $\widehat{\mathbf{T}}_{(X,Y)}(\omega)$ is never generated completely. An intrinsic stopping criterion based on the variation of the Frobenius norm in consecutive approximations is therefore used. The amount of numerical operations required in the ACA algorithm is $\mathcal{O}(k^2(m+n))$ [12]. One of the major advantages of applying the ACA algorithm to obtain low rank approximations of the BE block matrices corresponding to admissible cluster pairs is that it is an algebraic approach, implying that there is no need for (semi–)analytical expressions of the Green's functions $\hat{u}_{ij}^{\mathrm{G}}(\mathbf{x}', \mathbf{x}, \omega)$ and $\hat{t}_{ij}^{\mathbf{G}\mathbf{n}_{\mathrm{s}}}(\mathbf{x}', \mathbf{x}, \omega)$. The incorporation of Green's functions for layered soils has not yet been attempted before, however. The memory storage for these block BE matrices can be reduced even further by means of appropriate recompression techniques [38, 44, 45]. In this paper, a procedure based on the singular value decomposition (SVD) of the low rank approximations is employed [44]. Introducing the QR–decompositions of the matrices $\widehat{\mathbf{V}}_{\mathbf{T}_{(X,Y)}}(\omega) = \widehat{\mathbf{Q}}_{\mathbf{V}}\widehat{\mathbf{R}}_{\mathbf{V}}$ and $\widehat{\mathbf{W}}_{\mathbf{T}_{(X,Y)}}(\omega) = \widehat{\mathbf{Q}}_{\mathbf{W}}\widehat{\mathbf{R}}_{\mathbf{W}}$ in equation (5) gives:

$$\widetilde{\widehat{\mathbf{T}}}_{(X,Y)}(\omega) = \widehat{\mathbf{Q}}_{\mathbf{V}}\widehat{\mathbf{R}}_{\mathbf{V}}\widehat{\mathbf{R}}_{\mathbf{W}}^{\star}\widehat{\mathbf{Q}}_{\mathbf{W}}^{\star} \tag{7}$$

These matrix decompositions are calculated using a Householder transformation [46]. The SVD of the outer product of the two upper triangular matrices $\widehat{\mathbf{R}}_{\mathbf{V}}$ and $\widehat{\mathbf{R}}_{\mathbf{W}}$ is subsequently computed:

$$\widehat{\mathbf{R}}_{\mathbf{V}}\widehat{\mathbf{R}}_{\mathbf{W}}^{\star} = \widehat{\mathbf{U}}_{\mathbf{R}}\widehat{\mathbf{\Sigma}}\widehat{\mathbf{V}}_{\mathbf{R}}^{\star} \tag{8}$$

with $\widehat{\mathbf{\Sigma}} \in \mathbb{R}^{k\times k}$ a diagonal matrix containing the singular values in descending order. Combining equations (7) and (8) allows to write $\widetilde{\widehat{\mathbf{T}}}_{(X,Y)}(\omega)$ as:

$$\widetilde{\widehat{\mathbf{T}}}_{(X,Y)}(\omega) = \left(\widehat{\mathbf{Q}}_{\mathbf{V}}\widehat{\mathbf{U}}_{\mathbf{R}}\right)\widehat{\mathbf{\Sigma}}\left(\widehat{\mathbf{Q}}_{\mathbf{W}}\widehat{\mathbf{V}}_{\mathbf{R}}\right)^{\star} \tag{9}$$

which can be identified as the SVD of $\widetilde{\widehat{\mathbf{T}}}_{(X,Y)}(\omega)$, as the matrices $\widehat{\mathbf{Q}}_{\mathbf{V}}\widehat{\mathbf{U}}_{\mathbf{R}}$ and $\widehat{\mathbf{Q}}_{\mathbf{W}}\widehat{\mathbf{V}}_{\mathbf{R}}$ are both unitary [45]. A memory reduction is then obtained by discarding the smallest singular values and corresponding singular vectors in equation (9), hence reducing the rank, while maintaining the desired approximation accuracy. This recompression procedure is applied to every low rank approximation immediately after its assembly through ACA and only requires a limited amount of additional numerical operations of $\mathcal{O}(k^2(m+n+k))$ [45].

For cluster pairs (X, Y) not satisfying the admissibility criterion (4), the fundamental solutions show a singular behaviour which does not allow constructing a low rank approximation of the corresponding block BE matrices. These blocks are therefore computed exactly.

3.2 Solving the $\mathscr{H}$–BE equations

Following the procedure outlined above for every cluster pair (X, Y) leads to an approximation of the BE matrices $\widehat{\mathbf{T}}(\omega)$ and $\widehat{\mathbf{U}}(\omega)$ by their hierarchical representations $\widehat{\mathbf{T}}_{\mathscr{H}}(\omega)$ and $\widehat{\mathbf{U}}_{\mathscr{H}}(\omega)$, respectively, and the BE equation (3) can be replaced by:

$$\left[\widehat{\mathbf{T}}_{\mathscr{H}}(\omega) + \mathbf{I}\right] \underline{\hat{\mathbf{u}}}(\omega) = \widehat{\mathbf{U}}_{\mathscr{H}}(\omega)\underline{\hat{\mathbf{t}}}(\omega) \tag{10}$$

In order to solve equation (3), iterative Krylov subspace methods are well suited. The matrix–vector multiplication forms the core of iterative solvers and the complexity of this operation is only $\mathcal{O}(N_{\mathrm{DOF}} \log N_{\mathrm{DOF}})$ for $\mathscr{H}$–matrices [13]. In this paper, all equations are therefore solved by means of the generalized minimal residual method (GMRES) [47]. As will be illustrated in subsection 4.2, the contribution of the time required for solving equation (3) to the total computation time is negligible compared to the assembly time of the $\mathscr{H}$–matrices; no preconditioner is therefore incorporated in the iterative solver.

4 Validation

The BE method based on $\mathscr{H}$–matrices outlined in section 3 has been implemented in the MATLAB toolbox BEMFUN [48]. The core of this toolbox is implemented in C++ using the MATLAB MEX interface in order to achieve both a seamless integration with MATLAB and a high numerical efficiency. In the following subsections, three examples are considered to validate the numerical implementation and to demonstrate the effectiveness of the methodology. The first example is included to validate the correct implementation of $\mathscr{H}$–matrix arithmetics and does not involve Green's functions for a layered halfspace, while the second and the third example focus on the application of the novel method, incorporating Green's functions of a layered and homogeneous halfspace, respectively. All calculations have been performed on Intel® Xeon® E5520 (2.26 GHz) CPUs.

4.1 3D spherical cavity subjected to an internal pressure

A 3D spherical cavity with radius $r_0 = 1\,\mathrm{m}$ in a full space loaded by an internal pressure $\hat{p}(\omega) = 1\,\mathrm{Pa/Hz}$ is investigated in this subsection. The full space is characterized by a shear wave velocity $C_{\mathrm{s}} = 150\,\mathrm{m/s}$, a dilatational wave

velocity $C_\mathrm{p} = 300\,\mathrm{m/s}$ and a density $\rho = 1800\,\mathrm{kg/m^3}$. No material damping is taken into account.

The unit sphere is discretized by means of 3072 eight node quadrilateral boundary elements with element collocation. Both the classical and hierarchical BE method are used to calculate the response in a frequency range between 0 Hz and 100 Hz, where analytical full space fundamental solutions [23, 37] are employed. For the latter method, a hierarchical cluster tree is constructed based on the elements' center, as an element collocation scheme is used. A minimum number of elements $N_\mathrm{min} = 24$ is specified, resulting in $\log_2(3072/24) = 7$ cluster levels. Figure 1 shows the hierarchical block structure of the matrices of $\widehat{\mathbf{T}}_{\mathscr{H}}(\omega)$ and $\widehat{\mathbf{U}}_{\mathscr{H}}(\omega)$ arising from this hierarchical clustering, where a value of 0.95 is attributed to the parameter η in the admissibility criterion (4). A threshold $\varepsilon = 10^{-3}$ has been used in the ACA algorithm to obtain low rank approximations of the blocks corresponding to admissible cluster pairs, while a tolerance of 10^{-4} was specified in the iterative GRMES solver.

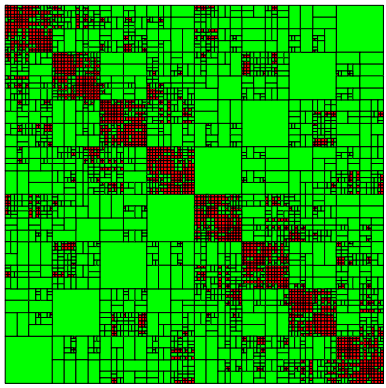

Figure 1: Hierarchical matrix decomposition corresponding to the BE model of a spherical cavity. The green blocks corresponding to admissible cluster pairs are approximated by means of ACA, while the red blocks corresponding to inadmissible cluster pairs are computed exactly.

Figure 2 shows the real and imaginary part of the radial displacement at the point $\{r = r_0, \theta = 0, z = 0\,\mathrm{m}\}$, calculated with the classical and the hierarchical BE method, respectively. A perfect agreement between the results of both methods can be observed. These results are furthermore compared to the

analytical solution for the radial displacement in the full space, defined as [37]:

$$\hat{u}_r(r,\omega) = \frac{r_0^3}{4\rho C_\mathrm{s}^2 r^2} \frac{1+i\omega_\mathrm{p}}{1+i\omega_0 - \left(\omega_0 \frac{C_\mathrm{p}}{2C_\mathrm{s}}\right)^2} \exp\left(-i\left(\frac{r}{r_0}-1\right)\omega_0\right) \tag{11}$$

where $\omega_\mathrm{p} = \omega r/C_\mathrm{p}$ and $\omega_0 = \omega r_0/C_\mathrm{p}$. The results of both numerical methods agree very well with the analytical solution (i.e. equation (11) evaluated for $r = r_0$) in the low frequency range, with some small deviations above 40 Hz.

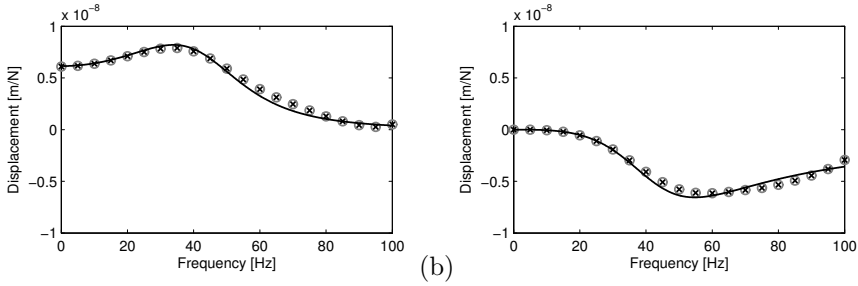

Figure 2: (a) Real and (b) imaginary part of the radial displacement at $\{r = r_0, \theta = 0, z = 0\,\mathrm{m}\}$ due to a unit harmonic pressure applied in a spherical cavity with $r_0 = 1\,\mathrm{m}$. The solution obtained with the hierarchical BE method (grey circles) is compared to the solution obtained with the classical BE method (black crosses) and the analytical solution (solid line) [37].

The integral representation theorem subsequently allows for the computation of the radiated wavefield in the soil from the displacements and tractions on the boundary. Figure 3 shows the real and imaginary part of the radial displacement at the point $\{r = 10\,\mathrm{m}, \theta = 0, z = 0\,\mathrm{m}\}$. The solutions of the classical and hierarchical BE method are clearly in good correspondence and agree with the analytical solution (i.e. equation (11) evaluated for $r = 10\,\mathrm{m}$).

The accuracy of the BE method based on $\mathscr{H}$–matrices is investigated in more detail in figure 4, showing the relative error $||\hat{u}_{r,\mathscr{H}}(r_0,\omega) - \hat{u}_{r,\mathrm{c}}(r_0,\omega)||/||\hat{u}_{r,\mathrm{c}}(r_0,\omega)||$. $\hat{u}_{r,\mathscr{H}}(r_0,\omega)$ and $\hat{u}_{r,\mathrm{c}}(r_0,\omega)$ represent the radial displacement on the boundary of the cavity, calculated with the hierarchical and the classical BE method, respectively. Although a threshold $\varepsilon = 10^{-3}$ is prescribed in the ACA algorithm for the approximation of the matrix blocks corresponding to admissible cluster pairs, the overall computational precision is $\mathcal{O}(10^{-4})$, except at high frequencies.

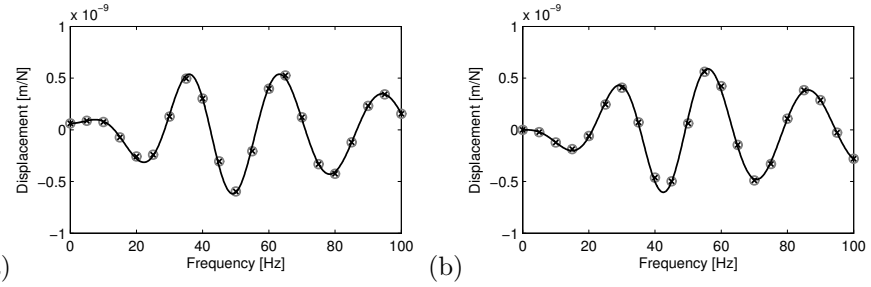

Figure 3: (a) Real and (b) imaginary part of the radial displacement at $\{r = 10\,\mathrm{m}, \theta = 0, z = 0\,\mathrm{m}\}$ due to a unit harmonic pressure applied in a spherical cavity with $r_0 = 1\,\mathrm{m}$. The solution obtained with the hierarchical BE method (grey circles) is compared to the solution obtained with the classical BE method (black crosses) and the analytical solution (solid line) [37].

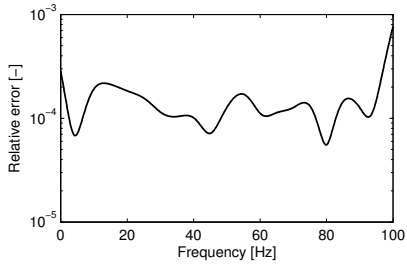

Figure 4: Relative error $||\hat{u}_{r,\mathscr{H}}(r_0,\omega) - \hat{u}_{r,\mathrm{c}}(r_0,\omega)||/||\hat{u}_{r,\mathrm{c}}(r_0,\omega)||$ on the boundary of a spherical cavity with $r_0 = 1\,\mathrm{m}$.

4.2 Impedance of a massless rigid square surface foundation on a horizontally layered halfspace

A massless rigid square surface foundation resting on a horizontally layered halfspace is considered in this subsection. The foundation side equals $d = 5\,\mathrm{m}$. The soil consists of two layers on a halfspace, each with a thickness of 2 m. The shear wave velocity C_s is equal to 150 m/s in the top layer, 250 m/s in the second layer, and 300 m/s in the underlying halfspace. The Poisson's ratio ν is 1/3 everywhere, resulting in dilatational wave velocities C_p of 300 m/s, 500 m/s, and 600 m/s, respectively. Material damping ratios $\beta_\mathrm{s} = \beta_\mathrm{p} = 0.025$ in both deviatoric and volumetric deformation are attributed to the layers and the

halfspace, while a uniform density $\rho = 1800\,\mathrm{kg/m^3}$ is considered throughout the medium.

The classical as well as the hierarchical BE method are employed to calculate the vertical soil impedance $\hat{K}^{\mathrm{s}}_{zz}(\omega)$, defined as:

$$\hat{K}^{\mathrm{s}}_{zz}(\omega) = \int_{\Sigma} \boldsymbol{\psi}_{zz} \cdot \hat{\mathbf{t}}^{\mathbf{n}_{\mathrm{s}}}_{\mathrm{s}}(\hat{\mathbf{u}}_{\mathrm{sc}}(\boldsymbol{\psi}_{zz}))\,\mathrm{d}S \tag{12}$$

where $\boldsymbol{\psi}_{zz}$ indicates the vertical rigid body translation of the foundation. The soil–structure interface Σ is discretized by means of four node quadrilateral boundary elements with element collocation. The tractions $\hat{\mathbf{t}}^{\mathbf{n}_{\mathrm{s}}}_{\mathrm{s}}(\hat{\mathbf{u}}_{\mathrm{sc}}(\boldsymbol{\psi}_{zz})$ due to imposed displacements $\boldsymbol{\psi}_{zz}$ are obtained by solving equations (3) and (3), respectively. As a surface foundation is considered, the system matrices $\widehat{\mathbf{T}}(\omega)$ and $\widehat{\mathbf{T}}_{\mathscr{H}}(\omega)$ are zero. The same values for the parameters η, $N_{\min}$, ε and the tolerance in the GMRES solver as specified in subsection 4.1 are used in the BE method based on $\mathscr{H}$–matrices. As mentioned in section 2, Green's functions for a layered halfspace are incorporated in both BE formulations [27,28], avoiding the necessity to discretize the free surface and the layer interfaces.

The vertical soil impedance $\hat{K}^{\mathrm{s}}_{zz}(\omega)$ can alternatively be written in the following form [49]:

$$\hat{K}^{\mathrm{s}}_{zz}(\omega) = K^{\mathrm{s}}_{zz0}\left(k_{zz}(a_0) + i a_0 c_{zz}(a_0)\right) \tag{13}$$

where $a_0 = \omega B/C_{\mathrm{s}}$ is a dimensionless frequency and $B = d/2$ a characteristic length of the foundation. K^{s}_{zz0} indicates the static stiffness, while $k_{zz}(a_0)$ and $c_{zz}(a_0)$ are dimensionless stiffness and damping coefficients, respectively. A BE mesh consisting of 30×30 equally sized elements is used. Up to nine elements per shear wavelength $\lambda_{\mathrm{s}} = C_{\mathrm{s}}/f = 2\pi B/a_0$ are provided at the maximum dimensionless frequency of 10 (determined by the shear wave velocity of the top layer). Figure 5 shows the coefficients $k_{zz}(a_0)$ and $c_{zz}(a_0)$ in a dimensionless frequency range between 0 and 10. A perfect match between the classical and hierarchical BE method can be observed.

The influence of the threshold ε used in the ACA algorithm on the accuracy and efficiency of the BE method based on $\mathscr{H}$–matrices is investigated in figures 6–8. The value of the threshold ε is varied logarithmically between 10^{-1} and 10^{-4}. It is clearly illustrated in figure 6 that ε should be smaller than 10^{-2} in order to obtain reliable results. The accuracy of the proposed methodology is also assessed in figure 7, which shows the relative error $||\hat{K}^{\mathrm{s}}_{zz,\mathscr{H}}(a_0) - \hat{K}^{\mathrm{s}}_{zz,\mathrm{c}}(a_0)||/||\hat{K}^{\mathrm{s}}_{zz,\mathrm{c}}(a_0)||$, where $\hat{K}^{\mathrm{s}}_{zz,\mathscr{H}}(a_0)$ and $\hat{K}^{\mathrm{s}}_{zz,\mathrm{c}}(a_0)$ represent the vertical soil impedance computed with the hierarchical and the classical BE method, respectively. The relative error considerably decreases for reduced values of ε. Furthermore, a decrease of almost one order of magnitude is observed for

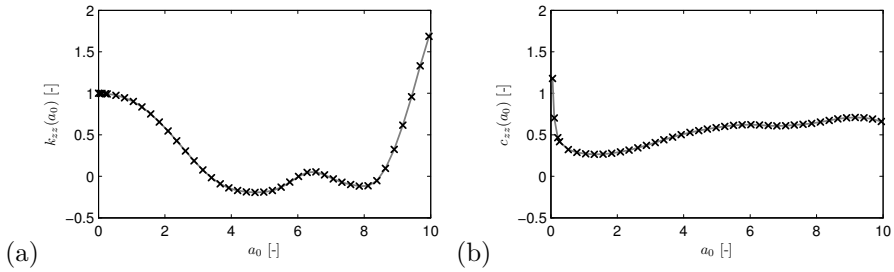

Figure 5: (a) Dimensionless stiffness coefficient $k_{zz}(a_0)$ and (b) damping coefficient $c_{zz}(a_0)$ of a massless rigid square surface foundation on a layered halfspace in function of the dimensionless frequency a_0. The solution obtained with the hierarchical BE method (grey line) is compared to the solution obtained with the classical BE method (black crosses).

increasing dimensionless frequencies in case $\varepsilon = 10^{-1}$ and $\varepsilon = 10^{-2}$, while the relative error is less dependent on the frequency for the other cases. The RAM memory usage with respect to the classical BE method is shown in figure 8. As expected, the efficiency decreases for reduced values of ε, as well as for an increasing dimensionless frequency a_0. Such trends have also been observed in hierarchical BE methods for anisotropic elastodynamic problems [19, 20]. Figures 6–8 clearly indicate that the overall computational precision and the RAM memory usage are strongly determined by the value of the threshold ε. A trade–off between accuracy and efficiency should hence be made when applying the proposed methodology.

The soil response due to a unit vertical rigid body translation $\boldsymbol{\psi}_{zz}$ of the foundation is shown in figures 9a and 9b at dimensionless frequencies $a_0 = 5$ and $a_0 = 10$, respectively; the classical and hierarchical BE approach yield exactly the same result. A relatively low frequency range is considered in this example, as the classical BE method is not well suited to provide accurate reference results at high frequencies within reasonable computation times. The BE method based on $\mathscr{H}$–matrices, however, is able to model high frequent wave propagation in a layered halfspace. The radiated wavefield at the surface of the soil is shown in figure 9c at a relatively high dimensionless frequency $a_0 = 50$. A BE mesh consisting of 100×100 equally sized elements is used for this calculation, providing six elements per shear wavelength $\lambda_s = C_s/f = 2\pi B/a_0$. The propagation of wave fronts parallel to the foundation edges can clearly be observed.

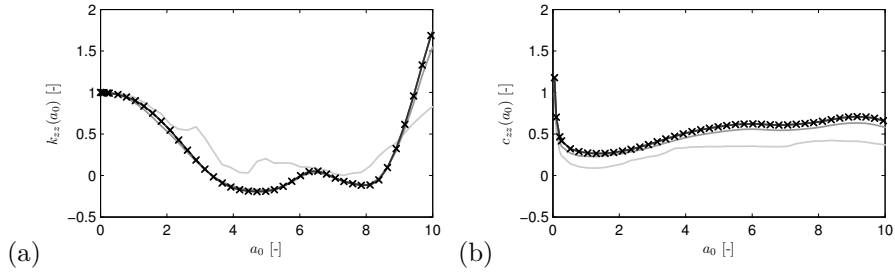

Figure 6: (a) Dimensionless stiffness coefficient $k_{zz}(a_0)$ and (b) damping coefficient $c_{zz}(a_0)$ of a massless rigid square surface foundation on a layered halfspace in function of the dimensionless frequency a_0. The solution obtained with the hierarchical BE method (solid lines) for the threshold ε used in the ACA algorithm varying from 10^{-1} (light grey line) to 10^{-4} (dark grey line) is compared to the solution obtained with the classical BE method (black crosses).

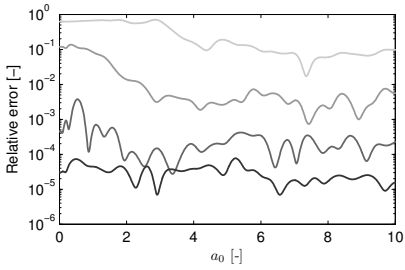

Figure 7: Relative error $||\hat{K}^{\mathrm{s}}_{zz,\mathscr{H}}(a_0) - \hat{K}^{\mathrm{s}}_{zz,\mathrm{c}}(a_0)||/||\hat{K}^{\mathrm{s}}_{zz,\mathrm{c}}(a_0)||$ in function of the dimensionless frequency a_0, for the threshold ε used in the ACA algorithm varying from 10^{-1} (light grey line) to 10^{-4} (dark grey line).

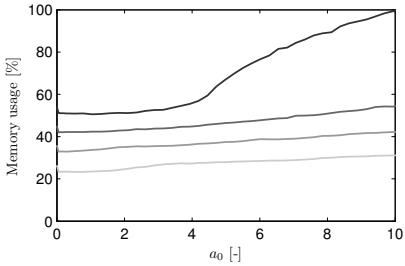

Figure 8: Memory usage with respect to the classical BE method in function of the dimensionless frequency a_0, for the threshold ε used in the ACA algorithm varying from 10^{-1} (light grey line) to 10^{-4} (dark grey line).

In order to demonstrate the effectiveness of the BE method based on $\mathscr{H}$–matrices, the vertical soil impedance $\hat{K}^{\mathrm{s}}_{zz}(\omega)$ is reconsidered at a particular dimensionless frequency $a_0 = \pi$, for an increasing number of boundary elements. As an element collocation scheme is applied, the number of degrees of freedom equals three times the number of elements. The stiffness and damping coefficients $k_{zz}(a_0 = \pi)$ and $c_{zz}(a_0 = \pi)$ are shown as a function of the number of degrees of freedom in figure 10. The results of the hierarchical and classical BE method both converge to a value $\hat{K}^{\mathrm{s}}_{zz} = K^{\mathrm{s}}_{zz0}\,(0.077 + ia_0 0.416)$ N/m and are in good correspondence with each other. The application of the classical BE method is, however, limited to a model size of 43200 degrees of freedom, as the storage of the complex floating point entries of $\widehat{\mathbf{U}}(\omega)$ in double precision requires $2 \times N^2_{\mathrm{DOF}} \times 8\,\mathrm{bytes} = 27.8\,\mathrm{GB}$ of RAM memory, which is the limit of the hardware employed for the calculations presented in this paper. Figure 11a compares the memory required to store the BE matrices $\widehat{\mathbf{U}}(\omega)$ and $\widehat{\mathbf{U}}_{\mathscr{H}}(\omega)$ on a double logarithmic plot, in which the slope of the curve corresponds to the power relating the number of degrees of freedom and the required memory. As expected, a quadratic trend $\mathcal{O}(N^2_{\mathrm{DOF}})$ can be observed for the classical BE method. For the hierarchical BE method, however, the memory requirement is of the order $\mathcal{O}(N_{\mathrm{DOF}} \log^3_{10} N_{\mathrm{DOF}})$, allowing for the extension of the model size up to 399675 degrees of freedom with 28 GB of RAM memory available. Applying the recompression procedure outlined in subsection 3.1 even allows to consider up to 468075 degrees of freedom with the same amount of memory. In comparison, 2380 GB and 3265 GB of RAM would, respectively, be required in order to handle such models with the classical BE method. Figure 11b shows the CPU time required to calculate $\hat{K}^{\mathrm{s}}_{zz}(a_0 = \pi)$, including both the time to assemble the matrices $\widehat{\mathbf{U}}(\omega)$ or $\widehat{\mathbf{U}}_{\mathscr{H}}(\omega)$ and to solve equation (3) or (3),

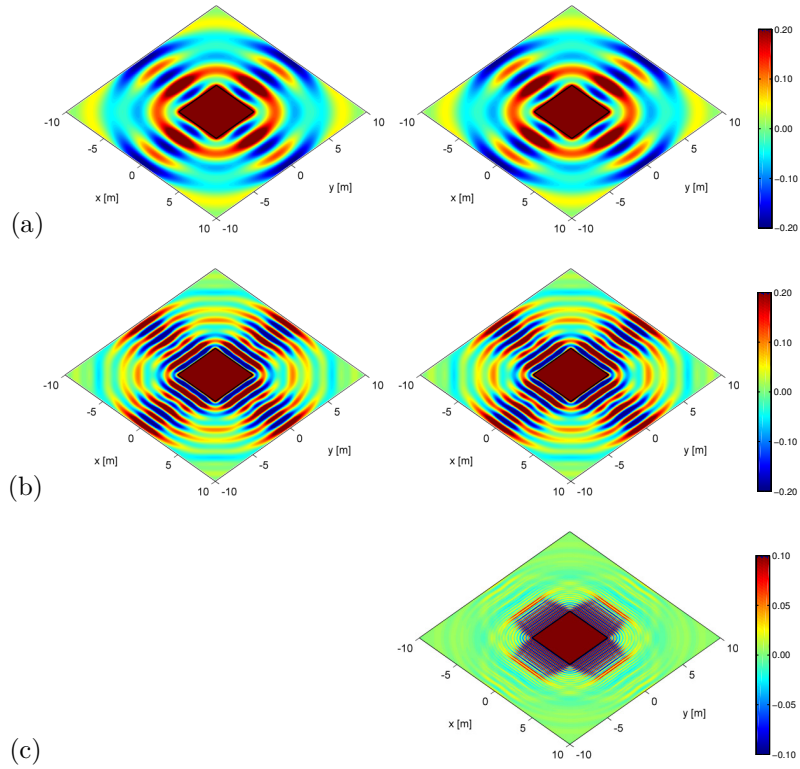

Figure 9: Real part of the vertical displacement $\hat{u}_z(\mathbf{x}, \omega)$ due to an imposed unit vertical rigid body translation $\boldsymbol{\psi}_{zz}$ of a massless rigid square surface foundation on a layered halfspace at a dimensionless frequency (a) $a_0 = 5$, (b) $a_0 = 10$ and (c) $a_0 = 50$, obtained with the classical (left) and the hierarchical (right) BE method. The classical BE method is not well suited to provide accurate reference results for (c) within reasonable computation times.

respectively. For relatively small models ($\mathcal{O}(10^3)$), the classical BE method turns out to be a little faster, but the hierarchical approach is considerably more efficient from a moderate model size on.

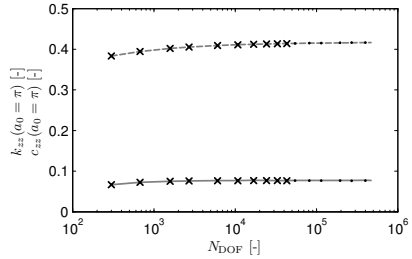

Figure 10: Dimensionless stiffness coefficient $k_{zz}(a_0 = \pi)$ (solid line) and damping coefficient $c_{zz}(a_0 = \pi)$ (dashed line) of a massless rigid square surface foundation on a layered halfspace for an increasing number of degrees of freedom. The solution obtained with the hierarchical BE method with (grey lines) and without recompression (black dots) is compared to the solution obtained with the classical BE method (black crosses).

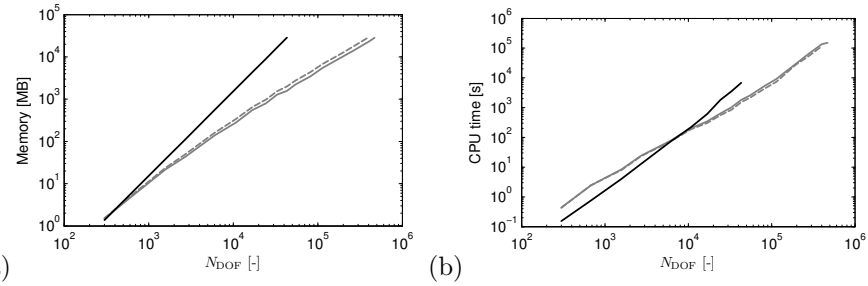

Figure 11: (a) RAM memory and (b) total CPU time required for an increasing number of degrees of freedom with the classical (black lines) and the hierarchical BE method with (solid grey lines) and without (dashed grey lines) recompression.

The contribution of the assembly and solution time to the total CPU time is further investigated in figure 12 (in case no recompression is applied). For the classical BE method, the assembly time shows a quadratic trend. The solution time of the direct solver, however, increases in a cubic way. The time required to solve equation (3) will therefore dominate the total solution

time of the classical BE method for large models. Figure 12 also shows that the contribution of the solution time is negligible compared to the assembly time for the hierarchical BE method. No effort has therefore been made to incorporate a preconditioner in the iterative GMRES solver, such as an $\mathscr{H}$–LU preconditioner proposed in [50], as speeding up the iterative solver will not result in a significant reduction of the total CPU time required in the hierarchical BE method.

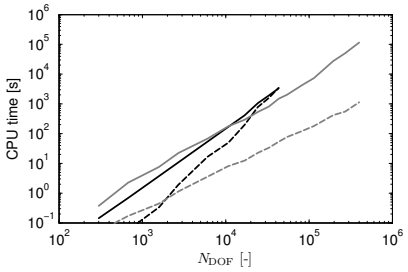

Figure 12: CPU time required to assemble the matrices $\widehat{\mathbf{U}}(\omega)$ or $\widehat{\mathbf{U}}_{\mathscr{H}}(\omega)$ (solid lines) and to solve equation (3) or (3) (dashed lines) with the classical (black) and the hierarchical (grey) BE method.

4.3 Diffraction of a vertically incident plane P–wave by a semi–spherical cavity

In this subsection, the diffraction of a vertically incident plane P–wave by a semi-spherical cavity with radius a, representing a canyon, is investigated (figure 13). For validation purposes [51–54], a homogeneous halfspace is considered, although the diffraction in a layered halfspace can be easily treated as well. The halfspace has a shear wave velocity $C_{\mathrm{s}} = 150\,\mathrm{m/s}$, a dilatational wave velocity $C_{\mathrm{p}} = 259.8\,\mathrm{m/s}$, a density $\rho = 1800\,\mathrm{kg/m^3}$ and a material damping ratio $\beta_{\mathrm{s}} = \beta_{\mathrm{p}} = 0.0025$ in both deviatoric and volumetric deformation. The P–wave is characterized by a dimensionless frequency $\bar{f}_{\mathrm{p}} = k_{\mathrm{p}}a/\pi = 2a/\lambda_{\mathrm{p}}$, where k_{p} and λ_{p} denote the dilatational wavenumber and wavelength, respectively. A BE mesh consisting of 19021 eight node quadrilateral boundary elements with nodal collocation is used to discretize the canyon. The same values for the parameters η, $N_{\min}$, ε and the tolerance in the GMRES solver as specified in subsection 4.1 are used in the BE method based on $\mathscr{H}$–matrices.

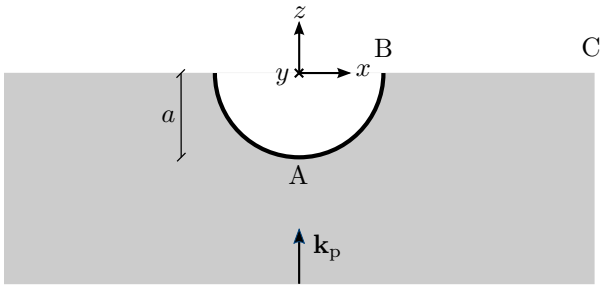

Figure 13: Semi–spherical canyon subjected to a vertically incident plane P–wave.

A subdomain formulation [55, 56] is employed, where the total wavefield is decomposed into an incident and scattered wavefield. Figure 14 and 15 show the modulus of the resulting horizontal and vertical displacements $\hat{u}_x(\mathbf{x}, \omega)$ and $\hat{u}_z(\mathbf{x}, \omega)$ along the path ABC (indicated on figure 13) as a function of the normalized horizontal distance x/a, at dimensionless frequencies $\bar{f}_\mathrm{p} = 1/4$ and $\bar{f}_\mathrm{p} = 1/2$, respectively. The displacements would be vertical with an amplitude of 2 m/Hz in the absence of the cavity. It is clearly illustrated in these figures that a mode conversion takes place due to the presence of the cavity, however, resulting in significant horizontal displacements; the latter are zero at $x/a = 0$ due to the symmetry of the problem. The results obtained with the BE method based on $\mathscr{H}$–matrices are compared to the solution of Sohrabi–Bidar et al. [51] and are in excellent agreement. Similar results have been obtained, amongst others, by Sánchez–Sesma [52], Reinoso et al. [53] and Chaillat et al. [54].

5 Application: through–soil coupling of closely spaced structures

It has been illustrated in the previous sections that the use of $\mathscr{H}$–matrices in the BE method combined with Green's functions for a horizontally layered halfspace results in a significant reduction of memory and CPU requirements, allowing to perform large scale BE computations. Furthermore, the method is also suited to tackle visco–elastodynamic problems, as illustrated in subsections 4.2 and 4.3. The proposed methodology hence offers perspectives to model larger problems involving wave propagation in a layered halfspace, with possible applications in seismology, railway induced vibrations and dynamic soil–structure interaction.

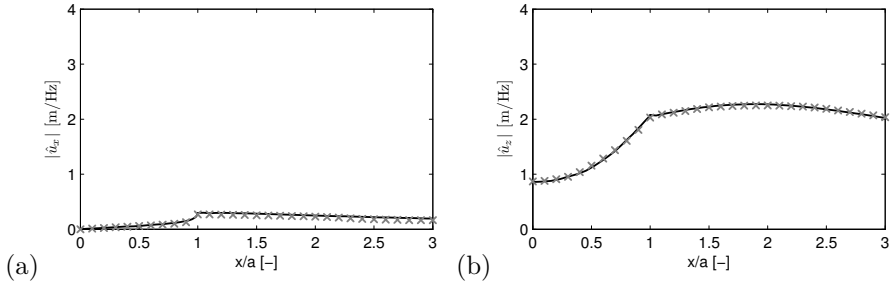

Figure 14: Modulus of the (a) horizontal and (b) vertical displacement $\hat{u}_x(\mathbf{x}, \omega)$ and $\hat{u}_z(\mathbf{x}, \omega)$ along the path ABC (indicated on figure 13) due to a vertically incident plane P–wave at a dimensionless frequency $\bar{f}_\mathrm{p} = 1/4$. The solution obtained with the hierarchical BE method (black lines) is compared to the solution of Sohrabi–Bidar et al. [51] (grey crosses).

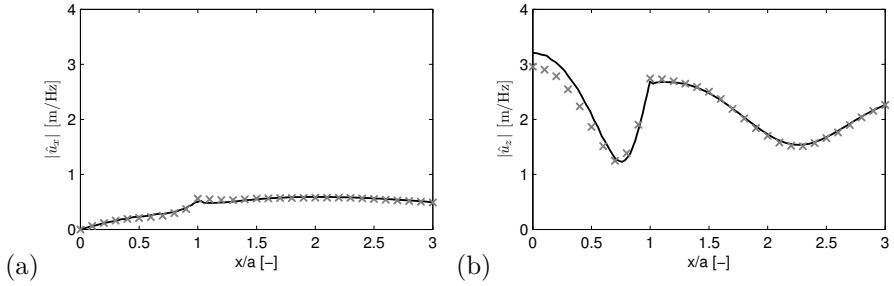

Figure 15: Modulus of the (a) horizontal and (b) vertical displacement $\hat{u}_x(\mathbf{x}, \omega)$ and $\hat{u}_z(\mathbf{x}, \omega)$ along the path ABC (indicated on figure 13) due to a vertically incident plane P–wave at a dimensionless frequency $\bar{f}_\mathrm{p} = 1/2$. The solution obtained with the hierarchical BE method (black lines) is compared to the solution of Sohrabi–Bidar et al. [51] (grey crosses).

One field of application is the numerical prediction of railway induced vibrations in an urban environment. While the interaction between the soil and multiple structures in dense urban areas subjected to seismic excitation has already been examined in a low frequency range ($< 10\,\mathrm{Hz}$) [57–59], the numerical prediction of railway induced vibrations involves much higher frequencies up to 80 Hz [60]. As the number of boundary elements strongly increases with frequency, classical BE models only allow to take into account through–soil coupling of very few structures and are unable to rigorously model wave propagation in dense urban areas characterized by many closely spaced structures. It is expected that structures close to the source of excitation will shield the surrounding buildings from the incident waves. In this section, the applicability of the proposed BE method based on $\mathscr{H}$–matrices is illustrated by means of a case study where the dynamic interaction between multiple buildings is investigated.

5.1 Model description

The case study considers a set of 12 identical masonry buildings resting on a layered halfspace (figure 16a). The same layered soil profile as introduced in subsection 4.2 is used. Figure 17 shows the frequency–wavenumber spectrum of the vertical free field velocity $i\omega\tilde{u}_z(C_r, \omega)$ due to vertical harmonic excitation at the surface of the layered halfspace, presented in terms of the phase velocity $C_r = \omega/k_r$ instead of the wavenumber k_r. Peaks in the spectrum of $i\omega\tilde{u}_z(C_r, \omega)$ correspond to surface waves of the layered halfspace. The Rayleigh wave dispersion curves are superimposed on figure 17; four modes with associated cut-on frequencies exist in the frequency range considered. As the soil stiffness gradually increases with depth, the spectrum of the vertical free field velocity is dominated by the fundamental Rayleigh wave of the layered halfspace.

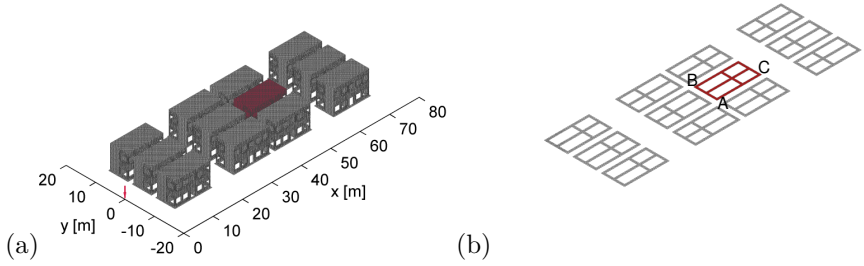

Figure 16: (a) Finite element and (b) boundary element mesh of the set of 12 masonry buildings.

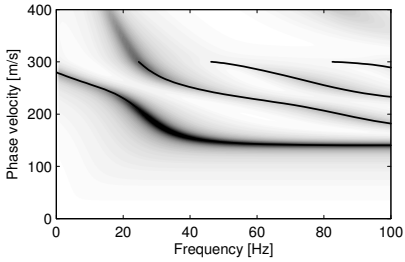

Figure 17: Frequency–wavenumber spectrum of the vertical free field velocity $i\omega\tilde{u}_z(C_r, \omega)$ due to vertical harmonic excitation at the surface of the layered halfspace. Superimposed are the Rayleigh wave dispersion curves of the first four modes.

Each masonry building has dimensions 12 m×6 m×8 m and has two stories, each subdivided into four rooms [61]. The interior and exterior walls have a thickness $t_{\mathrm{w}} = 0.10\,\mathrm{m}$ and consist of clay brick masonry. The floors are concrete slabs with a thickness $t_{\mathrm{fl}} = 0.20\,\mathrm{m}$. All floors are simply supported, corresponding to hinged joints at the slab edges. The structure is founded on a concrete strip foundation with a width $w_{\mathrm{f}} = 0.60\,\mathrm{m}$ and a thickness $t_{\mathrm{f}} = 0.20\,\mathrm{m}$. The buildings are modelled with the finite element method. The strip foundation, the walls and the floors are modelled by means of shell elements, using isotropic properties for the foundation and the floors and orthotropic properties for the masonry walls. The lintels above the door and the windows are modelled by means of beam elements. A detailed description of the single building model can be found in [61].

The 12 buildings are positioned in a symmetric layout with respect to the x–axis, with a separation distance of 2 m in the y–direction between the buildings. The front edges of four subsets of three buildings are aligned at $x = 6\,\mathrm{m}$, $x = 26\,\mathrm{m}$, $x = 40\,\mathrm{m}$ and $x = 60\,\mathrm{m}$, respectively.

The numerical prediction of railway induced vibrations in the built environment is a dynamic soil–structure interaction problem, coupling the source (railway track) and the receivers (buildings) through wave propagation in the soil [60,62]. In this case study, however, only the soil–structure interaction problem at the receiver side is addressed. The response of the buildings to an incident wavefield generated by a unit vertical point load acting on the surface of the layered halfspace at the origin of the coordinate system is therefore investigated, instead of an incident wavefield due to the passage of a train.

5.2 Coupled FE–BE model

A coupled FE–BE methodology in the frequency domain accounting for dynamic soil–structure interaction, based on a subdomain formulation [55, 56], is employed to calculate the response of the buildings to the incident wavefield. If N structures are considered, a weak variational formulation of the equilibrium of structure j ($j = 1, \ldots, N$) results in the following set of coupled FE–BE equations:

$$\left[\mathbf{K}_j + i\omega\mathbf{C}_j - \omega^2\mathbf{M}_j\right] \underline{\hat{\mathbf{u}}}_j(\omega) + \sum_{k=1}^{N} \hat{\mathbf{K}}^{\mathrm{s}}_{jk}(\omega)\underline{\hat{\mathbf{u}}}_k(\omega) = \underline{\hat{\mathbf{f}}}^{\mathrm{s}}_j(\omega)$$

$$\text{for} \quad j = 1 \ldots N \quad (14)$$

where $\underline{\hat{\mathbf{u}}}_j(\omega)$ collects the nodal degrees of freedom of structure j, while $\mathbf{K}_j$, $\mathbf{C}_j$ and $\mathbf{M}_j$ are the stiffness, damping and mass matrix of this structure. Rayleigh damping is assumed for the damping matrix $\mathbf{C}_j$ [61]. The diagonal blocks ($k = j$) of the dynamic soil stiffness matrix $\hat{\mathbf{K}}^{\mathrm{s}}_{jk}(\omega)$ represent dynamic soil–structure interaction for structure j, while the off–diagonal blocks ($k \neq j$) account for through–soil coupling of structures j and k. The force vector $\underline{\hat{\mathbf{f}}}^{\mathrm{s}}_j(\omega)$ denotes the dynamic soil–structure interaction forces at the soil–structure interface Σ_j due to the incident wavefield. A Craig-Bampton substructuring technique is furthermore used for every individual building, decomposing each structure j into its foundation and superstructure.

The hierarchical BE method outlined in section 3 is employed to evaluate the dynamic soil stiffness matrices $\hat{\mathbf{K}}^{\mathrm{s}}_{jk}(\omega)$ and the force vectors $\underline{\hat{\mathbf{f}}}^{\mathrm{s}}_j(\omega)$ arising from the incident wavefield. The free surface and the soil layers do not need to be discretized as Green's functions of a layered halfspace are employed. The finite elements of the foundations are coupled to a conforming boundary element mesh for the surrounding soil (figure 16b) and a nodal collocation scheme is used to facilitate the FE–BE coupling. As a nodal collocation scheme is used, the hierarchical clustering is based on the nodes rather than on the element centers. The same values for the parameters η, $N_{\min}$, ε and the tolerance in the GMRES solver as specified in subsection 4.1 are used in the BE method based on $\mathscr{H}$–matrices (where $N_{\min}$ indicates in this case a minimum number of nodes).

It also emphasized that a full 3D calculation is performed, without introducing additional assumptions concerning the lay–out of the buildings (i.e. no periodicity considerations are taken into account).

5.3 Numerical results

First, the response of the set of 12 buildings to an incident wavefield generated by a unit vertical harmonic point load at 10 Hz is considered. At this frequency, only one Rayleigh wave exists (figure 17); the Rayleigh wavelength in the soil equals $\lambda_{\mathrm{R}}(f) = C_{\mathrm{R}}(f)/f = 25.7\,\mathrm{m}$. The incident wavefield, characterized by cylindrical wave fronts, is shown in figure 18a. Figure 18b shows the wavefield in the soil in case the presence of all 12 buildings is simultaneously taken into account. As the Rayleigh wavelength is larger than the dimensions of the strip foundations, the wavefield remains nearly cylindrical.

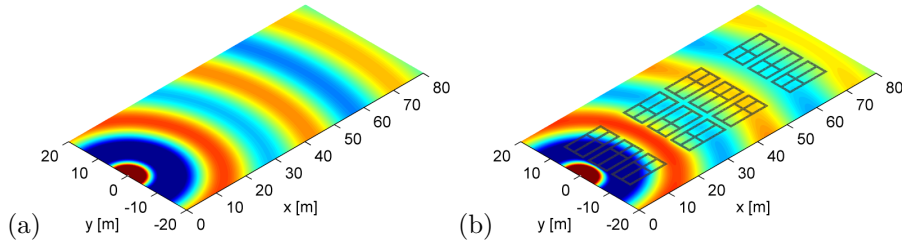

Figure 18: Real part of the vertical soil displacement $\hat{u}_z(\mathbf{x},\omega)$ at 10 Hz (a) without and (b) with accounting for the presence of the buildings.

The influence of through–soil coupling on the structural response is illustrated in figure 19. Figure 19a shows the vertical displacement $\hat{u}_z(\mathbf{x},\omega)$ of all buildings, in case the presence of the surrounding buildings is neglected for each building. This is obtained by solving equation (1) N times, in which the soil stiffness matrices $\hat{\mathbf{K}}^{\mathrm{s}}_{jk}(\omega)$ are not considered for $k \neq j$. Figure 19b illustrates the structural response in case the presence of all 12 buildings is simultaneously taken into account. Comparison of figures 19a and 19b indicates that the structural response is nearly identical for the three buildings closest to the source, while the response of the buildings further away from the source turns out to be more affected by the presence of the surrounding buildings.

The influence of through–soil coupling on the structural response is investigated in more detail for one particular building, which is indicated in red on figure 16. Figure 20 compares the modulus and phase of the vertical displacement $\hat{u}_z(\mathbf{x},\omega)$ along the front wall–foundation edge AB. The response is not symmetrical due to the presence of doors and windows in the individual masonry buildings. While the variation of the displacements along this edge is similar in both cases, the amplitude is slightly reduced if through–soil coupling is accounted for. This indicates that the buildings closer to the source shield the considered building from the incident wavefield. Furthermore, an almost constant phase

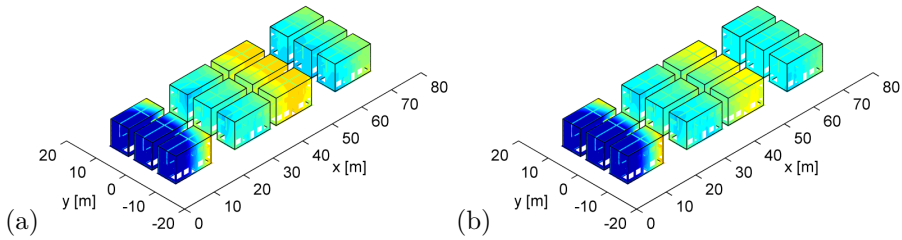

Figure 19: Real part of the vertical structural displacement $\hat{u}_z(\mathbf{x}, \omega)$ at 10 Hz (a) without and (b) with accounting for through–soil coupling of the surrounding buildings.

shift of 0.65 rad is introduced along the edge AB, as the Rayleigh wave fronts are slightly shifted due the presence of the buildings. Similarly, figure 21 compares the modulus and phase of the vertical displacement $\hat{u}_z(\mathbf{x}, \omega)$ along the side wall–foundation edge AC. The variation of the displacements along this edge is similar in both cases; a slight amplitude reduction and a phase shift of 0.65 rad can be observed here as well.

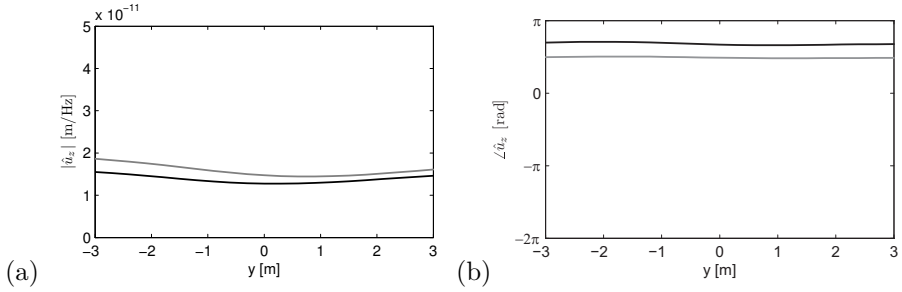

Figure 20: (a) Modulus and (b) phase of the vertical displacement $\hat{u}_z(\mathbf{x}, \omega)$ along the front wall–foundation edge AB at 10 Hz without (grey lines) and with (black lines) accounting for through–soil coupling of the surrounding buildings.

Second, the response of the set of 12 buildings to an incident wavefield generated by a unit vertical harmonic point load at a frequency of 50 Hz is considered. Although three modes exist at this frequency, the spectrum of the vertical free field velocity is still dominated by the fundamental Rayleigh wave (figure 17); the corresponding Rayleigh wavelength in the soil equals $\lambda_R(f) = C_R(f)/f = 2.9$ m. The incident wavefield, characterized by cylindrical wave fronts, is shown

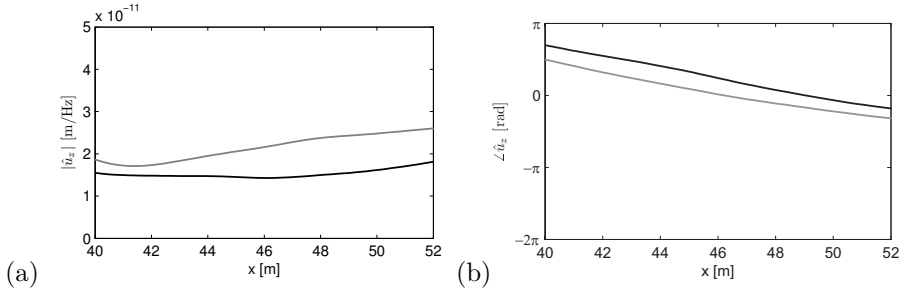

(a) (b)

Figure 21: (a) Modulus and (b) phase of the vertical displacement $\hat{u}_z(\mathbf{x}, \omega)$ along the side wall–foundation edge AC at 10 Hz without (grey lines) and with (black lines) accounting for through–soil coupling of the surrounding buildings.

in figure 22a. The dynamic interaction between the buildings and the halfspace significantly changes the wavefield (figure 22b), as the wavelength in the soil has the same order of magnitude as the dimensions of the strip foundations.

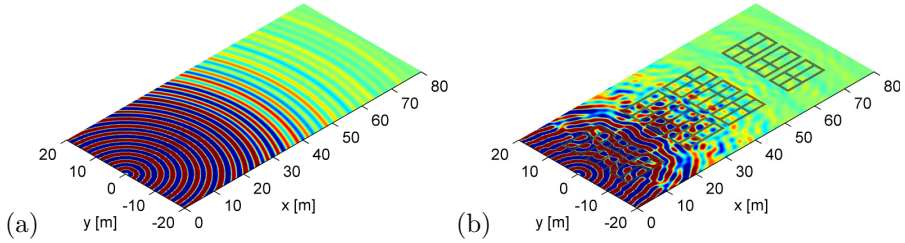

(a) (b)

Figure 22: Real part of the vertical soil displacement $\hat{u}_z(\mathbf{x}, \omega)$ at 50 Hz (a) without and (b) with accounting for the presence of the buildings.

The influence of through–soil coupling on the structural response is illustrated in figure 23. Figure 23a shows the vertical displacement $\hat{u}_z(\mathbf{x}, \omega)$ of all buildings, in case the presence of the surrounding buildings is neglected for each building, while figure 23b illustrates the structural response in case the presence of all 12 buildings is simultaneously taken into account. As in figure 18, the response of the three buildings closest to the source remains almost unaffected. The response of the other buildings, however, is considerably altered by the presence of the surrounding buildings.

The influence of through–soil coupling on the structural response is investigated in more detail for the same building as discussed before. Figures 24 and 25

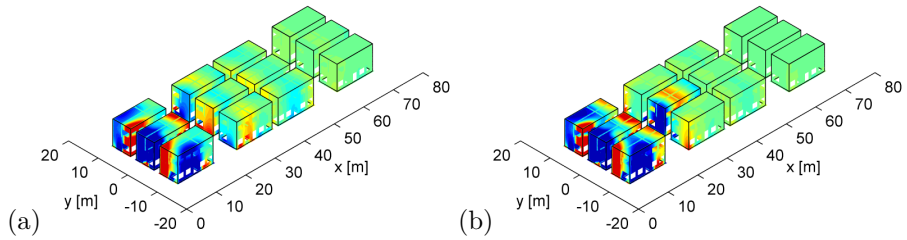

Figure 23: Real part of the vertical structural displacement $\hat{u}_z(\mathbf{x}, \omega)$ at 50 Hz (a) without and (b) with accounting for through–soil coupling of the surrounding buildings.

compare the modulus and phase of the vertical displacement $\hat{u}_z(\mathbf{x}, \omega)$ along the front wall–foundation edge AB and side wall–foundation edge AC, respectively. It is clearly illustrated that the variation of vertical displacements along both edges strongly differs when through–soil coupling is accounted for.

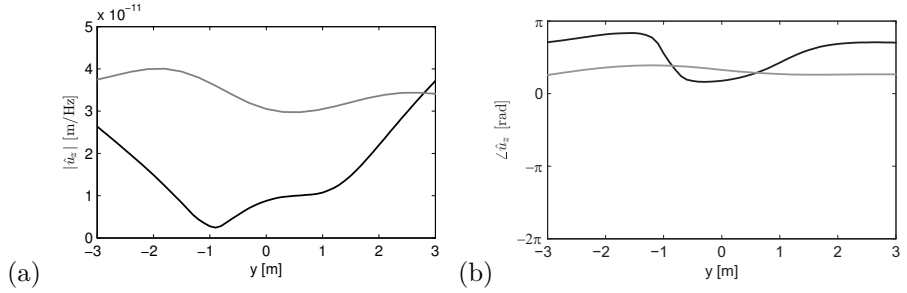

Figure 24: (a) Modulus and (b) phase of the vertical displacement $\hat{u}_z(\mathbf{x}, \omega)$ along the front wall–foundation edge AB at 50 Hz without (grey lines) and with (black lines) accounting for through–soil coupling of the surrounding buildings.

This case study indicates that wave propagation in the soil and the structural response are considerably affected in an urban environment. At low frequencies, this predominantly results in a shielding effect, reducing the amplitudes of the displacements, without drastically altering the wavefield. At higher frequencies, however, the wavelength in the soil becomes comparable to the foundation dimensions and the dynamic interaction between the buildings and the halfspace significantly changes the wavefield. It should furthermore be emphasized that this case study could not have been investigated as efficiently

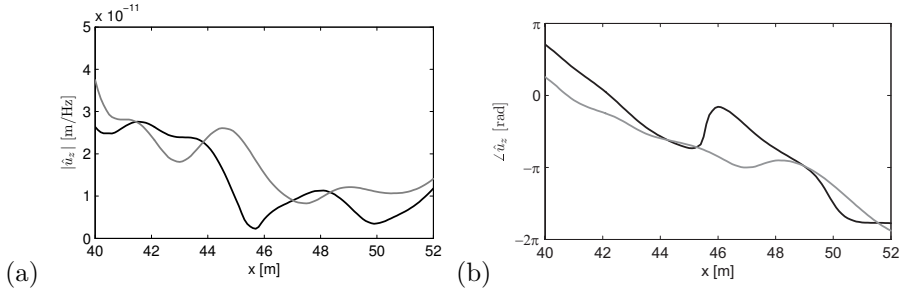

Figure 25: (a) Modulus and (b) phase of the vertical displacement $\hat{u}_z(\mathbf{x}, \omega)$ along the side wall–foundation edge AC at 50 Hz without (grey lines) and with (black lines) accounting for through–soil coupling of the surrounding buildings.

with existing BE formulations.

6 Conclusions

In this paper, the application of hierarchical matrices to boundary element methods based on Green's functions for a horizontally layered halfspace has been presented. The Green's functions are numerically computed by means of the direct stiffness method, as no closed form analytical expressions are available. Incorporating these Green's functions is advantageous, as there is no need to discretize the free surface and the layer interfaces. The ACA algorithm is used to compute low rank approximations of blocks corresponding to admissible cluster pairs, while an iterative method is employed to solve the resulting set of $\mathscr{H}$–BE equations.

The numerical implementation of the novel methodology has been validated and it has been demonstrated that although a compromise between accuracy and efficiency should be made, it is very efficient, very fast and sufficiently accurate. The method enables the fast evaluation of much larger boundary element models than before and is hence a valuable tool for researchers and engineers dealing with problems involving elastodynamic wave propagation in a stratified halfspace, providing the possibility to investigate complex problems in seismology and dynamic soil–structure interaction. The applicability of the method has clearly been illustrated by means of a case study that could not have been solved as efficiently with existing BE formulations. The dynamic

interaction between closely spaced structures was investigated and it was illustrated that through–soil coupling of buildings can significantly alter the structural response, especially at higher frequencies.

Acknowledgements

The first author is a doctoral fellow and the second author is a postdoctoral fellow of the Research Foundation Flanders (FWO). The financial support is gratefully acknowledged.

References

[1] J.-F. Semblat, A. Duval, P. Dangla, Seismic site effects in a deep alluvial basin: numerical analysis by the boundary element method, Computers and Geotechnics 29 (7) (2002) 573–585.

[2] G. Lombaert, G. Degrande, D. Clouteau, Numerical modelling of free field traffic induced vibrations, Soil Dynamics and Earthquake Engineering 19 (7) (2000) 473–488.

[3] D. Beskos, T. Krauthammer, I. Vardoulakis (Eds.), Dynamic soil-structure interaction, A.A. Balkema, 1984.

[4] V. Rokhlin, Rapid solution of integral equations of classical potential theory, Journal of Computational Physics 60 (1985) 187–207.

[5] W. Hackbusch, Z. Nowak, On the fast matrix multiplication in the boundary element method by panel clustering, Numerische Mathematik 54 (1989) 463–491.

[6] W. Hackbusch, A sparse matrix arithmetic based on $\mathscr{H}$-matrices. Part I: Introduction to $\mathscr{H}$-matrices, Computing 62 (2) (1999) 89–108.

[7] N. Nishimura, Fast multipole accelerated boundary integral equation methods, Applied Mechanics Reviews 22 (2002) 175–181.

[8] H. Fujiwara, The fast multipole method for solving integral equations of three-dimensional topography and basin problems, Geophysical Journal International 140 (1) (2000) 198–210.

[9] S. Chaillat, M. Bonnet, J.-F. Semblat, A new fast multi-domain BEM to model seismic wave propagation and amplification in 3D geological structures, Geophysical Journal International 177 (2009) 509–531.

[10] E. Grasso, S. Chaillat, M. Bonnet, J.-F. Semblat, Application of the multi-level time-harmonic fast multipole BEM to 3-D visco-elastodynamics, Engineering Analysis with Boundary Elements 36 (5) (2012) 744–758.

[11] S. Chaillat, M. Bonnet, Formulation and fast evaluation of the multipole expansions of the elastic half-space fundamental solutions, 8th European Solid Mechanics Conference, Graz, Austria (July 2012).

[12] S. Rjasanow, O. Steinbach, The Fast Solution of Boundary Integral Equations (Mathematical and Analytical Techniques with Applications to Engineering), Springer-Verlag New York, 2007.

[13] M. Bebendorf, Hierarchical Matrices: A Means to Efficiently Solve Elliptic Boundary Value Problems, 1st Edition, Springer Publishing Company, 2008.

[14] L. Banjai, W. Hackbusch, Hierarchical matrix techniques for low- and high-frequency Helmholtz problems, IMA Journal of Numerical Analysis 28 (1) (2008) 46–79.

[15] J. Ostrowski, Z. Andjelić, M. Bebendorf, B. Cranganu-Cretu, J. Smajić, Fast BEM-Solution of Laplace Problems with $\mathcal{H}$-Matrices and ACA, IEEE Transactions on Magnetics 42 (4) (2006) 627–630.

[16] M. Bebendorf, R. Grzhibovskis, Accelerating Galerkin BEM for linear elasticity using adaptive cross approximation, Mathematical Methods in the Applied Sciences 29 (14) (2006) 1721–1747.

[17] F. Maerten, Adaptive cross-approximation applied to the solution of system of equations and post-processing for 3D elastostatic problems using the boundary element method, Engineering Analysis with Boundary Elements 34 (5) (2010) 483–491.

[18] M. Messner, M. Schanz, An accelerated symmetric time-domain boundary element formulation for elasticity, Engineering Analysis with Boundary Elements 34 (11) (2010) 944–955.

[19] I. Benedetti, M. Aliabadi, A fast hierarchical dual boundary element method for three-dimensional elastodynamic crack problems, International Journal for Numerical Methods in Engineering 84 (9) (2010) 1038–1067.

[20] A. Milazzo, I. Benedetti, M. Aliabadi, Hierarchical fast BEM for anisotropic time-harmonic 3-D elastodynamics, Computers and Structures 96–97 (2012) 9–24.

[21] F. Rizzo, D. Shippy, An application of the correspondence principle of linear viscoelasticity theory, SIAM Journal on Applied Mathematics 21 (2) (1971) 321–330.

[22] L. Wheeler, E. Sternberg, Some theorems in classical elastodynamics, Archive for Rational Mechanics and Analysis 31 (1968) 51–90.

[23] J. Domínguez, Boundary elements in dynamics, Computational Mechanics Publications and Elsevier Applied Science, Southampton, United Kingdom, 1993.

[24] M. Bonnet, Boundary integral equation methods for solids and fluids, John Wiley and Sons, Chichester, United Kingdom, 1995.

[25] F. Rizzo, D. Shippy, M. Rezayat, A boundary integral equation method for radiation and scattering, International Journal for Numerical Methods in Engineering 21 (1985) 115–129.

[26] D. Aubry, D. Clouteau, A regularized boundary element method for stratified media, in: G. Cohen, L. Halpern, P. Joly (Eds.), Proceedings of the First International Conference on Mathematical and Numerical Aspects of Wave Propagation Phenomena, SIAM, Philadephia, Strasbourg, France, 1991, pp. 660–668.

[27] E. Kausel, J. Roësset, Stiffness matrices for layered soils, Bulletin of the Seismological Society of America 71 (6) (1981) 1743–1761.

[28] M. Schevenels, S. François, G. Degrande, EDT: An ElastoDynamics Toolbox for MATLAB, Computers & Geosciences 35 (8) (2009) 1752–1754.

[29] J. Talman, Numerical Fourier and Bessel transforms in logarithmic variables, Journal of Computational Physics 29 (1) (1978) 35–48.

[30] M. Schevenels, The impact of uncertain dynamic soil characteristics on the prediction of ground vibrations, Ph.D. thesis, Department of Civil Engineering, KU Leuven (2007).

[31] E. Pan, Static Green's functions in multilayered half spaces, Applied Mathematical Modelling 21 (8) (1997) 509–521.

[32] W. Thomson, Transmission of elastic waves through a stratified solid medium, Journal of Applied Physics 21 (1950) 89–93.

[33] N. Haskell, The dispersion of surface waves on multilayered media, Bulletin of the Seismological Society of America 73 (1953) 17–43.

[34] J. Dunkin, Computation of modal solutions in layered, elastic media at high frequencies, Bulletin of the Seismological Society of America 55 (2) (1965) 335–358.

[35] J. Luco, R. Apsel, On the Green's functions for a layered half-space. Part I, Bulletin of the Seismological Society of America 4 (1983) 909–929.

[36] R. Apsel, J. Luco, On the Green's functions for a layered half-space. Part II, Bulletin of the Seismological Society of America 73 (4) (1983) 931–951.

[37] E. Kausel, Fundamental solutions in elastodynamics: a compendium, Cambridge University Press, New York, 2006.

[38] L. Grasedyck, W. Hackbusch, Construction and arithmetics of $\mathscr{H}$-matrices, Computing 70 (2003) 295–334.

[39] S. Börm, L. Grasedyck, W. Hackbusch, Introduction to hierarchical matrices with applications, Engineering Analysis with Boundary Elements 27 (5) (2003) 405–422.

[40] A. George, Nested dissection of a regular finite element mesh, SIAM Journal on Numerical Analysis 10 (1973) 345–363.

[41] L. Grasedyck, R. Kriemann, S. Le Borne, Domain decomposition based $\mathscr{H}$-*LU* preconditioning, Numerische Mathematik 112 (4) (2009) 565–600.

[42] M. Bebendorf, Approximation of boundary element matrices, Numerische Mathematik 86 (2000) 565–589.

[43] M. Bebendorf, S. Rjasanow, Adaptive low–rank approximation of collocation matrices, Computing 70 (2003) 1–24.

[44] L. Grasedyck, Adaptive recompression of $\mathscr{H}$-matrices for BEM, Computing 74 (3) (2005) 205–223.

[45] M. Bebendorf, S. Kunis, Recompression techniques for adaptive cross approximation, Journal of Integral Equations and Applications 21 (3) (2009) 331–357.

[46] G. Golub, C. Van Loan, Matrix computations, 3rd Edition, John Hopkins University Press, Baltimore, MD, 1996.

[47] Y. Saad, M. Schultz, GMRES: a generalized minimal residual algorithm for solving nonsymmetric linear systems, SIAM Journal on Scientific and Statistical Computing 7 (3) (1986) 856–869.

[48] S. François, M. Schevenels, G. Degrande, BEMFUN: MATLAB toolbox for boundary elements in elastodynamics. Version 2.1 Build 16, User's guide BWM-2009-26, Department of Civil Engineering, KU Leuven (December 2009).

[49] G. Gazetas, Analysis of machine foundation vibrations: state of the art, Soil Dynamics and Earthquake Engineering 2 (1) (1983) 2–42.

[50] M. Bebendorf, Hierarchical *LU* decomposition based preconditioners for BEM, Computing 74 (2005) 225–247.

[51] A. Sohrabi-Bidar, M. Kamalian, M. K. Jafari, Time-domain BEM for three-dimensional site response analysis of topographic structures, International Journal for Numerical Methods in Engineering 79 (12) (2009) 1467–1492.

[52] F. Sánchez-Sesma, Diffraction of elastic waves by three-dimensional surface irregularities, Bulletin of the Seismological Society of America 73 (6) (1983) 1621–1636.

[53] E. Reinoso, L. Wrobel, H. Power, Three-dimensional scattering of seismic waves from topographical structures, Soil Dynamics and Earthquake Engineering 16 (1) (1997) 41–61.

[54] S. Chaillat, M. Bonnet, J.-F. Semblat, A multi-level fast multipole BEM for 3-D elastodynamics in the frequency domain, Computer Methods in Applied Mechanics and Engineering 197 (49–50) (2008) 4233–4249.

[55] D. Aubry, D. Clouteau, A subdomain approach to dynamic soil-structure interaction, in: V. Davidovici, R. Clough (Eds.), Recent advances in Earthquake Engineering and Structural Dynamics, Ouest Editions/AFPS, Nantes, 1992, pp. 251–272.

[56] D. Aubry, D. Clouteau, G. Bonnet, Modelling of wave propagation due to fixed or mobile dynamic sources, in: N. Chouw, G. Schmid (Eds.), Workshop Wave '94, Wave propagation and Reduction of Vibrations, Ruhr Universität Bochum, Germany, 1994, pp. 109–121.

[57] D. Clouteau, D. Aubry, Modification of the ground motion in dense urban areas, Journal of Computational Acoustics 9 (4) (2001) 1659–1675.

[58] M. Kham, J.-F. Semblat, P.-Y. Bard, P. Dangla, Seismic city-site interaction: main governing phemomena through simplified numerical models, Bulletin of the Seismological Society of America 96 (5) (2006) 1934–1951.

[59] G. Lombaert, D. Clouteau, The resonant multiple wave scattering in the seismic response of a city, Waves in Random and Complex Media 16 (3) (2006) 205–230.

[60] G. Lombaert, G. Degrande, J. Kogut, S. François, The experimental validation of a numerical model for the prediction of railway induced vibrations, Journal of Sound and Vibration 297 (3-5) (2006) 512–535.

[61] S. François, C. Karg, W. Haegeman, G. Degrande, A numerical model for foundation settlements due to deformation accumulation in granular soils under repeated small amplitude dynamic loading, International Journal for Numerical and Analytical Methods in Geomechanics 34 (3) (2010) 273–296.

[62] X. Sheng, C. Jones, D. Thompson, A theoretical model for ground vibration from trains generated by vertical track irregularities, Journal of Sound and Vibration 272 (3-5) (2004) 937–965.

Paper B

Coupled finite element – hierarchical boundary element methods for dynamic soil–structure interaction in the frequency domain

Published in the
International Journal for Numerical methods in Engineering 97(7) (2014) 505–530
http://dx.doi.org/10.1002/nme.4597

Coupled finite element – hierarchical boundary element methods for dynamic soil–structure interaction in the frequency domain

P. Coulier, S. François, G. Lombaert and G. Degrande
KU Leuven, Department of Civil Engineering,
Kasteelpark Arenberg 40, B-3001 Leuven, Belgium

Abstract

This paper discusses the coupling of finite element and fast boundary element methods for the solution of dynamic soil–structure interaction problems in the frequency domain. The application of hierarchical matrices in the boundary element formulation allows considering much larger problems compared to classical methods. Three coupling methodologies are presented and their computational performance is assessed through numerical examples. It is demonstrated that the use of hierarchical matrices renders a direct coupling approach the least efficient, as it requires the assembly of a dynamic soil stiffness matrix. Iterative solution procedures are presented as well, and it is shown that the application of such schemes to dynamic soil–structure interaction problems in the frequency domain is not trivial, as convergence can hardly be achieved if no relaxation procedure is incorporated. Aitken's Δ^2-method is therefore employed in sequential iterative schemes for the calculation of an optimized interface relaxation parameter, while a novel relaxation technique is proposed for parallel iterative algorithms. It is demonstrated that the efficiency of these algorithms strongly depends on the boundary conditions applied to each subdomain; the fastest convergence is observed if Neumann boundary conditions are imposed on the stiffest subdomain. The use of a dedicated solver for each subdomain hence results in a reduced computational effort. A monolithic coupling strategy, often used for the solution of fluid–structure interaction problems, is also introduced. The governing equations are simultaneously solved in this approach, while the assembly of a dynamic soil stiffness matrix is avoided.

Keywords: dynamic soil–structure interaction; FE–BE coupling; iterative methods; interface relaxation; $\mathscr{H}$–matrices; visco–elastodynamics.

1 Introduction

The numerical solution of three–dimensional (3D) dynamic soil–structure interaction (SSI) problems is a challenging task [1]. A domain decomposition approach is often introduced in numerical models, allowing for the application of different numerical techniques for the soil and the structure. The coupled finite element – boundary element (FE–BE) method is a well–known approach, in which the FE method allows to model structures with complex geometries while the BE method enables accounting for the radiation of waves in domains of (semi–)infinite extent. The complementarity of both methods can either be exploited in the time [2] or in the frequency domain [3].

In the past decades, a lot of attention has been paid to the development of efficient algorithms for the coupling of FE and BE models [4–6]. Direct and iterative coupling methodologies are generally distinguished. Furthermore, a distinction between conforming or non–conforming interface discretizations is made, where the coupling conditions are either imposed in a strong or weak sense. The latter allow for independent mesh sizes for each subdomain. FE–BE coupling algorithms for elastostatics are discussed, among others, by Elleithy et al. [7] and Margonari et al. [8], while Rüberg et al. [9] present an algorithm for time domain elastodynamics using non-conforming interfaces where the coupling conditions are incorporated in a weak sense by means of Lagrange multipliers.

The applicability of classical BE formulations to large scale problems is hindered by stringent memory and CPU requirements resulting from dense, fully populated unsymmetric matrices. This has led to the development of fast BE methods to improve the computational efficiency, including the fast multipole method (FMM) [10] and methods based on hierarchical matrices ($\mathscr{H}$–matrices) [11], which allow increasing the problem size compared to classical BE formulations. Recently, a $\mathscr{H}$-BE method for visco–elastodynamics in the frequency domain incorporating Green's functions for a horizontally layered halfspace has been presented [12]. These Green's functions are computed by means of the direct stiffness method [13, 14], as no closed form analytical expressions are available; their application avoids meshing of the free surface and layer interfaces to model wave propagation in a stratified medium.

The application of $\mathscr{H}$–matrices in BE formulations affects the efficiency of FE–BE coupling algorithms. This paper therefore aims to present suitable FE–$\mathscr{H}$-BE coupling procedures for the solution of dynamic SSI problems and to compare their computational performance. Throughout this paper, non–overlapping domains with conforming interface meshes are considered and all methods are formulated in the frequency domain. Three different FE–$\mathscr{H}$-BE

coupling methodologies are discussed. First, a classical direct coupling strategy is introduced, which requires the assembly of a dynamic soil stiffness matrix to obtain a global set of coupled equations. Next, iterative algorithms are presented; the governing equations are solved separately for each subdomain, while the boundary conditions at the soil–structure interface are updated until convergence is achieved. Sequential (Neumann–Dirichlet, Dirichlet–Neumann) as well as parallel (Neumann–Neumann, Dirichlet–Dirichlet) algorithms are considered. The application of iterative schemes to dynamic SSI problems in the frequency domain has only received limited attention in the literature so far [15], as it is not easy to achieve convergence with these algorithms [16]. Special attention is therefore paid to optimized interface relaxation techniques in order to ensure and/or speed up the convergence. For the sequential algorithms, Aitken's Δ^2–method [17] is employed, while a novel relaxation technique is presented for the parallel iterative schemes. Finally, a monolithic coupling approach is proposed, in which the governing equations of both subdomains are solved simultaneously, while the assembly of a dynamic soil stiffness matrix is avoided. Monolithic coupling schemes are often used to solve fluid–structure interaction problems [18, 19], but their application to dynamic SSI problems is not common.

The text is organized as follows. Section 2 briefly summarizes the governing equations of the FE and $\mathscr{H}$-BE method. Three FE–$\mathscr{H}$-BE coupling procedures are subsequently introduced in section 3. Numerical examples are investigated in section 4 in order to verify these coupling strategies and to assess their computational performance. This allows for the formulation of guidelines concerning the choice of an appropriate coupling strategy for a specific dynamic SSI problem. The applicability of coupled FE–$\mathscr{H}$-BE methods to large scale problems is finally demonstrated in section 5, where the wave impeding effect of a block of stiffened soil of finite length embedded in a halfspace is investigated.

2 Finite element and boundary element methods

The governing equations of the FE and $\mathscr{H}$-BE method are summarized in this section. It is assumed that finite elements are used to model the structural domain Ω_b, while boundary elements are employed to model wave propagation in the surrounding soil domain Ω_s. The domain Ω_b represents a generalized structure, comprising the actual structure and part of the soil domain, as depicted in figure 1. The soil–structure interface is denoted as Σ.

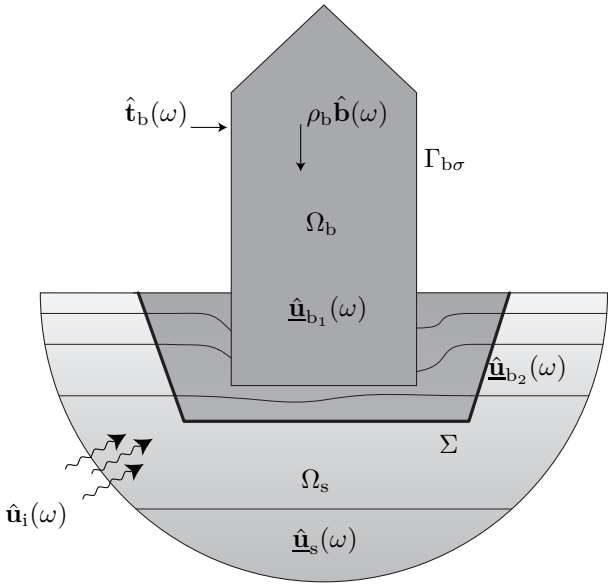

Figure 1: Geometry of the subdomains: structural domain Ω_b and soil domain Ω_s.

2.1 Finite element formulation

Finite element equations of the domain Ω_b are obtained by introducing a FE discretization in the weak variational formulation of the equilibrium equations of Ω_b (based on the principle of virtual work) and subsequently applying a Galerkin procedure. This provides the following set of equations [20]:

$$\left[\mathbf{K}_\mathrm{b} + i\omega\mathbf{C}_\mathrm{b} - \omega^2\mathbf{M}_\mathrm{b}\right]\underline{\hat{\mathbf{u}}}_\mathrm{b}(\omega) = \underline{\hat{\mathbf{f}}}_\mathrm{b}(\omega) + \underline{\hat{\mathbf{f}}}^\mathrm{s}_\mathrm{b}(\omega) \tag{1}$$

where a hat above a variable denotes its representation in the frequency domain. $\underline{\hat{\mathbf{u}}}_\mathrm{b}(\omega)$ collects the nodal degrees of freedom, while $\mathbf{K}_\mathrm{b}$, $\mathbf{C}_\mathrm{b}$, and $\mathbf{M}_\mathrm{b}$ are the stiffness, damping, and mass matrices, respectively. The bracketed term on the left hand side of equation (1) is identified as the dynamic stiffness matrix $\widehat{\mathbf{K}}_\mathrm{b}(\omega) = \mathbf{K}_\mathrm{b} + i\omega\mathbf{C}_\mathrm{b} - \omega^2\mathbf{M}_\mathrm{b}$ of the structure. The force vector $\underline{\hat{\mathbf{f}}}_\mathrm{b}(\omega)$ results from the body forces $\rho_\mathrm{b}\hat{\mathbf{b}}(\omega)$ on Ω_b and the tractions $\hat{\mathbf{t}}_\mathrm{b}(\omega)$ on the boundary $\Gamma_{\mathrm{b}\sigma}$, while $\underline{\hat{\mathbf{f}}}^\mathrm{s}_\mathrm{b}(\omega)$ is due to the incident wavefield $\hat{\mathbf{u}}_\mathrm{i}(\omega)$ on Σ (figure 1). Adequate solvers which account for the sparsity and symmetry of the system can be employed to solve equation (1).

2.2 Hierarchical boundary element formulation

The BE method is based on the discretization of the boundary Σ of a domain Ω_s with an appropriate number of boundary elements in order to numerically solve a boundary integral equation [21]. Throughout this paper, a regularized boundary integral equation is employed, in which the evaluation of Cauchy principal value (CPV) integrals is avoided [21–23]. The regularization procedure is based on the fact that the singularity of the static and dynamic Green's functions at the source point is similar. For an unbounded domain Ω_s, the displacements $\underline{\hat{\mathbf{u}}}(\omega)$ and tractions $\underline{\hat{\mathbf{t}}}(\omega)$ at the collocation points of the boundary Σ are related as follows:

$$\left[\widehat{\mathbf{T}}(\omega) + \mathbf{I}\right] \underline{\hat{\mathbf{u}}}(\omega) = \widehat{\mathbf{U}}(\omega)\underline{\hat{\mathbf{t}}}(\omega) \tag{2}$$

where $\widehat{\mathbf{T}}(\omega)$ and $\widehat{\mathbf{U}}(\omega)$ are BE collocation matrices, while $\mathbf{I}$ represents a unit matrix, corresponding to the integral free term in the boundary integral equation. The latter vanishes for a bounded domain. The computation of $\widehat{\mathbf{T}}(\omega)$ and $\widehat{\mathbf{U}}(\omega)$ requires integration of the Green's tractions and displacements over the boundary Σ, respectively. The integral representation theorem allows for the computation of the radiated wavefield in the soil $\underline{\hat{\mathbf{u}}}_s(\omega)$ from the displacements and tractions on Σ. In order to mitigate the occurrence of fictitious eigenfrequencies in the application of the BE method to external wave propagation problems, the Combined Helmholtz Integral Equation Formulation (CHIEF) proposed by Schenk [24] is employed.

The BE method leads to a reduction of the spatial problem dimension (i.e. surface instead of volume discretization), but the storage of the fully populated matrices $\widehat{\mathbf{T}}(\omega)$ and $\widehat{\mathbf{U}}(\omega)$ requires a quadratic amount of memory with respect to the number of degrees of freedom N_{DOF}, while a cubic amount of numerical operations is needed to solve the corresponding equation (2) by means of direct numerical solvers. The use of $\mathscr{H}$–matrices provides an elegant way to treat fully populated matrices with almost linear complexity [25], as they approximate the original matrices (with an arbitrary prescribed accuracy) by means of memory efficient representations. The reader is referred to the literature [11, 25, 26] for a comprehensive overview of fast BE methods based on $\mathscr{H}$–matrices. The construction of $\mathscr{H}$–matrices is based on the identification of admissible and inadmissible hierarchical cluster pairs in the BE mesh; the partially pivoted adaptive cross approximation (ACA) algorithm [27, 28] is employed to compute low rank approximations of matrix blocks corresponding to admissible cluster pairs. A major advantage of ACA is its purely algebraic character, avoiding the need for (semi–)analytical expressions of the Green's functions employed in the BE formulation, which enables its application to problems involving elastodynamic wave propagation in anisotropic [29] or

layered [12] media. All BE calculations in the remainder of this paper involve the application of $\mathscr{H}$–matrices.

Assembling hierarchical approximations $\widehat{\mathbf{T}}_{\mathscr{H}}(\omega)$ and $\widehat{\mathbf{U}}_{\mathscr{H}}(\omega)$ of the BE collocation matrices $\widehat{\mathbf{T}}(\omega)$ and $\widehat{\mathbf{U}}(\omega)$, respectively, allows replacing the BE equation (2) by:

$$\left[\widehat{\mathbf{T}}_{\mathscr{H}}(\omega) + \mathbf{I}\right] \underline{\hat{\mathbf{u}}}(\omega) = \widehat{\mathbf{U}}_{\mathscr{H}}(\omega)\underline{\hat{\mathbf{t}}}(\omega) \tag{3}$$

Equation (3) can be rewritten as:

$$\widehat{\mathbf{A}}_{\mathscr{H}}(\omega)\underline{\hat{\mathbf{x}}}(\omega) = \underline{\hat{\mathbf{b}}}(\omega) \tag{4}$$

where the vector of unknowns $\underline{\hat{\mathbf{x}}}(\omega)$ contains displacements, tractions or both, depending on whether a Neumann, Dirichlet or mixed Neumann–Dirichlet problem is considered. In order to solve equation (4), iterative Krylov subspace methods such as the generalized minimal residual method (GMRES) [30] are well suited. The matrix–vector multiplication forms the core of iterative solvers, and the complexity of this operation is only $\mathcal{O}(N_{\mathrm{DOF}} \log N_{\mathrm{DOF}})$ for $\mathscr{H}$–matrices [26]. A tolerance of 10^{-6} is adopted in the iterative solver for the relative residual norm $||\underline{\hat{\mathbf{b}}}(\omega) - \widehat{\mathbf{A}}_{\mathscr{H}}(\omega)\underline{\hat{\mathbf{x}}}(\omega)||/||\underline{\hat{\mathbf{b}}}(\omega)||$ in all numerical examples presented in this paper.

As will be clarified in section 3, equation (4) has to be solved for multiple right hand sides $\underline{\hat{\mathbf{b}}}(\omega)$ in FE–$\mathscr{H}$-BE coupling algorithms; the implementation of a suitable preconditioner is therefore desirable to reduce the computation time. A right preconditioner $\widehat{\mathbf{M}}(\omega)$ is used throughout this paper in order to lower the condition number of the coefficient matrix $\widehat{\mathbf{A}}_{\mathscr{H}}(\omega)$:

$$\widehat{\mathbf{A}}_{\mathscr{H}}(\omega)\widehat{\mathbf{M}}^{-1}(\omega)\underline{\hat{\mathbf{y}}}(\omega) = \underline{\hat{\mathbf{b}}}(\omega) \tag{5}$$

with $\widehat{\mathbf{M}}(\omega)\underline{\hat{\mathbf{x}}}(\omega) = \underline{\hat{\mathbf{y}}}(\omega)$. An example of an efficient preconditioner is the approximate $\mathscr{H}$–LU decomposition [31]; its computation requires, however, additional arithmetic operations. A much simpler strategy is applied in the present paper, following the approach recently adopted by Chaillat et al. [32] for the acceleration of the fast multipole method for elastodynamics. A block diagonal preconditioner $\widehat{\mathbf{M}}(\omega) = \mathrm{blkdiag}\left(\widehat{\mathbf{A}}_{\mathscr{H}}(\omega)\right)$ is employed, where the size of the diagonal blocks is determined by the lowest hierarchical cluster level. An inner GMRES solver with a moderate tolerance of 10^{-2} is applied to solve the preconditioning linear systems, resulting in a nested inner–outer iteration scheme. Furthermore, the flexible GMRES (FGMRES) algorithm [33] is employed for the outer iteration in order to avoid the explicit multiplication of $\widehat{\mathbf{M}}^{-1}(\omega)$ with the Krylov vectors. As $\widehat{\mathbf{M}}(\omega)$ is already computed and stored, the proposed approach is very cheap in terms of computational resources.

3 FE–$\mathscr{H}$-BE coupling procedures

Three procedures for the coupling of FE and $\mathscr{H}$-BE models are outlined in this section. The numerical verification and the assessment of the computational efficiency of these methods are subsequently addressed in section 4.

3.1 Direct FE–$\mathscr{H}$-BE coupling

In a classical direct coupling strategy [34], the governing equations of the FE and BE subdomain are straightforwardly combined, accounting for continuity of displacements and equilibrium of tractions at the soil–structure interface Σ. This results in a global coupled system of equations:

$$\left(\begin{bmatrix} \widehat{\mathbf{K}}_{\mathrm{b}_1\mathrm{b}_1}(\omega) & \widehat{\mathbf{K}}_{\mathrm{b}_1\mathrm{b}_2}(\omega) \\ \widehat{\mathbf{K}}_{\mathrm{b}_2\mathrm{b}_1}(\omega) & \widehat{\mathbf{K}}_{\mathrm{b}_2\mathrm{b}_2}(\omega) \end{bmatrix} + \begin{bmatrix} \mathbf{0} & \mathbf{0} \\ \mathbf{0} & \widehat{\mathbf{K}}^{\mathrm{s}}_{\mathrm{b}_2\mathrm{b}_2}(\omega) \end{bmatrix} \right) \begin{Bmatrix} \underline{\hat{\mathbf{u}}}_{\mathrm{b}_1}(\omega) \\ \underline{\hat{\mathbf{u}}}_{\mathrm{b}_2}(\omega) \end{Bmatrix} = \begin{Bmatrix} \underline{\hat{\mathbf{f}}}_{\mathrm{b}_1}(\omega) \\ \underline{\hat{\mathbf{f}}}_{\mathrm{b}_2}(\omega) \end{Bmatrix} + \begin{Bmatrix} \underline{\mathbf{0}} \\ \underline{\hat{\mathbf{f}}}^{\mathrm{s}}_{\mathrm{b}_2}(\omega) \end{Bmatrix} \tag{6}$$

where a subdivision into block matrices according to internal degrees of freedom $\underline{\hat{\mathbf{u}}}_{\mathrm{b}_1}(\omega)$ in the structural domain Ω_{b} and degrees of freedom $\underline{\hat{\mathbf{u}}}_{\mathrm{b}_2}(\omega)$ on the soil–structure interface Σ is introduced (figure 1). The corresponding number of degrees of freedom are indicated as n_{dof_1} and n_{dof_2}, respectively. $\widehat{\mathbf{K}}^{\mathrm{s}}_{\mathrm{b}_2\mathrm{b}_2}(\omega)$ represents the dynamic soil stiffness matrix and is defined as:

$$\widehat{\mathbf{K}}^{\mathrm{s}}_{\mathrm{b}_2\mathrm{b}_2}(\omega) = \int_{\Sigma} \mathbf{N}^{\mathrm{T}}_{\mathrm{b}_2}(\mathbf{x}) \mathbf{N}_{\mathrm{b}_2}(\mathbf{x}) \underline{\hat{\mathbf{t}}}(\mathbf{N}_{\mathrm{b}_2}(\mathbf{x}))(\omega) \, \mathrm{d}S = \mathbf{T}_{\mathrm{q}} \, \underline{\hat{\mathbf{t}}}(\mathbf{N}_{\mathrm{b}_2}(\mathbf{x}))(\omega) \tag{7}$$

where $\mathbf{N}_{\mathrm{b}_2}(\mathbf{x})$ indicates the FE shape functions on the soil–structure interface Σ, conforming with the BE interpolation functions. The frequency independent matrix $\mathbf{T}_{\mathrm{q}} = \int_{\Sigma} \mathbf{N}^{\mathrm{T}}_{\mathrm{b}_2}(\mathbf{x}) \mathbf{N}_{\mathrm{b}_2}(\mathbf{x}) \, \mathrm{d}S$ links the FE and BE discretizations. Both $\widehat{\mathbf{K}}^{\mathrm{s}}_{\mathrm{b}_2\mathrm{b}_2}(\omega)$ and $\mathbf{T}_{\mathrm{q}}$ have dimensions $(n_{\mathrm{dof}_2} \times n_{\mathrm{dof}_2})$.

Although equation (6) provides a straightforward solution to the dynamic SSI problem, it suffers some major drawbacks. Equation (7) requires the evaluation of tractions $\underline{\hat{\mathbf{t}}}(\mathbf{N}_{\mathrm{b}_2}(\mathbf{x}))(\omega)$ by means of the $\mathscr{H}$-BE method, which requires the solution of equation (5) for all shape functions $\mathbf{N}_{\mathrm{b}_2}(\mathbf{x})$ on Σ; the implemented FGMRES algorithm is only able to handle one right hand side at a time. Furthermore, addition of the dense unsymmetric dynamic soil stiffness matrix $\widehat{\mathbf{K}}^{\mathrm{s}}_{\mathrm{b}_2\mathrm{b}_2}(\omega)$ to the dynamic stiffness matrix of the structure strongly affects the sparsity of the system, reducing the efficiency of sparse FE solvers. The numerical examples in section 4 will demonstrate that this conventional

approach, in which the dynamic soil stiffness matrix $\widehat{\mathbf{K}}^{\mathrm{s}}_{\mathrm{b}_2\mathrm{b}_2}(\omega)$ is explicitly evaluated, does not provide an efficient solution procedure, especially for large problems.

The computational effort can be limited by considering a reduced kinematic basis for the displacement vector $\underline{\hat{\mathbf{u}}}_{\mathrm{b}_2}(\omega)$ on the interface Σ through the introduction of a modal decomposition $\underline{\hat{\mathbf{u}}}_{\mathrm{b}_2}(\omega) \simeq \mathbf{\Psi}_{\mathrm{b}_2}\underline{\hat{\boldsymbol{\alpha}}}(\omega)$, where $\mathbf{\Psi}_{\mathrm{b}_2}$ and $\underline{\hat{\boldsymbol{\alpha}}}(\omega)$ collect the mode shapes and the modal coordinates, respectively [35]. This allows rewriting equation (6) in terms of modal coordinates $\underline{\hat{\boldsymbol{\alpha}}}(\omega)$, and only a modal soil stiffness matrix $\mathbf{\Psi}^{\mathrm{T}}_{\mathrm{b}_2}\widehat{\mathbf{K}}^{\mathrm{s}}_{\mathrm{b}_2\mathrm{b}_2}(\omega)\mathbf{\Psi}_{\mathrm{b}_2}$ with dimensions $(n_{\mathrm{m}_2} \times n_{\mathrm{m}_2})$ has to be computed:

$$\mathbf{\Psi}^{\mathrm{T}}_{\mathrm{b}_2}\widehat{\mathbf{K}}^{\mathrm{s}}_{\mathrm{b}_2\mathrm{b}_2}(\omega)\mathbf{\Psi}_{\mathrm{b}_2} = \int_{\Sigma} \left(\mathbf{N}_{\mathrm{b}_2}(\mathbf{x})\mathbf{\Psi}_{\mathrm{b}_2}\right)^{\mathrm{T}} \mathbf{N}_{\mathrm{b}_2}(\mathbf{x})\underline{\hat{\mathbf{t}}}(\mathbf{N}_{\mathrm{b}_2}(\mathbf{x})\mathbf{\Psi}_{\mathrm{b}_2})(\omega)\,\mathrm{d}S \qquad (8)$$

As a result, equation (5) is only solved n_{m_2} times for tractions $\underline{\hat{\mathbf{t}}}(\mathbf{N}_{\mathrm{b}_2}(\mathbf{x})\mathbf{\Psi}_{\mathrm{b}_2})(\omega)$; the number of modes n_{m_2} is generally much lower than the number of degrees of freedom n_{dof_2} on the interface Σ. Although a substantial reduction in computation time can be achieved compared to the use of a full kinematic basis, the resulting modal soil stiffness matrix $\mathbf{\Psi}^{\mathrm{T}}_{\mathrm{b}_2}\widehat{\mathbf{K}}^{\mathrm{s}}_{\mathrm{b}_2\mathrm{b}_2}(\omega)\mathbf{\Psi}_{\mathrm{b}_2}$ remains dense and unsymmetric, consequently affecting the efficiency of sparse FE solvers. Furthermore, an appropriate choice of the modes $\mathbf{\Psi}_{\mathrm{b}_2}$ is required to obtain accurate results.

3.2 Iterative FE–$\mathscr{H}$-BE coupling

Iterative coupling procedures provide a valuable alternative to the conventional direct strategy outlined in the previous subsection. The governing equations are solved separately for each subdomain, while the boundary conditions at the soil–structure interface are updated until convergence is achieved. This methodology avoids the assembly and solution of a global system of coupled equations; it hence allows for the independent use of dedicated FE and $\mathscr{H}$-BE solvers in both subdomains. Iterative schemes are often used for dynamic SSI problems in the time domain to allow for the use of different time discretization schemes in the FE and BE subdomains [2, 36, 37]. Their application in the frequency domain remains rather limited, however, especially due to convergence difficulties [16]. Frequency domain iterative algorithms described in the literature mainly involve acoustic–acoustic [38] and acoustic–elastodynamic [16] coupling; the iterative coupling of FE and fast multipole BE models for visco–elastodynamics in the frequency domain is discussed by Grasso [15].

Four different iterative algorithms for the coupling of FE and $\mathscr{H}$-BE models are outlined in the following subsections. These methodologies are denoted as sequential Neumann–Dirichlet or Dirichlet–Neumann algorithms, and parallel Neumann–Neumann or Dirichlet–Dirichlet algorithms, indicating which kind of boundary conditions are imposed on the FE and BE subdomain, respectively.

3.2.1 Sequential Neumann–Dirichlet algorithm

At iteration step k of the sequential Neumann–Dirichlet procedure, the finite element subdomain is analyzed with Neumann boundary conditions $\underline{\hat{\mathbf{q}}}^k(\omega)$ at the soil–structure interface Σ:

$$\begin{bmatrix} \widehat{\mathbf{K}}_{\mathrm{b}_1\mathrm{b}_1}(\omega) & \widehat{\mathbf{K}}_{\mathrm{b}_1\mathrm{b}_2}(\omega) \\ \widehat{\mathbf{K}}_{\mathrm{b}_2\mathrm{b}_1}(\omega) & \widehat{\mathbf{K}}_{\mathrm{b}_2\mathrm{b}_2}(\omega) \end{bmatrix} \begin{Bmatrix} \underline{\hat{\mathbf{u}}}^k_{\mathrm{b}_1}(\omega) \\ \underline{\hat{\mathbf{u}}}^k_{\mathrm{b}_2}(\omega) \end{Bmatrix} = \begin{Bmatrix} \underline{\hat{\mathbf{f}}}_{\mathrm{b}_1}(\omega) \\ \underline{\hat{\mathbf{f}}}_{\mathrm{b}_2}(\omega) \end{Bmatrix} + \begin{Bmatrix} \underline{\mathbf{0}} \\ \underline{\hat{\mathbf{f}}}^{\mathrm{s}}_{\mathrm{b}_2}(\omega) \end{Bmatrix} + \begin{Bmatrix} \underline{\mathbf{0}} \\ \underline{\hat{\mathbf{q}}}^k(\omega) \end{Bmatrix} \tag{9}$$

where $\underline{\hat{\mathbf{q}}}^k(\omega)$ denotes the soil–structure interaction forces. Solving equation (9) by means of a standard finite element solver provides the internal and interface displacements $\underline{\hat{\mathbf{u}}}^k_{\mathrm{b}_1}(\omega)$ and $\underline{\hat{\mathbf{u}}}^k_{\mathrm{b}_2}(\omega)$. The latter are subsequently imposed as Dirichlet boundary conditions on the boundary element subdomain, allowing to solve the preconditioned equation (5) for the interface tractions $\underline{\hat{\mathbf{t}}}^k(\omega)$ using the FGMRES solver. These tractions are used to calculate equivalent nodal forces $\underline{\tilde{\hat{\mathbf{q}}}}^{k+1}(\omega)$:

$$\underline{\tilde{\hat{\mathbf{q}}}}^{k+1}(\omega) = -\int_{\Sigma} \mathbf{N}^{\mathrm{T}}_{\mathrm{b}_2}(\mathbf{x}) \mathbf{N}_{\mathrm{b}_2}(\mathbf{x}) \underline{\hat{\mathbf{t}}}^k(\omega)\, \mathrm{d}S = -\mathbf{T}_{\mathrm{q}}\, \underline{\hat{\mathbf{t}}}^k(\omega) \tag{10}$$

where a tilde above a variable indicates an unrelaxed quantity. The interaction forces are finally relaxed using an iteration dependent relaxation parameter λ^k:

$$\underline{\hat{\mathbf{q}}}^{k+1}(\omega) = \lambda^k \underline{\tilde{\hat{\mathbf{q}}}}^{k+1}(\omega) + (1-\lambda^k) \underline{\hat{\mathbf{q}}}^k(\omega) \tag{11}$$

Once the relaxed interaction forces $\underline{\hat{\mathbf{q}}}^{k+1}(\omega)$ are computed, a subsequent step in the iterative procedure is performed until convergence is obtained; an accuracy of 10^{-4} is prescribed for the relative residual norms $||\underline{\hat{\mathbf{u}}}^{k+1}_{\mathrm{b}_2}(\omega) - \underline{\hat{\mathbf{u}}}^k_{\mathrm{b}_2}(\omega)||/||\underline{\hat{\mathbf{u}}}^{k+1}_{\mathrm{b}_2}(\omega)||$ and $||\underline{\hat{\mathbf{q}}}^{k+1}(\omega) - \underline{\hat{\mathbf{q}}}^k(\omega)||/||\underline{\hat{\mathbf{q}}}^{k+1}(\omega)||$ of the interface displacements and interaction forces, respectively.

The choice of a suitable relaxation parameter λ^k in equation (11) is of great importance in order to ensure and/or speed up the convergence of the iterative algorithm. Constant relaxation parameters are considered, among others, by Elleithy et al. [7, 39] for linear elastostatics, von Estorff et al. [2] for transient elastodynamics, Hagen [40] for fluid–soil–structure interaction, and Grasso [15]

for visco–elastodynamics in the frequency domain. Convergence conditions have been established [7, 39] and parametric studies have been performed to identify the optimal choice of a constant relaxation parameter [2, 40]. Soares et al. [16] present an iterative procedure for the solution of fluid–structure interaction problems in the frequency domain, in which an optimized relaxation parameter is calculated in each iterative step by minimizing the square error functional of the interface fluxes.

In this paper, Aitken's Δ^2–method [17] is employed for the determination of an iteration dependent relaxation parameter λ^k. This method provides a simple but efficient procedure to determine λ^k, based on the results of two subsequent iterations. It is often applied in the iterative solution of fluid–structure interaction problems [41, 42] and has already been adopted for transient elastodynamic problems [37]; its application to elastodynamic problems formulated in the frequency domain is not common, however. The methodology is illustrated in figure 2b for a general iteration process involving a variable x and a function $f(x)$; the aim is to determine the solution $\overline{x} = f(\overline{x})$ through subsequent evaluations of $f(x)$. An unrelaxed estimation $\tilde{x}^{k+1} = f(x^k)$ is computed in step k of the iterative procedure; if no relaxation is applied (i.e. $\lambda^k \equiv 1$), the new approximation of $\overline{x}$ yields $x^{k+1} = \tilde{x}^{k+1}$ (cfr. equation (11)). This is illustrated in figure 2a. Application of this procedure would result in a staircase iteration path to the solution. In Aitken's Δ^2–method, however, the estimation $\tilde{x}^{k+1} = f(x^k)$ is combined with the result of the previous iteration step $k-1$, which allows for the determination of the new approximation x^{k+1} as the intersection of the linearized function $\tilde{f}^k(x)$ through the points $\left\{x^{k-1}, \tilde{x}^k = f(x^{k-1})\right\}^{\mathrm{T}}$ and $\left\{x^k, \tilde{x}^{k+1} = f(x^k)\right\}^{\mathrm{T}}$, and the function $y = x$, respectively. This corresponds to a single step of the secant method [42]. The relaxation parameter λ^k can hence be written in function of x^{k-1}, $\tilde{x}^k$, x^k and $\tilde{x}^{k+1}$:

$$\lambda^k = \frac{x^k - x^{k-1}}{x^k - \tilde{x}^{k+1} - x^{k-1} + \tilde{x}^k} \tag{12}$$

while the new approximation yields $x^{k+1} = \lambda^k \tilde{x}^{k+1} + (1 - \lambda^k) x^k$. Introducing the relation $x^k - x^{k-1} = \lambda^{k-1}\left(\tilde{x}^k - x^{k-1}\right)$ in equation (12) provides a recursive relation for the relaxation parameter λ^k:

$$\lambda^k = \lambda^{k-1} \frac{\tilde{x}^k - x^{k-1}}{x^k - \tilde{x}^{k+1} - x^{k-1} + \tilde{x}^k} \tag{13}$$

$$= -\lambda^{k-1} \frac{r^{k-1}}{r^k - r^{k-1}} \tag{14}$$

with the residual r^k defined as $r^k = x^k - \tilde{x}^{k+1}$.

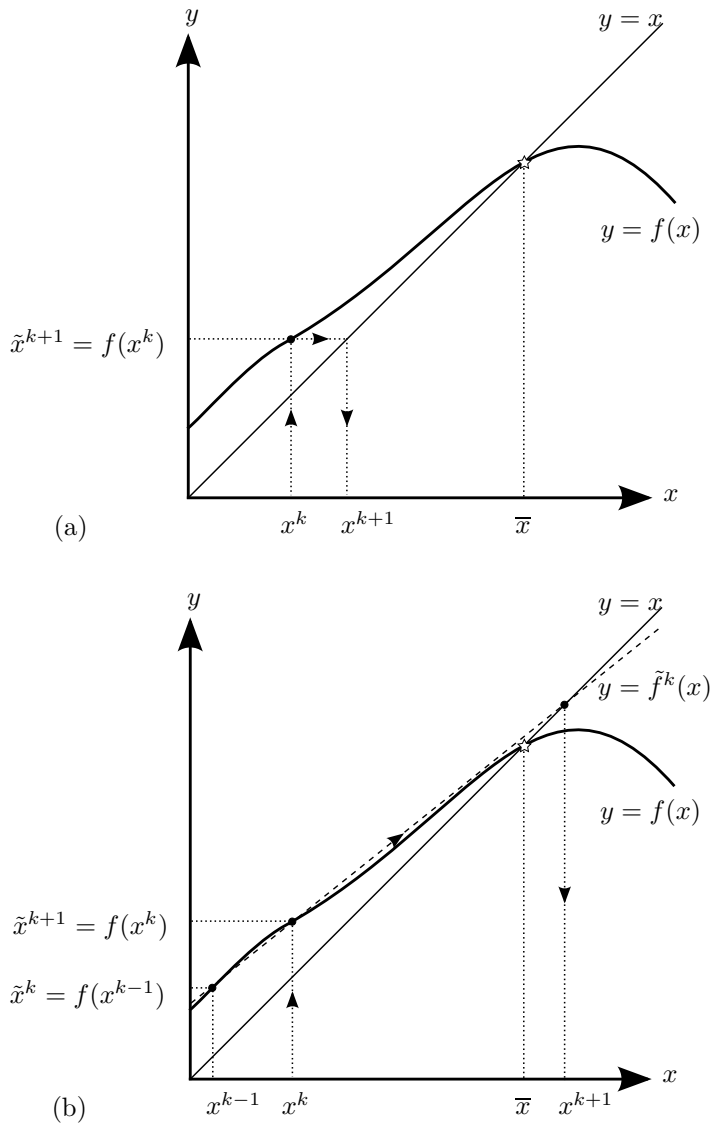

Figure 2: Interface relaxation technique employed in sequential iterative algorithms, involving the functions $y = x$ (thin solid line), $y = f(x)$ (thick solid line) and $y = \tilde{f}^k(x)$ (dashed line). The target solution $\overline{x} = f(\overline{x})$ is indicated with a star. The procedure (a) without relaxation is compared to (b) Aitken's Δ^2–method.

For the vectorized interaction forces $\underline{\hat{\mathbf{q}}}(\omega)$ considered in this subsection, however, the division in equation (14) is impossible. Following the approach presented by Irons and Tuck [43], the vectors are projected in the direction $\underline{\hat{\mathbf{r}}}^k(\omega) - \underline{\hat{\mathbf{r}}}^{k-1}(\omega) = \underline{\hat{\mathbf{q}}}^k(\omega) - \underline{\tilde{\hat{\mathbf{q}}}}^{k+1}(\omega) - \underline{\hat{\mathbf{q}}}^{k-1}(\omega) + \underline{\tilde{\hat{\mathbf{q}}}}^{k}(\omega)$:

$$\lambda^k = -\lambda^{k-1} \frac{\left(\underline{\hat{\mathbf{r}}}^k(\omega) - \underline{\hat{\mathbf{r}}}^{k-1}(\omega)\right)^{\mathrm{T}} \underline{\hat{\mathbf{r}}}^{k-1}(\omega)}{||\underline{\hat{\mathbf{r}}}^k(\omega) - \underline{\hat{\mathbf{r}}}^{k-1}(\omega)||^2} \tag{15}$$

with $\lambda^0 = 1$. Equation (15) can be evaluated at low computational cost, providing a simple and robust way to calculate an iteration dependent relaxation parameter, hence avoiding the need for an empirical trial–and–error process [2]. As all calculations are performed in the frequency domain, the relaxation parameter λ^k is a complex number. Although the modulus of this number could be limited (e.g. $||\lambda^k|| \leq 1$), this is not done in the present paper, as Soares et al. [16] have observed that faster convergence can be achieved with a non–restricted relaxation parameter for coupled acoustic–elastodynamic problems in the frequency domain.

An additional reduction of the computation time is achieved by providing an initial guess to the FGMRES solver that is employed to solve equation (5); the relaxed tractions $-\mathbf{T}_{\mathrm{q}}^{-1}\,\underline{\hat{\mathbf{q}}}^k(\omega)$ obtained in iteration $k-1$ are used as an initial guess for the determination of tractions $\underline{\hat{\mathbf{t}}}^k(\omega)$ in iteration k. Using a start vector in the first Neumann–Dirichlet iteration corresponding to the converged solution of the previous frequency step is also advantageous, provided that the frequency bin is sufficiently small.

3.2.2 Sequential Dirichlet–Neumann algorithm

The second iterative algorithm considered in this paper consist of a sequential Dirichlet–Neumann scheme; the type of boundary conditions applied to each subdomain is reversed compared to the procedure outlined in subsection 3.2.1. At iteration step k, Dirichlet boundary conditions $\underline{\hat{\mathbf{u}}}_{\mathrm{b}_2}^k(\omega)$ are imposed on the interface Σ of the FE subdomain, providing the interaction forces $\underline{\hat{\mathbf{q}}}^k(\omega)$ through the solution of equation (9) (and condensation of the internal degrees of freedom $\underline{\hat{\mathbf{u}}}_{\mathrm{b}_1}^k(\omega)$). The corresponding interface tractions $\underline{\hat{\mathbf{t}}}^k(\omega) = -\mathbf{T}_{\mathrm{q}}^{-1}\,\underline{\hat{\mathbf{q}}}^k(\omega)$ are applied to the BE subdomain, and unrelaxed interface displacements $\underline{\tilde{\hat{\mathbf{u}}}}_{\mathrm{b}_2}^{k+1}(\omega)$ are obtained by solving the preconditioned system of equations (5) using the FGMRES solver. Aitken's Δ^2–method is finally employed for the determination of an optimized relaxation parameter λ^k (with equation (15) now based on interface displacements instead of interaction forces), allowing

for the computation of relaxed interface displacements $\underline{\hat{\mathbf{u}}}_{\mathrm{b}_2}^{k+1}(\omega)$. This iterative procedure is repeated until convergence is achieved.

3.2.3 Parallel Neumann–Neumann algorithm

A parallel Neumann–Neumann iterative scheme is obtained if the interaction forces $\underline{\hat{\mathbf{q}}}^k(\omega)$ and corresponding interface tractions $\underline{\hat{\mathbf{t}}}^k(\omega) = -\mathbf{T}_{\mathrm{q}}^{-1}\,\underline{\hat{\mathbf{q}}}^k(\omega)$ are simultaneously imposed as Neumann boundary conditions on the interface Σ of the FE and BE subdomain, respectively. Solving equations (9) and (5) provides (incompatible) interface displacements $\underline{\hat{\mathbf{u}}}_{\mathrm{b}_2,\mathrm{FE}}^k(\omega)$ and $\underline{\hat{\mathbf{u}}}_{\mathrm{b}_2,\mathrm{BE}}^k(\omega)$, respectively. The discrepancy of interface displacements $\Delta\underline{\hat{\mathbf{u}}}_2^k(\omega) = \underline{\hat{\mathbf{u}}}_{\mathrm{b}_2,\mathrm{BE}}^k(\omega) - \underline{\hat{\mathbf{u}}}_{\mathrm{b}_2,\mathrm{FE}}^k(\omega)$ is subsequently employed to calculate an increment of interaction forces $\Delta\underline{\hat{\mathbf{q}}}^k(\omega)$. The displacement discrepancy $\Delta\underline{\hat{\mathbf{u}}}_{\mathrm{b}_2}^k(\omega)$ can either be imposed on the FE or the BE subdomain to compute this increment; this either yields unrelaxed interaction forces $\underline{\tilde{\hat{\mathbf{q}}}}_{\mathrm{FE}}^{k+1}(\omega) = \underline{\hat{\mathbf{q}}}^k(\omega) + \Delta\underline{\hat{\mathbf{q}}}_{\mathrm{FE}}^k(\omega)$ or $\underline{\tilde{\hat{\mathbf{q}}}}_{\mathrm{BE}}^{k+1}(\omega) = \underline{\hat{\mathbf{q}}}^k(\omega) + \Delta\underline{\hat{\mathbf{q}}}_{\mathrm{BE}}^k(\omega)$. Application of Aitken relaxation finally provides relaxed interaction forces $\underline{\hat{\mathbf{q}}}_{\mathrm{FE}}^{k+1}(\omega)$ or $\underline{\hat{\mathbf{q}}}_{\mathrm{BE}}^{k+1}(\omega)$, which are used in a subsequent step of the iterative scheme.

One can expect that the fastest convergence will be achieved if the force increment $\Delta\underline{\hat{\mathbf{q}}}^k(\omega)$ is calculated by imposing the displacement discrepancy $\Delta\underline{\hat{\mathbf{u}}}_{\mathrm{b}_2}^k(\omega)$ on the most flexible subdomain, as this will yield the smallest increment $\Delta\underline{\hat{\mathbf{q}}}^k(\omega)$. It is difficult, however, to quantify the flexibility of each subdomain a priori, especially as the latter is frequency dependent. Choosing either the FE or the BE subdomain for the calculation of $\Delta\underline{\hat{\mathbf{q}}}^k(\omega)$ hence requires an understanding of the dynamic behaviour of each subdomain; a wrong choice can significantly deteriorate the convergence of the iterative procedure.

A novel and more robust variant of the algorithm is therefore presented in this paper, where $\underline{\tilde{\hat{\mathbf{q}}}}_{\mathrm{FE}}^{k+1}(\omega)$ and $\underline{\tilde{\hat{\mathbf{q}}}}_{\mathrm{BE}}^{k+1}(\omega)$ are simultaneously accounted for in the determination of the relaxed interaction forces $\underline{\hat{\mathbf{q}}}^{k+1}(\omega)$. The concept is illustrated in figure 3 for a general iteration process in terms of a variable x and two functions $f(x)$ and $g(x)$, with solution $\overline{x} = f(\overline{x}) = g(\overline{x})$. The proposed approach is based on a simultaneous application of Aitken relaxation to $f(x)$ and $g(x)$. At iteration step k, two estimations $\tilde{x}_f^{k+1} = f(x^k)$ and $\tilde{x}_g^{k+1} = g(x^k)$ are calculated. These estimations are combined with the data points $\{x^{k-1}, \tilde{x}_f^k = f(x^{k-1})\}^{\mathrm{T}}$ and $\{x^{k-1}, \tilde{x}_g^k = g(x^{k-1})\}^{\mathrm{T}}$ obtained in the previous iteration step $k-1$ to define linear approximations $\tilde{f}^k(x)$ and $\tilde{g}^k(x)$ of the functions $f(x)$ and $g(x)$, respectively. The ordinate of the intersection of these linearized functions $\tilde{f}^k(x)$ and $\tilde{g}^k(x)$ provides a new approximation x^{k+1}

of the solution $\overline{x}$:

$$x^{k+1} = \frac{r_g^k}{r_g^k - r_f^k}\,\tilde{x}_f^{k+1} - \frac{r_f^k}{r_g^k - r_f^k}\,\tilde{x}_g^{k+1} \tag{16}$$

with $r_f^k = \tilde{x}_f^{k+1} - \tilde{x}_f^k$ and $r_g^k = \tilde{x}_g^{k+1} - \tilde{x}_g^k$. These residual vectors are defined differently compared to equation (14).

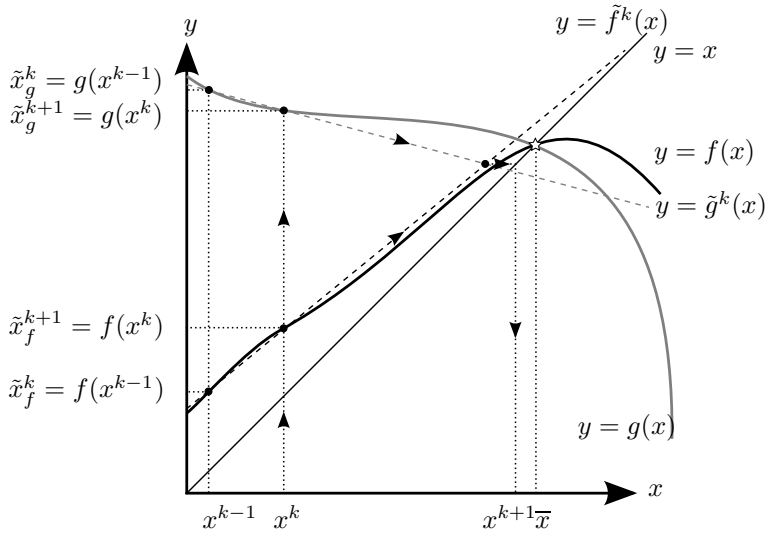

Figure 3: Interface relaxation technique employed in parallel iterative algorithms, involving the functions $y = f(x)$ (black solid line), $y = g(x)$ (grey solid line), $y = \tilde{f}^k(x)$ (black dashed line), $y = \tilde{g}^k(x)$ (grey dashed line), and $y = x$ (thin solid line). The target solution $\overline{x} = f(\overline{x}) = g(\overline{x})$ is indicated with a star.

For the vectorized interaction forces $\hat{\underline{\mathbf{q}}}(\omega)$, a projection in the direction $\hat{\underline{\mathbf{r}}}_{\mathrm{BE}}^k(\omega) - \hat{\underline{\mathbf{r}}}_{\mathrm{FE}}^k(\omega) = \tilde{\hat{\underline{\mathbf{q}}}}_{\mathrm{BE}}^{k+1}(\omega) - \tilde{\hat{\underline{\mathbf{q}}}}_{\mathrm{BE}}^{k}(\omega) - \tilde{\hat{\underline{\mathbf{q}}}}_{\mathrm{FE}}^{k+1}(\omega) + \tilde{\hat{\underline{\mathbf{q}}}}_{\mathrm{FE}}^{k}(\omega)$ is introduced in equation (16):

$$\begin{aligned}\hat{\underline{\mathbf{q}}}^{k+1}(\omega) = {} & \frac{\left(\hat{\underline{\mathbf{r}}}_{\mathrm{BE}}^k(\omega) - \hat{\underline{\mathbf{r}}}_{\mathrm{FE}}^k(\omega)\right)^{\mathrm{T}} \hat{\underline{\mathbf{r}}}_{\mathrm{BE}}^k(\omega)}{||\hat{\underline{\mathbf{r}}}_{\mathrm{BE}}^k(\omega) - \hat{\underline{\mathbf{r}}}_{\mathrm{FE}}^k(\omega)||^2}\,\tilde{\hat{\underline{\mathbf{q}}}}_{\mathrm{FE}}^{k+1}(\omega) \\ & - \frac{\left(\hat{\underline{\mathbf{r}}}_{\mathrm{BE}}^k(\omega) - \hat{\underline{\mathbf{r}}}_{\mathrm{FE}}^k(\omega)\right)^{\mathrm{T}} \hat{\underline{\mathbf{r}}}_{\mathrm{FE}}^k(\omega)}{||\hat{\underline{\mathbf{r}}}_{\mathrm{BE}}^k(\omega) - \hat{\underline{\mathbf{r}}}_{\mathrm{FE}}^k(\omega)||^2}\,\tilde{\hat{\underline{\mathbf{q}}}}_{\mathrm{BE}}^{k+1}(\omega)\end{aligned} \tag{17}$$

Equation (17) clearly indicates that $\tilde{\underline{\hat{\mathbf{q}}}}_{\mathrm{FE}}^{k+1}(\omega)$ and $\tilde{\underline{\hat{\mathbf{q}}}}_{\mathrm{BE}}^{k+1}(\omega)$ are simultaneously accounted for in the determination of a new estimate $\underline{\hat{\mathbf{q}}}^{k+1}(\omega)$, with iteration dependent weighting factors based on data of two subsequent iterations; these weighting factors can be calculated at low computational cost. This approach hence avoids the need for a priori information concerning the flexibility of the FE and BE subdomain.

3.2.4 Parallel Dirichlet–Dirichlet algorithm

The final iterative algorithm discussed in this paper is a parallel Dirichlet–Dirichlet strategy, which is very similar to the procedure outlined in subsection 3.2.3. Imposing Dirichlet boundary conditions $\underline{\hat{\mathbf{u}}}_{\mathrm{b}_2}^{k}(\omega)$ on Σ allows for the computation of interaction forces $\underline{\hat{\mathbf{q}}}_{\mathrm{FE}}^{k}(\omega)$ and $\underline{\hat{\mathbf{q}}}_{\mathrm{BE}}^{k}(\omega)$ through equations (9) and (5), respectively. The resulting force discrepancy $\Delta\underline{\hat{\mathbf{q}}}^{k}(\omega) = \underline{\hat{\mathbf{q}}}_{\mathrm{BE}}^{k}(\omega) - \underline{\hat{\mathbf{q}}}_{\mathrm{FE}}^{k}(\omega)$ is employed to calculate interface displacement increments $\Delta\underline{\hat{\mathbf{u}}}_{\mathrm{b}_2,\mathrm{FE}}^{k}(\omega)$ and $\Delta\underline{\hat{\mathbf{u}}}_{\mathrm{b}_2,\mathrm{BE}}^{k}(\omega)$, and unrelaxed displacements $\tilde{\underline{\hat{\mathbf{u}}}}_{\mathrm{b}_2,\mathrm{FE}}^{k+1}(\omega) = \underline{\hat{\mathbf{u}}}_{\mathrm{b}_2,\mathrm{FE}}^{k}(\omega) + \Delta\underline{\hat{\mathbf{u}}}_{\mathrm{b}_2,\mathrm{FE}}^{k}(\omega)$ and $\tilde{\underline{\hat{\mathbf{u}}}}_{\mathrm{b}_2,\mathrm{BE}}^{k+1}(\omega) = \underline{\hat{\mathbf{u}}}_{\mathrm{b}_2,\mathrm{BE}}^{k}(\omega) + \Delta\underline{\hat{\mathbf{u}}}_{\mathrm{b}_2,\mathrm{BE}}^{k}(\omega)$ can subsequently be obtained. The relaxed interface displacements $\underline{\hat{\mathbf{u}}}_{\mathrm{b}_2}^{k+1}(\omega)$ are finally computed by means of the relaxation procedure introduced in subsection 3.2.3; equation (17) in that case is based on interface displacements instead of interaction forces. The procedure is repeated until convergence is achieved.

3.3 Monolithic FE–$\mathscr{H}$-BE coupling

The coupling of FE and $\mathscr{H}$-BE models can also performed by means of a monolithic approach, in which the governing equations of both subdomains are solved simultaneously, while the assembly of a dynamic soil stiffness matrix is avoided. This approach fundamentally differs from the conventional direct coupling approach outlined in subsection 3.1 (equation (6)). Combining equations (1) and (3) and accounting for continuity of displacements and equilibrium of tractions at the soil–structure interface Σ yields:

$$\begin{bmatrix} \widehat{\mathbf{K}}_{\mathrm{b}_1\mathrm{b}_1}(\omega) & \widehat{\mathbf{K}}_{\mathrm{b}_1\mathrm{b}_2}(\omega) & \mathbf{0} \\ \widehat{\mathbf{K}}_{\mathrm{b}_2\mathrm{b}_1}(\omega) & \widehat{\mathbf{K}}_{\mathrm{b}_2\mathrm{b}_2}(\omega) & \mathbf{T}_{\mathrm{q}} \\ \mathbf{0} & \widehat{\mathbf{T}}_{\mathscr{H}}(\omega) + \mathbf{I} & -\widehat{\mathbf{U}}_{\mathscr{H}}(\omega) \end{bmatrix} \begin{Bmatrix} \underline{\hat{\mathbf{u}}}_{\mathrm{b}_1}(\omega) \\ \underline{\hat{\mathbf{u}}}_{\mathrm{b}_2}(\omega) \\ \underline{\hat{\mathbf{t}}}(\omega) \end{Bmatrix} = \begin{Bmatrix} \underline{\hat{\mathbf{f}}}_{\mathrm{b}_1}(\omega) \\ \underline{\hat{\mathbf{f}}}_{\mathrm{b}_2}(\omega) \\ \underline{\mathbf{0}} \end{Bmatrix} + \begin{Bmatrix} \underline{\mathbf{0}} \\ \underline{\hat{\mathbf{f}}}_{\mathrm{b}_2}^{\mathrm{s}}(\omega) \\ \underline{\mathbf{0}} \end{Bmatrix} \tag{18}$$

where the coupling matrix $\mathbf{T}_\mathrm{q}$ is defined in equation (7). The system size in this monolithic approach is $((n_{\mathrm{dof}_1} + 2n_{\mathrm{dof}_2}) \times (n_{\mathrm{dof}_1} + 2n_{\mathrm{dof}_2}))$, which is significantly larger than in the classical direct coupling strategy of subsection 3.1. The coefficient matrix is never assembled explicitly, however, as equation (18) is solved by means of an iterative GMRES solver. This requires an efficient evaluation of the matrix–vector product, indicating that the monolithic formulation (18) is only advantageous if a fast BE method (in casu a formulation based on $\mathscr{H}$–matrices) is employed. A monolithic approach is rarely used in elastodynamics [15]; the monolithic coupling of FE and fast multipole BE models presented by Margonari et al. [8] remains restricted to elastostatics. This strategy is more often applied for solving strongly coupled fluid–structure interaction problems [18, 19], as discretization methods commonly used for the fluid and the structure lead to sparse matrices.

The coefficient matrix in equation (18) is likely to be ill–conditioned, as the matrix entries arising from the FE and BE discretizations differ by several orders of magnitude. Convergence of the iterative solver will therefore be slow, and the incorporation of a suitable preconditioner is indispensable. The following simple right preconditioner $\widehat{\mathbf{M}}(\omega)$ is employed:

$$\widehat{\mathbf{M}}(\omega) = \begin{bmatrix} \mathrm{diag}\left(\widehat{\mathbf{K}}_{\mathrm{b}_1\mathrm{b}_1}(\omega)\right) & \mathbf{0} & \mathbf{0} \\ \mathbf{0} & \mathrm{diag}\left(\widehat{\mathbf{K}}_{\mathrm{b}_2\mathrm{b}_2}(\omega)\right) & \mathbf{T}_\mathrm{q} \\ \mathbf{0} & \mathrm{blkdiag}\left(\widehat{\mathbf{T}}_{\mathscr{H}}(\omega)\right) + \mathbf{I} & \mathrm{blkdiag}\left(-\widehat{\mathbf{U}}_{\mathscr{H}}(\omega)\right) \end{bmatrix} \tag{19}$$

where the size of the diagonal blocks of $\widehat{\mathbf{T}}_{\mathscr{H}}(\omega)$ and $\widehat{\mathbf{U}}_{\mathscr{H}}(\omega)$ is determined by the lowest hierarchical BE cluster level. The nested FGMRES solution procedure discussed in subsection 2.2 is employed here as well, avoiding the explicit assembly of $\widehat{\mathbf{M}}^{-1}(\omega)$.

4 Verification examples

In the following subsections, two examples are considered to verify the numerical implementation of the proposed FE–$\mathscr{H}$-BE coupling algorithms and to assess their computational performance. While the first example is related to a full space geometry, the second example involves Green's functions for a layered halfspace. All calculations have been performed on Intel® Xeon® E5520 (2.26 GHz) CPUs.

4.1 3D spherical cavity embedded in a layered space

Consider a 3D spherical cavity with inner radius $r_\mathrm{i} = 1\,\mathrm{m}$ embedded in a layered space, consisting of a spherical layer with outer radius $r_\mathrm{o} = 2\,\mathrm{m}$ and a homogeneous full space (figure 4a). The cavity is loaded by an internal pressure $\hat{p}(\omega) = 1\,\mathrm{Pa/Hz}$. The full space is characterized by a dilatational wave velocity $C_\mathrm{p} = 300\,\mathrm{m/s}$, a density $\rho = 1800\,\mathrm{kg/m^3}$, and a material damping ratio $\beta_\mathrm{p} = 0.025$ in volumetric deformation. The dilatational wave velocity in the spherical layer is defined as αC_p, where the following values are considered for the ratio α: (i) $\alpha = 1/2$, (ii) $\alpha = 1$ and (iii) $\alpha = 2$. The same material damping ratio and density as in the full space are used.

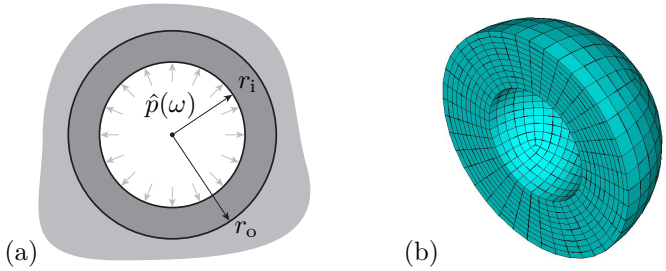

Figure 4: (a) 3D spherical cavity with inner radius r_i embedded in a layered space, consisting of a spherical layer with outer radius $r_\mathrm{o} = 2\,\mathrm{m}$ and a homogeneous full space, and subjected to an internal pressure $\hat{p}(\omega)$. Half of the FE discretization of the spherical layer is shown in (b).

The spherical layer is discretized by means of 6000 eight–node solid finite elements, which are coupled to a conforming BE mesh consisting of 600 four–node quadrilateral elements on the soil–structure interface (figure 4b). A nodal collocation scheme is used for the latter to facilitate the FE–BE coupling, resulting in 19866 FE and 1806 BE degrees of freedom. This results in 6.67 elements per dilatational wavelength $\lambda_\mathrm{p} = \alpha C_\mathrm{p}/f$ at a frequency of 100 Hz for $\alpha = 1/2$. Analytical full space fundamental solutions [14] are employed in the $\mathscr{H}$-BE formulation.

Each of the FE–$\mathscr{H}$-BE coupling strategies outlined in the section 3 is employed to calculate the response in the frequency range between 0 Hz and 100 Hz, with a frequency step of 1 Hz. A maximum of 200 iterations is prescribed for the iterative coupling algorithms. The sequential Neumann–Dirichlet algorithm presented in subsection 3.2.1 is unable to determine the static solution, as application of Neumann boundary conditions to the unconstrained structural domain Ω_b results in singular FE equations. The convergence behaviour at low frequencies is hence expected to be poor; the frequency sweep is therefore

performed from high to low frequencies. The sequential Dirichlet–Neumann algorithm of subsection 3.2.2, on the other hand, succeeds in solving the coupled problem for static excitation, as displacements are imposed on the boundary of the FE subdomain.

Figure 5 shows the real and imaginary part of the radial displacement at $r = r_o$, for the three values of the wave velocity ratio α. All methods yield accurate results in very good agreement with the analytical solution [44] for all values of the ratio α, with exception of the sequential Neumann–Dirichlet algorithm, which is unable to retrieve the correct solution within the prescribed number of iterations at [12,31–38,41–42,46,49–62,64–80,82–100] Hz for a wave velocity ratio $\alpha = 1/2$. At these particular frequencies, the relative residual norm of the interface displacements and interaction forces still exceeds the specified accuracy of 10^{-4}.

The integral representation theorem subsequently allows for the computation of the radiated wavefield in the full space from the displacements and tractions on the FE–$\mathscr{H}$-BE interface. Figure 6 shows the real and imaginary part of the radial displacement at $r = 10\,\mathrm{m}$. The solutions of the various coupling procedures are clearly in good correspondence with each other and agree with the analytical solution, except for the Neumann–Dirichlet algorithm at the aforementioned frequencies for the case $\alpha = 1/2$.

Figures 5 and 6 validate the numerical implementation of the FE–$\mathscr{H}$-BE coupling strategies presented in this paper. The computational performance of each method strongly differs, however. Figure 7 shows the CPU time required in each algorithm as a function of the frequency, for the three wave velocity ratios considered. It is observed that the computation time in the direct coupling approach significantly exceeds the computational effort of the alternative procedures due to the drawbacks summarized in subsection 3.1, rendering the conventional method the least efficient. The computation time remains quasi independent of the wave velocity ratio, but increases with frequency. This is caused by an increase of the time required for the assembly and solution of the $\mathscr{H}$-BE equations at higher frequencies [12]; a similar trend is also observed for the other coupling methodologies. The computational efficiency of the iterative coupling schemes, on the other hand, shows a much stronger correlation with the wave velocity ratio α. This is in particular the case for the sequential variants: the CPU time in the Neumann–Dirichlet algorithm strongly decreases for increasing values of α, while the reverse is observed for the Dirichlet–Neumann approach. This indicates that Neumann boundary conditions should be applied to the most stiff subdomain in order to achieve the fastest convergence. The efficiency of the parallel iterative algorithms depends less strongly on α due to the novel relaxation procedure introduced in subsection 3.2.3, as the contribution of each subdomain

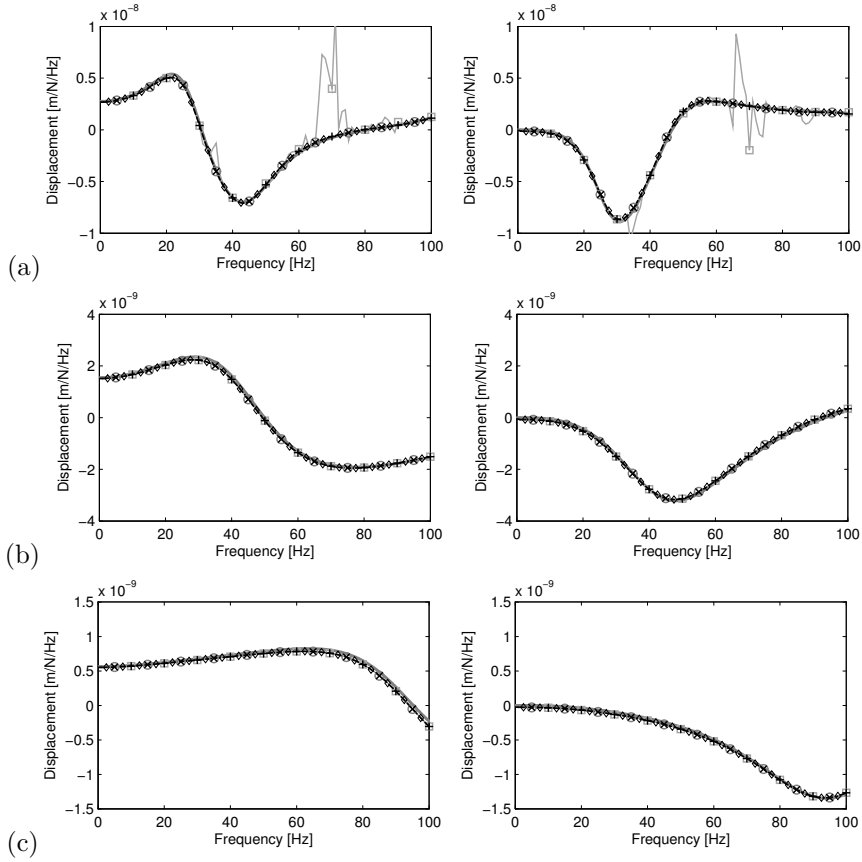

Figure 5: Real (left) and imaginary (right) part of the radial displacement at $r = r_o$ due to a unit harmonic pressure applied to a spherical cavity embedded in a layered space, for (a) $\alpha = 1/2$, (b) $\alpha = 1$ and (c) $\alpha = 2$. The solutions of the classical direct coupling approach (dashed black line), the iterative Neumann–Dirichlet (grey squares), Dirichlet–Neumann (black plus signs), Neumann–Neumann (grey circles) and Dirichlet–Dirichlet (black crosses) algorithms, and the monolithic coupling procedure (black rhombuses) are compared to the analytical solution (solid grey line) [44]. The markers are only drawn at a limited number of data points.

to the relaxed interaction forces or displacements is balanced in every step of the iterative procedure. Finally, figure 7 illustrates that the monolithic

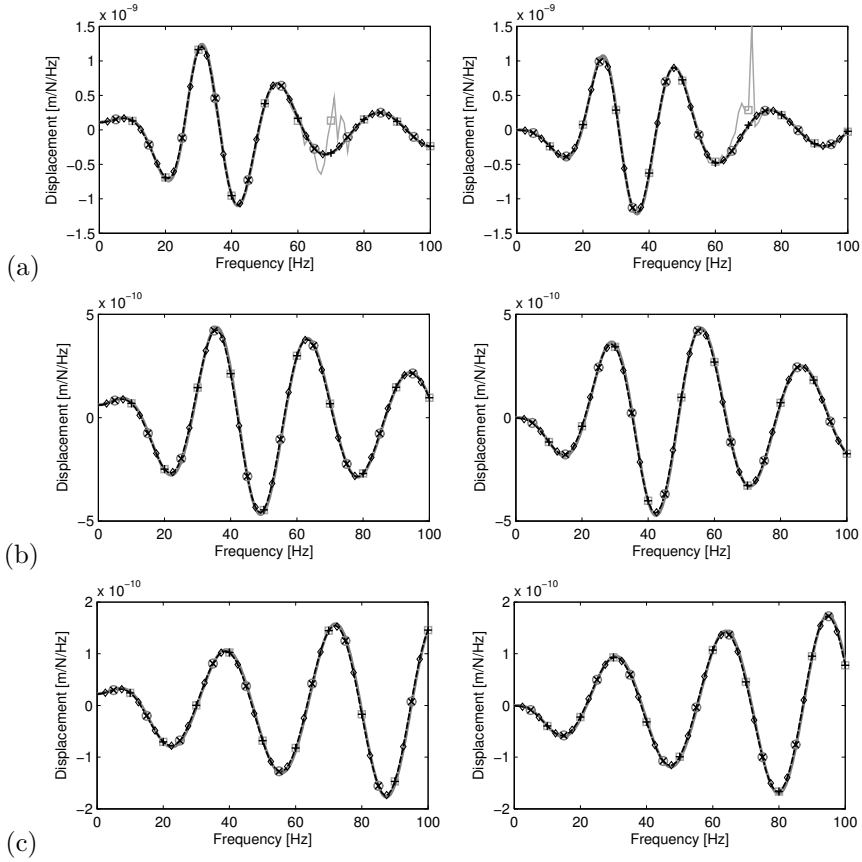

Figure 6: Real (left) and imaginary (right) part of the radial displacement at $r = 10\,\mathrm{m}$ due to a unit harmonic pressure applied to a spherical cavity embedded in a layered space, for (a) $\alpha = 1/2$, (b) $\alpha = 1$ and (c) $\alpha = 2$. The solutions of the classical direct coupling approach (dashed black line), the iterative Neumann–Dirichlet (grey squares), Dirichlet–Neumann (black plus signs), Neumann–Neumann (grey circles) and Dirichlet–Dirichlet (black crosses) algorithms, and the monolithic coupling procedure (black rhombuses) are compared to the analytical solution (solid grey line) [44]. The markers are only drawn at a limited number of data points.

coupling scheme is also relatively insensitive to the value of α, but the overall computational performance of this methodology remains relatively poor

compared to the iterative algorithms. The implementation of a more rigorous preconditioner than the one applied in this paper might result in an improved convergence behaviour. Algebraic multigrid preconditioning strategies adapted for hierarchical matrices [45] or approaches based on the sparse approximate inverse (SPAI) of the BE matrices [8] are worthwhile to be considered in future research.

Some important conclusions can be drawn from the results presented in figure 7. It is clear that the classical direct approach is not well suited to provide an efficient coupling of FE and $\mathscr{H}$-BE models. In particular, if there exists a strong stiffness contrast between the subdomains, a sequential iterative algorithm is preferred. It is recommended to impose Neumann boundary conditions on the most stiff subdomain; the reverse choice can significantly deteriorate the convergence behaviour. If such a contrast is not apparent, however, the parallel iterative algorithms as well as the monolithic approach provide a reliable and robust coupling of FE and $\mathscr{H}$-BE models.

The efficiency of the sequential iterative procedures is now investigated in more detail. In each global iterative step k, an iterative FGMRES solver is used to solve equation (5) for tractions $\hat{\underline{\mathbf{t}}}^{k}(\omega)$ or interface displacements $\tilde{\underline{\mathbf{u}}}_{\mathrm{b}_2}^{k+1}(\omega)$ in the Neumann–Dirichlet or Dirichlet–Neumann algorithm, respectively. Figures 8 and 9 show the number of FGMRES–iterations for the solution of equation (5) as a function of the frequency and the iteration step k. The number of FGMRES–iterations generally decreases in subsequent iteration steps, as the relaxed solution obtained in iteration $k-1$ is used as an initial guess in the FGMRES solver in iteration k. The number of global iterations strongly decreases for increasing values of the wave velocity ratio α in the Neumann–Dirichlet algorithm (figure 8), while the reverse is observed in the Dirichlet–Neumann approach (figure 9).

Numerical attempts have furthermore demonstrated that application of Aitken's Δ^2–method for the interface relaxation is crucial in order to ensure convergence in the sequential iterative algorithms. No convergence could be obtained with these algorithms in any of the examples in case a fixed value was attributed to the relaxation parameter λ^k (several constant values between 0 and 1 have been considered), in the entire frequency range of interest. Figure 10 shows the fluctuation of λ^k in the sequential Neumann–Dirichlet algorithm at a frequency of 100 Hz for $\alpha = 1$, clearly illustrating how the relaxation parameter changes throughout the iteration steps.

Finally, the effectiveness of the novel relaxation procedure for the parallel iterative algorithms introduced in subsection 3.2.3 is demonstrated. Figure 11 compares the CPU time in the iterative Neumann–Neumann algorithm using equation (17) for the determination of relaxed interaction forces $\hat{\underline{\mathbf{q}}}^{k+1}(\omega)$ to the

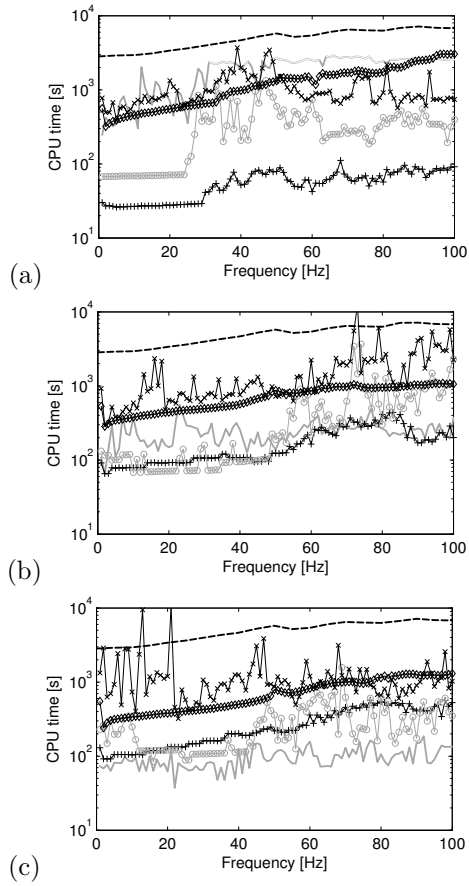

Figure 7: CPU time required in the classical direct coupling approach (dashed black line), the iterative Neumann–Dirichlet (solid grey line), Dirichlet–Neumann (black plus signs), Neumann–Neumann (grey circles) and Dirichlet–Dirichlet (black crosses) algorithms, and the monolithic coupling procedure (black rhombuses), for a spherical cavity embedded in a layered space with (a) $\alpha = 1/2$, (b) $\alpha = 1$ and (c) $\alpha = 2$. The lines are only drawn if convergence is achieved.

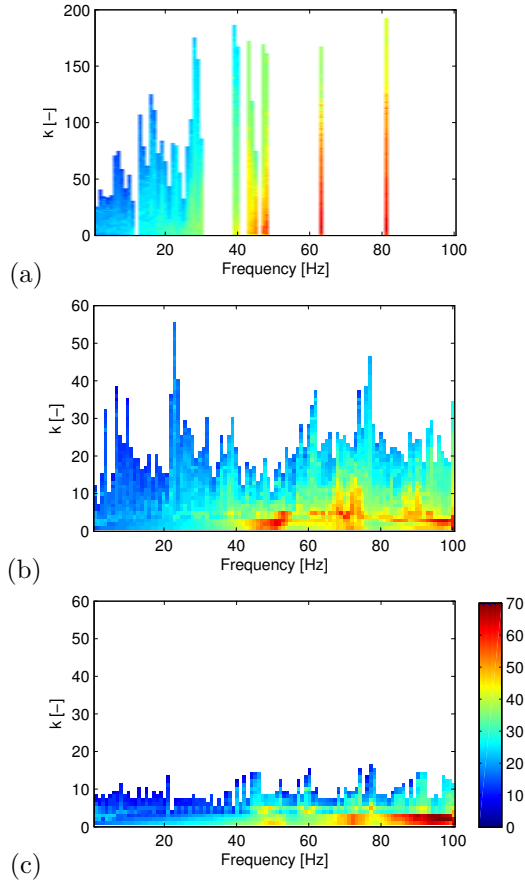

Figure 8: Number of FGMRES–iterations (colour code) to solve the $\mathscr{H}$-BE equation (5) for tractions in the iterative Neumann–Dirichlet algorithm as a function of the frequency and the iteration step k, for a spherical cavity embedded in a layered space with (a) $\alpha = 1/2$, (b) $\alpha = 1$ and (c) $\alpha = 2$. The bars are only drawn if convergence is achieved.

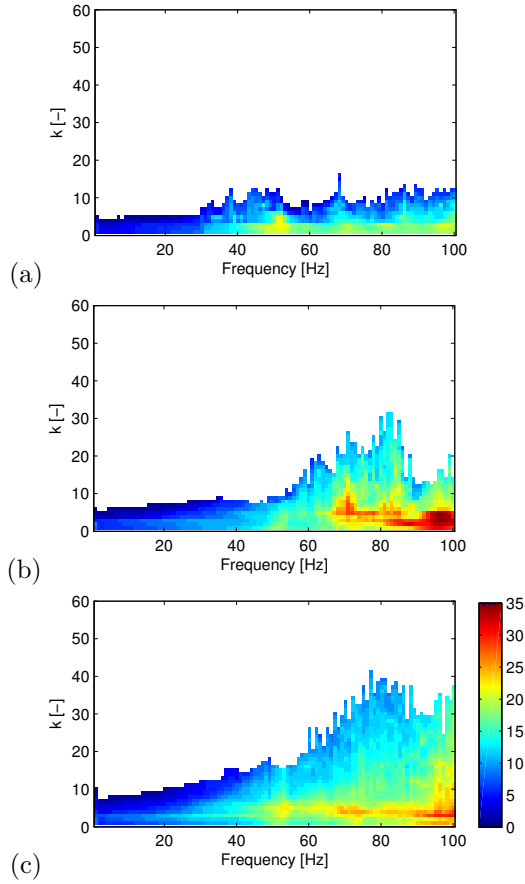

Figure 9: Number of FGMRES–iterations (colour code) to solve the $\mathscr{H}$-BE equation (5) for interface displacements in the iterative Dirichlet–Neumann algorithm as a function of the frequency and the iteration step k, for a spherical cavity embedded in a layered space with (a) $\alpha = 1/2$, (b) $\alpha = 1$ and (c) $\alpha = 2$.

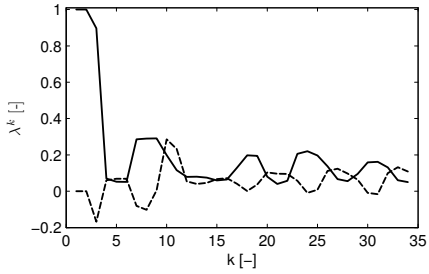

Figure 10: Real (solid line) and imaginary (dashed line) part of the Aitken relaxation parameter λ^k at 100 Hz in the sequential Neumann–Dirichlet iterative algorithm, for a spherical cavity embedded in a layered space with $\alpha = 1$.

cases where either $\hat{\underline{\mathbf{q}}}_{\mathrm{FE}}^{k+1}(\omega)$ or $\hat{\underline{\mathbf{q}}}_{\mathrm{BE}}^{k+1}(\omega)$ is employed, respectively. As indicated in subsection 3.2.3, the fastest convergence is achieved if the displacement discrepancy $\Delta\hat{\underline{\mathbf{u}}}_{\mathrm{b}_2}^{k}(\omega)$ is imposed on the most flexible subdomain, i.e. on the FE subdomain for $\alpha = 1/2$ and on the BE subdomain for $\alpha = 2$. The reverse choice strongly affects the convergence behaviour and the algorithm does even not convergence at some frequencies if $\hat{\underline{\mathbf{q}}}_{\mathrm{BE}}^{k+1}(\omega)$ is employed for $\alpha = 1/2$. The relaxation procedure corresponding to equation (17) proves to be a reliable alternative, as the associated CPU times only moderately depend on α and are often bounded by the computation times of the two other approaches.

4.2 Flexible surface foundation on a horizontally layered halfspace

A flexible square surface foundation on a horizontally layered halfspace is considered in this subsection. The concrete foundation has dimensions 5 m × 5 m × 0.25 m and a Young's modulus $E = 33\,\mathrm{GPa}$, a Poisson's ratio $\nu = 0.20$, and a density $\rho = 2500\,\mathrm{kg/m^3}$. Rayleigh damping with a modal damping ratio $\xi = 0.03$ in the first two flexible modes is used. A unit harmonic vertical point excitation is applied at the center of the foundation, within a frequency range between 0 Hz and 100 Hz.

The soil consists of two layers on a halfspace, each with a thickness of 2 m. The shear wave velocity C_{s} is equal to 150 m/s in the top layer, 250 m/s in the second layer, and 300 m/s in the underlying halfspace. The Poisson's ratio ν is 1/3 everywhere, resulting in dilatational wave velocities C_{p} of 300 m/s, 500 m/s, and 600 m/s, respectively. Material damping ratios $\beta_{\mathrm{s}} = \beta_{\mathrm{p}} = 0.025$ in both

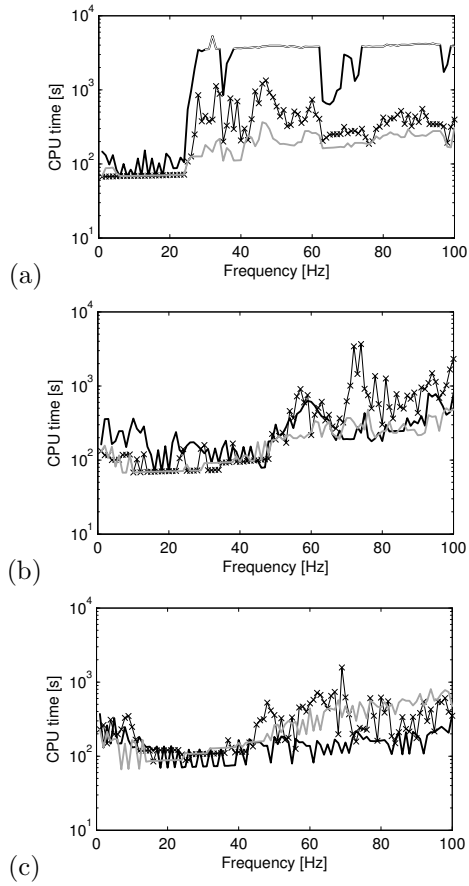

Figure 11: CPU time required in the parallel Neumann–Neumann algorithm in case the displacement discrepancy is imposed on the BE subdomain (solid black line), on the FE subdomain (solid grey line), and in case the relaxation procedure corresponding to equation (17) is employed (crosses), for a spherical cavity embedded in a layered space with (a) $\alpha = 1/2$, (b) $\alpha = 1$ and (c) $\alpha = 2$. The lines are only drawn if convergence is achieved.

deviatoric and volumetric deformation are attributed to the layers and the halfspace, while a uniform density $\rho = 1800\,\mathrm{kg/m^3}$ is considered throughout the medium.

The foundation is discretized by means of 30×30 square Kirchhoff plate elements, which are coupled to a conforming BE mesh for the soil using a nodal collocation scheme. Up to nine elements per shear wavelength $\lambda_\mathrm{s} = C_\mathrm{s}/f$ are provided at the maximum frequency of 100 Hz (determined by the shear wave velocity of the top layer). Green's functions for a layered halfspace are incorporated in the $\mathscr{H}$-BE formulation [12, 13, 46], avoiding the necessity to discretize the free surface and the layer interfaces. It is expected that the foundation will behave much stiffer than the soil in the frequency range of interest. In accordance with the findings of subsection 4.1, an iterative Neumann–Dirichlet coupling scheme is therefore employed. No analytical reference solution is available for this problem, however, and the monolithic coupling approach is therefore considered as well to provide verification.

Figure 12 shows the real and imaginary part of the vertical displacement $\hat{u}_z(\mathbf{x}, \omega)$ at the center of the foundation, calculated with both coupling procedures; a perfect agreement between the results is observed. The peak at 20 Hz is caused by resonance of the foundation on the layered halfspace. The iterative Neumann–Dirichlet is unable, however, to determine the static solution, and the frequency sweep is therefore performed from high to low frequencies.

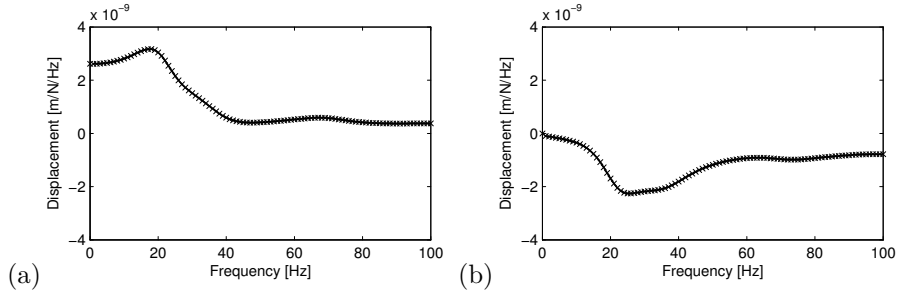

Figure 12: (a) Real and (b) imaginary part of the vertical displacement $\hat{u}_z(\mathbf{x}, \omega)$ at the center of a flexible surface foundation on a layered halfspace excited by a unit harmonic vertical point load at its center. The solution of the iterative Neumann–Dirichlet algorithm (solid line) is compared to the solution of the monolithic coupling procedure (crosses).

The vertical displacement of the foundation and the surrounding soil is shown in figures 13a and 13b at 25 Hz and 100 Hz, respectively. While the wave fronts at the surface of the soil remain almost perfectly cylindrical at 25 Hz, this is no longer the case at 100 Hz due to the dynamic interaction between the foundation and the soil.

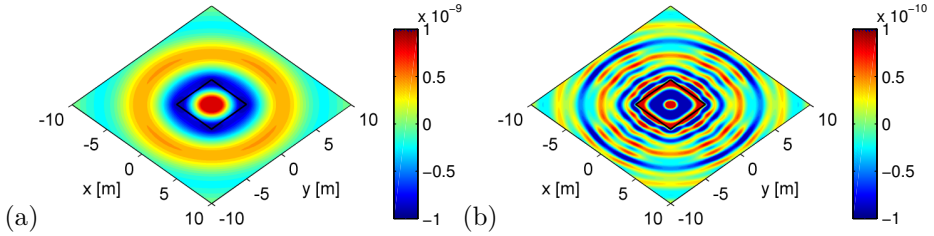

Figure 13: Real part of the vertical displacement $\hat{u}_z(\mathbf{x}, \omega)$ of the foundation and the soil for a flexible surface foundation on a layered halfspace excited by a unit harmonic vertical point load at its center at (a) 25 Hz and (b) 100 Hz.

Figure 14a shows the number of FGMRES–iterations as a function of the frequency and the iteration step k for the sequential Neumann–Dirichlet algorithm, in case no initial guess is provided to the FGMRES solver. The number of FGMRES–iterations remains almost independent of the iteration step k if this strategy is applied. It is illustrated in figure 14b that imposing the relaxed interaction forces obtained in step $k-1$ as initial guess in the FGMRES solver of step k is clearly beneficial, as the number of FGMRES–iterations in subsequent steps is strongly reduced. Using a start vector in the first Neumann–Dirichlet iteration corresponding to the converged solution of the previous frequency step is also advantageous; this results in a lower numbers of iteration steps per frequency. The peaks at 40 Hz and 62 Hz in figure 14 correspond to natural frequencies of the free foundation. Applying Neumann boundary conditions to the FE subdomain near a natural frequency results in large displacements, and additional iterations are hence required to balance the resulting mismatch of displacements and tractions on the interface. It should be emphasized that these natural frequencies differ from the resonance of the foundation on the soil at 20 Hz (apparent in figure 12), which is due to the dynamic SSI.

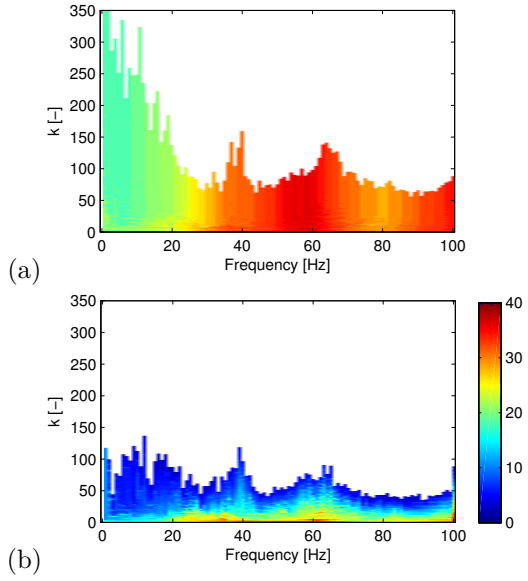

Figure 14: Number of FGMRES–iterations (colour code) to solve the $\mathscr{H}$-BE equation (5) for tractions in the iterative Neumann–Dirichlet algorithm as a function of the frequency and the iteration step k, for a flexible surface foundation on a layered halfspace. The numbers are shown (a) in case no initial guess is provided to the FGMRES solver, or (b) in case the relaxed tractions in iteration $k-1$ are used as an initial guess in iteration k, while the converged solution at a particular frequency is used as an initial guess for the first iteration at the subsequent frequency.

5 Application: subgrade stiffening as a mitigation measure for railway induced vibrations

The numerical examples considered in section 4 demonstrate the validity and efficiency of the presented coupling algorithms. These methodologies enable the fast evaluation of large coupled FE–$\mathscr{H}$-BE models, providing the possibility to analyze complex problems of dynamic SSI. The verification examples discussed in section 4 involve only a limited amount of degrees of freedom. An engineering application is therefore considered in this section to illustrate the applicability

of coupled FE–$\mathscr{H}$-BE models to large scale problems.

The application is related to the mitigation of railway induced vibrations, which can lead to annoyance in the built environment. An important category of vibration reduction measures are interventions in the propagation path between source (railway track) and receiver (building), such as vibration isolation screens [47], buried wall barriers [48], and wave impeding blocks [49]. Recently, the vibration reduction efficiency of subgrade stiffening has been investigated [50], where a block of stiffened soil is included in the transmission path, e.g. by means of jet grouting (figure 3a). In order reduce the computational effort, the geometry of these mitigation measures is often assumed to be invariant in the longitudinal direction, allowing for the application of an efficient two–and–a–half–dimensional (2.5D) approach, where a Fourier transform of the longitudinal coordinate allows representing the 3D response on a 2D mesh [51]. In practice, the construction of a jet grouting wall is limited to finite dimensions, however, and the assumption of longitudinal invariance of the geometry is therefore not fulfilled (figure 3b). Accounting for the finite length requires the solution of a full 3D dynamic SSI problem, which is computationally very demanding if a classical BE formulation is used; the FE–$\mathscr{H}$-BE methods proposed in this paper are much more appropriate to solve this problem.

The vibration reduction efficiency of a block of stiffened soil of finite length embedded in a halfspace is investigated in this section. A case study involving a block with a width $b = 2\,\mathrm{m}$, a depth $h = 2\,\mathrm{m}$, a length L_y, and situated at a distance $d = 4\,\mathrm{m}$ from the y–axis is considered (figure 3). In order to facilitate physical interpretation, the soil is assumed to be homogeneous, and an incident wavefield is generated by the application of a unit vertical harmonic point load at the origin of the coordinate system, rather than considering the passage of a train. The halfspace is characterized by a shear wave velocity $C_\mathrm{s} = 200\,\mathrm{m/s}$, a dilatational wave velocity $C_\mathrm{p} = 400\,\mathrm{m/s}$, a density $\rho = 2000\,\mathrm{kg/m^3}$, and material damping ratios $\beta_\mathrm{s} = \beta_\mathrm{p} = 0.025$ in both deviatoric and volumetric deformation. The Rayleigh wave velocity $C_\mathrm{R} = 186.7\,\mathrm{m/s}$ is frequency independent due to its non–dispersive behaviour in a homogeneous halfspace [52]. The block of stiffened soil has a shear wave velocity $C_\mathrm{s} = 550\,\mathrm{m/s}$, a dilatational wave velocity $C_\mathrm{p} = 950\,\mathrm{m/s}$, a density $\rho = 2000\,\mathrm{kg/m^3}$, and material damping ratios $\beta_\mathrm{s} = \beta_\mathrm{p} = 0.050$.

The block of stiffened soil is discretized by means of eight–node solid elements, which are coupled to a conforming mesh of four–node quadrilateral boundary elements for the surrounding soil domain. Halfspace Green's functions are employed in the $\mathscr{H}$-BE formulation. The numerical analysis is performed for a block of stiffened soil with a length of 15 m, 30 m, and 60 m; the properties of the resulting FE and BE discretizations are listed in table 1. As there exists

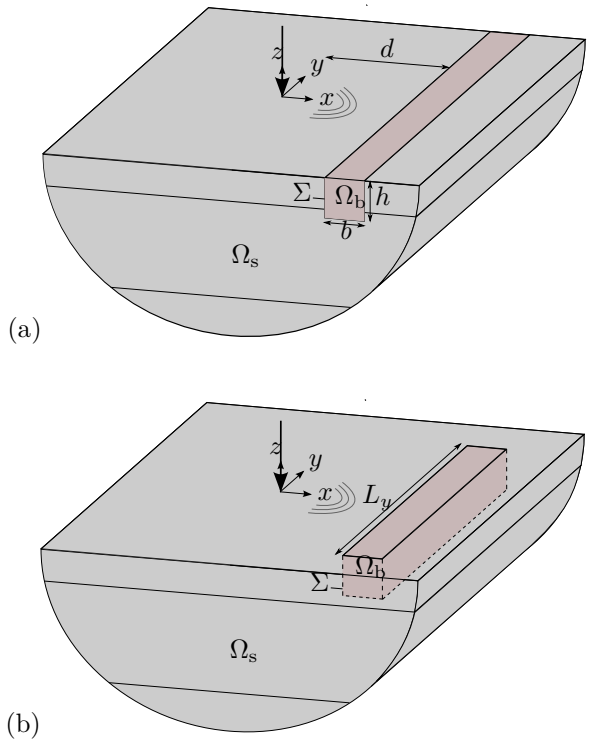

Figure 15: A block of stiffened soil Ω_b incorporated in the soil domain Ω_s, (a) assuming longitudinal invariance of the geometry or (b) accounting for the finite length L_y.

a strong stiffness contrast between the FE and $\mathscr{H}$-BE subdomain, an iterative Neumann–Dirichlet algorithm is employed for the solution of the 3D coupled FE–$\mathscr{H}$-BE problem.

Figures 16–18a show the real part of the vertical displacement $\hat{u}_z(\mathbf{x}, \omega)$ in the reference case (i.e. without subgrade stiffening) at a frequency of 15 Hz, 30 Hz, and 60 Hz, respectively. The wavefield in the soil is characterized by cylindrical wave fronts with a Rayleigh wavelength $\lambda_R(\omega) = 2\pi C_R/\omega$ equal to 12.45 m, 6.22 m, and 3.11 m, respectively. The real part of the vertical displacement $\hat{u}_z(\mathbf{x}, \omega)$ in case an infinitely long block of stiffened soil is embedded in the halfspace is shown in figures 16–18e. These results are obtained by means of a 2.5D coupled FE–BE calculation based on the assumption of longitudinal invariance of the geometry. At 15 Hz, the wavefield in the soil is only slightly

L_y [m]	# FE elements [–]	# FE nodes [–]	# FE DOFs [–]	# BE elements [–]	# BE nodes [–]	# BE DOFs [–]
15	3840	4941	14823	1568	1637	4911
30	7680	9801	29403	3008	3137	9411
60	15360	19521	58563	5888	6137	18411

Table 1: Properties of the FE and BE discretizations of a block of stiffened soil with a length of 15 m, 30 m, and 60 m.

affected by the presence of the block of stiffened soil (figure 16e), while a larger influence is observed at higher frequencies (figures 17–18e). The vibration reduction efficiency in each of these cases is characterized through the corresponding vertical insertion loss $\widehat{\mathrm{IL}}_z(\mathbf{x},\omega)$:

$$\widehat{\mathrm{IL}}_z(\mathbf{x},\omega) = 20\log_{10}\frac{|\hat{u}_z^{\mathrm{ref}}(\mathbf{x},\omega)|}{|\hat{u}_z(\mathbf{x},\omega)|} \tag{20}$$

Positive values of the insertion loss indicate a reduction of the vertical free field vibrations. It has been demonstrated in [50] that the wave impeding effect depends on the relation between the Rayleigh wavelength in the soil and the free bending wavelength in the block of stiffened soil, as the transmission of plane waves in the soil with a longitudinal wavelength smaller than the bending wavelength is hindered. The mitigation measure is only effective above a critical frequency depending on the stiffness contrast between the soil and the block of stiffened soil. The guideline formulated in [50] states that the critical frequency can be estimated as $\frac{C_{\mathrm{R}}^2}{2\pi h}\sqrt{\frac{12\rho}{E}} = 12\,\mathrm{Hz}$, where C_{R} is the Rayleigh wave velocity of the halfspace and h, ρ, and E are characteristics of the block of stiffened soil. The frequencies under concern are all above this critical frequency, and a wave impeding effect is hence observed in figures 16–18e. The area where vibration levels are significantly reduced clearly depends on the frequency, however, and a critical angle delimiting this area can be distinguished. An analytical expression for the latter is also given in [50].

Figures 16–18b–d show the real part of the vertical displacement $\hat{u}_z(\mathbf{x},\omega)$ and the insertion loss $\widehat{\mathrm{IL}}_z(\mathbf{x},\omega)$ in case a block of stiffened soil is included over a finite length of 15 m, 30 m, and 60 m at a frequency of 15 Hz, 30 Hz, and 60 Hz, respectively, computed by means of the 3D coupled FE–$\mathscr{H}$-BE iterative Neumann–Dirichlet method. At 15 Hz, neither a length of 15 m or 30 m is sufficient to create a wave impeding effect similar to the case where the block is assumed to be of infinite length; a block length of 60 m, however, does result in a comparable insertion loss. The wavefield in the soil and the insertion loss at 30 Hz resembles the result of the 2.5D calculation for a block with a length of 30 m or larger, while a good correspondence with the latter is achieved for all lengths at a frequency of 60 Hz.

The observations in figures 16–18 can be interpreted by comparing the length L_y of the block to the free bending wavelength $\lambda_{\mathrm{b}}(\omega)$ of an infinitely long beam. The latter yields $\lambda_{\mathrm{b}}(\omega) = 2\pi\left(\frac{Eh^2}{12\rho\omega^2}\right)^{1/4}$ for an Euler–Bernoulli beam and is equal to 14.50 m, 10.25 m, and 7.25 m at 15 Hz, 30 Hz, and 60 Hz, respectively. This indicates that the block should be approximately twice as long as the free bending wavelength $\lambda_{\mathrm{b}}(\omega)$ in order to create an efficient wave impeding barrier; a vibration reduction efficiency comparable to that of a block of infinite

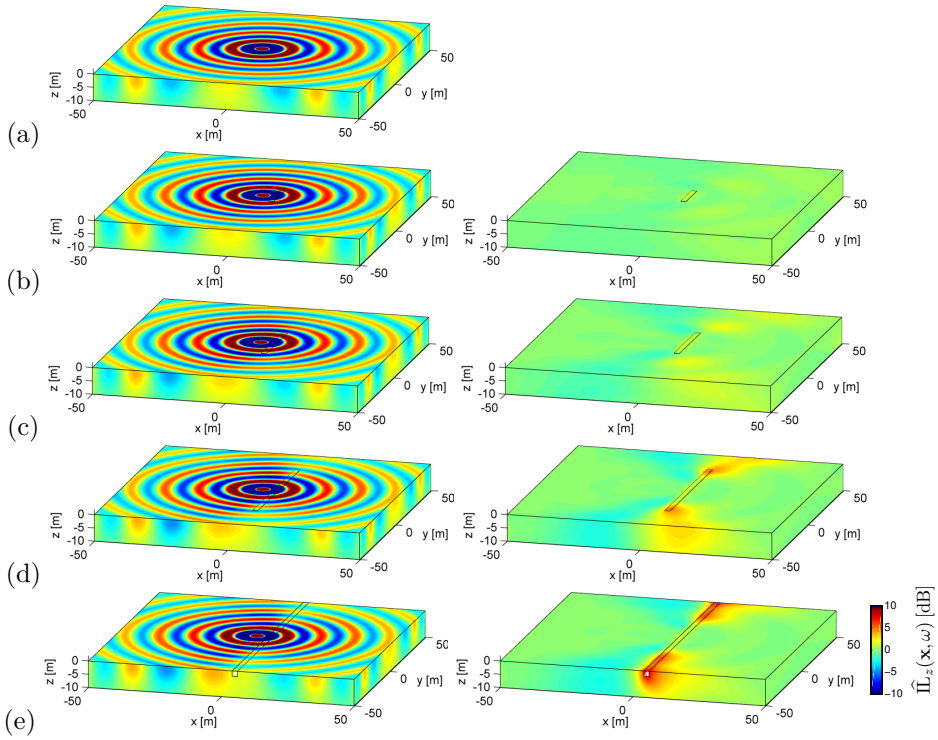

Figure 16: Real part of the vertical displacement $\hat{u}_z(\mathbf{x},\omega)$ due to harmonic excitation at 15 Hz (a) in the reference case and in case a block of stiffened soil is included with a length (b) $L_y = 15\,\mathrm{m}$, (c) $L_y = 30\,\mathrm{m}$, (d) $L_y = 60\,\mathrm{m}$, and (e) $L_y = \infty$ (left hand side). The corresponding insertion loss $\widehat{\mathrm{IL}}_z(\mathbf{x},\omega)$ is shown at the right hand side.

length is then achieved. The finite block is only able, however, to impede the transmission of that part of the wavefield that actually impinges on the block, which is clearly visible for a block of 15 m (figures 16–18b). Furthermore, diffraction occurs at the extremities of the finite block.

6 Conclusions

In this paper, the coupling of FE and $\mathscr{H}$-BE methods has been discussed, illustrating that a subdomain approach is well suited to efficiently solve

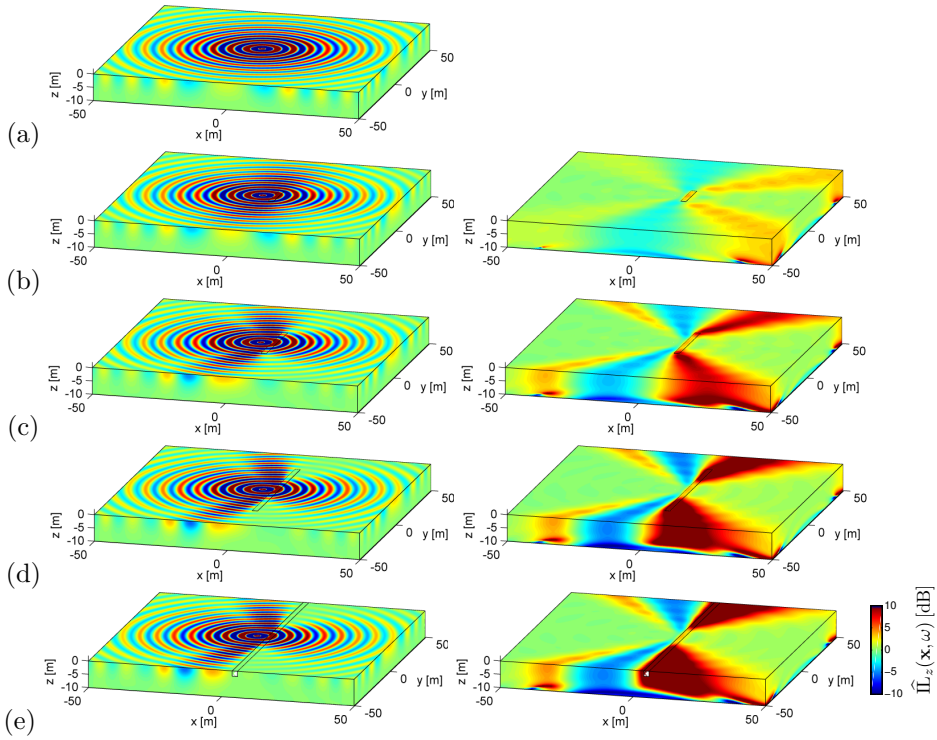

Figure 17: Real part of the vertical displacement $\hat{u}_z(\mathbf{x},\omega)$ due to harmonic excitation at 30 Hz (a) in the reference case and in case a block of stiffened soil is included with a length (b) $L_y = 15\,\mathrm{m}$, (c) $L_y = 30\,\mathrm{m}$, (d) $L_y = 60\,\mathrm{m}$, and (e) $L_y = \infty$ (left hand side). The corresponding insertion loss $\widehat{\mathrm{IL}}_z(\mathbf{x},\omega)$ is shown at the right hand side.

dynamic SSI problems in the frequency domain. The application of $\mathscr{H}$–matrices enables the fast evaluation of large BE models, and the incorporation of Green's functions for a layered halfspace avoids the need to discretize the free surface and the layer interfaces in the modelling of visco–elastodynamic wave propagation in a stratified medium, as illustrated in subsection 4.2.

Direct, iterative and monolithic coupling strategies have been considered in this paper and the numerical verification of each algorithm is presented. An assessment of the computational performance reveals that the direct coupling approach is the least efficient, as the assembly of a dynamic soil stiffness matrix requires the solution of a large amount of $\mathscr{H}$–BE equations. Iterative coupling

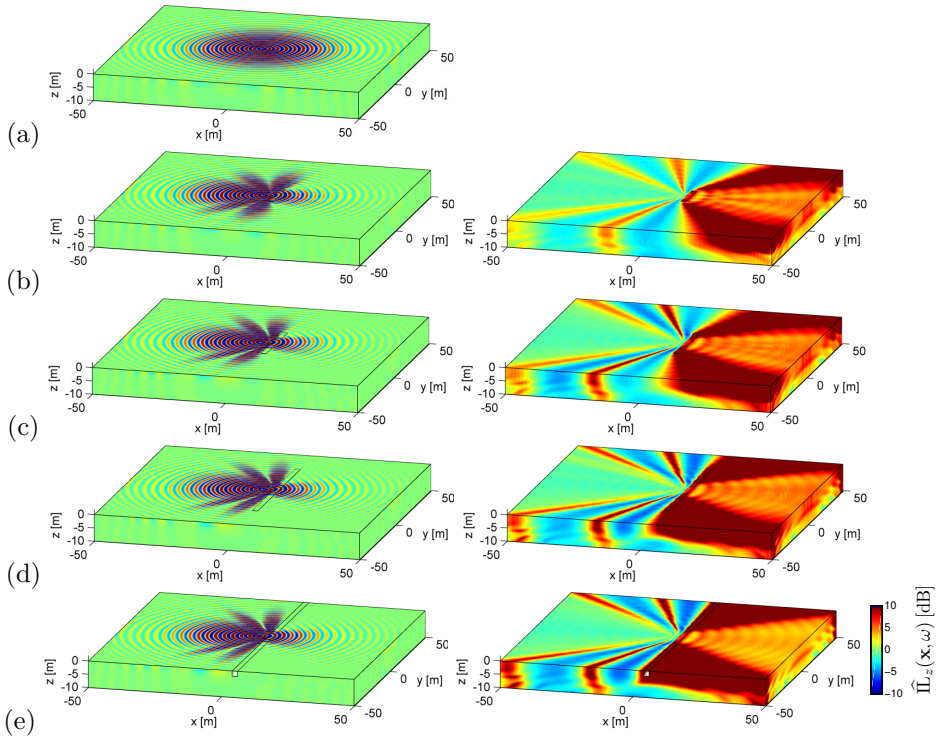

Figure 18: Real part of the vertical displacement $\hat{u}_z(\mathbf{x},\omega)$ due to harmonic excitation at 60 Hz (a) in the reference case and in case a block of stiffened soil is included with a length (b) $L_y = 15\,\mathrm{m}$, (c) $L_y = 30\,\mathrm{m}$, (d) $L_y = 60\,\mathrm{m}$, and (e) $L_y = \infty$ (left hand side). The corresponding insertion loss $\widehat{\mathrm{IL}}_z(\mathbf{x},\omega)$ is shown at the right hand side.

procedures are more efficient, provided that suitable boundary conditions are applied to each subdomain. It is demonstrated that sequential iterative algorithms should be preferred if there exists a strong stiffness contrast between the FE and $\mathscr{H}$-BE subdomain, with Neumann boundary conditions to be imposed on the most stiff subdomain. The application of Aitken's Δ^2–method for the determination of a proper interface relaxation parameter ensures and speeds up the convergence of these sequential algorithms. Parallel iterative algorithms provide a valuable alternative for cases where an a priori estimation of the flexibility of each subdomain is not evident and an appropriate novel relaxation procedure has been proposed for these algorithms. An efficient combination of FE and $\mathscr{H}$–BE models can also be achieved by means of

a monolithic coupling scheme, although the convergence in the examples considered turns out to be relatively slow. This might be improved by the incorporation of an enhanced preconditioner, which is a subject for further research.

Finally, an engineering application related to the mitigation of railway induced vibrations has been presented to illustrate the applicability of coupled FE–$\mathscr{H}$-BE methods to large scale problems. The vibration reduction efficiency of a block of stiffened soil in a homogeneous halfspace has been assessed through 3D calculations, indicating that the length of the block should be approximately twice the free bending wavelength of an infinitely long beam in order to create an efficient wave impeding barrier.

Acknowledgements

The first author is a doctoral fellow and the second author is a postdoctoral fellow of the Research Foundation Flanders (FWO). The results presented in section 5 have been obtained within the frame of the EU FP7 project RIVAS (Railway Induced Vibration Abatement Solutions) [53] under grant agreement No. 265754. The financial support is gratefully acknowledged.

References

[1] Beskos D, Krauthammer T, Vardoulakis I (eds.). *Dynamic soil-structure interaction*, A.A. Balkema, 1984.

[2] Von Estorff O, Hagen C. Iterative coupling of FEM and BEM in 3D transient elastodynamics. *Engineering Analysis with Boundary Elements* 2005; **29**:775–787.

[3] Clouteau D, Elhabre M, Aubry D. Periodic BEM and FEM-BEM coupling: application to seismic behaviour of very long structures. *Computational Mechanics* 2000; **25**:567–577.

[4] Zienkiewicz O, Kelly D, Bettes P. The coupling of the finite element method and boundary solution procedures. *International Journal for Numerical Methods in Engineering* 1977; **11**:355–375.

[5] Hsiao G. The coupling of boundary element and finite element methods. *Zeitschrift für Angewandte Mathematik und Mechanik* 1990; **70**:493–503.

[6] Costabel M, Stephan E. Coupling of finite and boundary element methods for an elastoplastic interface problem. *SIAM Journal on Numerical Analysis* 1990; **27**(5):1212–1226.

[7] Elleithy W, Al-Gahtani HJ, El-Gebeily M. Iterative coupling of BE and FE methods in elastostatics. *Engineering Analysis with Boundary Elements* 2001; **25**:685–695.

[8] Margonari M, Bonnet M. Fast multipole method applied to elastostatic BEM-FEM coupling. *Computers and Structures* 2004; **83**(10–11):700–717.

[9] Rüberg T, Schanz M. Coupling finite and boundary element methods for static and dynamic elastic problems with non-conforming interfaces. *Computer Methods in Applied Mechanics and Engineering* 2008; **198**(3–4):449–458.

[10] Chaillat S, Bonnet M, Semblat JF. A multi-level fast multipole BEM for 3-D elastodynamics in the frequency domain. *Computer Methods in Applied Mechanics and Engineering* 2008; **197**(49–50):4233–4249.

[11] Hackbusch W. A sparse matrix arithmetic based on $\mathscr{H}$-matrices. Part I: Introduction to $\mathscr{H}$-matrices. *Computing* 1999; **62**(2):89–108.

[12] Coulier P, François S, Lombaert G, Degrande G. Application of hierarchical matrices to boundary element methods for elastodynamics based on Green's functions for a horizontally layered halfspace. *Engineering Analysis with Boundary Elements* 2013; **37**(12):1745–1758.

[13] Kausel E, Roësset J. Stiffness matrices for layered soils. *Bulletin of the Seismological Society of America* 1981; **71**(6):1743–1761.

[14] Kausel E. *Fundamental solutions in elastodynamics: a compendium*. Cambridge University Press: New York, 2006.

[15] Grasso E. Modelling visco-elastic seismic wave propagation: a fast-multipole boundary element method and its coupling with finite elements. PhD Thesis, Université Paris-Est 2012.

[16] Soares Jr D, Godinho L. An optimized BEM–FEM iterative coupling algorithm for acoustic–elastodynamic interaction analyses in the frequency domain. *Computers and Structures* 2012; **106–107**:68–80.

[17] Aitken A. Studies in practical mathematics II: The evaluation of the latent roots and latent vectors of a matrix. *Proceedings of the Royal Society of Edinburgh* 1937; **57**:269–304.

[18] Hübner B, Walhorn E, Dinkler D. A monolithic approach to fluid-structure interaction using space-time finite elements. *Computer Methods in Applied Mechanics and Engineering* 2004; **193**(23–26):2087–2104.

[19] Michler C, Hulshoff S, van Brummelen E, de Borst R. A monolithic approach to fluid-structure interaction. *Computers and Fluids* 2004; **33**:839–848.

[20] Zienkiewicz O, Taylor R. *The finite element method, Volume 1: the basis*. Fifth edn., Butterworth-Heinemann: Oxford, United Kingdom, 2000.

[21] Bonnet M. *Boundary integral equation methods for solids and fluids*. John Wiley and Sons: Chichester, United Kingdom, 1995.

[22] Rizzo F, Shippy D, Rezayat M. A boundary integral equation method for radiation and scattering. *International Journal for Numerical Methods in Engineering* 1985; **21**:115–129.

[23] Aubry D, Clouteau D. A regularized boundary element method for stratified media. *Proceedings of the First International Conference on Mathematical and Numerical Aspects of Wave Propagation Phenomena*, Cohen G, Halpern L, Joly P (eds.), SIAM, Philadephia: Strasbourg, France, 1991; 660–668.

[24] Schenck H. Improved integral formulation for acoustic radiation problems. *Journal of the Acoustical Society of America* 1968; **44**:41–58.

[25] Grasedyck L, Hackbusch W. Construction and arithmetics of $\mathscr{H}$-matrices. *Computing* 2003; **70**:295–334.

[26] Bebendorf M. *Hierarchical Matrices: A Means to Efficiently Solve Elliptic Boundary Value Problems*. 1st edn., Springer Publishing Company, 2008.

[27] Rjasanow S, Steinbach O. *The Fast Solution of Boundary Integral Equations (Mathematical and Analytical Techniques with Applications to Engineering)*. Springer-Verlag New York, 2007.

[28] Bebendorf M, Rjasanow S. Adaptive low–rank approximation of collocation matrices. *Computing* 2003; **70**:1–24.

[29] Milazzo A, Benedetti I, Aliabadi M. Hierarchical fast BEM for anisotropic time-harmonic 3-D elastodynamics. *Computers and Structures* 2012; **96–97**:9–24.

[30] Saad Y, Schultz M. GMRES: a generalized minimal residual algorithm for solving nonsymmetric linear systems. *SIAM Journal on Scientific and Statistical Computing* 1986; **7**(3):856–869.

[31] Bebendorf M. Hierarchical *LU* decomposition based preconditioners for BEM. *Computing* 2005; **74**:225–247.

[32] Chaillat S, Semblat JF, Bonnet M. A preconditioned 3-D multi-region fast multipole solver for seismic wave propagation in complex geometries. *Communications in Computational Physics* 2012; **11**(2):594–609.

[33] Saad Y. A flexible inner-outer preconditioned GMRES algorithm. *SIAM Journal on Scientific and Statistical Computing* 1993; **14**(2):461–469.

[34] Von Estorff O, Kausel E. Coupling of boundary and finite elements for soil-structure interaction. *Earthquake Engineering and Structural Dynamics* 1989; **18**:1065–1075.

[35] Clouteau D, Arnst M, Al-Hussaini T, Degrande G. Freefield vibrations due to dynamic loading on a tunnel embedded in a stratified medium. *Journal of Sound and Vibration* 2005; **283**(1–2):173–199. URL `http://dx.doi.org/10.1016/j.jsv.2004.04.010`.

[36] Von Estorff O, Firuziaan M. Coupled BEM/FEM approach for nonlinear soil/structure interaction. *Engineering Analysis with Boundary Elements* 2000; **24**:605–621.

[37] François S, Masoumi H, Degrande G. An iterative coupled boundary-finite element method for the dynamic response of structures. *Proceedings of ISMA2006 International Conference on Noise and Vibration Engineering*, Sas P, De Munck M (eds.), Leuven, Belgium, 2006; 1701–1716.

[38] Soares Jr D, Godinho L, Pereira A, Dors C. Frequency domain analysis of acoustic wave propagation in heterogeneous media considering iterative coupling procedures between the method of fundamental solutions and Kansa's method. *International Journal for Numerical Methods in Engineering* 2012; **89**(7):914–938. URL `http://dx.doi.org/10.1002/nme.3274`.

[39] Elleithy W, Tanaka M. Interface relaxation algorithms for BEM-BEM coupling and FEM-BEM coupling. *Computer Methods in Applied Mechanics and Engineering* 2003; **192**:2977–2992.

[40] Hagen C. Wechselwirkungen zwischen Bauwerk, Boden und Fluid unter transienter Belastung. PhD Thesis, Technischen Universität Hamburg-Harburg 2005.

[41] Mok D, Wall W, Ramm E. Accelerated iterative substructuring schemes for instationary fluid-structure interaction. *Computational Fluid and Solid Mechanics*, Bathe K (ed.). Elsevier, 2001; 1325–1328.

[42] Küttler U, Wall W. Fixed-point fluid-structure interaction solvers with dynamic relaxation. *Computational Mechanics* 2008; **43**(1):61–72.

[43] Irons B, Tuck R. A version of the Aitken accelerator for computer iteration. *International Journal for Numerical Methods in Engineering* 1969; **1**(3):275–277.

[44] Chaillat S, Bonnet M, Semblat JF. A new fast multi-domain BEM to model seismic wave propagation and amplification in 3D geological structures. *Geophysical Journal International* 2009; **177**:509–531.

[45] Langer U, Pusch D. Data-sparse algebraic multigrid methods for large scale boundary element equations. *Applied Numerical Mathematics* 2005; **54**(3–4):406–424.

[46] Schevenels M, François S, Degrande G. EDT: An ElastoDynamics Toolbox for MATLAB. *Computers & Geosciences* 2009; **35**(8):1752–1754. URL `http://dx.doi.org/10.1016/j.cageo.2008.10.012`.

[47] Woods R. Screening of surface waves in soils. *Journal of the Soil Mechanics and Foundation Division, Proceedings of the ASCE* 1968; **94**(SM4):951–979.

[48] Andersen L, Nielsen S. Reduction of ground vibration by means of barriers or soil improvement along a railway track. *Soil Dynamics and Earthquake Engineering* 2005; **25**:701–716.

[49] Sheng X, Jones C, Thompson D. Modelling ground vibrations from railways using wavenumber finite- and boundary-element methods. *Proceedings of the Royal Society A - Mathematical, Physical and Engineering Sciences* 2005; **461**:2043–2070.

[50] Coulier P, François S, Degrande G, Lombaert G. Subgrade stiffening next to the track as a wave impeding barrier for railway induced vibrations. *Soil Dynamics and Earthquake Engineering* 2013; **48**:119–131. URL `http://dx.doi.org/10.1016/j.soildyn.2012.12.009`.

[51] François S, Schevenels M, Lombaert G, Galvín P, Degrande G. A 2.5D coupled FE-BE methodology for the dynamic interaction between longitudinally invariant structures and a layered halfspace. *Computer Methods in Applied Mechanics and Engineering* 2010; **199**(23-24):1536–1548. URL `http://dx.doi.org/10.1016/j.cma.2010.01.001`.

[52] Rayleigh J. On waves propagated along the plane surface of an elastic solid. *Proceedings of the London Mathematical Society* 1887; **17**:4–11.

[53] http://www.rivas-project.eu 2011.

Paper C

A spatial windowing technique to account for finite dimensions in 2.5D dynamic soil–structure interaction problems

Published in Soil Dynamics and Earthquake Engineering 59 (2014) 51–67
http://dx.doi.org/10.1016/j.soildyn.2014.01.006

A spatial windowing technique to account for finite dimensions in 2.5D dynamic soil–structure interaction problems

P. Coulier, A. Dijckmans, S. François, G. Degrande, G. Lombaert
KU Leuven, Department of Civil Engineering,
Kasteelpark Arenberg 40, B-3001 Leuven, Belgium

Abstract

The dynamic interaction between a layered halfspace and quasi translationally invariant structures such as roads, railway tracks, tunnels, dams, and lifelines can be modelled using a computationally efficient 2.5D approach, assuming invariance of the geometry in the longitudinal direction. This assumption is not always fulfilled in practice, however. Even for elongated structures, full 3D computations may be required for an accurate solution of the dynamic soil–structure interaction problem. This paper presents a spatial windowing technique for elastodynamic transmission and radiation problems that allows accounting for the finite length of a structure, still maintaining the computational efficiency of a 2.5D formulation. The proposed technique accounts for the diffraction occurring at the structure's edges, but not for its modal behaviour resulting from reflections of waves at its boundaries. Numerical examples of a barrier for vibration transmission and a surface foundation are discussed to demonstrate the accuracy and applicability of the proposed methodology. Full 3D calculations are performed to provide a rigorous validation for each of these examples. It is demonstrated that the proposed technique is appropriate as long as the response is not dominated by the resonant behaviour of individual modes of the structure.

1 Introduction

The numerical solution of three–dimensional (3D) dynamic soil–structure interaction (SSI) problems is a challenging task, in particular for structures with large dimensions. In order to obtain a substantial reduction of the computational effort, the geometry of the problem is in some cases assumed to be invariant in the longitudinal direction. This allows for the application of an efficient two-and-a-half-dimensional (2.5D) approach, where a Fourier transform of the longitudinal coordinate allows representing the 3D response on a 2D mesh. The assumption seems to be valid for roads, railway tracks, tunnels, dams, vibration isolation screens, lifelines, and alluvial valleys [1].

Many applications of the 2.5D concept can be found in the literature. Gavrić [2, 3] uses 2.5D finite elements (FE) to model thin–walled waveguides, while Stamos and Beskos [4] consider 2.5D boundary elements (BE) to model the seismic response of long lined tunnels embedded in a halfspace. In 2.5D BE formulations, analytical full space Green's functions are commonly used [5]. The discretization of the free surface and the layer interfaces can be avoided, however, by employing Green's functions for a layered halfspace [1]. Coupled FE–BE models allow to model complex geometries with the FE method and to account for the radiation of waves in domains of (semi–)infinite extent with the BE method. 2.5D coupled FE–BE formulations have been presented, among others, by Sheng et al. [6], Andersen and Nielsen [7], and Lombaert et al. [8] for the prediction of railway [6, 7] and road traffic [8] induced vibrations. The efficiency of coupled FE–BE methods is strongly reduced in the case of embedded structures, however, as the Green's functions have to be evaluated for a large number of source/receiver depths for the assembly of the BE matrices. Alternative numerical solution procedures in a 2.5D framework have therefore been formulated as well, such as a 2.5D finite–infinite element approach proposed by Yang et al. [9, 10] or a 2.5D perfectly matched layer (PML) technique described by François et al. [11].

The assumption of longitudinal invariance adopted in 2.5D models is not always fulfilled, however. For example, the length of a vibration isolation screen in the soil is in practice limited and of the same order of magnitude as the wavelength in the soil in the frequency range of interest. Rigorously accounting for the finite length requires the solution of a full 3D dynamic SSI problem, which is computationally very demanding in terms of memory and CPU requirements. The development of adequate numerical methods such as the fast multipole BE method [12] or BE methods based on hierarchical matrices ($\mathscr{H}$–matrices) [13] enables an efficient solution of such large scale problems, but the associated computation times remain relatively high.

In this paper, a spatial windowing technique for elastodynamic transmission and radiation problems is presented that allows accounting for the finite length of a structure, while still maintaining the computational efficiency of a 2.5D formulation. The spatial windowing technique has been proposed by Villot et al. [14] to include the effect of diffraction associated with the finite size of plane structures on sound transmission and radiation. The basic idea of this approach is to apply a spatial rectangular baffle to the structural velocity wavefield of an infinite structure; the windowed wavefield is subsequently employed to compute the radiated wavefield in the wavenumber domain. As a result, only a limited part of the infinite structure contributes to the sound radiation. This technique is mainly used in vibro–acoustic applications, e.g. for the calculation of the transmission loss of sandwich composite panels [15] or for the investigation of the vibro–acoustic response of finite multilayered structures [16] and orthogonally stiffened plates [17]. Spatial windowing is not well suited for acoustic applications at low frequencies (i.e. when individual modes of the structure dominate the response), as it is unable to account for reflected waves at the boundaries to reproduce the resonant behaviour of the modes [17]. At higher frequencies, however, the response shifts from the resonant to the non–resonant mass–law regime and application of the spatial windowing technique leads to results in good agreement with experiments [14, 16, 17].

The aim of this paper is to investigate whether the spatial windowing technique is suited to account for a structure's finite length in 2.5D dynamic SSI problems, using a coupled FE–BE method. Its application to dynamic SSI problems fundamentally differs from acoustic problems, however, as the resonant behaviour of individual modes is strongly affected by the dynamic interaction between the structure and the soil. The text is organized as follows. Section 2 briefly summarizes the governing equations of 3D and 2.5D coupled FE–BE methods. The spatial windowing technique is subsequently introduced in section 3. Numerical examples are considered in sections 4 and 5 to investigate the applicability of the proposed approach. The examples in section 4 involve barriers for vibration transmission in a homogeneous halfspace, which are structures with a finite length that is relatively large compared to the other dimensions. Application of the 2.5D approach hence seems to be appropriate for these cases. Both an empty and filled wave barrier are investigated to determine the influence of the modal behaviour of the structures on the accuracy of the proposed methodology. In section 5, the validity of the spatial windowing technique is further explored by considering a square surface foundation on the soil, which is a structure that can not at all be regarded as invariant. The importance of dynamic SSI is assessed by comparing a foundation on a horizontally layered halfspace to a foundation on a single layer on bedrock. A rigorous validation of the spatial windowing methodology is provided for each of these examples through full 3D computations based on

an efficient coupled FE–$\mathscr{H}$-BE method. Concluding remarks regarding the suitability of the proposed technique are summarized in section 5.

2 Coupled FE–BE methods for dynamic soil–structure interaction

Dynamic SSI problems can be solved by means of a subdomain formulation [18, 19], allowing for the application of different numerical techniques for the soil and the structure. In this paper, finite elements are used to model the structural domain Ω_b, while boundary elements on the soil–structure interface Σ are employed to model wave propagation in the surrounding soil domain Ω_s (figure 1a). Continuity of displacements and equilibrium of stresses are enforced on the interface Σ between the structure and the soil. In the following, it is assumed that tractions $\hat{\hat{\mathbf{t}}}_\mathrm{b}(\omega)$ are imposed on the boundary $\Gamma_{\mathrm{b}\sigma}$ of Ω_b, while an incident wavefield $\hat{\mathbf{u}}_\mathrm{i}(\omega)$ is present in the soil domain Ω_s. A hat above a variable denotes its representation in the frequency domain.

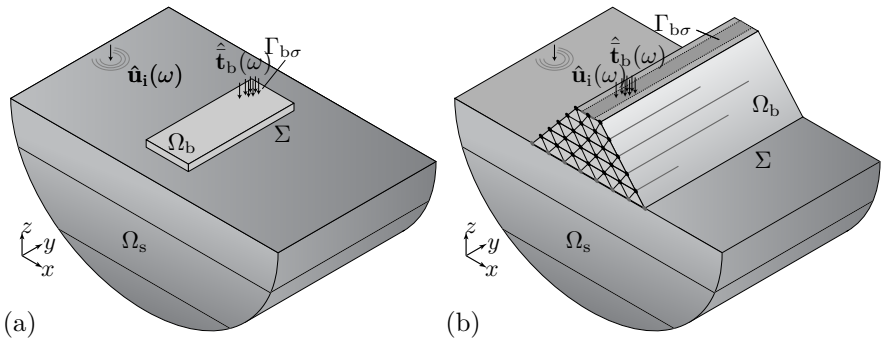

Figure 1: (a) The 3D and (b) the 2.5D dynamic SSI problem, coupling the structural domain Ω_b to the soil domain Ω_s on the soil–structure interface Σ.

2.1 3D coupled FE–BE method

If a structure with an arbitrary geometry is considered, the rigorous solution of a full 3D dynamic SSI problem is required. A weak variational formulation of the equilibrium of the structure Ω_b results in the following coupled FE–BE

equation [18, 20]:

$$\left[\mathbf{K}_\mathrm{b} + \mathbf{C}_\mathrm{b} - \omega^2\mathbf{M}_\mathrm{b} + \widehat{\mathbf{K}}_\mathrm{b}^\mathrm{s}(\omega)\right] \underline{\hat{\mathbf{u}}}_\mathrm{b}(\omega) = \underline{\hat{\mathbf{f}}}_\mathrm{b}(\omega) + \underline{\hat{\mathbf{f}}}_\mathrm{b}^\mathrm{s}(\omega) \tag{1}$$

where $\underline{\hat{\mathbf{u}}}_\mathrm{b}(\omega)$ collects the nodal degrees of freedom of Ω_b, while $\mathbf{K}_\mathrm{b}$, $\mathbf{C}_\mathrm{b}$, and $\mathbf{M}_\mathrm{b}$ are the finite element stiffness, damping, and mass matrices. $\widehat{\mathbf{K}}_\mathrm{b}^\mathrm{s}(\omega)$ is the dynamic soil stiffness matrix and is calculated by means of a 3D BE method. The force vector $\underline{\hat{\mathbf{f}}}_\mathrm{b}(\omega)$ results from tractions $\hat{\tilde{\mathbf{t}}}_\mathrm{b}(\omega)$ imposed on the boundary $\Gamma_{\mathrm{b}\sigma}$, whereas $\underline{\hat{\mathbf{f}}}_\mathrm{b}^\mathrm{s}(\omega)$ denotes dynamic SSI forces at the soil–structure interface Σ associated with the incident wavefield $\hat{\mathbf{u}}_\mathrm{i}(\omega)$ [18, 19]. Solving equation (1) provides the structural response $\underline{\hat{\mathbf{u}}}_\mathrm{b}(\omega)$, which corresponds to the soil displacement vector $\underline{\hat{\mathbf{u}}}_\mathrm{s}(\omega)$ on the soil–structure interface Σ due to continuity. The BE equations allow to retrieve the soil tractions $\underline{\hat{\mathbf{t}}}_\mathrm{s}(\omega)$ on Σ:

$$\underline{\hat{\mathbf{t}}}_\mathrm{s}(\omega) = \widehat{\mathbf{U}}^{-1}(\omega)\left(\widehat{\mathbf{T}}(\omega) + \mathbf{I}\right)\underline{\hat{\mathbf{u}}}_\mathrm{s}(\omega) \tag{2}$$

where $\widehat{\mathbf{U}}(\omega)$ and $\widehat{\mathbf{T}}(\omega)$ are BE matrices, requiring integration of the Green's displacements and tractions, respectively. The displacements $\underline{\hat{\mathbf{u}}}_\mathrm{s}(\omega)$ and tractions $\underline{\hat{\mathbf{t}}}_\mathrm{s}(\omega)$ on Σ are subsequently used to evaluate the radiated wavefield $\underline{\hat{\mathbf{u}}}_\mathrm{r}(\omega)$ in the soil through the discretized boundary integral equation:

$$\underline{\hat{\mathbf{u}}}_\mathrm{r}(\omega) = \widehat{\mathbf{U}}_\mathrm{s}(\omega)\underline{\hat{\mathbf{t}}}_\mathrm{s}(\omega) - \widehat{\mathbf{T}}_\mathrm{s}(\omega)\underline{\hat{\mathbf{u}}}_\mathrm{s}(\omega) \tag{3}$$

where $\widehat{\mathbf{U}}_\mathrm{s}(\omega)$ and $\widehat{\mathbf{T}}_\mathrm{s}(\omega)$ are BE transfer matrices.

3D FE–BE models can be used to solve dynamic SSI problems of any size as long as the proper computational resources are available. The fully populated unsymmetric matrices $\widehat{\mathbf{U}}(\omega)$ and $\widehat{\mathbf{T}}(\omega)$ arising from classical BE formulations lead to stringent memory and CPU requirements, however, restricting the applicability of the method to problems of moderate size. These drawbacks can be circumvented through the application of fast BE methods [12, 13]. In this paper, a fast BE method based on $\mathscr{H}$–matrices [21] is employed for the solution of 3D problems; the reader is referred to the literature [13, 22, 23] for a comprehensive overview of this methodology. The application of $\mathscr{H}$–matrices renders the conventional FE–BE coupling strategy of equation (1) less efficient, however, as it requires the assembly of a dynamic soil stiffness matrix [24]. An alternative iterative Neumann–Dirichlet algorithm is therefore employed, in which the governing equations of the FE and BE subdomain are solved separately, while the boundary conditions at the soil–structure interface are updated until convergence is achieved. A detailed description of this coupling approach can be found in [24].

Although the application of fast BE methods allows increasing the problem size considerably compared to classical BE formulations, the solution of large scale

problems remains computationally very demanding. Additional assumptions can be made to simplify the problem, as will be discussed in the next subsection.

2.2 2.5D coupled FE–BE method

In the case of structures with a longitudinally invariant geometry (figure 1b), the longitudinal coordinate y can be transformed to the wavenumber k_y by means of a forward Fourier transform $\mathscr{F}[f(y), k_y] = \int_{-\infty}^{+\infty} f(y) \exp(ik_y y)\, \mathrm{d}y$, resulting in a computationally efficient 2.5D solution procedure in the frequency–wavenumber domain. As the 3D response can hence be represented on a 2D mesh [1], a substantial reduction of the number of degrees of freedom (and the associated matrix dimensions) is achieved. The governing equations are briefly summarized in this subsection; an extensive discussion of the 2.5D coupled FE–BE methodology can be found in [1, 25].

The dynamic equilibrium equation of the coupled FE–BE system reads as follows in the frequency–wavenumber domain [1]:

$$\left[\tilde{\mathbf{K}}_{\mathrm{b}}(k_y,\omega) + \mathbf{C}_{\mathrm{b}} - \omega^2 \mathbf{M}_{\mathrm{b}} + \tilde{\mathbf{K}}^{\mathrm{s}}_{\mathrm{b}}(k_y,\omega)\right] \underline{\tilde{\mathbf{u}}}_{\mathrm{b}}(k_y,\omega) = \underline{\tilde{\mathbf{f}}}_{\mathrm{b}}(k_y,\omega) + \underline{\tilde{\mathbf{f}}}^{\mathrm{s}}_{\mathrm{b}}(k_y,\omega) \tag{4}$$

where a tilde above a variable denotes its representation in the frequency–wavenumber domain. This equilibrium equation is similar to the 3D coupled FE–BE equation (1), except that the stiffness matrices, the displacement vector, and the load vectors become wavenumber dependent. Solving equation (4) provides the structural response $\underline{\tilde{\mathbf{u}}}_{\mathrm{b}}(k_y,\omega)$, corresponding to the soil displacements $\underline{\tilde{\mathbf{u}}}_{\mathrm{s}}(k_y,\omega)$ on the soil–structure interface Σ. The BE equations allow to retrieve the soil tractions $\underline{\tilde{\mathbf{t}}}_{\mathrm{s}}(k_y,\omega)$:

$$\underline{\tilde{\mathbf{t}}}_{\mathrm{s}}(k_y,\omega) = \widetilde{\mathbf{U}}^{-1}(k_y,\omega) \left(\widetilde{\mathbf{T}}(k_y,\omega) + \mathbf{I}\right) \underline{\tilde{\mathbf{u}}}_{\mathrm{s}}(k_y,\omega) \tag{5}$$

where $\widetilde{\mathbf{U}}(k_y,\omega)$ and $\widetilde{\mathbf{T}}(k_y,\omega)$ are wavenumber dependent BE matrices. The representation theorem expressed in the frequency–wavenumber domain finally allows for the computation of the radiated wavefield $\underline{\tilde{\mathbf{u}}}_{\mathrm{r}}(k_y,\omega)$ in the soil [1]. The latter corresponds to the discretized boundary integral equation (3), where each variable should be replaced by its wavenumber dependent counterpart:

$$\underline{\tilde{\mathbf{u}}}_{\mathrm{r}}(k_y,\omega) = \widetilde{\mathbf{U}}_{\mathrm{s}}(k_y,\omega) \underline{\tilde{\mathbf{t}}}_{\mathrm{s}}(k_y,\omega) - \widetilde{\mathbf{T}}_{\mathrm{s}}(k_y,\omega) \underline{\tilde{\mathbf{u}}}_{\mathrm{s}}(k_y,\omega) \tag{6}$$

The application of a 2.5D approach in the frequency–wavenumber domain implies that the equations have to be assembled and solved for each wavenumber k_y. The response in the frequency–spatial domain can finally

be found by means of an inverse Fourier transform $\mathscr{F}^{-1}\left[\tilde{f}(k_y), y\right] = \frac{1}{2\pi}\int_{-\infty}^{+\infty} \tilde{f}(k_y)\exp\left(-ik_y y\right)\,\mathrm{d}k_y$ from the wavenumber k_y to the longitudinal coordinate y, using an efficient Filon quadrature scheme [26].

3 2.5D coupled FE–BE method with spatial windowing

The spatial windowing technique has been presented by Villot et al. [14] to account for the finite size of a plane structure in sound transmission and radiation calculations. This section describes how this technique can be incorporated in the 2.5D coupled FE–BE method to account for the finite length of a structure in dynamic SSI problems.

Consider a plane wave with a constant longitudinal wavenumber k_{y0} travelling along an infinite structure. The displacement field in the spatial domain yields:

$$\hat{u}(y,\omega) = \frac{1}{2\pi}\hat{u}_0(\omega)\exp\left(-ik_{y0}y\right) \tag{7}$$

while the wavenumber spectrum corresponds to a Dirac delta function at $k_y = k_{y0}$ (figure 2a):

$$\tilde{u}(k_y,\omega) = \int_{-\infty}^{+\infty} \frac{1}{2\pi}\hat{u}_0(\omega)\exp\left(-ik_{y0}y\right)\exp\left(ik_y y\right)\,\mathrm{d}y \tag{8}$$

$$= \hat{u}_0(\omega)\delta\left(k_y - k_{y0}\right) \tag{9}$$

A structure with a finite length L_y, situated between y_1 and $y_2 = y_1 + L_y$, is only able to contribute to the radiation of waves into the soil domain Ω_s from y_1 to y_2. The wavenumber spectrum of the displacement field is consequently determined by applying a forward Fourier transform to equation (7), restricting the integration in equation (8) to $y \in [y_1, y_2]$:

$$\tilde{u}_\mathrm{sw}(k_y,\omega) = \int_{y_1}^{y_2} \frac{1}{2\pi}\hat{u}_0(\omega)\exp\left(-ik_{y0}y\right)\exp\left(ik_y y\right)\,\mathrm{d}y \tag{10}$$

$$= \frac{1}{2\pi}\hat{u}_0(\omega)\frac{\exp\left[i\left(k_y - k_{y0}\right)y_2\right]}{i\left(k_y - k_{y0}\right)}\left(1 - \exp\left[-i\left(k_y - k_{y0}\right)L_y\right]\right) \tag{11}$$

with $\lim_{k_y \to k_{y0}} \tilde{u}_{\mathrm{sw}}(k_y, \omega) = \frac{1}{2\pi}\hat{u}_0(\omega)L_y$. The subscript 'sw' refers to a spatially windowed quantity. Equation (11) reveals that spatial windowing results in a distribution of the energy over the entire wavenumber range [14], while it was originally concentrated at $k_y = k_{y0}$. This is illustrated in figure 2.

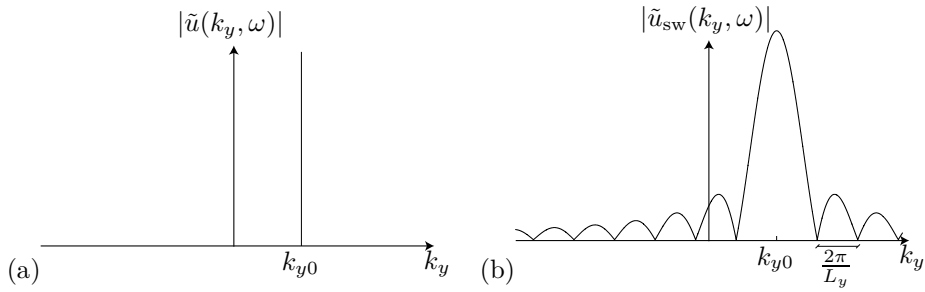

Figure 2: Wavenumber spectrum of a plane wave with wavenumber k_{y0} propagating in an infinite structure (a) before and (b) after application of the spatial windowing technique.

Application of the spatial windowing technique in the framework of the 2.5D FE–BE methodology outlined in subsection 2.2 implies that the contribution of each wavenumber component of the displacement vector $\underline{\tilde{\mathbf{u}}}_{\mathrm{s}}(k_y, \omega)$ is distributed over the entire wavenumber domain according to equation (11). The spatially windowed displacement vector $\underline{\tilde{\mathbf{u}}}_{\mathrm{s,sw}}(k_y, \omega)$ can hence be expressed as:

$$\begin{aligned}\underline{\tilde{\mathbf{u}}}_{\mathrm{s,sw}}(k_y, \omega) &= \underline{\tilde{\mathbf{u}}}_{\mathrm{s}}(k_y, \omega) * \left[\frac{1}{2\pi}\frac{\exp(ik_y y_2)}{ik_y}\left(1 - \exp\left[-ik_y L_y\right]\right)\right] \\ &= \underline{\tilde{\mathbf{u}}}_{\mathrm{s}}(k_y, \omega) * \tilde{w}(k_y) \end{aligned} \tag{12}$$

where $*$ indicates convolution. Spatially windowed interface tractions $\underline{\tilde{\mathbf{t}}}_{\mathrm{s,sw}}(k_y, \omega)$ are defined analogously. The radiated wavefield in the soil $\underline{\tilde{\mathbf{u}}}_{\mathrm{r,sw}}(k_y, \omega)$ is finally computed by means of the representation formula (6), substituting $\underline{\tilde{\mathbf{u}}}_{\mathrm{s}}(k_y, \omega)$ and $\underline{\tilde{\mathbf{t}}}_{\mathrm{s}}(k_y, \omega)$ by their spatially windowed equivalents $\underline{\tilde{\mathbf{u}}}_{\mathrm{s,sw}}(k_y, \omega)$ and $\underline{\tilde{\mathbf{t}}}_{\mathrm{s,sw}}(k_y, \omega)$, respectively.

The windowing function $\tilde{w}(k_y)$ in equation (12) has zeros at $k_y = 2\pi n/L_y$, with $n = \pm 1, \pm 2, \pm 3, \ldots$ A sufficiently fine wavenumber sampling is required for an accurate representation of the lobes of $\tilde{w}(k_y)$; the interval between two subsequent zeros $\Delta k_y = 2\pi/L_y$ (figure 2) is therefore discretized using 16 samples for all calculations presented in this paper. The resulting sampling of $\tilde{w}(k_y)$ hence depends on the length L_y and can be finer or coarser than the sampling of $\underline{\tilde{\mathbf{u}}}_{\mathrm{s}}(k_y, \omega)$ and $\underline{\tilde{\mathbf{t}}}_{\mathrm{s}}(k_y, \omega)$; either $\tilde{w}(k_y)$ or $\underline{\tilde{\mathbf{u}}}_{\mathrm{s}}(k_y, \omega)$ and $\underline{\tilde{\mathbf{t}}}_{\mathrm{s}}(k_y, \omega)$ needs to be upsampled before the convolution of equation (12) can be performed.

A fine sampling of $\tilde{w}(k_y)$ is in particular required for very elongated structures, but the additional computational cost for upsampling $\underline{\tilde{\mathbf{u}}}_{\mathrm{s}}(k_y, \omega)$ and $\underline{\tilde{\mathbf{t}}}_{\mathrm{s}}(k_y, \omega)$ is negligible.

Equation (12) indicates that the spatial windowing technique only entails postprocessing of the original 2.5D results. A major limitation of the technique is, however, its inability to account for reflected waves generated at the boundaries of a finite structure to reproduce the resonant behaviour of the modes; only the diffraction due to a structure's finite length is considered.

4 Application of spatial windowing to elongated structures: vibration isolation screen

Numerical examples are considered in sections 4 and 5 to validate the spatial windowing technique and to investigate its applicability. The examples in section 4 involve structures of which one dimension is relatively large compared to the other dimensions, while this is not the case in section 5. For each case, a rigorous validation is provided by means of 3D calculations through the FE–$\mathscr{H}$-BE methodology mentioned in subsection 2.1. All calculations have been performed on Intel® Xeon® E5520 (2.26 GHz) CPUs.

The applications in subsections 4.1 and 4.2 are related to railway induced ground vibration, which can lead to vibration annoyance in buildings in close proximity of railway tracks. In order to reduce the levels of building vibration, mitigation measures on the transmission path between source (railway track) and receiver (building) can be implemented. Examples of such measures are vibration isolation screens [27], buried wall barriers [7], and wave impeding blocks [6]. In subsection 4.1, an open trench is discussed, which aims at reflecting the impinging waves and is known to be very effective for a trench depth greater than about 0.60 times the Rayleigh wavelength in the soil [27]. Trenches are assumed to be infinitely long in most of the numerical studies reported in the literature [28–30]; this assumption is not fulfilled in practice, however. A numerical and experimental study on trenches of finite length has been presented by Banerjee et al. [31]. It is shown next how the spatial windowing technique allows accounting for the finite length of the trench. As this merely involves postprocessing of the original 2.5D results, parametric studies to investigate the effect of a finite length can be performed at relatively low computational cost. The case of an in–filled trench will be discussed in subsection 4.2.

4.1 Open trench

The vibration reduction efficiency of an open trench in a halfspace is investigated in this subsection. The halfspace is characterized by a shear wave velocity $C_\mathrm{s} = 200\,\mathrm{m/s}$, a dilatational wave velocity $C_\mathrm{p} = 400\,\mathrm{m/s}$, a density $\rho = 2000\,\mathrm{kg/m^3}$, and material damping ratios $\beta_\mathrm{s} = \beta_\mathrm{p} = 0.025$ in deviatoric and volumetric deformation. The trench has a width $w = 2\,\mathrm{m}$, a depth $d = 2\,\mathrm{m}$, a length L_y, is situated at a distance $\mathscr{D} = 4\,\mathrm{m}$ from the y–axis, and is positioned symmetrically with respect to the x-axis, i.e. $y_1 = -L_y/2$ and $y_2 = L_y/2$ (figure 3a). The width of the trench is chosen in view of the case study of an in–filled trench that will be considered in subsection 4.2. The numerical analysis is performed for trenches with a length of 15 m, 30 m, and 60 m. The dimensionless trench depth $\bar{d}$ is defined as $d/\lambda_\mathrm{R}(f)$, where $\lambda_\mathrm{R}(f)$ is the frequency dependent Rayleigh wavelength in the soil; a value $\bar{d} = 0.60$ is obtained at 56 Hz. In order to facilitate physical interpretation, an incident wavefield is generated by the application of a unit vertical harmonic point load at the origin of the coordinate system, rather than considering a train passage.

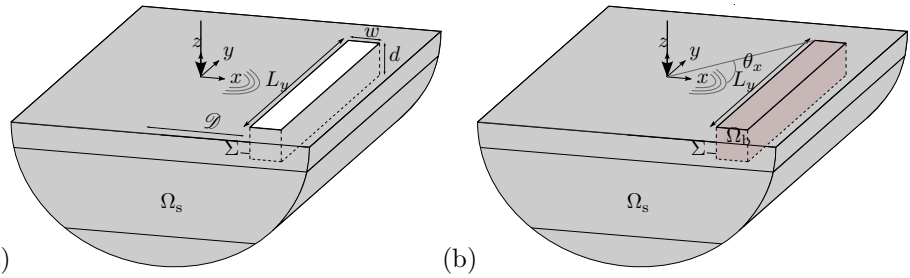

Figure 3: The soil domain Ω_s with (a) an open trench or (b) a block of stiffened soil Ω_b with finite length L_y.

The spatial windowing technique outlined in section 3 is used to calculate the wavefield in the soil, accounting for the presence of the open trench with length L_y. The interface Σ of the trench is modelled with 30 2.5D boundary elements; the element dimensions are limited in order to ensure that 10 elements per shear wavelength $\lambda_\mathrm{s} = C_\mathrm{s}/f$ are used at a frequency of 100 Hz. Coupling of the boundary elements to finite elements is not required, as no in–fill material is considered. The 2.5D computations with spatial windowing are compared to 3D $\mathscr{H}$-BE calculations, where four–node quadrilateral boundary elements are employed to discretize the interface Σ. The properties of the resulting 3D discretizations are listed in table 1; the last three columns are irrelevant for the present application. Eight elements per shear wavelength are provided at

100 Hz. Figures 4a and 4b show the BE discretization of an open trench with a length of 60 m used in the 2.5D BE model with spatial windowing and the 3D $\mathscr{H}$-BE model, respectively. These figures clearly illustrate that the 2.5D approach results in a significant reduction of the number of elements. The discretization of the free surface is avoided in both approaches by employing Green's functions for a halfspace in the 2.5D BE and 3D $\mathscr{H}$-BE formulations [1, 21].

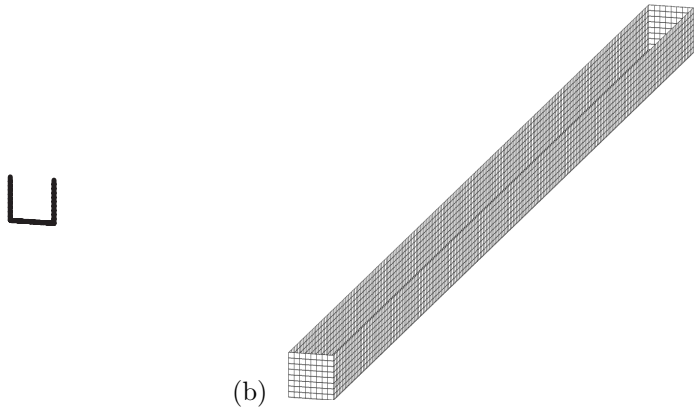

(a) (b)

Figure 4: BE discretization of an open trench with a length of 60 m used in (a) the 2.5D BE model with spatial windowing and (b) the 3D $\mathscr{H}$-BE model.

The vibration reduction efficiency of a trench is characterized through the vertical insertion loss $\widehat{\mathrm{IL}}_z(\mathbf{x},\omega)$:

$$\widehat{\mathrm{IL}}_z(\mathbf{x},\omega) = 20\log_{10}\frac{|\hat{u}_z^{\mathrm{ref}}(\mathbf{x},\omega)|}{|\hat{u}_z(\mathbf{x},\omega)|} \tag{13}$$

which compares the vertical displacement $\hat{u}_z^{\mathrm{ref}}(\mathbf{x},\omega)$ in the reference case (without a trench) to the vertical displacement $\hat{u}_z(\mathbf{x},\omega)$ in case a trench is included; positive values of the insertion loss indicate a reduction of the vertical free field vibrations. Figures 5–7 show the insertion loss $\widehat{\mathrm{IL}}_z(\mathbf{x},\omega)$ for a trench with a length of 15 m, 30 m, and 60 m at 15 Hz, 30 Hz, and 60 Hz, respectively. The dimensionless trench depth equals $\bar{d} = 0.16$ at 15 Hz, $\bar{d} = 0.32$ at 30 Hz, and $\bar{d} = 0.64$ at 60 Hz. The insertion loss remains rather limited at 15 Hz, as a significant part of the energy still passes underneath the trench. The penetration depth of the Rayleigh waves decreases at higher frequencies, causing reflection of the waves by the trench and resulting in insertion losses up to 10 dB and more at 30 Hz and 60 Hz. Extending the length of the trench leads

L_y [m]	# BE elements [−]	# BE nodes [−]	# BE DOFs [−]	# FE elements [−]	# FE nodes [−]	# FE DOFs [−]
15	1568	1637	4911	3840	4941	14823
30	3008	3137	9411	7680	9801	29403
60	5888	6137	18411	15360	19521	58563

Table 1: Properties of the BE and FE discretizations of an open trench (only BE) or a block of stiffened soil (BE and FE) with a length of 15 m, 30 m, and 60 m.

to an enlargement of the area where vibration levels are effectively reduced. The results are furthermore compared to rigorous 3D $\mathscr{H}$-BE calculations, and an almost perfect agreement between the spatially windowed 2.5D and the 3D computations is observed for all trench lengths and at all frequencies under concern. The correspondence is not only apparent at the surface of the halfspace, but also at depth. A quantitative assessment of the accuracy of the spatial windowing technique is given in figure 8. This figure shows the relative error $\hat{\varepsilon}(\mathbf{x},\omega)$, which is defined as:

$$\hat{\varepsilon}(\mathbf{x},\omega) = \frac{|\hat{u}_{z,\mathrm{sw}}(\mathbf{x},\omega) - \hat{u}_z(\mathbf{x},\omega)|}{|\hat{u}_{z\mathrm{i}}(\mathbf{x},\omega)|} \tag{14}$$

where $\hat{u}_{z,\mathrm{sw}}(\mathbf{x},\omega)$ and $\hat{u}_z(\mathbf{x},\omega)$ represent the vertical displacement obtained with a 2.5D model with spatial windowing and a 3D model, respectively, while $\hat{u}_{z\mathrm{i}}(\mathbf{x},\omega)$ is the incident wavefield. The error $|\hat{u}_{z,\mathrm{sw}}(\mathbf{x},\omega) - \hat{u}_z(\mathbf{x},\omega)|$ is normalized in equation (14) with respect to the incident wavefield $\hat{u}_{z\mathrm{i}}(\mathbf{x},\omega)$ instead of $\hat{u}_z(\mathbf{x},\omega)$; this avoids a blow up of $\hat{\varepsilon}(\mathbf{x},\omega)$ if $\hat{u}_z(\mathbf{x},\omega)$ attains a very small value, which is especially the case behind the trench. It is clear in figure 8 that the error is negligibly small at 15 Hz for all trench lengths. The error also remains limited at higher frequencies, although some larger deviations (up to 50%) can be observed in concentrated areas, mainly near the trench's edges. The error is sufficiently small in the main region of interest (i.e. just behind the trench) to conclude that the proposed spatial windowing technique is capable of accurately accounting for the finite length of the trench. As there is no in–fill material in the open trench, the wavefield in the soil cannot be affected by the resonant behaviour of structural modes, explaining why the spatial windowing technique is particularly well suited for the case under concern. The existence of structural modes might affect the accuracy of the proposed technique, however, as will be investigated in the following subsection.

The 2.5D calculations based on the assumption of longitudinal invariance (i.e. without spatial windowing) are shown in figures 5–7d. A comparison of figures 5–7a–c and 5–7d clearly indicates that accounting for the finite length of the trench is important to correctly assess the vibration reduction efficiency. A trench of limited length is only able to reflect that part of the wavefield that impinges on the trench, which is clearly visible for a trench of 15 m (figures 5–7a). Furthermore, diffraction around the edges of a finite trench leads to a decreased efficiency in part of the shadow zone. Both phenomena are accounted for in the spatial windowing technique.

The results can also be interpreted by considering the insertion loss $\widetilde{\mathrm{IL}}_z(x,\bar{k}_y,z,\omega)$ in the frequency–wavenumber domain. The latter is defined in a similar way as in equation (13), but now for the frequency–wavenumber domain representation of the vertical free field displacement. The dimensionless

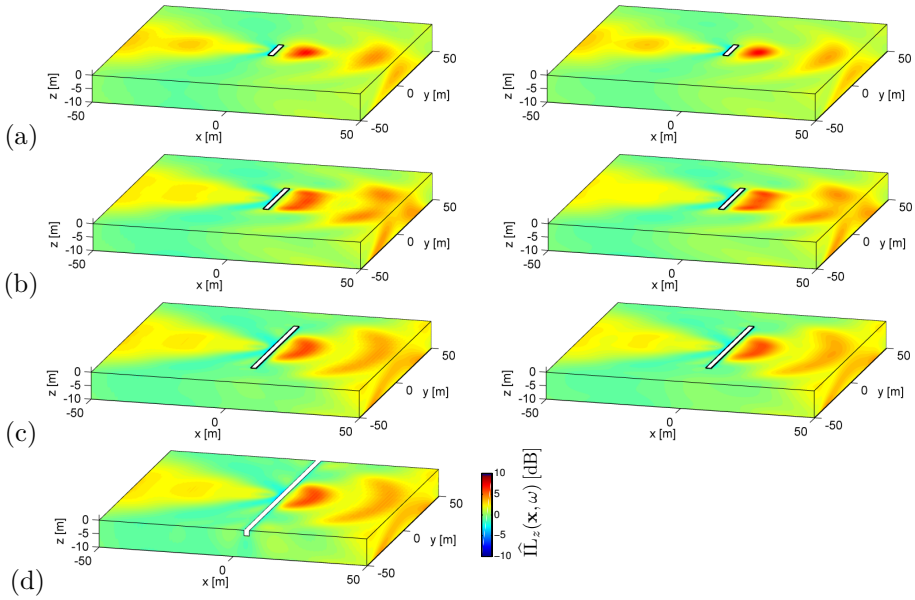

Figure 5: Vertical insertion loss $\widehat{\mathrm{IL}}_z(\mathbf{x},\omega)$ at 15 Hz for an open trench in a halfspace with a length (a) $L_y = 15\,\mathrm{m}$, (b) $L_y = 30\,\mathrm{m}$, (c) $L_y = 60\,\mathrm{m}$, and (d) $L_y = \infty$, calculated by means of a 2.5D BE model with spatial windowing (left hand side) or a 3D $\mathscr{H}$-BE model (right hand side).

wavenumber $\bar{k}_y$ is defined as $\bar{k}_y = k_y C_\mathrm{s}/\omega$, where C_s is the shear wave velocity of the halfspace. Figure 9d shows the insertion loss $\widetilde{\mathrm{IL}}_z(x = 8\,\mathrm{m}, \bar{k}_y, z = 0\,\mathrm{m}, \omega)$ on the surface of the halfspace at 8 m from the point of excitation for an infinitely long open trench in a halfspace; the insertion loss is only shown in a range $0 \leq \bar{k}_y \leq \bar{k}_\mathrm{R}$, with $\bar{k}_\mathrm{R} = C_\mathrm{s}/C_\mathrm{R}$ the dimensionless wavenumber corresponding to a Rayleigh wave propagating in the y-direction. Outside this range, waves do not propagate in the x-direction, as the lateral wavenumber $\bar{k}_x = -i\sqrt{\bar{k}_y^2 - \bar{k}_\mathrm{R}^2}$ is imaginary for $\bar{k}_y > \bar{k}_\mathrm{R}$, resulting in evanescent waves. The dispersion curve of a Rayleigh wave propagating in the y-direction is a horizontal line due to its non–dispersive character in a homogeneous halfspace. It is observed in figure 9d that no significant reduction of vibration levels can be achieved below 20 Hz, as the dimensionless trench depth $\bar{d}$ is only 0.20 at this frequency. The insertion loss increases up to 4 to 6 dB in the frequency range between 20 Hz and 45 Hz, while it tends to 10 dB and more above 45 Hz. This frequency corresponds to a dimensionless trench depth $\bar{d} = 0.50$, approximately confirming the rule of

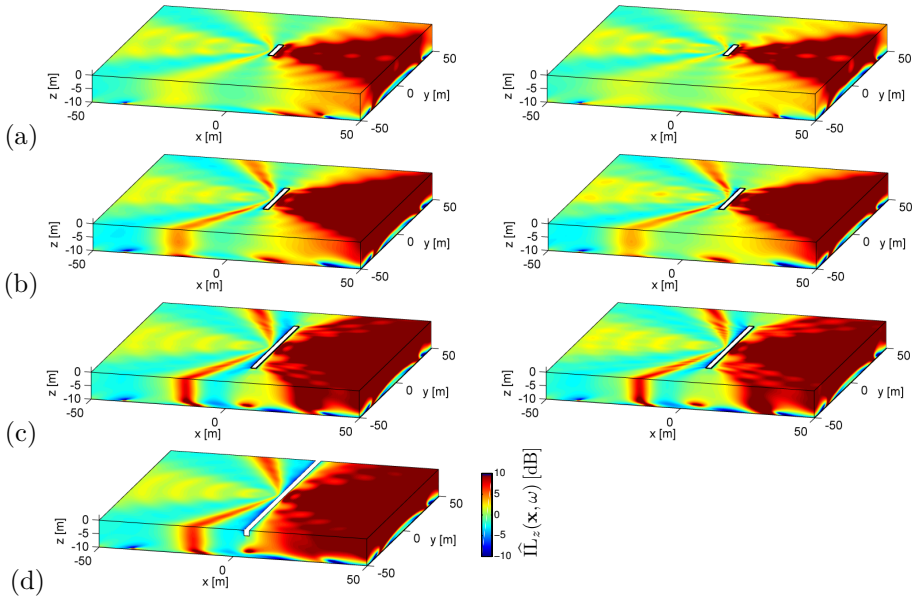

Figure 6: Vertical insertion loss $\widehat{\mathrm{IL}}_z(\mathbf{x},\omega)$ at 30 Hz for an open trench in a halfspace with a length (a) $L_y = 15\,\mathrm{m}$, (b) $L_y = 30\,\mathrm{m}$, (c) $L_y = 60\,\mathrm{m}$, and (d) $L_y = \infty$, calculated by means of a 2.5D BE model with spatial windowing (left hand side) or a 3D $\mathscr{H}$-BE model (right hand side).

thumb which states that an open trench is effective from $\bar{d} = 0.60$ on [27].

Figures 9a–c show the insertion loss $\widetilde{\mathrm{IL}}_z(x = 8\,\mathrm{m}, \bar{k}_y, z = 0\,\mathrm{m}, \omega)$ for an open trench in a halfspace with a length of 15 m, 30 m, or 60 m, respectively; these results are obtained by means of the spatial windowing technique. The displacements on the interface Σ that are used for the determination of the vertical displacement $\tilde{u}_z(x = 8\,\mathrm{m}, \bar{k}_y, z = 0\,\mathrm{m}, \omega)$ in the soil and the corresponding insertion loss $\widetilde{\mathrm{IL}}_z(x = 8\,\mathrm{m}, \bar{k}_y, z = 0\,\mathrm{m}, \omega)$ in figure 9d are thus first modified by the convolution operation defined in equation (12) and are subsequently used in the representation formula (6) for the computation of $\tilde{u}_{z,\mathrm{sw}}(x = 8\,\mathrm{m}, \bar{k}_y, z = 0\,\mathrm{m}, \omega)$ and the insertion loss $\widetilde{\mathrm{IL}}_z(x = 8\,\mathrm{m}, \bar{k}_y, z = 0\,\mathrm{m}, \omega)$ in figures 9a–c. As indicated above, a trench of finite length is only able to reflect that part of the wavefield that actually impinges on the trench and no reduction of vibration levels is achieved for wavenumbers $\bar{k}_y$ larger than

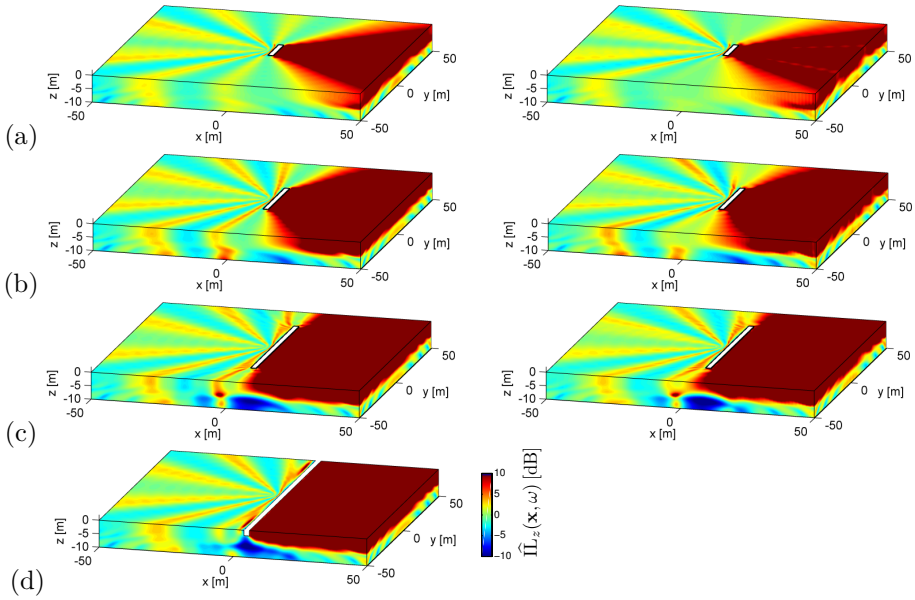

Figure 7: Vertical insertion loss $\widehat{\mathrm{IL}}_z(\mathbf{x},\omega)$ at 60 Hz for an open trench in a halfspace with a length (a) $L_y = 15\,\mathrm{m}$, (b) $L_y = 30\,\mathrm{m}$, (c) $L_y = 60\,\mathrm{m}$, and (d) $L_y = \infty$, calculated by means of a 2.5D BE model with spatial windowing (left hand side) or a 3D $\mathscr{H}$-BE model (right hand side).

$\bar{k}_\mathrm{R} \sin\theta_x$, where $\sin\theta_x$ corresponds to (figure 3):

$$\sin\theta_x = \frac{L_y/2}{\sqrt{\mathscr{D}^2 + (L_y/2)^2}} \tag{15}$$

This is confirmed in figures 9a–c, as the insertion loss in the $(\omega, \bar{k}_y)$–domain remains limited for $\bar{k}_y > \bar{k}_\mathrm{R} \sin\theta_x$.

The computational effort for the 2.5D computations (with or without spatial windowing) is considerably lower than for the full 3D calculations, as is demonstrated in tables 2 and 3. Table 2 summarizes the amount of RAM memory required for the storage of the BE matrices $\widetilde{\mathbf{U}}(k_y,\omega)$ and $\widetilde{\mathbf{T}}(k_y,\omega)$ or $\widehat{\mathbf{U}}(\omega)$ and $\widehat{\mathbf{T}}(\omega)$ in the 2.5D BE or 3D $\mathscr{H}$-BE models, respectively. The amount of RAM memory that would have been required in a classical 3D BE model without the application of $\mathscr{H}$–matrices is indicated as well. It is clearly illustrated in table 2 that the 2.5D approach results in a substantial reduction

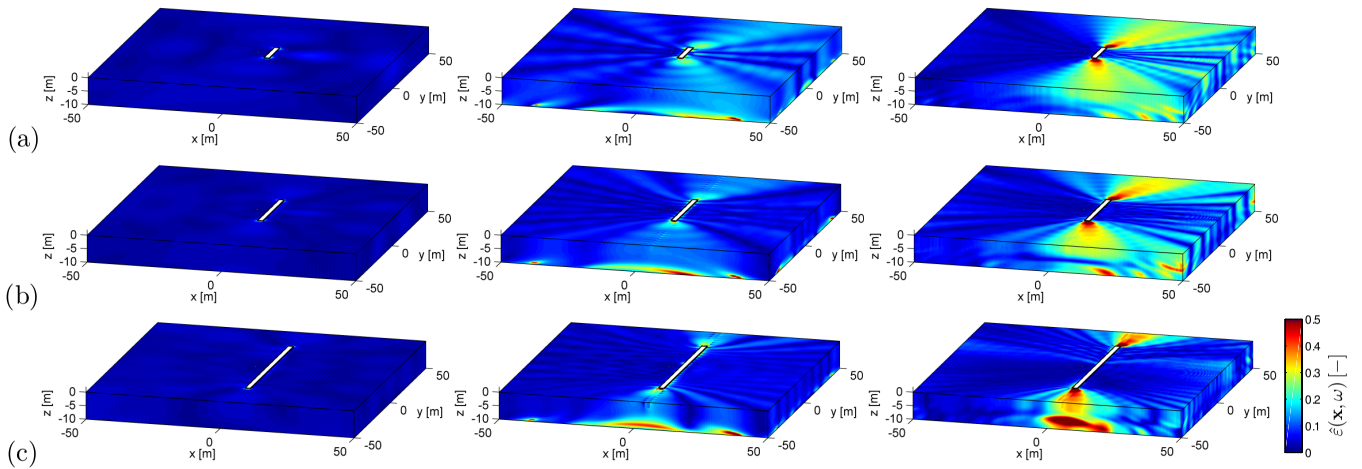

Figure 8: Relative error $\hat{\varepsilon}(\mathbf{x},\omega)$ for an open trench in a halfspace with a length (a) $L_y = 15\,\mathrm{m}$, (b) $L_y = 30\,\mathrm{m}$, and (c) $L_y = 60\,\mathrm{m}$ at 15 Hz (left), 30 Hz (middle), and 60 Hz (right).

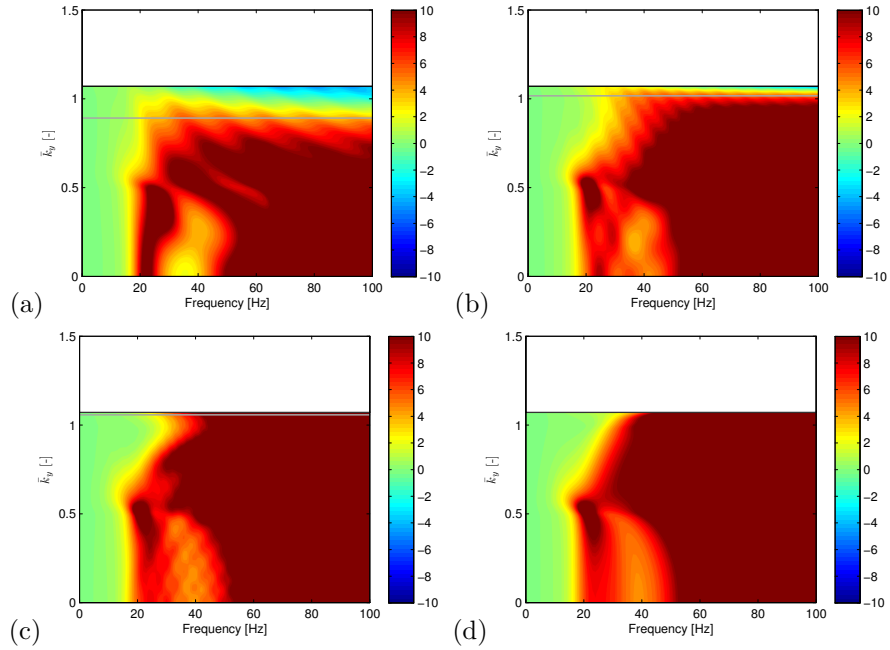

Figure 9: Vertical insertion loss $\widetilde{\mathrm{IL}}_z(x = 8\,\mathrm{m}, \bar{k}_y, z = 0\,\mathrm{m}, \omega)$ for an open trench in a halfspace with a length (a) $L_y = 15\,\mathrm{m}$, (b) $L_y = 30\,\mathrm{m}$, (c) $L_y = 60\,\mathrm{m}$, and (d) $L_y = \infty$, calculated by means of a 2.5D BE model with spatial windowing. Superimposed are the dispersion curve of a Rayleigh wave in the y-direction (black line) and the curve $\bar{k}_y = \bar{k}_\mathrm{R} \sin\theta_x$ (grey line).

of the required RAM memory. The efficiency in terms of computation time is assessed in table 3. The computation time for a 3D open trench with a length of $L_y = 15\,\mathrm{m}$ is comparable to that of a 2.5D calculation, while it significantly exceeds the latter for larger trench lengths. As the 2.5D equations are solved independently for each wavenumber k_y in the frequency–wavenumber domain, the 2.5D calculations can easily be parallelized. The use of MATLAB's Parallel Computing Toolbox [32] allows for a distributed computation on eight cores, leading to a speed–up by a factor that is slightly less than eight (due to the communication overhead). The value of 1.8 h listed in table 3 indicates the total computation time on all cores; the actual computation time is only 0.25 h. A similar parallelization can not be applied to the 3D $\mathscr{H}$-BE models, however.

		15 Hz	30 Hz	60 Hz
2.5D	$\widetilde{\mathbf{U}}(k_y,\omega)$	0.55	0.55	0.55
	$\widetilde{\mathbf{T}}(k_y,\omega)$	0.55	0.55	0.55
3D ($L_y = 15\,\mathrm{m}$)	$\widehat{\mathbf{U}}(\omega)$	164 (368)	170 (368)	186 (368)
	$\widehat{\mathbf{T}}(\omega)$	174 (368)	176 (368)	194 (368)
3D ($L_y = 30\,\mathrm{m}$)	$\widehat{\mathbf{U}}(\omega)$	348 (1351)	363 (1351)	419 (1351)
	$\widehat{\mathbf{T}}(\omega)$	371 (1351)	380 (1351)	524 (1351)
3D ($L_y = 60\,\mathrm{m}$)	$\widehat{\mathbf{U}}(\omega)$	793 (5172)	925 (5172)	1437 (5172)
	$\widehat{\mathbf{T}}(\omega)$	847 (5172)	1380 (5172)	1743 (5172)

Table 2: RAM memory (in MB) required for the storage of the BE matrices $\widetilde{\mathbf{U}}(k_y,\omega)$ and $\widetilde{\mathbf{T}}(k_y,\omega)$ or $\widehat{\mathbf{U}}(\omega)$ and $\widehat{\mathbf{T}}(\omega)$ in the 2.5D BE or 3D $\mathscr{H}$-BE models of an open trench and a stiff wave barrier. The amount of RAM memory that would have been required in classical 3D BE models without the application of $\mathscr{H}$–matrices is given between brackets.

	15 Hz	30 Hz	60 Hz
2.5D	1.8	1.8	1.8
3D ($L_y = 15\,\mathrm{m}$)	2.0	2.0	2.1
3D ($L_y = 30\,\mathrm{m}$)	2.6	2.6	2.7
3D ($L_y = 60\,\mathrm{m}$)	4.3	4.6	5.5

Table 3: Computation time (in hours) required for the 2.5D BE or 3D $\mathscr{H}$-BE calculations involving an open trench in a halfspace.

4.2 Stiff wave impeding vibration barrier

For stability reasons, the construction of an open trench in the soil is limited to shallow depths; the use of either soft or stiff in–fill materials allows for an increase of depth. If a soft in–fill material is used, the behaviour of a filled trench resembles that of an open trench [30]. The use of a stiff in–fill material, however, fundamentally alters the physical mechanism that leads to a reduction of vibration levels. A recent investigation using a 2.5D approach has revealed that a vibration isolation screen with a stiff in–fill material (e.g. created by means of jet grouting) can act as a wave impeding barrier [33]; the effectiveness depends on the stiffness contrast between the soil and the in–fill material.

The spatial windowing technique proposed in this paper allows assessing the vibration reduction efficiency for a jet grouting wall of finite length (figure 3b). The case study of an open trench discussed in subsection 4.1 is reconsidered, introducing an in–fill material with a shear wave velocity $C_\mathrm{s} = 550\,\mathrm{m/s}$ and a dilatational wave velocity $C_\mathrm{p} = 950\,\mathrm{m/s}$; the same density and material damping ratios as in the halfspace are used. The 2.5D boundary elements are now coupled to a conforming mesh of 2.5D finite elements to model the block of stiffened soil. 3D FE–$\mathscr{H}$-BE validation calculations are performed as well, coupling eight–node solid finite elements to four–node quadrilateral boundary elements. The properties of the 3D discretizations are summarized in table 1. The 2.5D and 3D finite element discretizations result in 27.5 or 22 elements per shear wavelength in the barrier at 100 Hz, respectively.

Figures 10–12 show the insertion loss $\widehat{\mathrm{IL}}_z(\mathbf{x},\omega)$ that is achieved by the inclusion of a block of stiffened soil with a length of 15 m, 30 m, and 60 m in the halfspace at a frequency of 15 Hz, 30 Hz, and 60 Hz, respectively. The results of the 2.5D FE–BE models with spatial windowing are compared to the 3D FE–$\mathscr{H}$-BE computations and, as in subsection 4.1, a good correspondence between the models is observed. Some discrepancies are apparent, however, especially if a block with a length of 15 m is considered at 60 Hz (figure 12a). The relative error $\hat{\varepsilon}(\mathbf{x},\omega)$, defined in equation (14), is shown in figure 13 for a quantitative comparison in each of these cases. The error is negligibly small at 15 Hz for all barrier lengths and remains limited at higher frequencies for barrier lengths of 30 m and 60 m, except near the barrier's edges. A much larger discrepancy between the 2.5D results with spatial windowing and the 3D results is revealed for a barrier of 15 m at 60 Hz, however.

The observed discrepancies can be attributed to the modal behaviour of the finite block, which is not accounted for by the spatial windowing technique. This is investigated in figure 14. Figure 14a shows the mode count $N(f)$ for each of the stiff wave barriers considered above. An increasing length of the block results in a larger number of flexible modes within the frequency range between 0 and 100 Hz. The distribution of the natural frequencies in the frequency domain is characterized by the modal density $n(f) = \mathrm{d}N(f)/\mathrm{d}f$ [34]. In order to evaluate the latter, a continuous function is fitted through the discrete curve. In the low frequency range, the dynamic response is dominated by the resonating behaviour of individual modes. At higher frequencies, however, the response is determined by multiple overlapping modes and the contribution of individual modes can no longer be distinguished [34]. The transition from the low to the high frequency regime is quantified through the modal overlap $M(f) = \eta f n(f)$, where $\eta = 2\beta_\mathrm{s}$ is the loss factor; a modal overlap $M = 1$ is commonly chosen as the limit of the low frequency range [34]. Figure 14b shows the modal overlap $M(f)$ for a block of stiffened soil with a length of 15 m,

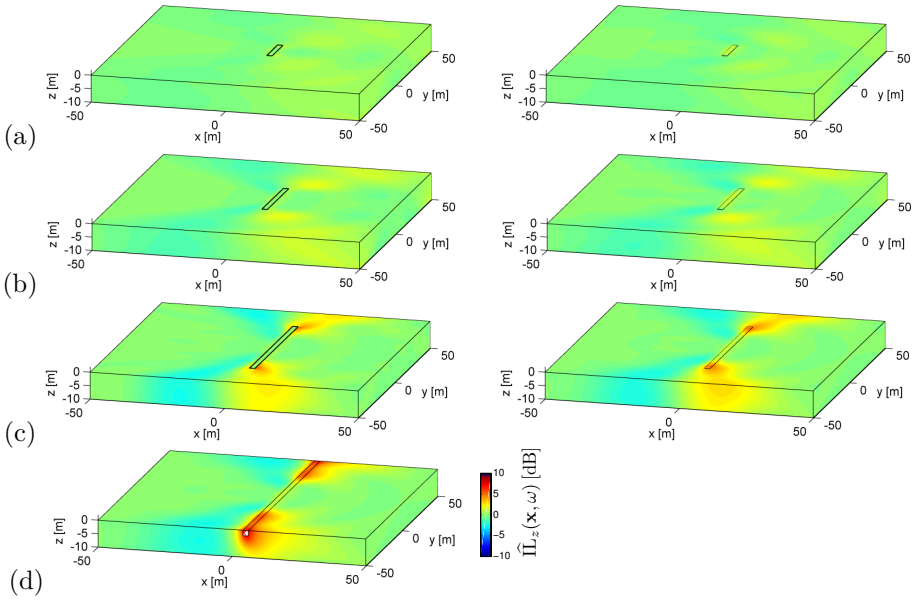

Figure 10: Vertical insertion loss $\widehat{\mathrm{IL}}_z(\mathbf{x},\omega)$ at 15 Hz for a block of stiffened soil in a halfspace with a length (a) $L_y = 15\,\mathrm{m}$, (b) $L_y = 30\,\mathrm{m}$, (c) $L_y = 60\,\mathrm{m}$, and (d) $L_y = \infty$, calculated by means of a 2.5D FE–BE model with spatial windowing (left hand side) or a 3D FE–$\mathscr{H}$-BE model (right hand side).

30 m, and 60 m. It is observed that the modal overlap increases with the block length; individual modes are only expected to dominate the response below 95 Hz, 45 Hz, and 20 Hz, respectively. This explains why the spatial windowing technique gives a better correspondence with the 3D FE–$\mathscr{H}$-BE computations if applied to a stiff wave barrier with a larger length. Even in the low frequency range ($M(f) < 1$), however, the overall influence of the resonating behaviour of individual modes remains rather limited due to the strong dynamic SSI (i.e. due to the associated radiation damping in the soil). This indicates that the proposed technique is an accurate and efficient tool to account for the finite length of the block of stiffened soil.

The 3D results are also compared to 2.5D results based on the assumption of longitudinal invariance (figures 10–12d). At 15 Hz, neither a length of 15 m or 30 m is sufficient to create a wave impeding effect similar to the case where the block is assumed to be of infinite length; implementing the block over a length of 60 m, however, does results in a comparable insertion loss. The insertion

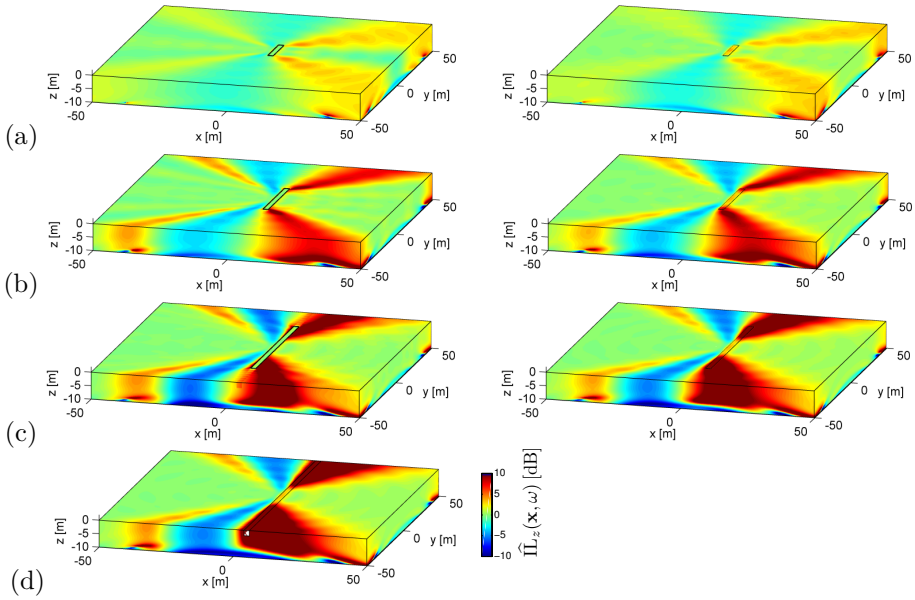

Figure 11: Vertical insertion loss $\widehat{\mathrm{IL}}_z(\mathbf{x},\omega)$ at 30 Hz for a block of stiffened soil in a halfspace with a length (a) $L_y = 15\,\mathrm{m}$, (b) $L_y = 30\,\mathrm{m}$, (c) $L_y = 60\,\mathrm{m}$, and (d) $L_y = \infty$, calculated by means of a 2.5D FE–BE model with spatial windowing (left hand side) or a 3D FE–$\mathscr{H}$-BE model (right hand side).

loss at 30 Hz resembles the result of the 2.5D calculation from a length of 30 m on, while a good correspondence with the latter is achieved for all lengths at a frequency of 60 Hz.

The observations in figures 10–12 can be explained by considering the insertion loss $\widetilde{\mathrm{IL}}_z(x,\bar{k}_y,z,\omega)$ in the frequency–wavenumber domain. Figure 15d shows the insertion loss $\widetilde{\mathrm{IL}}_z(x = 8\,\mathrm{m},\bar{k}_y,z = 0\,\mathrm{m},\omega)$ for an infinitely long block of stiffened soil in a halfspace; the insertion loss is only shown in a range $0 \leq \bar{k}_y \leq \bar{k}_\mathrm{R}$. Superimposed on figure 15d is the dispersion curve $\bar{k}_y = \bar{k}_\mathrm{b}(\omega)$ of a free bending wave in an infinitely long Timoshenko beam with the same properties as the block of stiffened soil [35]. The region where a substantial insertion loss is obtained in the $(\omega,\bar{k}_y)$–domain is clearly bounded by the Rayleigh wave dispersion curve $\bar{k}_y = \bar{k}_\mathrm{R}$ and the free bending wave dispersion curve $\bar{k}_y = \bar{k}_\mathrm{b}(\omega)$. As reported in [33], the transmission of propagating plane waves with a wavenumber $\bar{k}_y$ larger than $\bar{k}_\mathrm{b}(\omega)$ (i.e. with a trace wavelength λ_y smaller

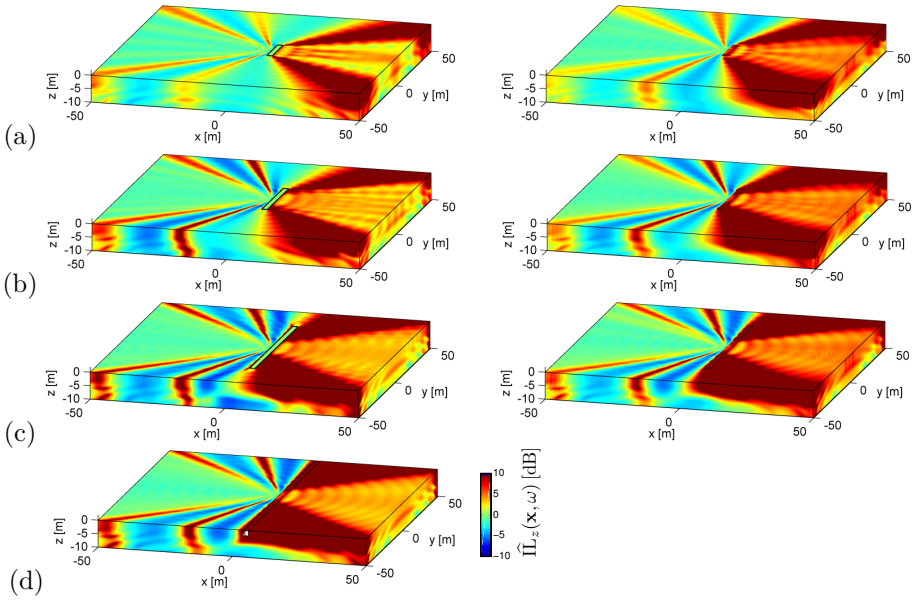

Figure 12: Vertical insertion loss $\widehat{\mathrm{IL}}_z(\mathbf{x},\omega)$ at 60 Hz for a block of stiffened soil in a halfspace with a length (a) $L_y = 15\,\mathrm{m}$, (b) $L_y = 30\,\mathrm{m}$, (c) $L_y = 60\,\mathrm{m}$, and (d) $L_y = \infty$, calculated by means of a 2.5D FE–BE model with spatial windowing (left hand side) or a 3D FE–$\mathscr{H}$-BE model (right hand side).

than $\lambda_\mathrm{b}(\omega)$) is impeded by the block of stiffened soil, as the admittance of a beam of infinite length is then dominated by its bending stiffness and decreases proportionally to $\bar{k}_y^{-4}$ at a given radial frequency ω [35]. The intersection of the Rayleigh wave and the free bending wave dispersion curves hence determines the critical radial frequency from which the block of stiffened soil can act as a wave impeding barrier; a value of $2\pi \times 12\,\mathrm{Hz}$ is obtained in the present case [33]. In the spatial domain, a reduction of vibration levels is only achieved in an area delimited by a critical angle $\theta_\mathrm{c}(\omega) = \sin^{-1}\left(\bar{k}_\mathrm{b}(\omega)/\bar{k}_\mathrm{R}\right)$, which can clearly be distinguished on figures 10–12d. An analytical expression for $\theta_\mathrm{c}(\omega)$ as a function of the geometric and dynamic properties of the stiff wave barrier is given in [33].

Figures 15a–c show the insertion loss $\widetilde{\mathrm{IL}}_z(x = 8\,\mathrm{m}, \bar{k}_y, z = 0\,\mathrm{m}, \omega)$ for a block of stiffened soil in a halfspace with a length of 15 m, 30 m, or 60 m, respectively; these results are obtained by means of the spatial windowing technique. Large insertion losses are only observed in a part of the region indicated on figure 15d.

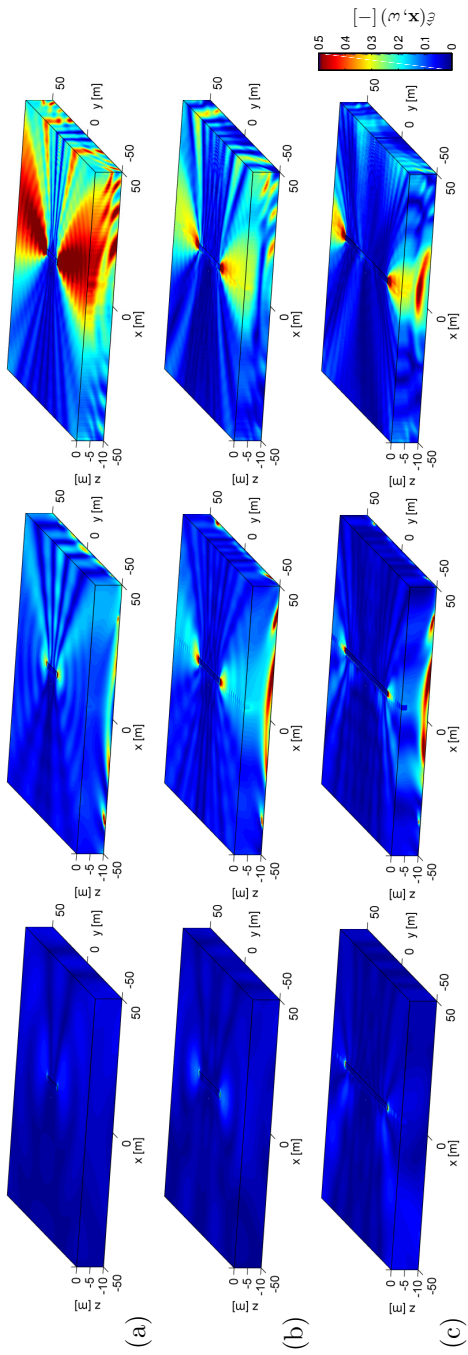

Figure 13: Relative error $\hat{\varepsilon}(\mathbf{x}, \omega)$ for a block of stiffened soil in a halfspace with a length (a) $L_y = 15\,\mathrm{m}$, (b) $L_y = 30\,\mathrm{m}$, and (c) $L_y = 60\,\mathrm{m}$ at 15 Hz (left), 30 Hz (middle), and 60 Hz (right).

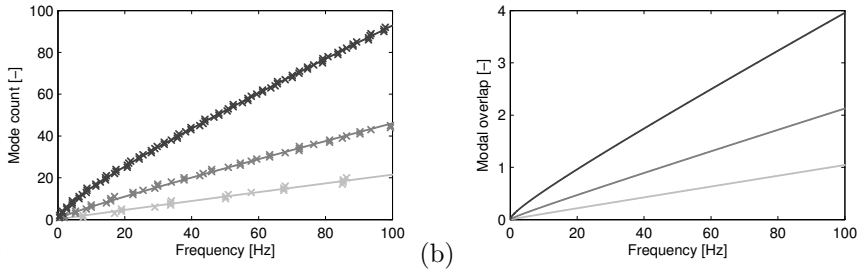

(a) (b)

Figure 14: (a) Discrete (crosses) and fitted (solid line) mode count $N(f)$ and (b) modal overlap $M(f)$, for a block of stiffened soil with a length of 15 m, 30 m, and 60 m (light to dark grey lines).

The explanation for this observation is twofold. First, a finite block is only able to impede the transmission of that part of the wavefield that actually impinges on the block, and no reduction of vibration levels is obtained for $\bar{k}_y > \bar{k}_\mathrm{R} \sin\theta_x$, where $\sin\theta_x$ is defined in equation (15). This is similar to the behaviour of a finite trench discussed in subsection 4.1. Second, the results indicate that the block should be approximately twice as long as the free bending wavelength $\lambda_\mathrm{b}(\omega)$ in order to develop a similar behaviour as a beam of infinite length and thus to hinder the transmission of plane waves with a longitudinal wavelength smaller than $\lambda_\mathrm{b}(\omega)$. Lines corresponding to these two additional conditions are superimposed on figures 15a–c, clearly delimiting a reduced area of significant insertion loss in the $\left(\omega, \bar{k}_y\right)$–domain. Both phenomena result in an upward shift of the critical frequency with respect to the case of an infinite length, yielding critical frequencies of 35.2 Hz, 22.9 Hz, and 14.7 Hz for lengths of 15 m, 30 m, and 60 m, respectively. Stiffening of the soil over a length of 60 m hence suffices to mimic the dynamic behaviour of a block of infinite length.

The FE discretization of the block of stiffened soil leads to sparse and symmetric stiffness and mass matrices; the required RAM memory for the storage of these matrices is rather limited. The memory usage associated with the BE discretization consequently remains dominant; a comparison between the 2.5D and 3D BE models is given in table 2. A comparison of the 2.5D FE–BE and 3D FE-$\mathscr{H}$-BE in terms of computation time is shown in table 4; the efficiency of the 2.5D approach is clear. The large computation times for a 3D stiff wave barrier with a length of 60 m are due to convergence difficulties in the iterative Neumann–Dirichlet FE–BE coupling algorithm. It should furthermore be noted that the computation time of the 2.5D models represents the total computation time on all eight cores used in the parallelized calculation; the actual computation time is only 0.30 h.

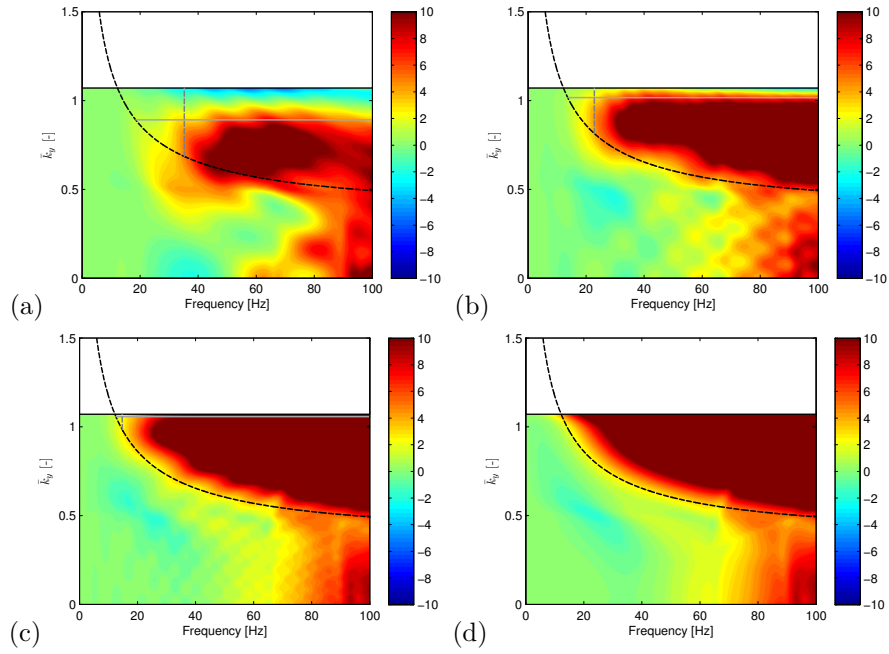

Figure 15: Vertical insertion loss $\widetilde{\mathrm{IL}}_z(x = 8\,\mathrm{m}, \bar{k}_y, z = 0\,\mathrm{m}, \omega)$ for a block of stiffened soil in a halfspace with a length (a) $L_y = 15\,\mathrm{m}$, (b) $L_y = 30\,\mathrm{m}$, (c) $L_y = 60\,\mathrm{m}$, and (d) $L_y = \infty$, calculated by means of a 2.5D FE–BE model with spatial windowing. Superimposed are the dispersion curve of a Rayleigh wave in the y-direction (solid black line), the free bending wave dispersion curve in an infinitely long beam (dashed black line), the curve $\bar{k}_y = \bar{k}_\mathrm{R} \sin\theta_x$ (solid grey line), and the curve $L_y = 2\lambda_\mathrm{b}(\omega)$ (dashed grey line).

	15 Hz	30 Hz	60 Hz
2.5D	2.1	2.1	2.1
3D ($L_y = 15\,\mathrm{m}$)	2.5	2.3	2.3
3D ($L_y = 30\,\mathrm{m}$)	4.0	6.3	4.4
3D ($L_y = 60\,\mathrm{m}$)	24.4	12.6	13.2

Table 4: Computation time (in hours) required for the 2.5D FE–BE or 3D FE–$\mathscr{H}$-BE calculations involving a stiff wave barrier in a halfspace.

5 Application of spatial windowing to short structures: surface foundation

It has been demonstrated in subsections 4.1 and 4.2 that the proposed spatial windowing technique is an accurate and efficient tool to account for the finite length of structures. The validity of the methodology is now further explored in this section. The importance of the actual length of the structure, its modal behaviour, and the dynamic SSI are investigated. The structure under concern is a square surface foundation on a horizontally layered halfspace; the geometry thus strongly differs from the open trenches and stiff wave barriers previously discussed. In subsection 5.1, the flexibility is neglected and the foundation is modelled as a rigid body. The influence of flexible foundation modes on the accuracy of the methodology will subsequently be investigated in subsections 5.2 and 5.3.

5.1 Rigid surface foundation on a horizontally layered halfspace

The concrete foundation has a width $w = 5\,\mathrm{m}$, a length $L_y = 5\,\mathrm{m}$, a thickness $t = 0.25\,\mathrm{m}$, a Young's modulus $E = 33\,\mathrm{GPa}$, a Poisson's ratio $\nu = 0.20$, and a density $\rho = 2500\,\mathrm{kg/m^3}$. A hysteretic damping ratio $\beta = 0.03$ is included through application of the correspondence principle. The foundation is loaded by a unit harmonic vertical point load at its center. While a homogeneous halfspace has been considered in subsections 4.1 and 4.2 to facilitate physical interpretation, the soil in reality is often stratified; a layered halfspace is therefore included in this subsection. The soil consists of two layers on a halfspace, each with a thickness of 2 m. The shear wave velocity C_s is equal to 150 m/s in the top layer, 250 m/s in the second layer, and 300 m/s in the underlying halfspace. The Poisson's ratio ν is 1/3 everywhere, resulting in dilatational wave velocities C_p of 300 m/s, 500 m/s, and 600 m/s, respectively.

Material damping ratios $\beta_\mathrm{s} = \beta_\mathrm{p} = 0.025$ in deviatoric and volumetric deformation are attributed to the layers and the halfspace, while a uniform density $\rho = 1800\,\mathrm{kg/m^3}$ is considered throughout the medium.

The spatial windowing technique is employed to compute the response of the foundation and the wavefield in the soil based on a 2.5D calculation. The soil–foundation interface is discretized with 30 2.5D boundary elements, while 30×30 square quadrilateral boundary elements are used in the 3D validation calculations. This corresponds to nine elements per shear wavelength in the top layer at 100 Hz. As the rigid body translation of a longitudinally invariant structure is entirely two–dimensional (2D) and corresponds to plane strain conditions [1], the 2.5D calculation is restricted to $\bar{k}_y = 0$.

Figure 16 shows the real part of the vertical displacement $\hat{u}_z(\mathbf{x}, \omega)$ of the foundation and the soil at 25 Hz and 100 Hz. Results obtained with the 2.5D BE model (which represents an infinitely long rigid foundation), the 2.5D BE model with spatial windowing, and the 3D $\mathscr{H}$-BE model are compared. The 2.5D model is unable to account for variations in the longitudinal direction, as it is restricted to $\bar{k}_y = 0$ and thus purely 2D; the displacements consequently strongly differ from the 3D results at both frequencies under concern. Application of the spatial windowing technique distributes the energy over the entire wavenumber domain, which enables the correct representation of the variation of the wavefield in the longitudinal direction. This leads to a very good agreement with the 3D calculations. The response of the foundation is also affected, however, and does not longer correspond to a uniform vertical translation.

The three numerical methodologies are furthermore compared in figure 17, which shows the free field mobility along the line $y = 0\,\mathrm{m}$ at several distances from the foundation in the frequency range between 0 Hz and 100 Hz. As can be expected, there is a significant deviation between the 2.5D and 3D mobilities; the assumption of longitudinal invariance generally results in an overestimation of the free field mobility, especially in the far field. A very good agreement is achieved between the 2.5D model with spatial windowing and the 3D model, although some discrepancies arise in the near field. Figures 16 and 17 illustrate the appropriateness of the proposed methodology, even if applied to a short structure which is not quasi translationally invariant. The actual dimensions of the structure are not important; the spatial windowing technique is effective as long as the response is not dominated by the modal behaviour of the structure.

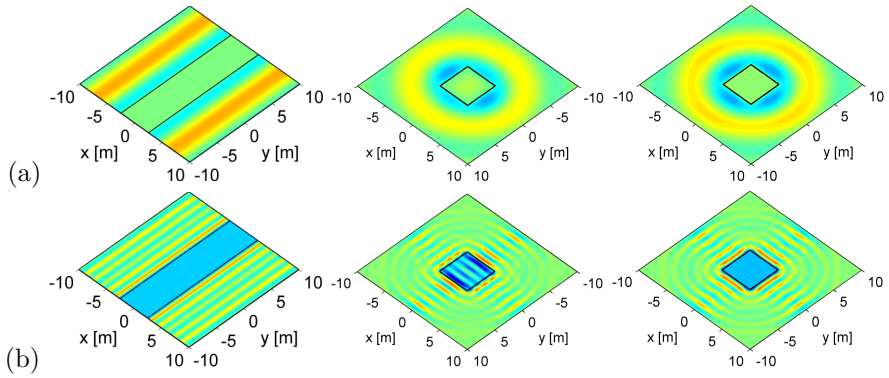

Figure 16: Real part of the vertical displacement $\hat{u}_z(\mathbf{x}, \omega)$ of the foundation and the soil for a rigid surface foundation on a layered halfspace excited at its center by a unit harmonic vertical point load at (a) 25 Hz and (b) 100 Hz. The results are calculated by means of a 2.5D BE model (left), a 2.5D BE model with spatial windowing (middle), and a 3D $\mathscr{H}$-BE model (right).

5.2 Flexible surface foundation on a horizontally layered halfspace

In order to account for the flexibility of the foundation, the structure is discretized with Kirchhoff plate elements which are coupled to the boundary elements on the soil–foundation interface. Within the frequency range of interest, the free foundation has natural frequencies at 24 Hz, 35 Hz, 40 Hz, and 62 Hz; only the modes at 40 Hz and 62 Hz can be excited by the loading under concern, however, as the projection of the excitation force on the other mode shapes equals zero.

Figure 18 shows the real part of the vertical displacement $\hat{u}_z(\mathbf{x}, \omega)$ of the foundation and the soil at 25 Hz and 100 Hz. Results obtained with the 2.5D FE–BE model (for an infinitely long flexible foundation), the 2.5D FE–BE model with spatial windowing, and the 3D FE–$\mathscr{H}$-BE model are compared. At 25 Hz, a reasonable agreement between the results of the three models is observed, as the wavelength in the soil remains large compared to the dimensions of the foundation. At higher frequencies, however, the wavefield in the soil is more strongly affected by the presence of the foundation; a 2.5D calculation is unable to accurately represent the wavefield obtained with a 3D calculation. Application of the spatial windowing technique modifies the wavefield considerably, resulting in a much better agreement with the 3D

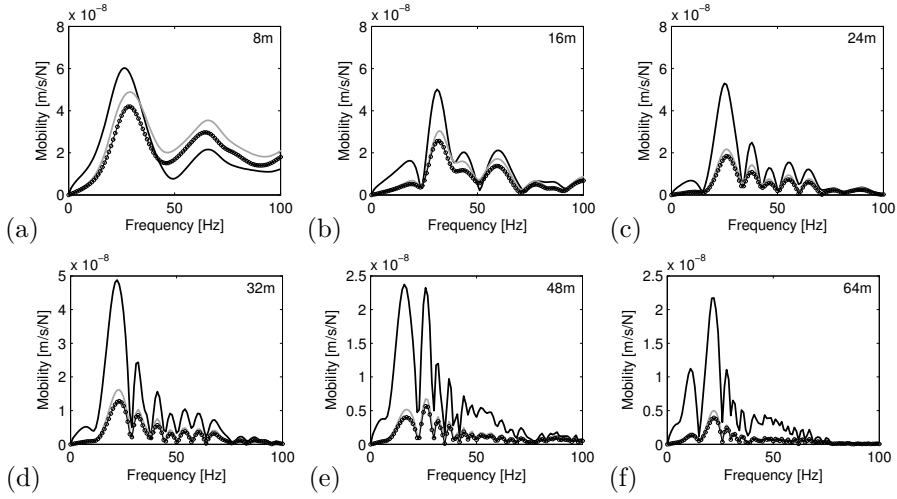

Figure 17: Free field mobility along the line $y = 0\,\mathrm{m}$ at (a) 8 m, (b) 16 m, (c) 24 m, (d) 32 m, (e) 48 m, and (f) 64 m from the center of a rigid surface foundation on a layered halfspace excited at its center by a unit harmonic vertical point load. The results are calculated by means of a 2.5D BE model (black line), a 2.5D BE model with spatial windowing (circles), and a 3D $\mathscr{H}$-BE model (grey line).

calculations.

Figure 19 shows the free field mobility along the line $y = 0\,\mathrm{m}$ at several distances from the foundation in the frequency range between 0 Hz and 100 Hz. Below 25 Hz, the three numerical methodologies yield the same result, as the wavelength in the soil remains large compared to the dimensions of the foundation. Discrepancies between the 2.5D and 3D model are observed at higher frequencies, but these are much smaller than in the case of the rigid foundation considered in subsection 5.1. The deviations are more pronounced in the near field and are almost negligible in the far field. The mobilities obtained after application of spatial windowing are in much better correspondence with the 3D results, although the agreement at $x = 8\,\mathrm{m}$ remains relatively poor.

The natural frequencies of the free foundation at 40 Hz and 62 Hz are not apparent in figure 19 due to the strong dynamic SSI and the associated radiation damping. This is also illustrated in figure 20, which shows the modulus and phase of the vertical displacement $\hat{u}_z(\omega)$ at the center of the foundation. The peak at 20 Hz corresponds to resonance of the foundation on the layered

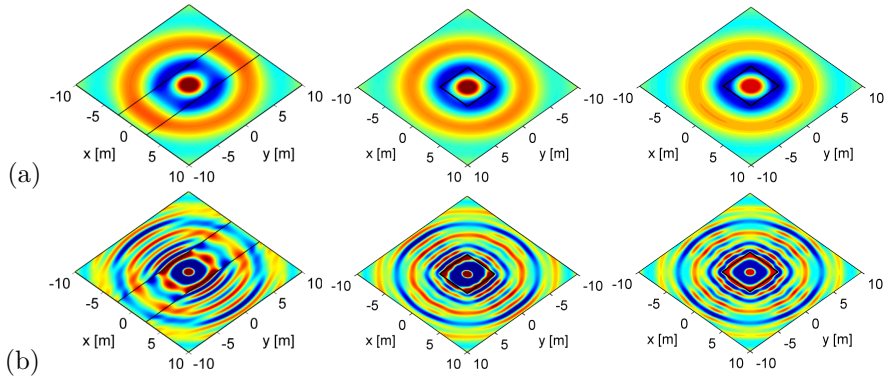

Figure 18: Real part of the vertical displacement $\hat{u}_z(\mathbf{x}, \omega)$ of the foundation and the soil for a flexible surface foundation on a layered halfspace excited at its center by a unit harmonic vertical point load at (a) 25 Hz and (b) 100 Hz. The results are calculated by means of a 2.5D FE–BE model (left), a 2.5D FE–BE model with spatial windowing (middle), and a 3D FE–$\mathscr{H}$-BE model (right).

halfspace; it is not a natural frequency of the foundation. The response is thus not dominated by the modal behaviour of the foundation, explaining the suitability of the spatial windowing technique in the case under concern.

5.3 Flexible surface foundation on a single layer on bedrock

In order to further explore the limitations of the spatial windowing technique, a case study is discussed in this subsection where the eigenmodes of the foundation prevail in the response of the 3D coupled soil–foundation system. The layered halfspace considered in subsections 5.1 and 5.2 is replaced by a single layer on bedrock, with the same wave velocities and material damping ratios as the top layer of the aforementioned halfspace. The layer thickness h, however, is set to 0.375 m, which results in a cut–on frequency of $C_\mathrm{s}/(4h) = 100$ Hz; the surface waves hence remain evanescent in the whole frequency range under concern. The soil's shear modulus $\mu = \rho C_\mathrm{s}^2$ is furthermore reduced by a factor of ten by decreasing the soil density ρ to $180\,\mathrm{kg/m^3}$ to achieve a considerable stiffness contrast between the soil and the structure.

Figure 21 compares the modulus and phase of the vertical displacement $\hat{u}_z(\omega)$ at the center of the foundation, calculated with the 2.5D FE–BE model (for

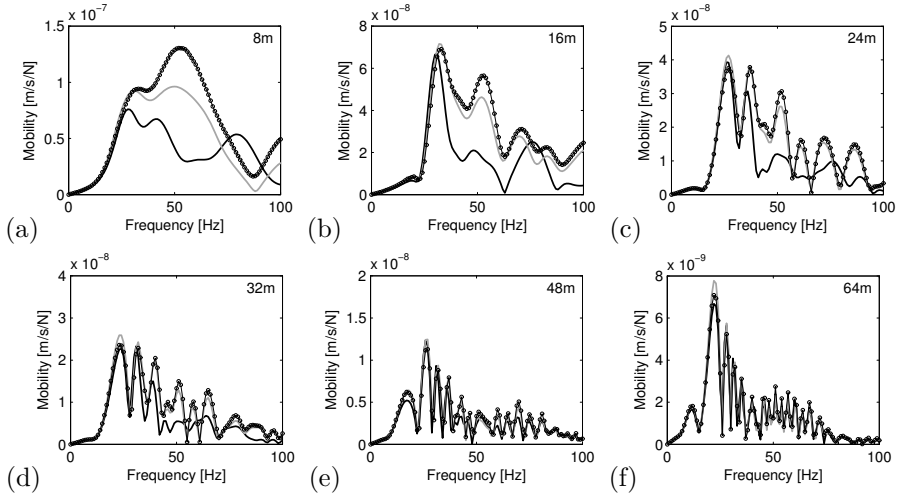

Figure 19: Free field mobility along the line $y = 0\,\mathrm{m}$ at (a) 8 m, (b) 16 m, (c) 24 m, (d) 32 m, (e) 48 m, and (f) 64 m from the center of a flexible surface foundation on a layered halfspace excited at its center by a unit harmonic vertical point load. The results are calculated by means of a 2.5D FE–BE model (black line), a 2.5D FE–BE model with spatial windowing (circles), and a 3D FE–$\mathscr{H}$-BE model (grey line).

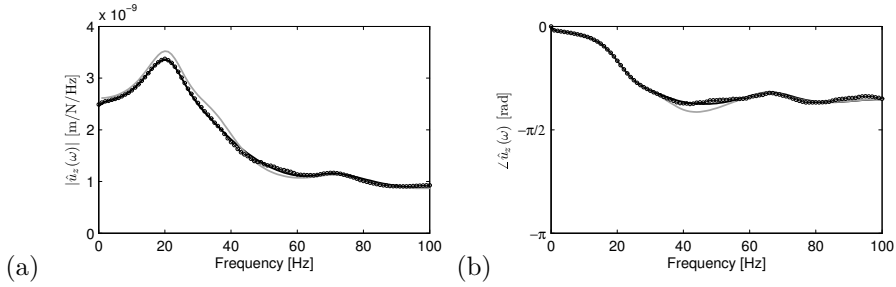

Figure 20: (a) Modulus and (b) phase of the vertical displacement $\hat{u}_z(\omega)$ at the center of a flexible surface foundation on a layered halfspace excited at its center by a unit harmonic vertical point load. The results are calculated by means of a 2.5D FE–BE model (black line), a 2.5D FE–BE model with spatial windowing (circles), and a 3D FE–$\mathscr{H}$-BE model (grey line).

an infinitely long flexible foundation), the 2.5D FE–BE model with spatial windowing, and the 3D FE–$\mathscr{H}$-BE model. As there are no propagative surface waves in the soil, the radiation damping is very limited, and the eigenmodes of the foundation consequently prevail in the response of the 3D coupled soil–foundation system. The resonance peaks near 40 Hz and 62 Hz can clearly be distinguished in figure 21, which is also due to the low soil stiffness. The 2.5D approach gives a reasonable correspondence with these results below 40 Hz, but large discrepancies are observed at higher frequencies. Application of the spatial windowing technique does not lead to a better agreement with the 3D results, however. This example illustrates the shortcoming of the technique in case of low radiation damping in the soil, as it does not succeed to account for the dominant modal behaviour of the structure. It is emphasized that the prevalence of the structural modes is caused by the lack of radiation damping rather than the limited material damping in the soil. An increase of the latter results in a decrease of the peak values of $\hat{u}_z(\omega)$ but does not prevent the appearance of these resonances.

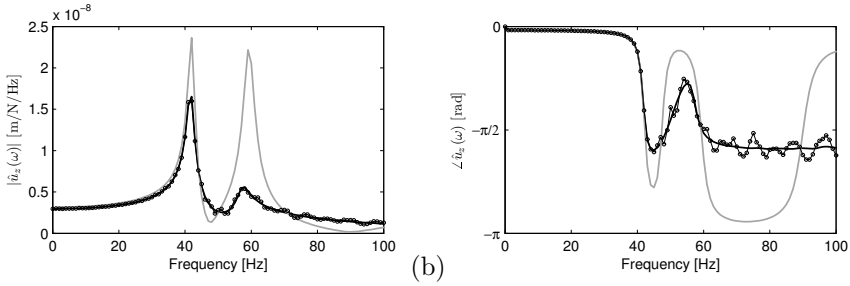

Figure 21: (a) Modulus and (b) phase of the vertical displacement $\hat{u}_z(\omega)$ at the center of a flexible surface foundation on a single layer on bedrock excited at its center by a unit harmonic vertical point load. The results are calculated by means of a 2.5D FE–BE model (black line), a 2.5D FE–BE model with spatial windowing (circles), and a 3D FE–$\mathscr{H}$-BE model (grey line).

6 Conclusions

In this paper, a spatial windowing technique has been presented that allows accounting for the effect of finite dimensions in 2.5D models for dynamic SSI. This technique enables the application of 2.5D models even if the assumption of longitudinal invariance is not fulfilled, hence maintaining the associated computational efficiency. The method redistributes the contribution of each

wavenumber component over the entire wavenumber domain and can as such be regarded as a postprocessing of the original 2.5D results. Spatial windowing only accounts for the diffraction occurring at the structure's extremities, however, and the existence of structural modes is not considered.

Numerical examples of elongated and short structures have been discussed to investigate the applicability of the proposed technique: an open trench as a vibration isolation screen, a stiff wave impeding barrier, a rigid and flexible surface foundation on a layered halfspace, and a flexible surface foundation on a single layer on bedrock. For each of these examples, full 3D calculations have been performed to provide a rigorous validation. It is demonstrated that the proposed technique is accurate as long as the modal behaviour of the structure does not dominate the response; the methodology is in that case even appropriate for short structures which are not quasi translationally invariant. The modal behaviour has only a limited influence in most of the applications due to the dynamic SSI and the associated radiation damping in the soil. If this is not the case, however, the spatial windowing technique reaches its limits of suitability.

Acknowledgements

The first author is a doctoral fellow and the third author is a postdoctoral fellow of the Research Foundation Flanders (FWO). The results presented in subsection 4.2 have been obtained within the frame of the EU FP7 project RIVAS (Railway Induced Vibration Abatement Solutions) [36] under grant agreement No. 265754. The financial support is gratefully acknowledged.

References

[1] S. François, M. Schevenels, G. Lombaert, P. Galvín, G. Degrande, A 2.5D coupled FE-BE methodology for the dynamic interaction between longitudinally invariant structures and a layered halfspace, Computer Methods in Applied Mechanics and Engineering 199 (23-24) (2010) 1536–1548.

[2] L. Gavrić, Finite element computation of dispersion properties of thin-walled waveguides, Journal of Sound and Vibration 173 (1) (1994) 113–124.

[3] L. Gavrić, Computation of propagative waves in free rail using finite element technique, Journal of Sound and Vibration 183 (3) (1995) 531–543.

[4] A. Stamos, D. Beskos, 3-D seismic response analysis of long lined tunnels in half-space, Soil Dynamics and Earthquake Engineering 15 (1996) 111–118.

[5] A. Tadeu, J. Antonio, E. Kausel, 3D scattering of waves by a cylindrical irregular cavity of infinite length in a homogeneous elastic medium, Computer Methods in Applied Mechanics and Engineering 191 (2002) 3015–3033.

[6] X. Sheng, C. Jones, D. Thompson, Modelling ground vibrations from railways using wavenumber finite- and boundary-element methods, Proceedings of the Royal Society A - Mathematical, Physical and Engineering Sciences 461 (2005) 2043–2070.

[7] L. Andersen, S. Nielsen, Reduction of ground vibration by means of barriers or soil improvement along a railway track, Soil Dynamics and Earthquake Engineering 25 (2005) 701–716.

[8] G. Lombaert, G. Degrande, D. Clouteau, Numerical modelling of free field traffic induced vibrations, Soil Dynamics and Earthquake Engineering 19 (7) (2000) 473–488.

[9] Y. Yang, H. Hung, A 2.5D finite-infinite element approach for modelling visco-elastic bodies subjected to moving loads, International Journal for Numerical Methods in Engineering 51 (2001) 1317–1336.

[10] Y. Yang, H. Hung, D. Chang, Train-induced wave propagation in layered soils using finite/infinite element simulation, Soil Dynamics and Earthquake Engineering 23 (2003) 263–278.

[11] S. François, M. Schevenels, G. Lombaert, G. Degrande, A 2.5D displacement based PML for elastodynamic wave propagation, International Journal for Numerical Methods in Engineering 90 (7) (2012) 819–837.

[12] S. Chaillat, M. Bonnet, J.-F. Semblat, A multi-level fast multipole BEM for 3-D elastodynamics in the frequency domain, Computer Methods in Applied Mechanics and Engineering 197 (49–50) (2008) 4233–4249.

[13] W. Hackbusch, A sparse matrix arithmetic based on $\mathscr{H}$-matrices. Part I: Introduction to $\mathscr{H}$-matrices, Computing 62 (2) (1999) 89–108.

[14] M. Villot, C. Guigou, L. Gagliardini, Predicting the acoustical radiation of finite size multi-layered structures by applying spatial windowing on infinite structures, Journal of Sound and Vibration 245 (3) (2001) 433–455.

[15] S. Ghinet, N. Atalla, The transmission loss of curved laminates and sandwich composite panels, Journal of the Acoustical Society of America 118 (2) (2005) 774–790.

[16] D. Rhazi, N. Atalla, Transfer matrix modeling of the vibroacoustic response of multi–materials structures under mechanical excitation, Journal of Sound and Vibration 329 (13) (2010) 2532–2546.

[17] J. Legault, A. Mejdi, N. Atalla, Vibro-acoustic response of orthogonally stiffened panels: the effects of finite dimensions, Journal of Sound and Vibration 330 (24) (2011) 5928–5948.

[18] D. Aubry, D. Clouteau, A subdomain approach to dynamic soil-structure interaction, in: V. Davidovici, R. Clough (Eds.), Recent advances in Earthquake Engineering and Structural Dynamics, Ouest Editions/AFPS, Nantes, 1992, pp. 251–272.

[19] D. Aubry, D. Clouteau, G. Bonnet, Modelling of wave propagation due to fixed or mobile dynamic sources, in: N. Chouw, G. Schmid (Eds.), Workshop Wave '94, Wave propagation and Reduction of Vibrations, Ruhr Universität Bochum, Germany, 1994, pp. 109–121.

[20] O. Von Estorff, E. Kausel, Coupling of boundary and finite elements for soil-structure interaction, Earthquake Engineering and Structural Dynamics 18 (1989) 1065–1075.

[21] P. Coulier, S. François, G. Lombaert, G. Degrande, Application of hierarchical matrices to boundary element methods for elastodynamics based on Green's functions for a horizontally layered halfspace, Engineering Analysis with Boundary Elements 37 (12) (2013) 1745–1758.

[22] L. Grasedyck, W. Hackbusch, Construction and arithmetics of $\mathscr{H}$-matrices, Computing 70 (2003) 295–334.

[23] M. Bebendorf, Hierarchical Matrices: A Means to Efficiently Solve Elliptic Boundary Value Problems, 1st Edition, Springer Publishing Company, 2008.

[24] P. Coulier, S. François, G. Lombaert, G. Degrande, Coupled finite element – hierarchical boundary element methods for dynamic soil–structure interaction in the frequency domain, International Journal for Numerical Methods in Engineering 97 (7) (2014) 505–530.

[25] Z. Ozdemir, P. Coulier, M. Lak, S. François, G. Lombaert, G. Degrande, Numerical evaluation of the dynamic response of pipelines to vibrations induced by the operation of a pavement breaker, Soil Dynamics and Earthquake Engineering 44 (2013) 153–167.

[26] L. Filon, On a quadrature formula for trigonometric integrals, Proceedings of the Royal Society of Edinburgh 49 (1929) 38–47.

[27] R. Woods, Screening of surface waves in soils, Journal of the Soil Mechanics and Foundation Division, Proceedings of the ASCE 94 (SM4) (1968) 951–979.

[28] S. Ahmad, T. Al-Hussaini, Simplified design for vibration screening by open and in-filled trenches, Journal of Geotechnical Engineering, Proceedings of the ASCE 117 (1) (1991) 67–88.

[29] H. Hung, Y. Yang, D. Chang, Wave barriers for reduction of train-induced vibrations in soils, Journal of Geotechnical Engineering, Proceedings of the ASCE 130 (12) (2004) 1283–1291.

[30] S. François, M. Schevenels, B. Thyssen, J. Borgions, G. Degrande, Design and efficiency of a vibration isolating screen in the soil, Soil Dynamics and Earthquake Engineering 39 (2012) 113–127.

[31] P. Banerjee, S. Ahmad, K. Chen, Advanced application of BEM to wave barriers in multi-layered three-dimensional soil media, Earthquake Engineering and Structural Dynamics 16 (1988) 1041–1060.

[32] The MathWorks, MATLAB Parallel Computing Toolbox User's Guide (2013).

[33] P. Coulier, S. François, G. Degrande, G. Lombaert, Subgrade stiffening next to the track as a wave impeding barrier for railway induced vibrations, Soil Dynamics and Earthquake Engineering 48 (2013) 119–131.

[34] F. Fahy, P. Gardonio, Sound and Structural Vibration: Radiation, Transmission and Response, 2nd Edition, Academic Press, Oxford, 2007.

[35] P. Hagedorn, A. DasGupta, Vibrations and Waves in Continuous Mechanical Systems, John Wiley & Sons, Chichester, United Kingdom, 2007.

[36] http://www.rivas-project.eu (2011).

Paper D

Subgrade stiffening next to the track as a wave impeding barrier for railway induced vibrations

Published in Soil Dynamics and Earthquake Engineering 48 (2013) 119–132
http://dx.doi.org/10.1016/j.soildyn.2012.12.009

Subgrade stiffening next to the track as a wave impeding barrier for railway induced vibrations

P. Coulier, S. François, G. Degrande, G. Lombaert
KU Leuven, Department of Civil Engineering,
Kasteelpark Arenberg 40, B-3001 Leuven, Belgium

Abstract

This paper studies the efficiency of subgrade stiffening next to the track as a mitigation measure for railway induced vibrations by means of a two-and-a-half-dimensional coupled finite element – boundary element methodology. An analysis in the frequency–wavenumber domain for a homogeneous halfspace reveals that the block of stiffened soil next to the track can act as a wave impeding barrier. It is demonstrated that the wave impeding effect depends on the relation between the Rayleigh wavelength in the soil and the free bending wavelength in the block of stiffened soil, as the transmission of plane waves in the soil with a longitudinal wavelength smaller than the bending wavelength is hindered. This leads to a critical frequency from which this mitigation measure starts to be effective, depending on the stiffness contrast between the soil and the block of stiffened soil. The existence of a critical angle delimiting an area where vibration levels are reduced in case of harmonic excitation on the rail is also demonstrated. Two applications involving a layered halfspace are finally discussed to demonstrate that the performance of this mitigation measure critically depends on the soil characteristics.

1 Introduction

Railway induced vibrations are an important source of annoyance in the built environment. Vibrations in buildings (1–80 Hz) can disturb sensitive equipment and cause discomfort to inhabitants, while re–radiated noise (16–250 Hz) may be perceived when bending resonances of floors and walls are excited.

During the last decades, a lot of research has been performed to obtain efficient and cost-effective vibration countermeasures [1,2]. Three categories of vibration reduction methods can generally be distinguished. The most effective way is to tackle the problem at the source as this affects all nearby structures. These methods include the use of ballast mats [3], soft railpads [4], under–sleeper pads [5] and floating slab tracks [6] and are frequently used for new railway infrastructure. Interventions on the propagation path between source and receiver, such as an open trench in the soil [7], form a second category of methods to reduce the vibration levels. Their main advantage is that no modifications of the track are required, but their implementation may, however, be infeasible due to practical limitations. The third category of vibration reduction methods consists of measures taken at the receiver side, such as base isolation [8]; these are only effective for the structure where the mitigation measure is applied to.

Renewed attention has recently been paid to vibration reduction technologies on the transmission path, but installed close to the track as part of the railway infrastructure [9]. These measures include vibration isolation screens [10, 11], buried wall barriers [12], subgrade stiffening [13, 14], wave impeding blocks [15, 16] and wave reflectors [17]. Subgrade stiffening is often applied under railway tracks on soft soils with the aim of reducing settlements or track displacements [18]. Common techniques to obtain the desired stiffening include deep vibro compaction, deep soil mixing, gravel or cement columns, hydraulic fracture injection with stable cement-bentonite mixtures, and vacuum consolidation [19]. Subgrade stiffening is also known to lead to reduced ground-borne vibration levels due to the increase of the effective stiffness of the soil beneath the railway track. Vibrations are therefore expected to be reduced in the lower frequency range for all vehicle speeds and at all distances from the track. Subgrade stiffening seems to be a good solution for sites with an originally soft soil [13].

Although subgrade stiffening under the track is expected to be the most efficient way to reduce vibration levels, its practical implementation often requires interruption of train traffic and might cause risk of track uplifting. This paper therefore focuses on subgrade stiffening next to the track, where a block of stiffened soil next to the track acts as a wave impeding vibration

barrier. The aim of this paper is threefold. The first objective is to analyze the effectiveness of the proposed mitigation measure. In order to facilitate physical interpretation, a homogeneous visco-elastic halfspace is therefore considered in section 2. The reduction of vibration levels is studied in case of harmonic excitation on the rail, as well as during the passage of a train, using a coupled finite element – boundary element (FE–BE) methodology. Second, simple design guidelines which allow to estimate the efficiency of subgrade stiffening next to the track in an early design stage will be presented. The third objective is to demonstrate that the performance of this mitigation measure critically depends on the soil characteristics. Therefore, two applications involving a layered halfspace are investigated in section 3. These two cases differ as a weak stiffness contrast between the soil and the block of stiffened soil exists in the first case, while the contrast is much stronger in the second case.

2 Analysis and interpretation for a homogeneous halfspace

2.1 Dynamic properties of the track, the soil and the stiffened soil

A conventional railway line on the Spanish network of ADIF between Barcelona and Gerona is considered throughout this section. The track cross section is shown in figure 1.

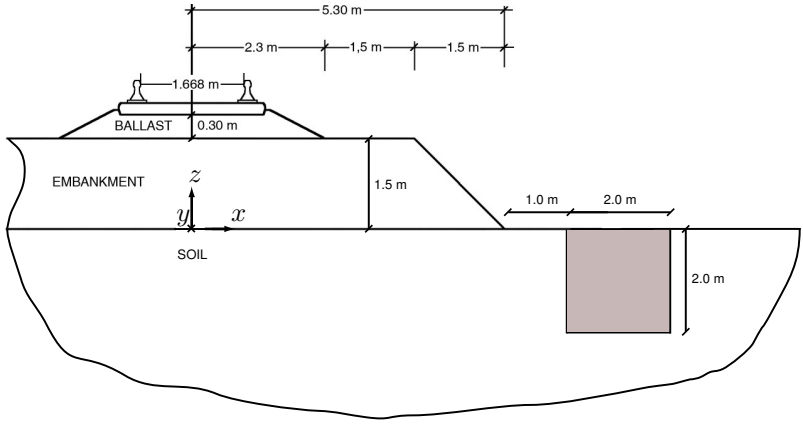

Figure 1: Track cross section.

The track consists of UIC 54 rails supported by rail pads on concrete sleepers, which are founded on a ballast layer and the embankment. The rails are modelled as Euler-Bernoulli beams with a bending stiffness $E_\mathrm{r}I_\mathrm{r} = 4.83 \times 10^6$ Nm^2 and a mass per unit length $\rho_\mathrm{r}A_\mathrm{r} = 54.4$ kg/m for each rail. A wide track gauge of 1.668 m is used on this conventional Spanish track. The rail pads have a stiffness $k_\mathrm{rp} = 153.4 \times 10^6$ N/m and a damping coefficient $c_\mathrm{rp} = 13.5 \times 10^3$ Ns/m. The following sleeper characteristics are considered: a length $l_\mathrm{sl} = 2.60$ m, a width $b_\mathrm{sl} = 0.250$ m, a height $h_\mathrm{sl} = 0.230$ m (under the rail), a centre-to-centre distance $d_\mathrm{sl} = 0.60$ m and a mass $m_\mathrm{sl} = 315$ kg.

A ballast layer with a thickness $t = 0.30$ m (under the sleepers) is also included in the track model. The ballast has a shear wave velocity $C_\mathrm{s} = 340$ m/s, a dilatational wave velocity $C_\mathrm{p} = 635$ m/s, a density $\rho = 1700$ kg/m^3 and a material damping ratio $\beta_\mathrm{s} = \beta_\mathrm{p} = 0.020$ in both deviatoric and volumetric deformation. The embankment has a thickness $t = 1.50$ m, a shear wave velocity $C_\mathrm{s} = 140$ m/s, a dilatational wave velocity $C_\mathrm{p} = 290$ m/s and a density $\rho = 1700$ kg/m^3. The same material damping ratios as for the ballast are used. The remaining geometric dimensions of the ballast and embankment are indicated on figure 1.

The soil properties at the site under consideration in reality vary with depth. Throughout this section, however, the soil is assumed to be homogeneous in order to facilitate physical interpretation of the results. A halfspace with a shear wave velocity $C_\mathrm{s} = 200$ m/s, a dilatational wave velocity $C_\mathrm{p} = 400$ m/s, a density $\rho = 2000$ kg/m^3 and a material damping ratio $\beta_\mathrm{s} = \beta_\mathrm{p} = 0.025$ in both deviatoric and volumetric deformation is considered. The phase velocity C_R of the Rayleigh waves is equal to 186 m/s [21]. The efficiency of subgrade stiffening at the actual site, taking the layered nature of the soil into account, will be discussed in subsection 3.1.

The reference case outlined above is compared to the case where a block of soil with a width and depth of 2 m located at 1 m from the tail of the embankment is stiffened (figure 1). The block of stiffened soil has a shear wave velocity $C_\mathrm{s} = 550$ m/s, a dilatational wave velocity $C_\mathrm{p} = 950$ m/s, a density $\rho = 2000$ kg/m^3 and a material damping ratio $\beta_\mathrm{s} = \beta_\mathrm{p} = 0.050$ in both deviatoric and volumetric deformation.

2.2 The numerical model

Several subproblems have to be addressed in order to investigate the vibration reduction efficiency of subgrade stiffening next to the track, such as the train–track interaction problem which allows to determine the dynamic axle loads,

the track–soil interaction problem for the calculation of the transfer functions, and the computation of the response to moving loads [20, 22].

The response in the free field at distances sufficiently far from the track is dominated by dynamic axle loads if the train speed is small compared to the Rayleigh wave velocity C_{R}. Although several mechanisms contribute to the generation of these dynamic axle loads, often only those originating from the track unevenness are taken into account [20]. This kind of dynamic excitation can be calculated based on a compliance formulation in a moving frame of reference, which requires the vehicle and track compliance. The interaction forces are subsequently combined with the transfer functions between the track and the free field, which are determined from the track–soil interaction problem.

The track–soil interaction problem is solved by means of a coupled FE–BE methodology formulated in the frequency domain [23]. The domains Ω_1 and Ω_2 are modelled by means of finite elements, while boundary elements on the soil–structure interfaces Σ_1 and Σ_2 are used to model the soil domain Ω_{s} (figure 2). Green's functions for a horizontally layered halfspace are used as fundamental solutions in the BE formulation [24, 25]. By assuming invariance of the geometry in the longitudinal direction, a computationally efficient two-and-a-half-dimensional (2.5D) approach can be applied. The longitudinal coordinate y is transformed to the wavenumber k_y by means of a forward Fourier transform, and all calculations can be performed in the frequency–wavenumber domain. Although the track has a periodic layout due to the discrete support of the sleepers, an equivalent continuous model is employed. An equivalent rail pad stiffness $\overline{k}_{\mathrm{rp}} = k_{\mathrm{rp}}/d_{\mathrm{sl}}$, damping coefficient $\overline{c}_{\mathrm{rp}} = c_{\mathrm{rp}}/d_{\mathrm{sl}}$ and a uniformly distributed sleeper mass $\overline{m}_{\mathrm{sl}} = m_{\mathrm{sl}}/d_{\mathrm{sl}}$ per unit length are calculated. The sleepers are assumed to be rigid in the plane of the track cross section and not to contribute to the longitudinal stiffness of the track. A detailed description of the governing equations of the equivalent continuous rails/rail pads/sleepers–system can be found in [20].

If N structures are considered, a weak variational formulation of the equilibrium of structure j $(j = 1, \ldots, N)$ results in the following set of coupled FE–BE equations [23]:

$$\left[\tilde{\mathbf{K}}_j(k_y,\omega) - \omega^2\mathbf{M}_j\right]\tilde{\underline{\mathbf{u}}}_j(k_y,\omega) + \sum_{k=1}^{N}\tilde{\mathbf{K}}^{\mathrm{s}}_{jk}(k_y,\omega)\tilde{\underline{\mathbf{u}}}_k(k_y,\omega) = \tilde{\underline{\mathbf{f}}}_j(k_y,\omega) \quad (1)$$

where a tilde above a variable denotes its representation in the frequency–wavenumber domain. $\tilde{\underline{\mathbf{u}}}_j(k_y,\omega)$ collects the nodal degrees of freedom of structure j, while $\tilde{\mathbf{K}}_j(k_y,\omega)$ and $\mathbf{M}_j$ are the finite element stiffness and mass matrix of this structure. $\tilde{\mathbf{K}}^{\mathrm{s}}_{jk}(k_y,\omega)$ is a dynamic soil stiffness matrix, representing the through–soil coupling of structures j and k for $j \neq k$, and is

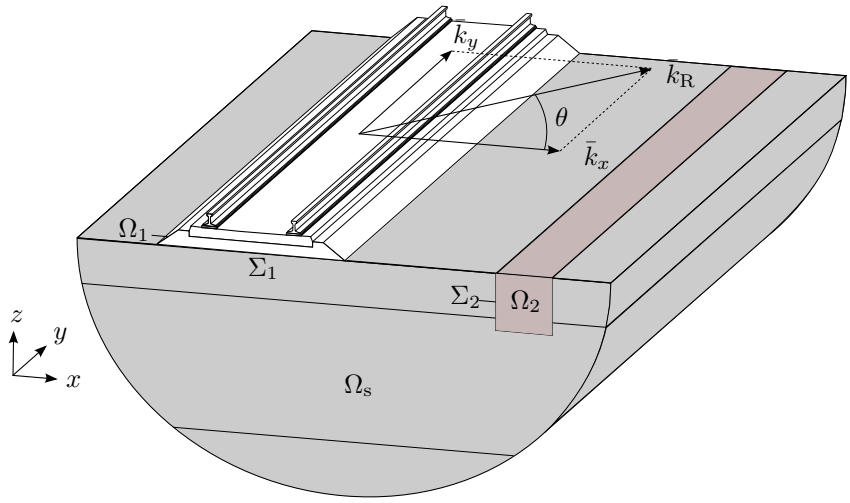

Figure 2: The 2.5D dynamic soil–structure interaction problem.

computed by means of the BE method. The force vector $\tilde{\underline{\mathbf{f}}}_j(k_y, \omega)$ results from the external forces on structure j [23]. In this paper, the number of structures N will be limited to $N = 1$ in the reference case (where only the track is considered) or $N = 2$ in the case a block of stiffened soil is introduced next to the track.

Figure 3 shows the finite element discretization. Eight–node quadrilateral finite elements are used to model the ballast, the embankment and the block of stiffened soil, which are coupled to a conforming BE mesh for the surrounding soil. The element dimensions are limited in order to ensure that at least 10 elements per minimal shear wavelength $\lambda_\mathrm{s} = 2\pi C_\mathrm{s}/\omega$ are used up to 100 Hz (determined by the shear wave velocity of the embankment), resulting in a maximum element size $l_e = 0.13\,\mathrm{m}$.

Solving the set of coupled FE–BE equations (1) provides the structural response in the frequency–wavenumber domain. The wavenumber domain formulation of the integral representation theorem [23] subsequently allows for the calculation of the radiated wavefield in the soil. The response in the frequency–spatial domain can finally be found by means of an inverse Fourier transform.

The influence of subgrade stiffening on each of the aforementioned subproblems is investigated separately in the next subsections. The train–track and the track–soil interaction problems will be addressed in subsections 2.3 and 2.4, respectively, while the overall efficiency of subgrade stiffening during the

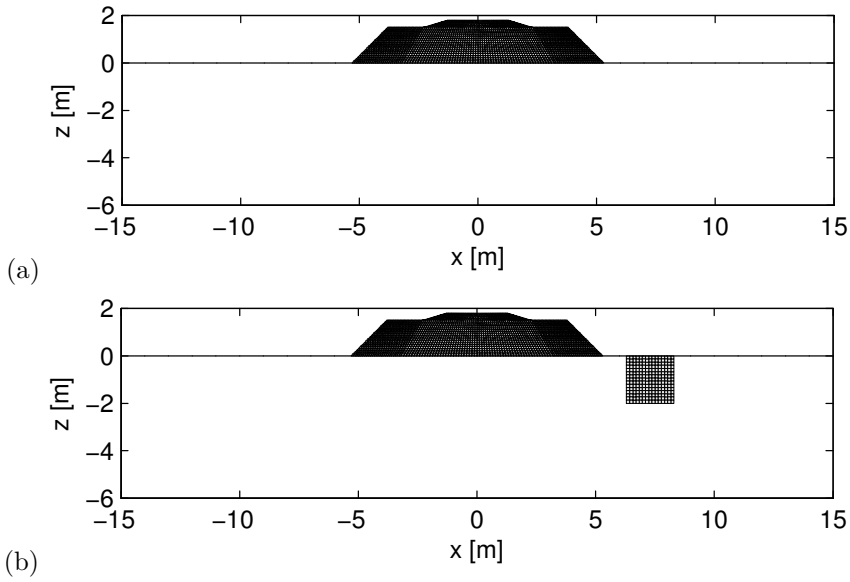

Figure 3: Finite element discretization (a) in the reference case and (b) in the case of stiffening next to the track.

passage of a Renfe S599 train will finally be evaluated in subsection 2.6.

2.3 The track compliance in the frequency domain

The dynamic axle loads are computed by means of a compliance formulation in a moving frame of reference based on the vehicle compliance, the track compliance, and the track unevenness. It can be anticipated, however, that subgrade stiffening next to the track will only have a minor impact on the track compliance, so that the dynamic axle loads will not be affected. In order to verify this, the track compliance is computed by applying a unit harmonic vertical point load to the right rail at $y = 0\,\mathrm{m}$ in both cases. The response in the frequency–wavenumber domain is found from the solution of equation (1), and an inverse Fourier transform provides the response in the frequency–spatial domain.

Figure 4 shows that the rail receptance $\hat{u}_\mathrm{r}(y = 0\,\mathrm{m}, \omega)$ is not significantly modified by the presence of the block of stiffened soil next to the track, in the frequency range considered. The track compliance, and hence the dynamic

axle loads, will remain unaffected, which implies that the efficiency of subgrade stiffening can be assessed by investigating the transfer functions only.

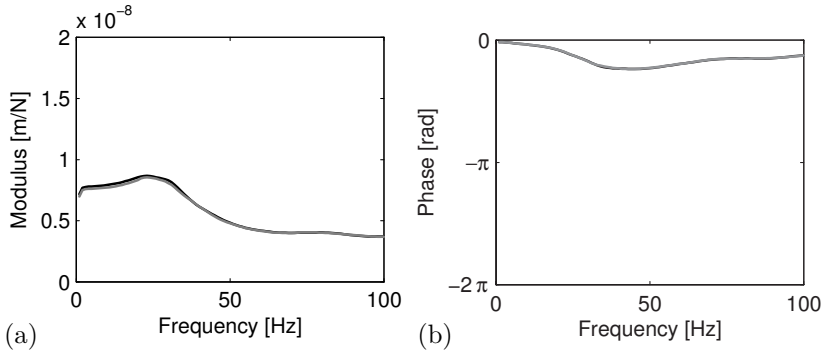

Figure 4: (a) Modulus and (b) phase of the rail receptance $\hat{u}_{\mathrm{r}}(y = 0\,\mathrm{m}, \omega)$ in the reference case (black line) and in the case of stiffening next to the track (grey line).

2.4 The free field impulse response in the frequency–wavenumber domain

As indicated in subsection 2.2, the radiated wavefield in the soil in the frequency–wavenumber domain can be obtained by application of the integral representation theorem [23]. Figure 5a and 5b show the logarithm of the modulus of the vertical free field velocity $i\omega\tilde{u}_z\left(x = 64\,\mathrm{m}, \bar{k}_y, z = 0\,\mathrm{m}, \omega\right)$ as a function of the dimensionless longitudinal wavenumber $\bar{k}_y$ and the frequency $\omega/2\pi$ in the reference case and in the case of stiffening next to the track, respectively. The dimensionless wavenumber $\bar{k}_y$ is defined as $\bar{k}_y = k_y C_{\mathrm{s}}/\omega = C_{\mathrm{s}}/C_y$, where C_{s} is the shear wave velocity of the halfspace and C_y is the phase velocity of the waves. Superimposed on both figures is the dispersion curve $\bar{k}_y = \bar{k}_{\mathrm{R}} = C_{\mathrm{s}}/C_{\mathrm{R}}$ of a Rayleigh wave propagating in the y-direction. This dispersion curve is a horizontal line $\bar{k}_{\mathrm{R}} = 1.073$ (as the halfspace has a Poisson ratio $\nu = 1/3$) due to the non-dispersive character of the Rayleigh wave in a homogeneous halfspace.

The contribution of longitudinal wavenumbers $\bar{k}_y$ larger than $\bar{k}_{\mathrm{R}}$ to the free field response is very limited, as can be seen in figures 5a and 5b. This is due

to the fact that the lateral wavenumber $\bar{k}_x = -i\sqrt{\bar{k}_y^2 - \bar{k}_\mathrm{R}^2}$ is imaginary for $\bar{k}_y > \bar{k}_\mathrm{R}$, and the wave in the x-direction hence becomes evanescent.

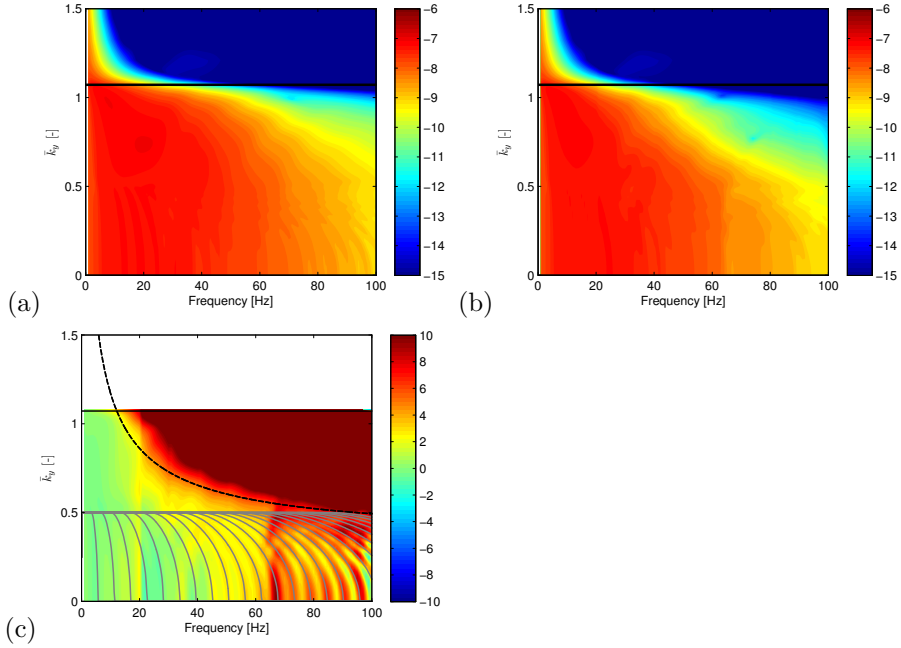

Figure 5: Logarithm of the modulus of the vertical free field velocity $i\omega\tilde{u}_z\left(x = 64\,\mathrm{m}, \bar{k}_y, z = 0\,\mathrm{m}, \omega\right)$ (a) in the reference case and (b) in the case of subgrade stiffening next to the track. The corresponding insertion loss $\widetilde{\mathrm{IL}}_z\left(x = 64\,\mathrm{m}, \bar{k}_y, z = 0\,\mathrm{m}, \omega\right)$ is shown in (c). Superimposed are the dispersion curve of a Rayleigh wave in the y-direction (solid black line), the free bending wave dispersion curve in an infinitely long beam (dashed black line) and the relation between $\bar{k}_y$ and ω given by equation (9) (solid grey lines).

The efficiency of a mitigation measure can be quantified in the frequency–wavenumber domain through the vertical insertion loss $\widetilde{\mathrm{IL}}_z(x, \bar{k}_y, z, \omega)$:

$$\widetilde{\mathrm{IL}}_z(x, \bar{k}_y, z, \omega) = 20\log_{10}\frac{|\tilde{u}_z^{\mathrm{ref}}(x, \bar{k}_y, z, \omega)|}{|\tilde{u}_z(x, \bar{k}_y, z, \omega)|} \qquad [\mathrm{dB}] \tag{2}$$

Positive values of the insertion loss indicate a reduction of the vertical free field vibrations. Figure 5c shows the insertion loss $\widetilde{\mathrm{IL}}_z\left(x = 64\,\mathrm{m}, \bar{k}_y, z = 0\,\mathrm{m}, \omega\right)$. The insertion loss is only shown in a range $0 \leq \bar{k}_y \leq \bar{k}_\mathrm{R}$, as propagating

waves only exist in this range. A clearly delimited area in the $(\bar{k}_y, \omega)$–domain corresponding to a significant insertion loss can be distinguished in this figure.

Figure 5c can physically be explained by regarding the block of stiffened soil as an infinitely long beam. The partial differential equation describing the transverse displacement $u_z(y,t)$ of a Timoshenko beam can be transformed to the frequency–wavenumber domain and reads as follows [26]:

$$\left(-\rho A\omega^2 + EIk_y^4 - \rho I\left(1+\frac{E}{\kappa\mu}\right)\omega^2 k_y^2 + \frac{\rho^2 I}{\kappa\mu}\omega^4\right)\tilde{u}_z(k_y,\omega) = \tilde{f}(k_y,\omega) \tag{3}$$

where E is the Young's modulus, μ the shear modulus, ρ the density, A the cross sectional area, I the moment of inertia for bending with respect to the horizontal axis and κ the shear coefficient of the beam. Figure 6 shows the normalized admittance $|\tilde{Y}(\bar{k}_y,\omega)/\tilde{Y}(\bar{k}_y=0,\omega)|$, where the admittance $\tilde{Y}(k_y,\omega)$ is defined as the ratio of the transverse velocity $i\omega\tilde{u}_z(k_y,\omega)$ and the external loading $\tilde{f}(k_y,\omega)$. The dimensionless wavenumber $\bar{k}_y$ is defined as above.

The dispersion relation follows from equation (3) and can be written as:

$$\left(-\frac{E}{\rho}k_y^2 + \omega^2\right)\left(-\frac{\kappa\mu}{\rho}k_y^2 + \omega^2\right) - \frac{\kappa\mu A}{\rho I}\omega^2 = 0 \tag{4}$$

The dispersion relation (4) comprises two branches of the dispersion curve, corresponding to a bending and shear mode, respectively [26]. Below a certain radial cut-on frequency equal to $\sqrt{\frac{\kappa\mu A}{\rho I}}$, there is a single branch which corresponds to real wavenumbers, and thus a propagating (bending) mode. The cut-on frequency equals $2\pi \times 138\,\mathrm{Hz}$ in the present case, which implies that only the bending mode is of importance in the frequency range considered.

Superimposed on figure 6 is the dispersion curve $\bar{k}_y = \bar{k}_\mathrm{b}$ of a free bending wave in the beam which satisfies the dispersion relation (4). This figure clearly illustrates that the amplitude of propagating bending waves in a beam becomes very small for wavenumbers $\bar{k}_y$ larger than $\bar{k}_\mathrm{b}$, which equivalently corresponds to wavelengths λ_y smaller than the free bending wavelength λ_b. The response is then dominated by the bending stiffness of the beam and the amplitude decreases proportionally to k_y^{-4} at a given radial frequency ω (cfr. equation (3)).

Figure 5c can now be interpreted based on the interaction of the Rayleigh wave in the soil and bending waves in the block of stiffened soil. At low frequencies, the wavenumber $\bar{k}_\mathrm{b}$ is larger than the wavenumber $\bar{k}_\mathrm{R}$, and the Rayleigh wave propagates through the block of stiffened soil. From a critical frequency on, the wavefield contains propagating plane waves ($\bar{k}_y \leq \bar{k}_\mathrm{R}$) with a wavenumber $\bar{k}_y$

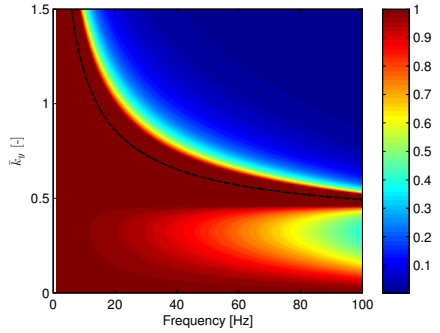

Figure 6: Normalized admittance $|\tilde{Y}(\bar{k}_y, \omega)/\tilde{Y}(\bar{k}_y = 0, \omega)|$ of a beam with the dynamic properties of the block of stiffened soil next to the track. Superimposed is the free bending wave dispersion curve (dashed black line).

larger than $\bar{k}_\mathrm{b}$ (i.e. with a wavelength λ_y smaller than λ_b). The transmission of these plane waves is impeded by the block of stiffened soil as soon as $\bar{k}_y$ is slightly larger than $\bar{k}_\mathrm{b}$ (cfr. figure 6). This explains why the zone of significant insertion loss in figure 5c is clearly delimited by the free bending wave dispersion curve. The critical radial frequency ω_c from which the block of stiffened soil can act as a wave impeding barrier is determined by the intersection of the Rayleigh wave and the free bending wave dispersion curves:

$$\omega_\mathrm{c} = C_\mathrm{R}^2 \sqrt{\frac{\rho A}{EI}} \sqrt{\frac{E\mu\kappa}{(E - \rho C_\mathrm{R}^2)\,(\mu\kappa - \rho C_\mathrm{R}^2)}} \tag{5}$$

which equals $2\pi \times 12\,\mathrm{Hz}$ in the actual case. If the shear deformation and rotational inertia of the block of stiffened soil are neglected, equation (3) reduces to the Euler–Bernoulli beam equation, and the critical frequency can be approximated as:

$$\omega_\mathrm{c} \simeq C_\mathrm{R}^2 \sqrt{\frac{\rho A}{EI}} = \frac{C_\mathrm{R}^2}{h} \sqrt{\frac{12\rho}{E}} \tag{6}$$

where h is the depth of the block of stiffened soil, if bending with respect to the horizontal axis is considered. It is clear from the discussion above that the mitigation measure can only be effective for frequencies above ω_c. Equations (5) and (6) reveal that the critical frequency strongly depends on the stiffness contrast between the soil and the block of stiffened soil, indicating that this mitigation measure will be more effective at sites with a soft soil. These

expressions furthermore illustrate that increasing the depth h of the stiffened block is beneficial, as this results in a reduction of the critical frequency. A minimal width is also required, however, in order to ensure that the block of stiffened soil behaves as a beam. Equation (6) is of great practical importance, as it provides a simple design guideline to assess the expected vibration reduction efficiency of soil stiffening next to the track, without the need of an extensive FE–BE calculation.

The physical mechanism outlined above closely resembles the phenomenon of coincidence in acoustics [27], where sound waves impinging on an infinite plate are freely transmitted if the wavelength of bending waves in the plate equals the trace wavelength of the acoustic waves in the air. In acoustics, the transmission loss below coincidence is predominantly related to the so-called mass law [27]. At the coincidence frequency, a prominent dip occurs in the transmission loss. At higher frequencies, the transmission loss increases significantly due to the increased bending stiffness. In the present case, a reduction of vibration levels is only seen above coincidence, attributed to the bending stiffness of the block of stiffened soil next to the track, while the inertia effect is negligible. An increase of the density with respect to the original soil is, however, also expected to be beneficial.

The propagating plane waves ($\bar{k}_y \leq \bar{k}_\mathrm{R}$) are characterized by a wave propagation direction $\theta = \sin^{-1}\left(\bar{k}_y/\bar{k}_\mathrm{R}\right)$ (figure 2). As a result, a reduction of vibration levels will only be obtained in an area delimited by a critical angle $\theta_\mathrm{c}(\omega) = \sin^{-1}\left(\bar{k}_\mathrm{b}/\bar{k}_\mathrm{R}\right)$, defined as:

$$\sin\theta_\mathrm{c}(\omega) = C_\mathrm{R}\sqrt{\rho\frac{E+\mu\kappa \pm \sqrt{\left(E-\mu\kappa\right)^2 + \frac{4E(\mu\kappa)^2 A}{\rho I\omega^2}}}{2E\mu\kappa}} \tag{7}$$

where the plus and minus signs correspond to the first and second branch of the beam dispersion curve, respectively. As indicated above, only the first branch is of interest in the frequency range considered. At limiting high frequencies, the critical angle related to this branch can be approximated as:

$$\sin\theta_\mathrm{c} = C_\mathrm{R}\sqrt{\frac{\rho}{\mu\kappa}} \tag{8}$$

Figure 5c furthermore exhibits a regular pattern of regions where an increased insertion loss can be observed, for $0 < \bar{k}_y < s$, where $s = C_\mathrm{s}/C_\mathrm{p} = 0.5$ in the present case. This can be explained by the fact that the P-wave travels faster through the block of stiffened soil than in the halfspace, which introduces a phase shift between the wave fronts in the reference case and in the case where stiffening next to the track is included. The following expression gives the

relation between wavenumbers $\bar{k}_y$ and radial frequencies ω which result in a phase shift equal to a multiple of 2π:

$$\left(\sqrt{\left(\frac{\omega}{C_\mathrm{R}}\right)^2-\left(\frac{\bar{k}_y\omega}{C_\mathrm{s}}\right)^2}-\sqrt{\left(\frac{\omega}{C_\mathrm{p}}\right)^2-\left(\frac{\bar{k}_y\omega}{C_\mathrm{s}}\right)^2}\right)x-\omega\frac{w}{\Delta C_\mathrm{p}}=2\pi n \quad \text{for} \quad n=0,1,2,\ldots \tag{9}$$

with $x = 64\,\mathrm{m}$ the location under consideration, $w = 2\,\mathrm{m}$ the width of the block of stiffened soil and $\Delta C_\mathrm{p} = 550\,\mathrm{m/s}$ the difference in dilatational wave velocities between the halfspace and the stiffened block. The square roots between brackets are the dimensionless lateral wavenumbers $\bar{k}_{x\mathrm{R}}$ for the Rayleigh wave and $\bar{k}_{x\mathrm{p}}$ for the P-wave, respectively, while the term $\omega w/\Delta C_\mathrm{p}$ denotes the phase shift. Lines corresponding to the relation given by equation (9) are superimposed on figure 5c. These lines coincide almost perfectly with the regions where an increased insertion loss is observed, especially at frequencies above 50 Hz, as the wavelength in the soil then becomes comparable to the dimensions of the block of stiffened soil.

The physical mechanism on which the effectiveness of subgrade stiffening next to the track is based has been interpreted in the frequency–wavenumber domain. In the following, it is shown how this mechanism becomes apparent in the frequency–spatial domain.

2.5 The free field impulse response in the frequency–spatial domain

The track and soil response in the frequency–spatial domain can be found by means of an inverse Fourier transform. Figures 7a and 7b show the real part of the vertical displacement $\hat{u}_z(\mathbf{x},\omega)$ at 5 Hz in the reference case and in the case of stiffening next to the track, respectively, due to a unit harmonic vertical point load applied to the right rail at $y = 0\,\mathrm{m}$. The Rayleigh wavelength $\lambda_\mathrm{R} = 2\pi C_\mathrm{R}/\omega$ in the soil is much larger than the width of the track, resulting in a wave field characterized by nearly cylindrical wave fronts. The corresponding insertion loss $\widehat{\mathrm{IL}}_z(\mathbf{x},\omega)$ is shown in figure 7c. As the considered frequency is smaller than the critical frequency $\omega_\mathrm{c}/2\pi$, the block of stiffened soil is unable to impede the propagation of the Rayleigh wave, and the insertion loss is zero almost everywhere in the soil domain.

Figure 8 shows the real part of the vertical displacement $\hat{u}_z(\mathbf{x},\omega)$ at a frequency of 30 Hz, which is above the critical frequency $\omega_\mathrm{c}/2\pi$. The wave fronts at the

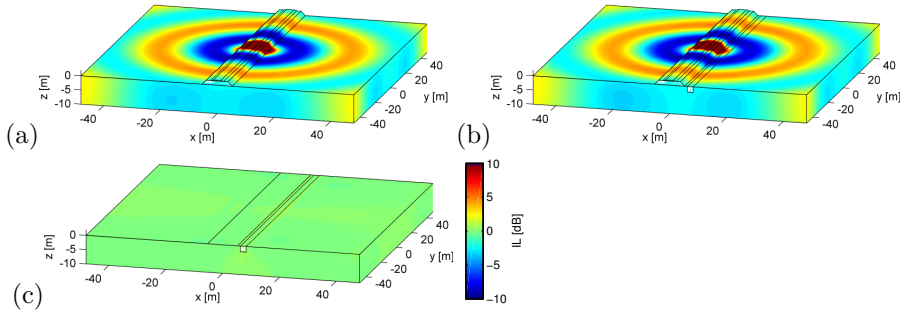

Figure 7: Real part of the vertical displacement $\hat{u}_z(\mathbf{x}, \omega)$ due to harmonic excitation on the right rail at 5 Hz (a) in the reference case and (b) in the case of stiffening next to the track, and (c) the corresponding insertion loss $\widehat{\mathrm{IL}}_z(\mathbf{x}, \omega)$.

surface of the soil are no longer cylindrical due to the dynamic interaction between the track and the halfspace. The critical angle at the considered frequency equals $\theta_\mathrm{c} = \sin^{-1}(0.73/1.073) = 43°$. This angle is indicated on figure 8c, which confirms that a significant reduction of vibration levels is obtained for $\theta > \theta_\mathrm{c}$. The insertion loss reaches values of 10 dB and more in this region. The reduction is not only obtained at the surface of the halfspace, but also at depth, although some localized areas can be identified with increased vibration levels with respect to the reference case. The angle $\sin^{-1}\left(s/\bar{k}_\mathrm{R}\right) = \sin^{-1}(0.50/1.073) = 28°$ is also indicated on figure 8c, which delimits the area where an interference pattern as considered in equation (9) is visible. Lines of constructive and destructive interference between direct and reflected Rayleigh waves can furthermore be observed at the opposite side of the track (i.e. where no soil stiffening is applied).

Figure 9 shows the real part of the vertical displacement $\hat{u}_z(\mathbf{x}, \omega)$ at a frequency of 60 Hz. As in figure 8, the wave fronts are not cylindrical. The critical angle at this frequency is $\theta_\mathrm{c} = \sin^{-1}(0.57/1.073) = 32°$, and is clearly visible in figure 9c. The interference pattern in the area bounded by the angle $\sin^{-1}\left(s/\bar{k}_\mathrm{R}\right)$ is even more clear than in figure 8. Lines of constructive and destructive interference at the opposite side of the track can be observed as well.

It follows from the previous discussion that a reduction of vibration levels is only obtained above the critical frequency $\omega_\mathrm{c}/2\pi$, predominantly in the area delimited by the critical angle $\theta_\mathrm{c}(\omega)$. The reduction on a line perpendicular to the track at the position where the load is applied is less than in other points. This is confirmed in figure 10, which shows the free field mobility at a lateral

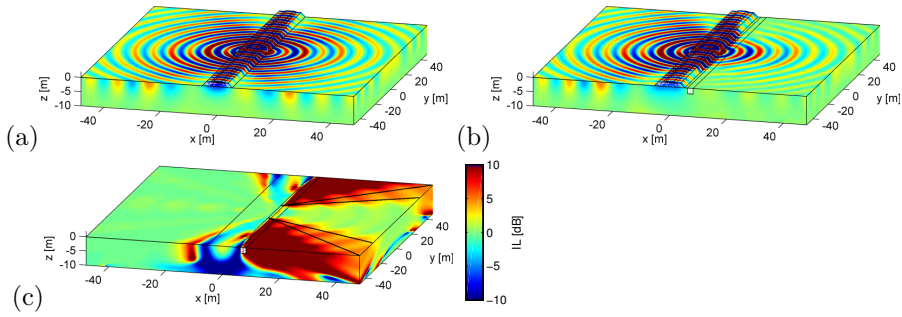

Figure 8: Real part of the vertical displacement $\hat{u}_z(\mathbf{x}, \omega)$ due to harmonic excitation on the right rail at 30 Hz (a) in the reference case and (b) in the case of stiffening next to the track, and (c) the corresponding insertion loss $\widehat{\mathrm{IL}}_z(\mathbf{x}, \omega)$.

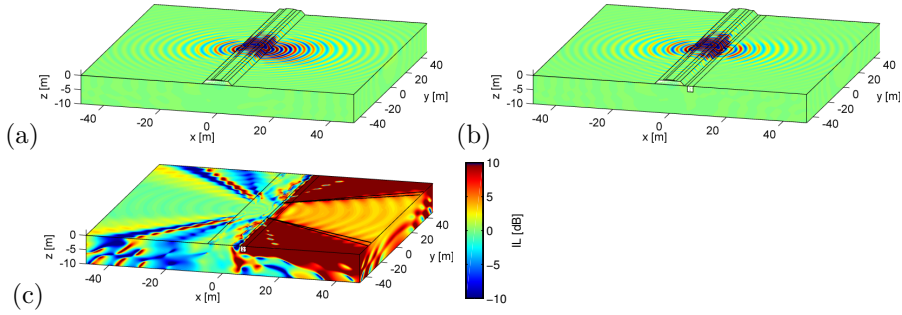

Figure 9: Real part of the vertical displacement $\hat{u}_z(\mathbf{x}, \omega)$ due to harmonic excitation on the right rail at 60 Hz (a) in the reference case and (b) in the case of stiffening next to the track, and (c) the corresponding insertion loss $\widehat{\mathrm{IL}}_z(\mathbf{x}, \omega)$.

distance of 24 m from the center of the track, at $y = 0$ m and at $y = 24$ m. This implies that, if the passage of a train is considered, the contribution of the dynamic axle loads moving towards or away from a receiver will be mitigated more effectively than the contribution of the dynamic axle loads located close to the receiver. The passage of a train is discussed in more detail in the next subsection.

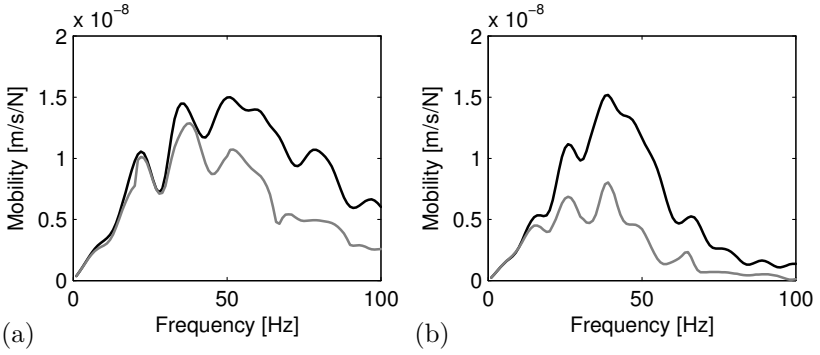

Figure 10: Free field mobility at $x = 24$ m and (a) $y = 0$ m and (b) $y = 24$ m in the reference case (black line) and in the case of stiffening next to the track (grey line).

2.6 The free field response during the passage of a Renfe S599 train

Finally, the vibration reduction efficiency of the proposed mitigation measure during the passage of a Renfe S599 train at a speed of 160 km/h is investigated. This type of train consists of two motor coaches and a central carriage and has a total length of 75.98 m. Each carriage is supported by two bogies and has four axles. The number of axles N_a, the carriage length L_t, the distance L_b between bogies, the axle distance L_a, and the unsprung axle mass M_u of the carriages are summarized in table 2. Only these unsprung masses are taken into account, as the carriage's primary and secondary suspension isolate the body and the bogie from the wheelset at frequencies above a few Hertz [28].

As indicated in subsection 2.2, only the dynamic axle loads originating from the track unevenness are taken into account. A track with an unevenness profile according to the FRA class 3 [29] is assumed. The free field velocity due to a train passage is characterized by an increasing vibration level when the train is approaching, a nearly stationary vibration level during the passage of the train

	N_a [−]	L_t [m]	L_b [m]	L_a [m]	M_u [kg]
Two motor coaches	4	25.85	17.73	2.50	1940
One central carriage	4	24.28	18.00	2.50	1704

Table 1: Characteristics of the Renfe S599 train.

and a decreasing vibration level when the train is moving away. It has been shown that the dominating stationary part of the free field velocity can be well approximated by a prediction in which the dynamic axle loads are applied at fixed positions [30]. This approach is employed throughout this section.

Figure 11 shows the one–third octave band RMS spectra of the vertical free field vibration velocity during the passage of a Renfe S599 train at a speed of 160 km/h. In the reference case, the frequency content of the free field vibrations close to the track is mainly situated in a frequency range between 20 Hz and 100 Hz, while at larger distances from the track, material damping in the soil results in a strong attenuation of the response at high frequencies. In the case of subgrade stiffening next to the track, a reduction of vibration levels is obtained above the critical frequency of 12 Hz. Superimposed on figure 11 are ISO vibration criterion curves for the effect of vibrations on people in buildings [31], indicating that subgrade stiffening can be used as an effective mitigation measure in order to comply with vibration criteria. Subgrade stiffening has furthermore a negligible effect on the vibration levels at the opposite side of the track, as the interference patterns observable in case of harmonic excitation (cfr. figures 8c and 9c) cancel each other out during the passage of a train.

The efficiency of the mitigation measure is investigated in more detail in figure 12, which shows the vertical insertion loss $\widehat{\mathrm{IL}}_z(\mathbf{x},\omega)$ for several locations at increasing distance from the track. The insertion loss is defined in a similar way as in equation (2), but now for the one–third octave band RMS spectra of the vertical free field vibration velocity. This figure clearly confirms that a reduction can be obtained above the critical frequency $\omega_c/2\pi$. Generally speaking, the insertion loss is higher at locations closer to the track, while an increase of insertion loss with frequency can be observed at a particular location.

The results in figure 12 can be understood by considering figure 13, which shows a top view of the track, the block of stiffened soil next to the track and the free field. The fixed positions of the dynamic axle loads $\hat{\mathbf{g}}_k(\omega)$ are indicated, as well as two receiver locations $\mathbf{x}_1 = \{x_1, 0, 0\}^{\mathrm{T}}$ and $\mathbf{x}_2 = \{x_2, 0, 0\}^{\mathrm{T}}$ in the free field,

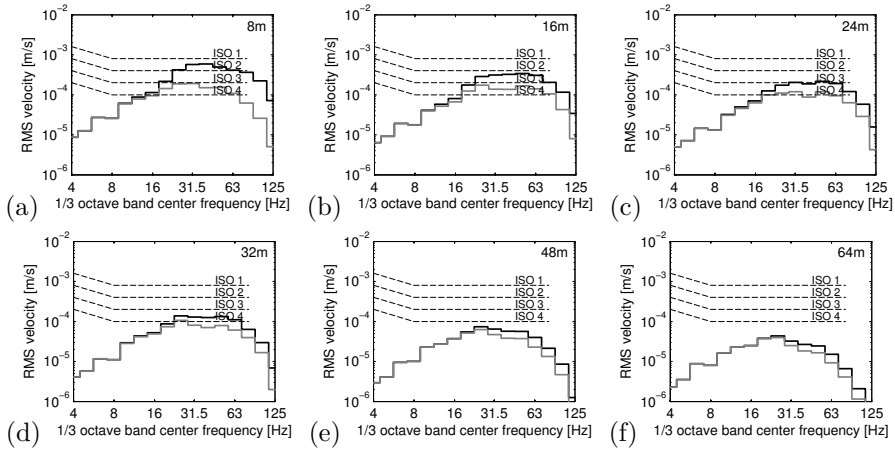

Figure 11: One–third octave band RMS spectra of the vertical free field vibrations in the reference case (black line) and in the case of stiffening next to the track (grey line) at a distance of (a) 8 m, (b) 16 m, (c) 24 m, (d) 32 m, (e) 48 m and (f) 64 m from the center of the track due to the passage of a Renfe S599 train at a speed of 160 km/h.

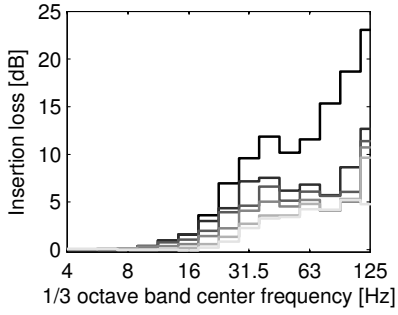

Figure 12: Vertical insertion loss $\widehat{\mathrm{IL}}_z(\mathbf{x},\omega)$ at 8 m, 16 m, 24 m, 32 m, 48 m and 64 m from the center of the track (black to light grey lines) due to the passage of a Renfe S599 train at a speed of 160 km/h.

with $x_1 < x_2$. At each axle load position, thin grey lines indicate the critical angle $\theta_c(\omega)$, delimiting the area in which the free field vibrations resulting from excitation at the considered position are significantly reduced. Figure 13a illustrates that, at a particular radial frequency $\omega_1 > \omega_c$, the contribution of all axle loads to the free field vibration at the location $\mathbf{x}_1$ is significantly reduced, except for the axle loads $\hat{\mathbf{g}}_{i-1}(\omega)$ to $\hat{\mathbf{g}}_{i+1}(\omega)$ (as $\mathbf{x}_1$ is not situated within the area where a significant reduction can be expected for these axle loads). At the location $\mathbf{x}_2$ further away from the track, however, the transfer of a smaller number of axle loads is effectively mitigated by the block of stiffened soil, as the contribution of the axle loads $\hat{\mathbf{g}}_{i-3}(\omega)$ to $\hat{\mathbf{g}}_{i+3}(\omega)$ will not be reduced. This indicates that subgrade stiffening next to the track is less efficient at locations further away from the track. At a higher radial frequency ω_2 ($\omega_c < \omega_1 < \omega_2$), the critical angle $\theta_c(\omega_2)$ decreases corresponding to equation (7), which implies that the area in which the transfer to the free field is reduced, enlarges. As illustrated in figure 13b, the contribution of all axle loads to the free field vibrations at $\mathbf{x}_1$ will be reduced at this frequency except for $\hat{\mathbf{g}}_i(\omega)$, while the contribution of all axle loads, except $\hat{\mathbf{g}}_{i-1}(\omega)$ to $\hat{\mathbf{g}}_{i+1}(\omega)$, will be reduced at $\mathbf{x}_2$.

The previous discussion reveals that the contribution to the free field vibration of a larger number of axle loads is significantly reduced if a receiver location closer to the track is considered, and for increasing frequencies. These trends are confirmed in figure 12. The free field vibration in the near field is dominated by the closest axle loads (which contribution will not be reduced), while all axle loads contribute almost equally to the response in the far field. The actual value of the insertion loss $\widehat{\mathrm{IL}}_z(\mathbf{x}, \omega)$ obtained at a particular receiver location $\mathbf{x}$ is therefore determined by a trade–off between the relative importance of each axle load and the possibility to mitigate the transfer from the axle load to the free field.

2.7 Comparison with results from literature

It is instructive to compare the results outlined in this section with previous studies [12, 13, 15, 32, 33]. The current results confirm that subgrade stiffening is more efficient at sites with a soft soil and that increasing the stiffness of the block of soil next to the track is beneficial. It has also been observed in [13] that trenches backfilled with concrete serve as 'concave lenses', where a reduction of the vibration levels is predominantly achieved behind and in front of the source. This can be related to the existence of a critical angle, as outlined in subsection 2.4. A more comprehensive explanation of the underlying physics is, however, formulated in the present paper. This study furthermore demonstrates the necessity of 2.5D/3D models to correctly reveal

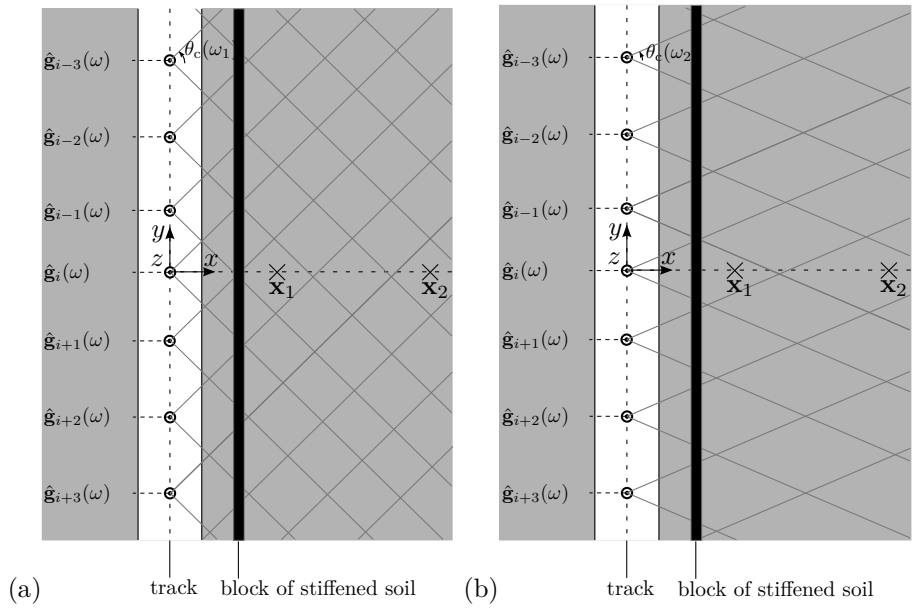

Figure 13: Top view of the track (white), the block of stiffened soil next to the track (black) and the free field (grey). The fixed positions of the dynamic axle loads $\hat{\mathbf{g}}_{i-3}(\omega)$ to $\hat{\mathbf{g}}_{i+3}(\omega)$ are indicated with circles. Superimposed at each axle load position are thin grey lines indicating the critical angle $\theta_c(\omega)$ at a radial frequency (a) ω_1 and (b) ω_2, with $\omega_c < \omega_1 < \omega_2$.

the underlying physical mechanism and indicates that the use of 2D models is not sufficient.

The proposed mitigation measure can also be compared to alternative methods such as vibration isolation screens. Open trenches aim at reflecting the impinging waves and are effective for trench depths of about one Rayleigh wavelength [10]. The construction of open trenches is, however, for stability reasons limited to shallow depths; the use of in–fill materials allows to increase the depth. If a soft in–fill material is used, the behaviour of a filled trench resembles that of an open trench. The use of a stiff in–fill material, however, results in a wave impeding effect closely related to the physical mechanism outlined in the present paper, and the vibration reduction of such a trench is no longer based on the reflection of incident waves [34].

3 Case studies involving a layered halfspace

In this section, two case studies involving a layered halfspace are discussed to indicate that the effectiveness of this mitigation measure critically depends on the soil characteristics of the site where it is applied. The validity of equations (5) and (7) for the critical frequency and angle, respectively, will be verified in both cases, demonstrating their usefulness as a design tool, even in the case of a layered halfspace. For the sake of brevity, only the transfer functions between the track and the free field will be investigated for these case studies.

3.1 Site near Gerona

In the first case, the conventional railway line between Barcelona and Gerona introduced in section 2 is reconsidered, accounting now for the actual dynamic soil characteristics. Geotechnical tests (active and passive SASW tests, seismic refraction tests) have been performed at the site, and an inverse problem was solved to retrieve the soil layering and corresponding shear and dilatational wave velocities. The resulting soil profile is listed in table 2, together with estimated values for the soil density and material damping ratios. This table indicates that the layered halfspace consists of relatively stiff layers, with the ground water table at a depth of 2 m.

Layer	h [m]	C_s [m/s]	C_p [m/s]	β_s [−]	β_p [−]	ρ [kg/m^3]
1	1	275	740	0.025	0.025	2000
2	1	325	740	0.025	0.025	2000
3	4	380	1450	0.025	0.025	2000
4	7	470	2280	0.025	0.025	2000
5	∞	600	2580	0.025	0.025	2000

Table 2: Dynamic soil characteristics at the site near Gerona.

The propagation of Rayleigh waves is dispersive due to the variation of the soil properties with depth. Multiple modes with associated cut-on frequencies exist. Figure 14 shows the dimensionless Rayleigh wave dispersion curves $\bar{k}_\mathrm{R} = k_\mathrm{R} C_\mathrm{s1}/\omega$, with C_s1 the shear wave velocity of the top layer. Six modes exist in the frequency range considered.

The insertion loss $\widetilde{\mathrm{IL}}_z\left(x = 64\,\mathrm{m}, \bar{k}_y, z = 0\,\mathrm{m}, \omega\right)$ between the reference case and the case where stiffening next to the track is included is shown in figure 14,

where the same geometric and dynamic properties for the block of stiffened soil next to the track as in section 2 are used. The insertion loss is only shown in the range where propagating waves exist. This figure reveals that the physical mechanism outlined in section 2 is still identified in the case of a layered halfspace, as the region where a significant insertion loss is obtained is bounded by the fundamental Rayleigh wave dispersion curve and the free bending wave dispersion curve. The critical radial frequency ω_c can be determined by iteratively solving equation (5), where C_R has to be replaced by $C_R(\omega)$ due to the dispersive nature of the Rayleigh wave. Due to the weak stiffness contrast between the soil and the block of stiffened soil, the critical frequency is as high as $2\pi \times 51\,\text{Hz}$. This suggests that applying soil stiffening next to the track at the considered site is not effective to mitigate railway induced vibrations.

An interference pattern can furthermore be observed in figure 14 at high frequencies and low wavenumbers. This pattern is, however, more complicated than in the case of a homogeneous halfspace (figure 5c) due to multiple reflections and refractions at the layer interfaces.

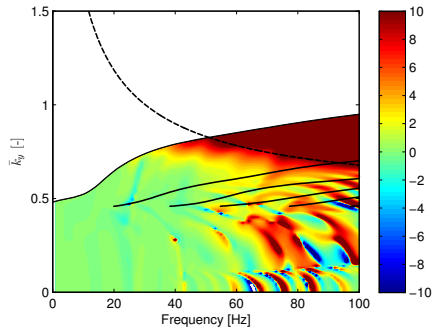

Figure 14: Insertion loss $\widetilde{\text{IL}}_z\left(x = 64\,\text{m}, \bar{k}_y, z = 0\,\text{m}, \omega\right)$ at the site near Gerona. Superimposed are the Rayleigh wave dispersion curves (solid black lines) and the free bending wave dispersion curve in an infinitely long beam (dashed black line).

Figures 15 and 16 show the real part of the vertical displacement $\hat{u}_z(\mathbf{x}, \omega)$ at a frequency of 30 Hz and 60 Hz, respectively. It is clear that the block of stiffened soil is unable to impede the propagation of the Rayleigh waves at 30 Hz, while it starts to be more effective at 60 Hz. The area where a significant insertion loss can be observed is, however, not as clearly delimited as in the case of a homogeneous halfspace.

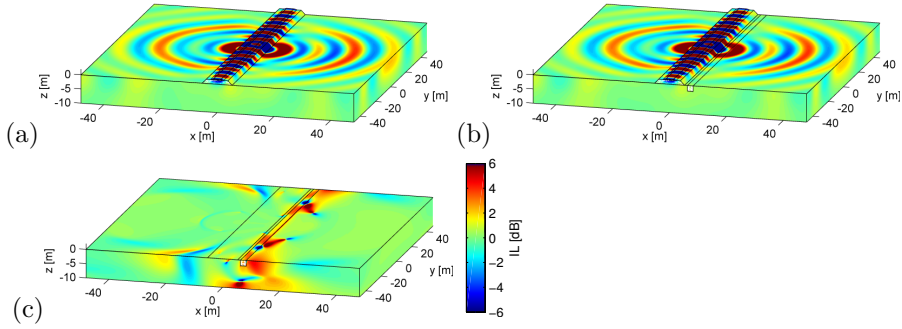

Figure 15: Real part of the vertical displacement $\hat{u}_z(\mathbf{x}, \omega)$ at the site near Gerona due to harmonic excitation on the right rail at 30 Hz (a) in the reference case and (b) in the case of stiffening next to the track, and (c) the corresponding insertion loss $\widehat{\mathrm{IL}}_z(\mathbf{x}, \omega)$.

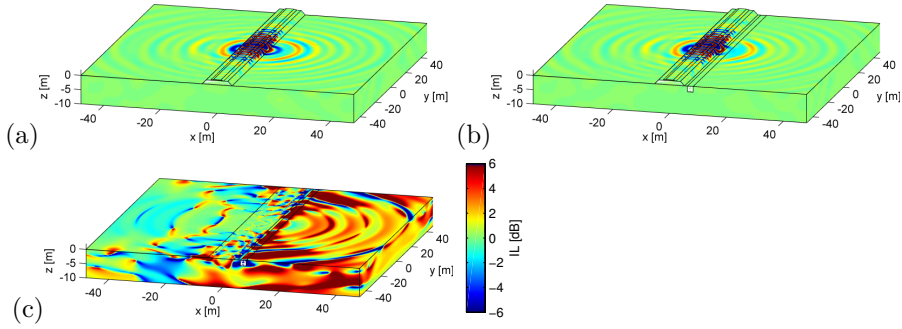

Figure 16: Real part of the vertical displacement $\hat{u}_z(\mathbf{x}, \omega)$ at the site near Gerona due to harmonic excitation on the right rail at 60 Hz (a) in the reference case and (b) in the case of stiffening next to the track, and (c) the corresponding insertion loss $\widehat{\mathrm{IL}}_z(\mathbf{x}, \omega)$.

Figure 17 shows the free field mobility at a lateral distance of 24 m from the center of the track, at $y = 0$ m and at $y = 24$ m. This confirms that the effectiveness of the proposed mitigation measure at the considered site is very limited. No significant reduction can be observed at $y = 24$ m, as the critical angle at 100 Hz equals 45°.

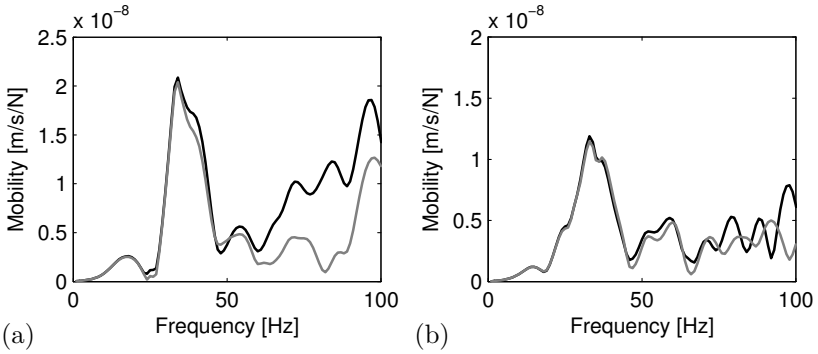

Figure 17: Free field mobility at the site near Gerona at $x = 24$ m and (a) $y = 0$ m and (b) $y = 24$ m in the reference case (black line) and in the case of stiffening next to the track (grey line).

3.2 Site near Murcia

A conventional Spanish railway line connecting Murcia and Orihuela is considered as a second case. The properties of the rails, rail pads and sleepers are the same as outlined in section 2. The sleepers are supported by a ballast layer, a form layer and an embankment with a thickness of 0.25 m, 0.40 m and 0.55 m, respectively. The width varies linearly from 2.60 m under the sleepers to 10.60 m at the track–soil interface. The ballast has the same dynamic properties as in section 2, while the form layer and the embankment are characterised by shear wave velocities $C_s = 215$ m/s and $C_s = 200$ m/s, and dilatational wave velocities $C_p = 715$ m/s and $C_p = 665$ m/s, respectively. These two layers have a density $\rho = 1900$ kg/m^3 and the same material damping ratios as the ballast. The finite element discretization of the track is shown in figure 18.

Geotechnical tests have been performed at this site as well and resulted in the soil profile summarized in table 3, in which the soil density and material damping ratios are estimated values. The soil at this site consists of relatively soft layers with a density varying between 1875 kg/m^3 and 2000 kg/m^3; it is

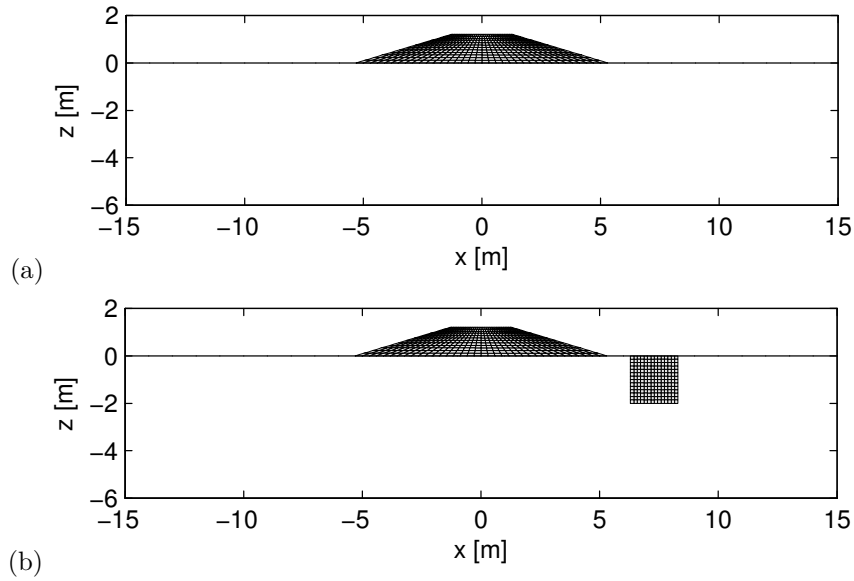

Figure 18: Finite element discretization (a) in the reference case and (b) in the case of stiffening next to the track for the site near Murcia.

important to notice that the layers on top of the halfspace are assumed to have a lower density than the block of stiffened soil.

Layer	h [m]	C_s [m/s]	C_p [m/s]	β_s [−]	β_p [−]	ρ [kg/m^3]
1	10	150	500	0.025	0.025	1875
2	20	200	665	0.025	0.025	1875
3	10	240	665	0.025	0.025	1885
4	∞	280	690	0.025	0.025	2000

Table 3: Dynamic soil characteristics at the site near Murcia.

The insertion loss $\widetilde{\mathrm{IL}}_z\left(x = 64\,\mathrm{m}, \bar{k}_y, z = 0\,\mathrm{m}, \omega\right)$ between the reference case and the case where stiffening next to the track is included is shown in figure 19. The insertion loss is only shown in the range where propagating waves exist. The dimensionless Rayleigh wave dispersion curves of the first four modes are superimposed on this figure, although a larger number of Rayleigh modes exists in the frequency range considered. The shear wave velocity of the top layer is

used to define the dimensionless wavenumbers. The significant stiffness contrast between the soil and the block of stiffened soil results in a low value of $2\pi \times 8\,\mathrm{Hz}$ for the critical radial frequency. This indicates that soil stiffening next to the track is very effective at this site. The region where a significant insertion loss is obtained is, as expected, bounded by the fundamental Rayleigh wave dispersion curve and the free bending wave dispersion curve.

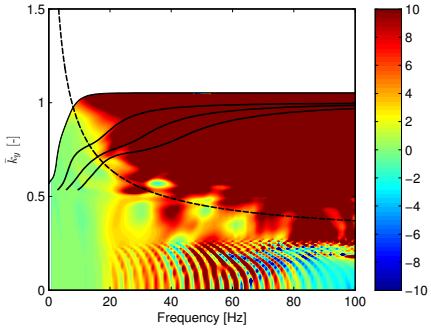

Figure 19: Insertion loss $\widetilde{\mathrm{IL}}_z\left(x = 64\,\mathrm{m}, \bar{k}_y, z = 0\,\mathrm{m}, \omega\right)$ at the site near Murcia. Superimposed are the Rayleigh wave dispersion curves of the first four modes (solid black lines) and the free bending wave dispersion curve in an infinitely long beam (dashed black line).

Figures 20 and 21 show the real part of the vertical displacement $\hat{u}_z(\mathbf{x}, \omega)$ at a frequency of 30 Hz and 60 Hz, respectively. A significant insertion loss is obtained at both frequencies. The reduction does not only appear in the area $\theta > \theta_\mathrm{c}$, but also for angles $\theta < \theta_\mathrm{c}$. While the former can be explained based on the physical mechanism outlined in section 2, the latter can be attributed to the additional inertia of the block of stiffened soil with respect to the reference case. As indicated in subsection 2.4, this can be related to the mass law in acoustics [27].

Figure 22 shows the free field mobility at a lateral distance of 24 m from the center of the track, at $y = 0\,\mathrm{m}$ and at $y = 24\,\mathrm{m}$. This confirms that the proposed mitigation measure is very effective in a wide frequency range.

4 Conclusions

In this paper, the efficiency of subgrade stiffening as a mitigation measure for railway induced vibrations has been investigated. An analysis in the frequency–

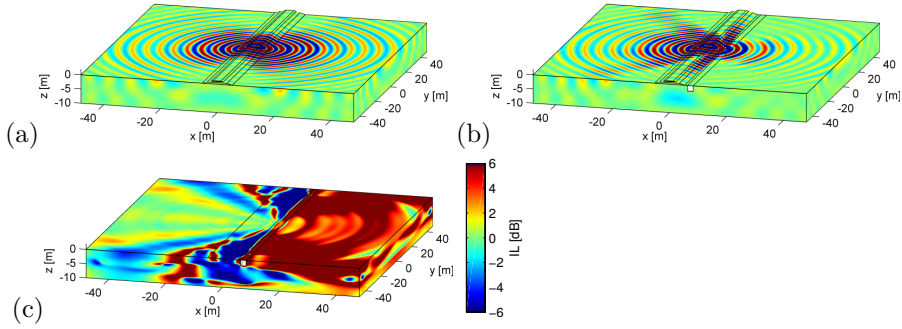

Figure 20: Real part of the vertical displacement $\hat{u}_z(\mathbf{x}, \omega)$ at the site near Murcia due to harmonic excitation on the right rail at 30 Hz (a) in the reference case and (b) in the case of stiffening next to the track, and (c) the corresponding insertion loss $\widehat{\mathrm{IL}}_z(\mathbf{x}, \omega)$.

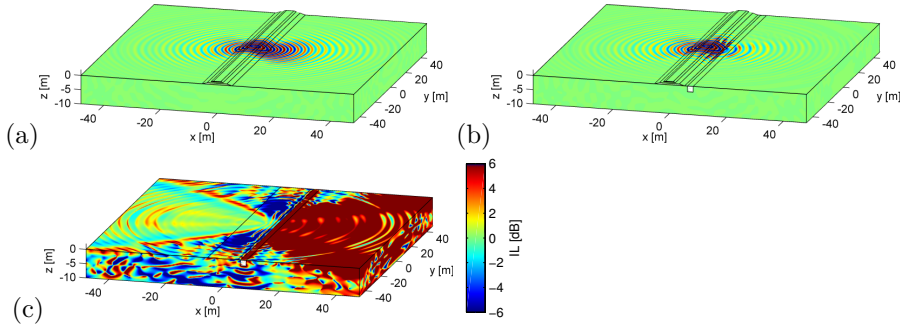

Figure 21: Real part of the vertical displacement $\hat{u}_z(\mathbf{x}, \omega)$ at the site near Murcia due to harmonic excitation on the right rail at 60 Hz (a) in the reference case and (b) in the case of stiffening next to the track, and (c) the corresponding insertion loss $\widehat{\mathrm{IL}}_z(\mathbf{x}, \omega)$.

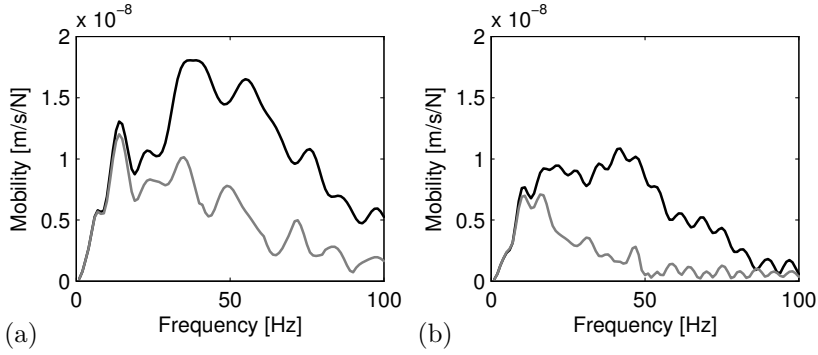

Figure 22: Free field mobility at the site near Murcia at $x = 24\,\mathrm{m}$ and (a) $y = 0\,\mathrm{m}$ and (b) $y = 24\,\mathrm{m}$ in the reference case (black line) and in the case of stiffening next to the track (grey line).

wavenumber domain has clearly illustrated that the block of stiffened soil next to the track can act as a wave impeding barrier. The wave impeding effect does, however, critically depend on the relation between the Rayleigh wavelength in the soil and the free bending wavelength in the block of stiffened soil next to the track. This leads to the existence of a critical radial frequency ω_c from which this mitigation measure starts to be effective, as well as a critical angle $\theta_c(\omega)$ delimiting the area where the vibration levels are reduced. The expressions for ω_c and $\theta_c(\omega)$ have a practical implication, as they allow to assess the expected efficiency of soil stiffening in an early design stage, without the need of an extensive FE–BE calculation.

The passage of a train has been eventually been investigated, revealing that the free field vibration levels can significantly be reduced. It was shown that the number of axle loads of which the contribution to the free field vibration at a certain location is reduced, decreases with the distance from the track and increases with the frequency.

Two applications have furthermore been discussed in this paper, taking the layered structure of the soil into account. These case studies have illustrated that the performance of the proposed mitigation measure strongly depends on the stiffness contrast between the soil and the block of stiffened soil.

Acknowledgements

The results presented in this paper have been obtained within the frame of the EU FP7 project RIVAS (Railway Induced Vibration Abatement Solutions) [9]. The authors would like to thank Vicente Cuéllar (CEDEX), Miguel Rodríguez (ADIF) and Goran Vukotic (Keller Terra) for providing valuable data and advice on the properties of the rolling stock, the track, the soil and the block of stiffened soil. The first author is a doctoral fellow and the second author is a postdoctoral fellow of the Research Foundation Flanders (FWO). The financial support is gratefully acknowledged.

References

[1] C.J.C. Jones. Use of numerical-models to determine the effectiveness of anti-vibration systems for railways. *Proceedings of the Institution of Civil Engineers-Transport*, 105(1):43–51, 1994.

[2] A.M. Kaynia, C. Madshus, and P. Zackrisson. Ground vibration from high speed trains: prediction and countermeasure. *Journal of Geotechnical and Geoenvironmental Engineering, Proceedings of the ASCE*, 126(6):531–537, 2000.

[3] R. Müller. Mitigation measures for open lines against vibration and ground-borne noise: a Swiss overview. In Burkhard Schulte-Werning, David Thompson, Pierre-Etienne Gautier, Carl Hanson, Brian Hemsworth, James Nelson, Tatsuo Maeda, and Paul de Vos, editors, *Noise and Vibration Mitigation for Rail Transportation Systems*, volume 99 of *Notes on Numerical Fluid Mechanics and Multidisciplinary Design*, pages 264–270. Springer Berlin / Heidelberg, 2008.

[4] R. Hildebrand. Effect of soil stabilization on audible band railway ground vibration. *Soil Dynamics and Earthquake Engineering*, 24:411–424, 2004.

[5] H. Loy. Mitigating vibration using under-sleeper pads. *Railway Gazette International*, 168(4):40–43, 2012.

[6] G. Lombaert, G. Degrande, B. Vanhauwere, B. Vandeborght, and S. François. The control of ground borne vibrations from railway traffic by means of continuous floating slabs. *Journal of Sound and Vibration*, 297(3-5):946–961, 2006.

[7] A. Karlström and A. Boström. Efficiency of trenches along railways for trains moving at sub- or supersonic speeds. *Soil Dynamics and Earthquake Engineering*, 27:625–641, 2007.

[8] J.P. Talbot and H.E.M. Hunt. A generic model for evaluating the performance of base-isolated buildings. *Journal of Low Frequency Noise, Vibration and Active Control*, 22(3):149–160, 2003.

[9] http://www.rivas-project.eu, 2011.

[10] R.D. Woods. Screening of surface waves in soils. *Journal of the Soil Mechanics and Foundation Division, Proceedings of the ASCE*, 94(SM4):951–979, 1968.

[11] K.R. Massarsch. Vibration isolation using gas-filled cushions. In *Proceedings of the Geo-Frontiers 2005 Congress*, Austin, Texas, January 2005. American Society of Civil Engineers.

[12] C.J.C. Jones, D.J. Thompson, and J.I. Andreu-Medina. Initial theoretical study of reducing surface-propagating vibration from trains using earthworks close to the track. In *Proceedings of the 8th International Conference on Structural Dynamics, EURODYN 2011*, pages 684–691, Leuven, Belgium, July 2011.

[13] L. Andersen and S.R.K. Nielsen. Reduction of ground vibration by means of barriers or soil improvement along a railway track. *Soil Dynamics and Earthquake Engineering*, 25:701–716, 2005.

[14] A.T. Peplow and A.M. Kaynia. Prediction and validation of traffic vibration reduction due to cement column stabilization. *Soil Dynamics and Earthquake Engineering*, 27:793–802, 2007.

[15] H.H. Hung, Y.B. Yang, and D.W. Chang. Wave barriers for reduction of train-induced vibrations in soils. *Journal of Geotechnical Engineering, Proceedings of the ASCE*, 130(12):1283–1291, 2004.

[16] X. Sheng, C.J.C. Jones, and D.J. Thompson. Prediction of ground vibration from trains using the wavenumber finite and boundary element methods. *Journal of Sound and Vibration*, 293:575–586, 2006.

[17] V.V. Krylov. Scattering of Rayleigh waves by heavy masses as method of protection against traffic-induced ground vibrations. In H. Takemiya, editor, *Environmental vibrations. Prediction, Monitoring, Mitigation and Evaluation*, pages 393–398. Taylor and Francis Group, London, 2005.

[18] D. Adam, A. Vogel, and A. Zimmermann. Ground improvement techniques beneath existing rail tracks. *Ground Improvement*, 11(4):229–235, 2007.

[19] B.O. Skipp, editor. *Ground dynamics and man made processes*. Thomas Telford, 1998.

[20] G. Lombaert, G. Degrande, J. Kogut, and S. François. The experimental validation of a numerical model for the prediction of railway induced vibrations. *Journal of Sound and Vibration*, 297(3-5):512–535, 2006.

[21] J.W.S. Rayleigh. On waves propagated along the plane surface of an elastic solid. *Proceedings of the London Mathematical Society*, 17:4–11, 1887.

[22] X. Sheng, C.J.C. Jones, and D.J. Thompson. A theoretical model for ground vibration from trains generated by vertical track irregularities. *Journal of Sound and Vibration*, 272(3-5):937–965, 2004.

[23] S. François, M. Schevenels, G. Lombaert, P. Galvín, and G. Degrande. A 2.5D coupled FE-BE methodology for the dynamic interaction between longitudinally invariant structures and a layered halfspace. *Computer Methods in Applied Mechanics and Engineering*, 199(23-24):1536–1548, 2010.

[24] E. Kausel and J.M. Roësset. Stiffness matrices for layered soils. *Bulletin of the Seismological Society of America*, 71(6):1743–1761, 1981.

[25] M. Schevenels, S. François, and G. Degrande. EDT: An ElastoDynamics Toolbox for MATLAB. *Computers & Geosciences*, 35(8):1752–1754, 2009.

[26] P. Hagedorn and A. DasGupta. *Vibrations and Waves in Continuous Mechanical Systems*. John Wiley & Sons, Chichester, United Kingdom, 2007.

[27] L. Cremer, M. Heckl, and B.A.T. Petersson. *Structure-borne sound: Structural vibrations and sound radiation at audio frequencies*. Springer, Berlin, 3rd edition, 2005.

[28] K. Knothe and S.L. Grassie. Modelling of railway track and vehicle/track interaction at high frequencies. *Vehicle Systems Dynamics*, 22: 209–262, 1993.

[29] V.K. Garg and R.V. Dukkipati. *Dynamics of railway vehicle systems*. Academic Press, Canada, 1984.

[30] H. Verbraken, G. Lombaert, and G. Degrande. Verification of an empirical prediction method for railway induced vibrations by means of numerical simulations. *Journal of Sound and Vibration*, 330(8):1692–1703, 2011.

[31] International Organization for Standardization. *ISO 2631-2:1989: Evaluation of human body exposure to whole-body vibration - Part 2: Continuous and shock-induced vibration in buildings (1 to 80 Hz)*, 1989.

[32] S. Ahmad and T.M. Al-Hussaini. Simplified design for vibration screening by open and in-filled trenches. *Journal of Geotechnical Engineering, Proceedings of the ASCE*, 117(1): 67–88, 1991.

[33] R.K. Shrivastava and N.S.V. Kameswara Rao. Response of soil media due to impulse loads and isolation using trenches. *Soil Dynamics and Earthquake Engineering*, 22(6): 695–702, 2002.

[34] S. François, M. Schevenels, B. Thyssen, J. Borgions, and G. Degrande. Design and efficiency of a vibration isolating screen in the soil. *Soil Dynamics and Earthquake Engineering*, 39:113–127, 2012.

Paper E

The influence of source–receiver interaction on the numerical prediction of railway induced vibrations

Published in the Journal of Sound and Vibration 333(12) (2014) 2520–2538
http://dx.doi.org/10.1016/j.jsv.2014.01.017

The influence of source–receiver interaction on the numerical prediction of railway induced vibrations

P. Coulier, G. Lombaert, G. Degrande
KU Leuven, Department of Civil Engineering,
Kasteelpark Arenberg 40, B-3001 Leuven, Belgium

Abstract

The numerical prediction of vibrations in buildings due to railway traffic is a complicated problem where wave propagation in the soil couples the source (railway tunnel or track) and the receiver (building). This through–soil coupling is often neglected in state–of–the–art numerical models in order to reduce the computational cost. In this paper, the effect of this simplifying assumption on the accuracy of numerical predictions is investigated. A coupled finite element – boundary element methodology is employed to analyze the interaction between a building and a railway tunnel at depth or a ballasted track at the surface of a homogeneous halfspace, respectively. Three different soil types are considered. It is demonstrated that the dynamic axle loads can be calculated with reasonable accuracy using an uncoupled strategy in which through–soil coupling is disregarded. If the transfer functions from source to receiver are considered, however, large local variations in terms of vibration insertion gain are induced by source–receiver interaction, reaching up to 10 dB and higher, although the overall wave field is only moderately affected. A global quantification of the significance of through–soil coupling is made, based on the mean vibrational energy entering a building. This approach allows assessing the common assumption in seismic engineering that source–receiver interaction can be neglected if the distance between source and receiver is sufficiently large compared to the wavelength of waves in the soil. It is observed that the interaction between a source at depth and a receiver mainly affects the power flow distribution if the distance between source and receiver is smaller than the dilatational wavelength in the soil. Interaction effects for a railway track at grade are observed if the source–receiver distance is smaller than six Rayleigh wavelengths. A similar trend is revealed if the passage of a freight train is considered. The overall influence of dynamic through–soil coupling in terms of power flow remains limited to 2 dB, but the insertion gain at particular locations can easily reach 10 dB. This is of the same order of magnitude as other sources of uncertainty in the numerical prediction of railway induced vibrations; this should hence be accounted for when performing vibration predictions.

1 Introduction

Railway induced vibrations are an important source of annoyance in the built environment. Vibrations in buildings ($1 - 80\,\mathrm{Hz}$) can disturb sensitive equipment and cause discomfort to people, while re–radiated noise ($16 - 250\,\mathrm{Hz}$) may be perceived when eigenmodes of floors and walls are excited.

The numerical prediction of railway induced vibrations is a complicated problem, involving various complex physical phenomena such as the generation of dynamic axle loads [1], three–dimensional (3D) wave propagation in the soil and dynamic soil–structure interaction (SSI) [2,3]. In the past decades, several numerical models have been developed; the current state–of–the–art includes semi–analytical [4, 5], finite–infinite element [6] and coupled finite element – boundary element (FE–BE) [1, 3] models. Computational restrictions as well as the lack of knowledge on appropriate model parameters necessitate the introduction of simplifying assumptions in these models. For instance, the assumption of translational invariance or periodicity along the longitudinal direction of a railway tunnel or track is commonly made, allowing for efficient two–and–a–half–dimensional (2.5D) or periodic formulations in the frequency–wavenumber domain [7, 8]. Furthermore, the soil is usually assumed to be horizontally layered and to behave as a linear elastic isotropic medium, while a perfect contact at the soil–structure interfaces is imposed and the presence of nearby structures is neglected. Some of these assumptions are violated in reality, however, and it is therefore important to investigate to which extent these assumptions affect the accuracy of numerical predictions. Several deviations from standard conditions have been recently considered, such as the effect of an inclined soil stratification [9], soil inhomogeneities [10], non–linear soil behaviour [11], ballast layer solidification [12], the interaction between neighbouring tunnels [13], and the presence of voids at the tunnel–soil interface [14].

In the majority of the numerical models, dynamic SSI at the source (railway tunnel or track) and at the receiver (building) are assumed to be uncoupled, disregarding through–soil coupling of source and receiver. Such an uncoupled approach is well established in seismic engineering, where the distance between source and receiver is sufficiently large compared to the wavelength of waves in the soil, especially in case of far–fault ground motions [15, 16]. Although dynamic through–soil coupling of adjacent structures is receiving increasing attention in the literature (e.g. the interaction of rigid [17,18] and flexible [19,20] surface foundations, pile–soil–pile interaction [21] and city site effects [22–24]), limited attention has been paid so far, however, to source–receiver interaction in the case of railway induced vibrations [25]. Stupazzini and Paolucci [26]

present a case where the coupling between an eight–storey building and a surface or underground railway line is taken into account using the spectral element method. In dense urban areas, the distance between source and receiver indeed is of the same order of magnitude as the wavelength in the soil in the frequency range of interest. An example is the recently constructed HST–tunnel in Antwerp (Belgium) which, at certain locations, is situated at a distance of only 4 m from building foundations [27]; in Chengdu (China), a new museum and subway line are planned within a distance of 20 m [28]. It is likely that through–soil coupling of source and receiver will alter the propagation of waves in these cases; the validity of uncoupled numerical models therefore requires further investigation.

The aim of this paper is hence to quantify and assess the influence of source–receiver interaction on the numerical prediction of railway induced vibrations. The paper is organized as follows. Section 2 summarizes the governing equations and identifies which variables are possibly affected by source–receiver interaction. Two case studies are subsequently discussed, which are evaluated by means of a 2.5D coupled FE–BE methodology. Section 3 focuses on the interaction between a railway tunnel and a four storey portal frame; three different soil types and two different foundation designs are considered. Both local and global indicators are introduced to characterize the effect of source–receiver interaction on the dynamic axle loads and the transfer functions from tunnel to building. The second case study in section 4 involves a railway track at grade; transfer functions as well as vibrations due to the passage of a freight train are discussed. Concluding remarks are formulated in section 5.

2 Numerical prediction of railway induced vibrations

Figure 1 gives an overview of a general source–receiver interaction problem, involving a railway tunnel and a building. The numerical prediction of railway induced vibrations requires the computation of the response to moving loads, the determination of the dynamic axle loads, and the solution of the dynamic SSI problem for the calculation of the transfer functions from source (tunnel) to receiver (building) [1,29]. Although the governing equations of each subproblem are well known [1,29], they are summarized in this section to identify quantities of interest that might be affected by source–receiver interaction.

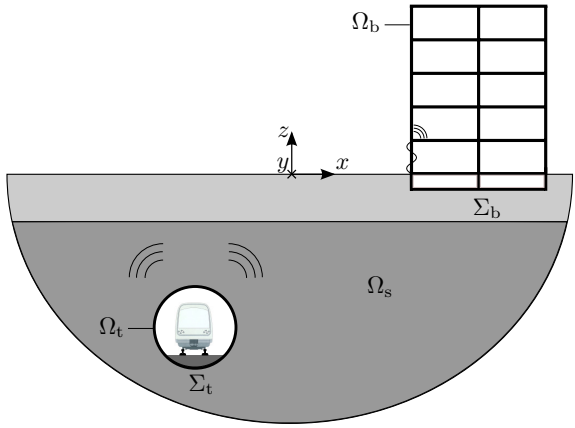

Figure 1: Dynamic soil–structure interaction problem, coupling the source Ω_t (tunnel) and receiver Ω_b (building) through wave propagation in the soil domain Ω_s. The soil–structure interfaces are denoted as Σ_t and Σ_b, respectively.

2.1 Response due to moving loads

The coupled tunnel–soil–building system shown in figure 1 is subjected to multiple moving loads acting on the rails. In a fixed frame of reference, the body load $\rho\mathbf{b}(\mathbf{x},t)$ resulting from n axle loads in the vertical direction $\mathbf{e}_z$ and moving at a constant speed v in the direction $\mathbf{e}_y$ can be written as [1]:

$$\rho\mathbf{b}(\mathbf{x},t) = \sum_{k=1}^{n} \delta\left(x - x_{k0}\right) \delta\left(y - y_{k0} - vt\right) \delta\left(z - z_{k0}\right) g_k(t)\mathbf{e}_z \tag{1}$$

where $\mathbf{x}_{k0} = \{x_{k0}, y_{k0}, z_{k0}\}^\mathrm{T}$ and $g_k(t)$ indicate the initial position and the time history of the k^th axle load, respectively. A Fourier transform applied to equation (1) allows to obtain the frequency domain representation $\rho\hat{\mathbf{b}}(\mathbf{x},\omega)$ of the body load [30], where a hat above a variable denotes its representation in the frequency domain. The vibration response $\hat{u}_i(\mathbf{x},\omega)$ at an arbitrary receiver $\mathbf{x}$ due to the moving loads is calculated as the superposition of the load distribution along the source line and can be formulated as follows [30]:

$$\hat{u}_i(\mathbf{x},\omega) = \sum_{k=1}^{n} \int_{-\infty}^{+\infty} g_k(\tau)\hat{h}_{zi}\left(\mathbf{x}'_k(\tau),\mathbf{x},\omega\right) \exp\left(-i\omega\tau\right)\, \mathrm{d}\tau \tag{2}$$

$\hat{h}_{zi}\left(\mathbf{x}',\mathbf{x},\omega\right)$ is the transfer function, representing the displacement at a location $\mathbf{x}$ in the direction $\mathbf{e}_i$ due to a unit harmonic load applied at a location $\mathbf{x}'$ in the

direction $\mathbf{e}_z$, while $\tau = (y' - y_{k0})/v$. Equation (2) indicates that the response due to the moving loads can be calculated from the time history $g_k(t)$ of the axle loads and the transfer functions $\hat{h}_{zi}(\mathbf{x}', \mathbf{x}, \omega)$.

Assuming translational invariance of the geometry in the longitudinal direction $\mathbf{e}_y$ allows to write the transfer function $\hat{h}_{zi}(x_{k0}, y_{k0} + v\tau, z_{k0}, x, y, z, \omega)$ as $\hat{h}_{zi}(x_{k0}, 0, z_{k0}, x, y - y_{k0} - v\tau, z, \omega)$. Equation (2) can subsequently be simplified using a Fourier transform from the coordinate y to the wavenumber k_y [1], resulting in the following expression in the frequency–wavenumber domain [1]:

$$\tilde{u}_i(x, k_y, z, \omega) = \sum_{k=1}^{n} \hat{g}_k(\omega - k_y v) \tilde{h}_{zi}(x_{k0}, 0, z_{k0}, x, k_y, z, \omega) \exp(i k_y y_{k0}) \quad (3)$$

where a tilde above a variable denotes its representation in the frequency–wavenumber domain. Equation (3) clearly illustrates that the response in the frequency–wavenumber domain is the product of the (shifted) frequency spectrum of the axle loads (accounting for the Doppler effect) and the transfer functions. The response in the frequency–spatial domain can be found by means of an inverse Fourier from the wavenumber k_y to the longitudinal coordinate y, using an efficient Filon quadrature scheme [31].

2.2 Axle loads

Random excitation due to rail and wheel roughness is one of the main excitation mechanisms giving rise to dynamic forces on the track [32]. The dynamic axle loads $\hat{\mathbf{g}}(\omega)$ originating from the unevenness $\hat{\mathbf{u}}_{\mathrm{w/r}}(\omega)$ experienced by the vehicle at the vehicle–rail contact points can be calculated in the frequency domain using a compliance formulation in a moving frame of reference, based on the vehicle and track compliance matrices $\hat{\mathbf{C}}^{\mathrm{v}}(\omega)$ and $\hat{\mathbf{C}}^{\mathrm{tr}}(\omega)$ [1]:

$$\left[\hat{\mathbf{C}}^{\mathrm{v}}(\omega) + \hat{\mathbf{C}}^{\mathrm{tr}}(\omega)\right] \hat{\mathbf{g}}(\omega) = -\hat{\mathbf{u}}_{\mathrm{w/r}}(\omega) \quad (4)$$

where the vector $\hat{\mathbf{g}}(\omega)$ collects the n axle loads $\hat{g}_k(\omega)$. The vehicle compliance $\hat{\mathbf{C}}^{\mathrm{v}}(\omega)$ is usually computed by modelling the vehicle as a multi–body system, possibly accounting for the wheels, axles, bogies and coaches. Each element $\hat{C}^{\mathrm{v}}_{ij}(\omega)$ of this compliance matrix represents the displacements at the vehicle–rail contact point i due to a unit harmonic load at the contact point j. The frequency spectrum of the rail unevenness $\hat{\mathbf{u}}_{\mathrm{w/r}}(\omega)$ is calculated from the wavenumber representation $\tilde{u}_{\mathrm{w/r}}(k_y)$ of the unevenness profile $u_{\mathrm{w/r}}(y)$ and the initial axle positions $\mathbf{x}_{k0}$. The elements $\hat{C}^{\mathrm{tr}}_{ij}(\omega)$ of the track compliance matrix $\hat{\mathbf{C}}^{\mathrm{tr}}(\omega)$ can be calculated in a moving frame of reference based on

the frequency–wavenumber domain transfer function $\tilde{h}_{zz}(x_j, 0, z_j, x_i, k_y, z_i, \omega)$, which represent the vertical displacement of the rail due to a unit harmonic vertical load on the rail [1]:

$$\hat{C}_{ij}^{\mathrm{tr}}(\omega - k_y v) = \frac{1}{2\pi} \int_{-\infty}^{+\infty} \tilde{h}_{zz}(x_j, 0, z_j, x_i, k_y, z_i, \omega) \exp\left(-ik_y \left(y_i - y_j\right)\right) \mathrm{d}k_y \quad (5)$$

In case of a low train speed compared to the critical wave speeds in the tunnel–soil–building system, however, a calculation of the track compliance $\hat{C}_{ij}^{\mathrm{tr}}(\omega)$ in a fixed frame of reference is sufficiently accurate [30]. Equation (5) indicates that the track compliance $\hat{\mathbf{C}}^{\mathrm{tr}}(\omega)$ (and consequently the generation of the dynamic axle loads $\hat{\mathbf{g}}(\omega)$) depends on the transfer functions and might hence be affected by source–receiver interaction.

2.3 Transfer functions

The calculation of the vibration response $\tilde{u}_i(x, k_y, z, \omega)$ at a receiver $\mathbf{x}$ and the determination of the track compliance matrix $\hat{\mathbf{C}}^{\mathrm{tr}}(\omega)$ according to equations (3) and (5), respectively, requires the computation of the transfer functions $\tilde{h}_{zi}\left(x', 0, z', x, k_y, z, \omega\right)$. These transfer functions are computed by means of a coupled FE–BE methodology based on a subdomain formulation, accounting for dynamic SSI. The structural domains are modelled by means of finite elements, while boundary elements on the soil–structure interfaces are used to model the soil domain Ω_{s} (figure 1). Green's functions for a horizontally layered halfspace are employed as fundamental solutions in the BE formulation [33, 34]. As indicated in subsection 2.1, the translational invariance of the geometry in the longitudinal direction is exploited to formulate the governing equations in the frequency–wavenumber domain, resulting in a computationally efficient 2.5D approach. An extensive discussion of the 2.5D coupled FE–BE methodology can be found in [8]. In the following, the dependence of the displacement on the receiver coordinates x and z and the dependence of the transfer functions on the source coordinates x' and z' and the receiver coordinates x and z will be omitted for brevity.

If a railway tunnel and building are considered as in figure 1, the governing set of FE–BE equations reads as follows:

$$\left(\begin{bmatrix} \tilde{\mathbf{K}}_{\mathrm{t}}(k_y, \omega) & \mathbf{0} \\ \mathbf{0} & \tilde{\mathbf{K}}_{\mathrm{b}}(k_y, \omega) \end{bmatrix} - \omega^2 \begin{bmatrix} \mathbf{M}_{\mathrm{t}} & \mathbf{0} \\ \mathbf{0} & \mathbf{M}_{\mathrm{b}} \end{bmatrix} + \begin{bmatrix} \tilde{\mathbf{K}}_{\mathrm{tt}}^{\mathrm{s}}(k_y, \omega) & \tilde{\mathbf{K}}_{\mathrm{tb}}^{\mathrm{s}}(k_y, \omega) \\ \tilde{\mathbf{K}}_{\mathrm{bt}}^{\mathrm{s}}(k_y, \omega) & \tilde{\mathbf{K}}_{\mathrm{bb}}^{\mathrm{s}}(k_y, \omega) \end{bmatrix} \right) \begin{Bmatrix} \underline{\tilde{\mathbf{u}}}_{\mathrm{t}}(k_y, \omega) \\ \underline{\tilde{\mathbf{u}}}_{\mathrm{b}}(k_y, \omega) \end{Bmatrix} = \begin{Bmatrix} \underline{\tilde{\mathbf{f}}}_{\mathrm{t}}(k_y, \omega) \\ \underline{0} \end{Bmatrix} \quad (6)$$

$\underline{\tilde{\mathbf{u}}}_{\mathrm{t}}(k_y,\omega)$ and $\underline{\tilde{\mathbf{u}}}_{\mathrm{b}}(k_y,\omega)$ collect the nodal degrees of freedom of the tunnel and the building, while $\tilde{\mathbf{K}}_{\mathrm{t}}(k_y,\omega)$, $\tilde{\mathbf{K}}_{\mathrm{b}}(k_y,\omega)$, $\mathbf{M}_{\mathrm{t}}$ and $\mathbf{M}_{\mathrm{b}}$ represent the finite element stiffness and mass matrices. The matrices $\tilde{\mathbf{K}}^{\mathrm{s}}_{ij}(k_y,\omega)$ are dynamic soil stiffness matrices (with indices i and j indicating 't' or 'b'), with the off–diagonal terms $\tilde{\mathbf{K}}^{\mathrm{s}}_{\mathrm{tb}}(k_y,\omega)$ and $\tilde{\mathbf{K}}^{\mathrm{s}}_{\mathrm{bt}}(k_y,\omega)$ accounting for through–soil coupling of tunnel and building; the force vector $\underline{\tilde{\mathbf{f}}}_{\mathrm{t}}(k_y,\omega)$ results from the external loading on the tunnel. Solving equation (6) allows for the computation of the required transfer functions $\tilde{h}_{zi}\,(k_y,\omega)$ in the frequency–wavenumber domain.

The dynamic soil stiffness matrices $\tilde{\mathbf{K}}_{ij}(k_y,\omega)$ in equation (6) are calculated by means of the BE method, which is used to evaluate soil tractions $\underline{\tilde{\mathbf{t}}}_{\mathrm{s}}(k_y,\omega)$ on the soil–structure interface Σ_i due to imposed displacements on the soil–structure interface Σ_j [8]:

$$\begin{aligned}\tilde{\mathbf{K}}_{ij}(k_y,\omega) &= \int_{\Sigma_i} \mathbf{N}_i^{\mathrm{T}}\mathbf{N}_i\underline{\tilde{\mathbf{t}}}_{\mathrm{s}}\,(\mathbf{N}_j)\,(k_y,\omega)\,\mathrm{d}\Gamma \\ &= \int_{\Sigma_i} \mathbf{N}_i^{\mathrm{T}}\mathbf{N}_i\tilde{\mathbf{U}}^{-1}(k_y,\omega)\left[\tilde{\mathbf{T}}(k_y,\omega)+\mathbf{I}\right]\mathbf{N}_j\,\mathrm{d}\Gamma \end{aligned} \tag{7}$$

where $\mathbf{N}_i$ and $\mathbf{N}_j$ are shape functions on Σ_i and Σ_j. $\tilde{\mathbf{U}}(k_y,\omega)$ and $\tilde{\mathbf{T}}(k_y,\omega)$ are BE system matrices, requiring integration of the Green's displacements and tractions, respectively. The BE model is based on a regularized boundary integral equation which avoids the evaluation of Cauchy principal value (CPV) integrals of the strongly singular Green's tractions [8]. This regularization is based on the fact that the singularity of the static and dynamic fundamental solutions at the source point correspond [35]. In order to mitigate the occurrence of fictitious eigenfrequencies in the application of the BE method to external wave propagation problems, the Combined Helmholtz Integral Equation Formulation (CHIEF) proposed by Schenk [36] is employed.

The collocation matrices $\tilde{\mathbf{U}}(k_y,\omega)$ and $\tilde{\mathbf{T}}(k_y,\omega)$ are fully populated and unsymmetric, however, resulting in stringent memory and CPU requirements: a quadratic amount of memory (with respect to the number of degrees of freedom) is required to store these matrices, while direct numerical solvers require a cubic amount of numerical operations to solve the corresponding set of BE equations. Furthermore, dense unsymmetric dynamic soil stiffness matrices $\tilde{\mathbf{K}}^{\mathrm{s}}_{ij}(k_y,\omega)$ strongly affect the sparsity of the FE–BE system, reducing the efficiency of sparse finite element solvers when applied to equation (6). This indicates that a significant computational effort is needed to assemble and solve the coupled set of equations (6) in order to fully account for through–soil coupling of source and receiver.

It is therefore often preferred to enhance the efficiency of numerical models by disregarding the off–diagonal soil stiffness matrices $\tilde{\mathbf{K}}^{\mathrm{s}}_{\mathrm{tb}}(k_y,\omega)$ and $\tilde{\mathbf{K}}^{\mathrm{s}}_{\mathrm{bt}}(k_y,\omega)$

in the FE–BE equation (6), resulting in an uncoupled two–step approach. In the first step, only the tunnel–soil system is considered and the presence of the building is neglected. The governing set of FE–BE equations hence reads as follows:

$$\left[\tilde{\mathbf{K}}_{\mathrm{t}}(k_y,\omega) - \omega^2\mathbf{M}_{\mathrm{t}} + \tilde{\mathbf{K}}^{\mathrm{s}}_{\mathrm{t}}(k_y,\omega)\right]\underline{\tilde{\mathbf{u}}}_{\mathrm{t}}(k_y,\omega) = \underline{\tilde{\mathbf{f}}}_{\mathrm{t}}(k_y,\omega) \tag{8}$$

The dynamic soil stiffness matrix $\tilde{\mathbf{K}}^{\mathrm{s}}_{\mathrm{t}}(k_y,\omega)$ in equation (8) corresponds to $\tilde{\mathbf{K}}^{\mathrm{s}}_{\mathrm{tt}}(k_y,\omega)$ in equation (6). From a computational point of view, however, these matrices slightly differ due to the global regularization procedure employed in the BE method, which involves the rigid body motion of the entire BE mesh [8]. This regularization affects the computation of the weakly singular boundary integrals. As a result, the entries of the 3×3 block diagonal of the BE matrix $\tilde{\mathbf{T}}(k_y,\omega)$ (and consequently $\tilde{\mathbf{K}}^{\mathrm{s}}_{\mathrm{t}}(k_y,\omega)$ and $\tilde{\mathbf{K}}^{\mathrm{s}}_{\mathrm{tt}}(k_y,\omega)$) are not the same, although the differences are very small. Solving equation (8) provides the tunnel displacements $\underline{\tilde{\mathbf{u}}}_{\mathrm{t}}(k_y,\omega)$. The BE equations allow to retrieve the tractions $\underline{\tilde{\mathbf{t}}}_{\mathrm{t}}(k_y,\omega)$ at the tunnel–soil interface, which are used to evaluate the radiated wavefield in the soil $\underline{\tilde{\mathbf{u}}}_{\mathrm{s}}(k_y,\omega)$ through the discretized boundary integral equation [8]:

$$\underline{\tilde{\mathbf{u}}}_{\mathrm{s}}(k_y,\omega) = \tilde{\mathbf{U}}_{\mathrm{s}}(k_y,\omega)\underline{\tilde{\mathbf{t}}}_{\mathrm{t}}(k_y,\omega) - \tilde{\mathbf{T}}_{\mathrm{s}}(k_y,\omega)\underline{\tilde{\mathbf{u}}}_{\mathrm{t}}(k_y,\omega) \tag{9}$$

where $\tilde{\mathbf{U}}_{\mathrm{s}}(k_y,\omega)$ and $\tilde{\mathbf{T}}_{\mathrm{s}}(k_y,\omega)$ are BE transfer matrices. The response of the building is subsequently determined in the second step:

$$\left[\tilde{\mathbf{K}}_{\mathrm{b}}(k_y,\omega) - \omega^2\mathbf{M}_{\mathrm{b}} + \tilde{\mathbf{K}}^{\mathrm{s}}_{\mathrm{b}}(k_y,\omega)\right]\underline{\tilde{\mathbf{u}}}_{\mathrm{b}}(k_y,\omega) = \underline{\tilde{\mathbf{f}}}^{\mathrm{s}}_{\mathrm{b}}(\underline{\tilde{\mathbf{u}}}_{\mathrm{s}})(k_y,\omega) \tag{10}$$

The force vector $\underline{\tilde{\mathbf{f}}}^{\mathrm{s}}_{\mathrm{b}}(\underline{\tilde{\mathbf{u}}}_{\mathrm{s}})(k_y,\omega)$ denotes the dynamic SSI forces at the building–soil interface Σ_{b} resulting from the incident wavefield $\underline{\tilde{\mathbf{u}}}_{\mathrm{s}}(k_y,\omega)$:

$$\underline{\tilde{\mathbf{f}}}^{\mathrm{s}}_{\mathrm{b}}(\underline{\tilde{\mathbf{u}}}_{\mathrm{s}})(k_y,\omega) = \int_{\Sigma_{\mathrm{b}}} \mathbf{N}^{\mathrm{T}}_{\mathrm{b}}\mathbf{N}_{\mathrm{b}}\tilde{\mathbf{U}}^{-1}(k_y,\omega)\underline{\tilde{\mathbf{u}}}_{\mathrm{s}}(k_y,\omega)\,\mathrm{d}\Gamma \tag{11}$$

where the BE system matrix $\tilde{\mathbf{U}}(k_y,\omega)$ is determined based on a BE discretization of the interface Σ_{b}; only a one–way coupling of source and receiver is provided in this approach. The calculation of a force vector resulting from an incident wavefield by means of the 2.5D FE–BE methodology is discussed in more detail in [37]. Solving equation (10) finally gives the building displacements $\underline{\tilde{\mathbf{u}}}_{\mathrm{b}}(k_y,\omega)$.

The uncoupled strategy outlined in equations (8)–(10) enables a more efficient solution of the dynamic SSI problem and is therefore generally favoured in numerical models [1, 7], both for the determination of the track compliance $\hat{\mathbf{C}}^{\mathrm{tr}}(\omega)$ as well as for the calculation of the transfer functions $\tilde{h}_{zi}\,(k_y,\omega)$. Through–soil coupling of source and receiver is, however, not rigorously accounted for in this approach. The influence of this approximation on $\hat{\mathbf{C}}^{\mathrm{tr}}(\omega)$ and $\tilde{h}_{zi}\,(k_y,\omega)$ will be investigated in sections 3 and 4.

3 Dynamic interaction between a railway tunnel and a building

3.1 Case description

A case study involving a railway tunnel situated under a building is analyzed in this section. A cross section of the tunnel and the building is shown in figure 2.

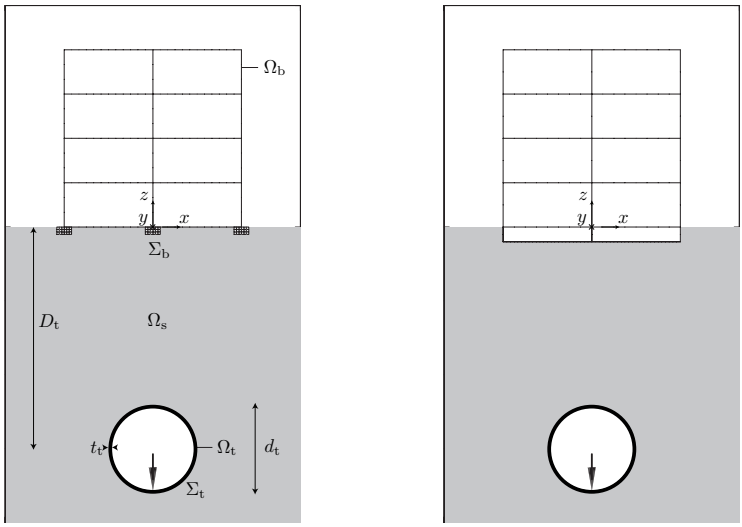

(a) (b)

Figure 2: Railway tunnel Ω_t situated at a depth D_t below a four storey portal frame Ω_b founded (a) on three embedded strip foundations and (b) on a box foundation. A unit harmonic vertical point load is applied to the tunnel invert at $\mathbf{x} = \{0\,\mathrm{m}, 0\,\mathrm{m}, -D_t - d_t/2 + t_t\}^T$.

The concrete tunnel has a circular cross section and is embedded in a homogeneous linear elastic halfspace, with its centre situated at a depth D_t below the free surface. The tunnel has an outer diameter $d_t = 5.75\,\mathrm{m}$ and a wall thickness $t_t = 0.25\,\mathrm{m}$. The concrete has a Young's modulus $E_t = 50\,\mathrm{GPa}$, a Poisson's ratio $\nu_t = 0.30$, a density $\rho_t = 2500\,\mathrm{kg/m^3}$ and a hysteretic material damping ratio $\beta_t = 0.025$. There is no track incorporated in the tunnel model. The building is a four storey portal frame (subscript 'pf') consisting of four

floors and two spans, with a total width $w_{\mathrm{pf}} = 12\,\mathrm{m}$ and a total height $h_{\mathrm{pf}} = 12\,\mathrm{m}$. The wall thickness equals $t_{\mathrm{pf,w}} = 0.25\,\mathrm{m}$, while the thickness of the slabs is equal to $t_{\mathrm{pf,s}} = 0.20\,\mathrm{m}$. The walls and slabs are made of reinforced concrete with a Young's modulus $E_{\mathrm{pf}} = 30\,\mathrm{GPa}$, a Poisson's ratio $\nu_{\mathrm{pf}} = 0.30$, a density $\rho_{\mathrm{pf}} = 2500\,\mathrm{kg/m^3}$ and a hysteretic material damping ratio $\beta_{\mathrm{pf}} = 0.03$. The portal frame is either founded on three embedded strip foundations (figure 2a) or on a box foundation (figure 2b). The 2.5D methodology discussed in section 2 is applied for both the tunnel and the building, implying that a building with continuous walls and slabs is modelled. The number of the finite and boundary elements is adjusted to provide ten elements per shear wavelength at the highest frequency of interest (80 Hz). It has been verified that this suffices to obtain accurate results.

In order to investigate the influence of the soil properties, three different soil types are examined, representing a soft, medium and stiff soil in dry conditions. The dynamic soil characteristics are summarized in table 1.

Type	C_{s} [m/s]	C_{p} [m/s]	β_{s} [–]	β_{p} [–]	ρ [kg/m^3]
Soft	100	200	0.03	0.03	1800
Medium	200	400	0.03	0.03	1800
Stiff	300	600	0.03	0.03	1800

Table 1: Dynamic soil characteristics.

3.2 Vibration insertion gain

The interaction of a tunnel embedded in a soft soil (table 1) situated at a depth $D_{\mathrm{t}} = 5\,\mathrm{m}$ with a portal frame founded on three embedded strip foundations (figure 2a) is first analyzed. Each of the strip foundations (subscript 'sf') has a width $w_{\mathrm{sf}} = 1\,\mathrm{m}$, a height $h_{\mathrm{sf}} = 0.5\,\mathrm{m}$ and the following material parameters: $E_{\mathrm{sf}} = 33.3\,\mathrm{GPa}$, $\nu_{\mathrm{sf}} = 0.20$, $\rho_{\mathrm{sf}} = 2500\,\mathrm{kg/m^3}$ and $\beta_{\mathrm{sf}} = 0.03$. Discretization results in 384 FE and 288 BE degrees of freedom (DOFs) for the tunnel as well as 1581 FE and 252 BE DOFs for the building, respectively. All calculations presented in this section have been performed on Intel® Xeon® E5520 (2.26 GHz) CPUs. An uncoupled calculation takes 4.1 h per frequency, while 6.6 h per frequency is required if source–receiver interaction is accounted for. As the 2.5D equations are solved independently for each wavenumber k_y in the frequency–wavenumber domain, the calculations can easily be parallelized. The use of MATLAB's Parallel Computing Toolbox [38] allows for a distributed computation on eight cores, leading to a speed–up by a factor that is slightly less than eight (due to the communication overhead). The actual computation

times are hence 32.6 min and 52.4 min per frequency for the uncoupled and coupled model, respectively.

Through–soil coupling of source and receiver might affect the track compliance $\hat{\mathbf{C}}^{\mathrm{tr}}(\omega)$ and hence, according to equation (4), the dynamic axle loads $\hat{\mathbf{g}}(\omega)$. Figure 3 shows the vertical tunnel displacement $\hat{u}_{\mathrm{t}}(\mathbf{x},\omega)$ due to vertical harmonic excitation at $\mathbf{x} = \{0\,\mathrm{m}, 0\,\mathrm{m}, -D_{\mathrm{t}} - d_{\mathrm{t}}/2 + t_{\mathrm{t}}\}^{\mathrm{T}}$ within a frequency range between 0 Hz and 80 Hz. Both the uncoupled and coupled methodologies outlined in the previous subsection are employed and it is clear that the presence of the building does not significantly modify the result, although small deviations can be observed at low frequencies. This result implies that the track compliance $\hat{\mathbf{C}}^{\mathrm{tr}}(\omega)$ and the dynamic axle loads $\hat{\mathbf{g}}(\omega)$, can be calculated with reasonable accuracy using an uncoupled strategy in which through–soil coupling is disregarded.

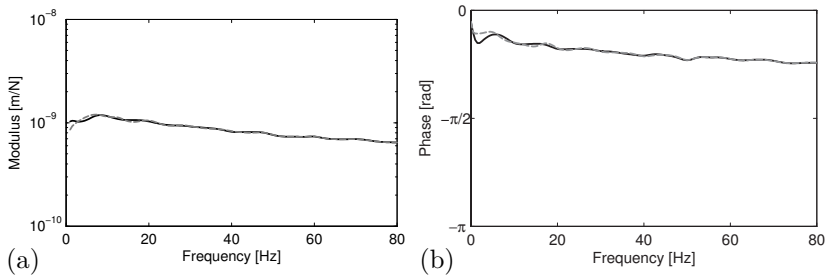

Figure 3: (a) Modulus and (b) phase of the vertical tunnel displacement $\hat{u}_{\mathrm{t}}(\mathbf{x},\omega)$ due to vertical harmonic excitation in the tunnel at $\mathbf{x} = \{0\,\mathrm{m}, 0\,\mathrm{m}, -D_{\mathrm{t}} - d_{\mathrm{t}}/2 + t_{\mathrm{t}}\}^{\mathrm{T}}$, calculated with the uncoupled (solid black line) and coupled (dashed grey line) approach. The tunnel is embedded in a soft soil and situated at a depth $D_{\mathrm{t}} = 5\,\mathrm{m}$ below the free surface.

Next, the transfer functions from tunnel to building are considered. Figures 4a and 4b show the real part of the vertical displacement $\hat{u}_z(\mathbf{x},\omega)$ at 25 Hz as obtained with the uncoupled and coupled approach, respectively, due to vertical harmonic excitation of the tunnel at $\{0\,\mathrm{m}, 0\,\mathrm{m}, -D_{\mathrm{t}} - d_{\mathrm{t}}/2 + t_{\mathrm{t}}\}^{\mathrm{T}}$.

A visual comparison of figures 4a and 4b indicates that source–receiver interaction at 25 Hz modestly affects the displacements in the soil and in the building. The interaction effect can be quantified by means of the vibration insertion gain $\widehat{\mathrm{IG}}_i(\mathbf{x},\omega)$ in the direction $\mathbf{e}_i$ $(i = x, y, z)$ at a specific location $\mathbf{x}$ in the soil or in the building, which compares the vibration levels obtained

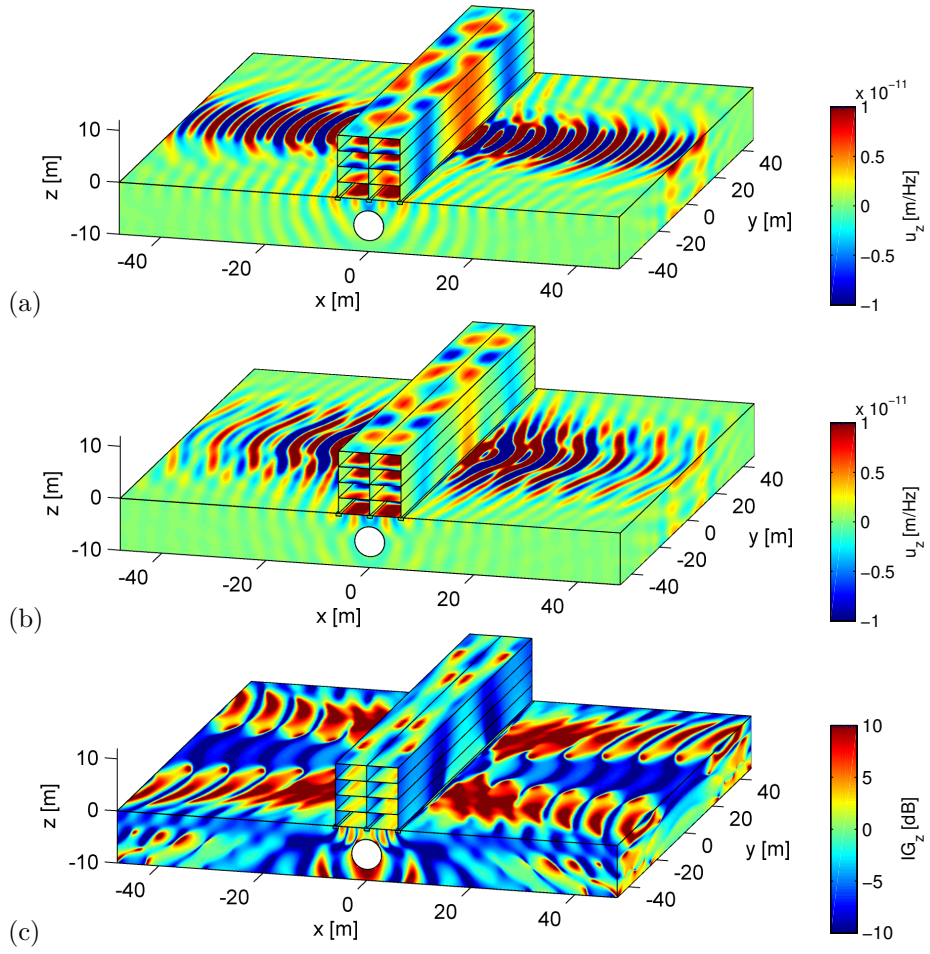

Figure 4: Real part of the vertical soil and building displacement $\hat{u}_z(\mathbf{x},\omega)$ due to vertical harmonic excitation in the tunnel at $\{0\,\mathrm{m}, 0\,\mathrm{m}, -D_\mathrm{t}-d_\mathrm{t}/2+t_\mathrm{t}\}^\mathrm{T}$ at a frequency of 25 Hz as obtained with (a) the uncoupled and (b) the coupled approach, and (c) the corresponding insertion gain $\widehat{\mathrm{IG}}_z(\mathbf{x},\omega)$. The tunnel is embedded in a soft soil and situated at a depth $D_\mathrm{t} = 5\,\mathrm{m}$ below the free surface.

with the uncoupled (superscript 'u') and coupled (superscript 'c'):

$$\widehat{\mathrm{IG}}_i(\mathbf{x},\omega) = 20\log_{10}\frac{|\hat{u}_i^{\mathrm{c}}(\mathbf{x},\omega)|}{|\hat{u}_i^{\mathrm{u}}(\mathbf{x},\omega)|} \tag{12}$$

Figure 4c shows the vertical insertion gain $\widehat{\mathrm{IG}}_z(\mathbf{x},\omega)$ at 25 Hz. The coupling seems to mainly shift the zones of high or low response, resulting in considerable spatial variation of the insertion gain both in the soil and the building, reaching up to 10 dB and higher. A strong spatial variation is also observed if insertion gains $\widehat{\mathrm{IG}}_x(\mathbf{x},\omega)$ and $\widehat{\mathrm{IG}}_y(\mathbf{x},\omega)$ are considered, but there is no clear correspondence between these insertion gains at a certain location $\mathbf{x}$.

Figure 5 shows the real part of the vertical displacement $\hat{u}_z(\mathbf{x},\omega)$ as obtained with the uncoupled and coupled approach at a frequency of 75 Hz; a different colour scale is used in comparison with figure 4. The displacements are very similar in the uncoupled and coupled approach, suggesting that source–receiver interaction is negligible at this frequency. The vertical insertion gain $\widehat{\mathrm{IG}}_z(\mathbf{x},\omega)$ is shown in figure 5c. Although the insertion gain is close to 0 dB at many locations of the considered spatial domain, large local deviations up to 10 dB are observed as well, both in the soil and in the building. This can be attributed to the fact that the wave fronts in both approaches are slightly shifted relatively to each other.

Figures 4–5c indicate that the insertion gain highly depends on the location $\mathbf{x}$. This is illustrated in more detail in figure 6, in which insertion gains $\widehat{\mathrm{IG}}_i(\mathbf{x},\omega)$ are shown as a grey patch for locations $\mathbf{x}$ corresponding to a grid of points located on the first floor of the four storey portal frame, within a range from $y = -10$ m to $y = +10$ m. The spatial variability is clearly apparent in this figure; the dependence of the insertion gains on the direction $\mathbf{e}_i$ is also demonstrated.

Figures 4–6 reveal that the vibration insertion gain $\widehat{\mathrm{IG}}_i(\mathbf{x},\omega)$ strongly depends on the location $\mathbf{x}$ and the direction $\mathbf{e}_i$. A global quantifier which eliminates this dependency is therefore considered as well in this paper. A common approach to evaluate global variations in acoustic measurements or numerical simulations is to compare spatially averaged sound pressure fields in a specific room [39]. Applying a spatial averaging procedure to the source–receiver interaction problem under consideration is, however, less appropriate, as the selection of an averaging area would be rather arbitrary. Furthermore, the dependence on the direction $\mathbf{e}_i$ would remain. An alternative power flow approach [40,41] is therefore introduced in the following subsection as a global measure for through–soil coupling of source and receiver.

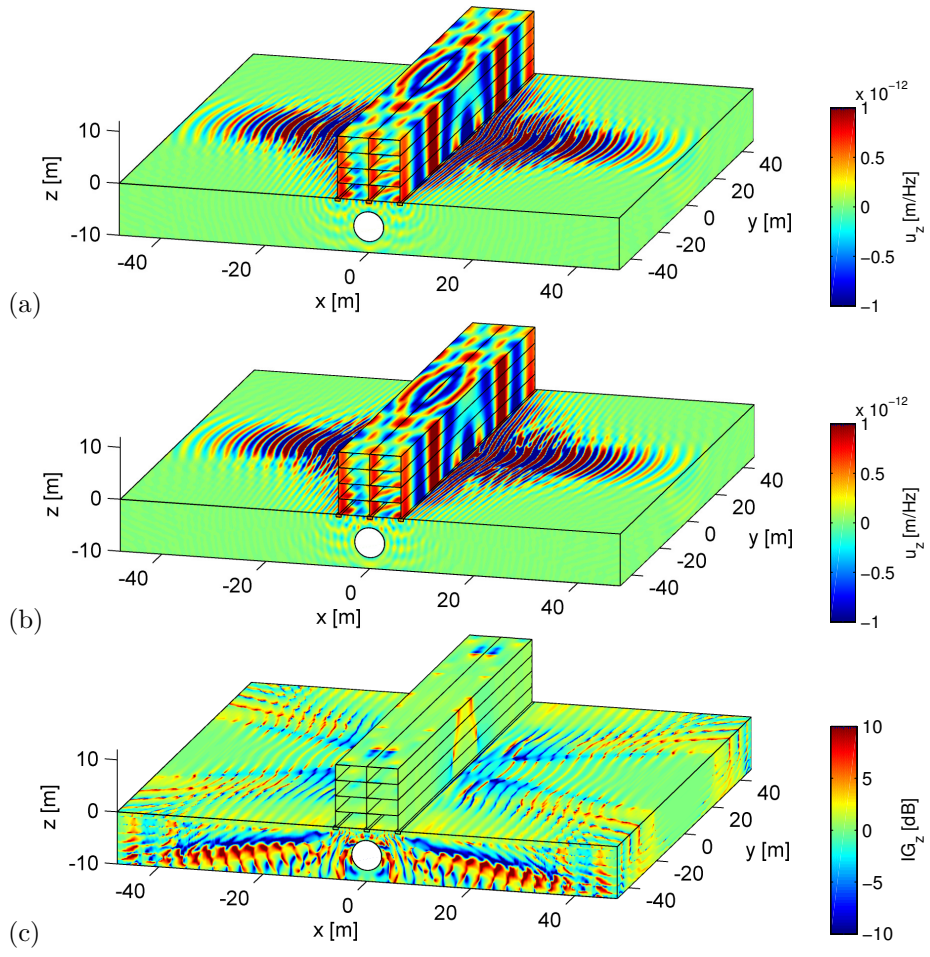

Figure 5: Real part of the vertical soil and building displacement $\hat{u}_z(\mathbf{x},\omega)$ due to vertical harmonic excitation in the tunnel at $\{0\,\mathrm{m}, 0\,\mathrm{m}, -D_\mathrm{t}-d_\mathrm{t}/2+t_\mathrm{t}\}^\mathrm{T}$ at a frequency of 75 Hz as obtained with (a) the uncoupled and (b) the coupled approach, and (c) the corresponding insertion gain $\widehat{\mathrm{IG}}_z(\mathbf{x},\omega)$. The tunnel is embedded in a soft soil and situated at a depth $D_\mathrm{t} = 5\,\mathrm{m}$ below the free surface.

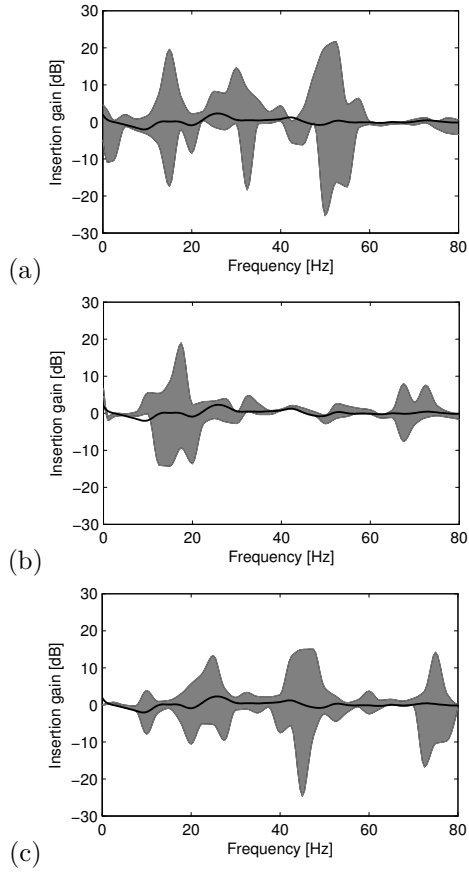

Figure 6: Vibration insertion gains (a) $\widehat{\mathrm{IG}}_x(\mathbf{x},\omega)$, (b) $\widehat{\mathrm{IG}}_y(\mathbf{x},\omega)$ and (c) $\widehat{\mathrm{IG}}_z(\mathbf{x},\omega)$ on the first floor of the four storey portal frame founded on three embedded strip foundations in a range $y \in [-10\,\mathrm{m}, 10\,\mathrm{m}]$ (grey patch). Superimposed is the power flow insertion gain $\widehat{\mathrm{PFIG}}(\omega)$ (black line).

3.3 Power flow insertion gain

The basic principles of power flow analysis are briefly summarized in this subsection. The reader is referred to the literature [42, 43] for a detailed description of the methodology.

Consider an infinitesimal surface $d\Gamma$ through an arbitrary point Q of a continuum Ω, characterized by its unit outward normal vector $\mathbf{n}$ (figure 7). Time dependent tractions $\mathbf{t}^{\mathbf{n}}(t)$ are acting on this surface. The instantaneous

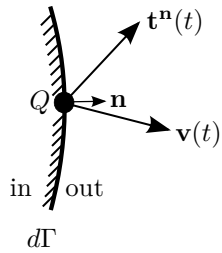

Figure 7: Infinitesimal surface $d\Gamma$ with a unit outward normal $\mathbf{n}$ through an arbitrary point Q of a continuum Ω.

power flow $p^{\mathbf{n}}(t)$ through $d\Gamma$ at time t is the rate of work performed by the tractions $\mathbf{t}^{\mathbf{n}}(t)$, defined as the inner product of the traction vector $\mathbf{t}^{\mathbf{n}}(t)$ and the velocity vector $\mathbf{v}(t)$ [42, 43]:

$$p^{\mathbf{n}}(t) = -\mathbf{t}^{\mathbf{n}}(t) \cdot \mathbf{v}(t) \tag{13}$$

where the velocity vector $\mathbf{v}(t)$ is defined as $\mathbf{v}(t) = \partial \mathbf{u}(t)/\partial t$. A positive inner product of $\mathbf{t}^{\mathbf{n}}(t)$ and $\mathbf{v}(t)$ corresponds to the transmission of energy per unit of time through the surface $d\Gamma$ from the outer to the inner side, as defined in figure 7 [44]; the minus sign in equation (13) thus ensures a positive power flow $p^{\mathbf{n}}(t)$ from the inner to the outer side. The instantaneous power flow can be rewritten by introducing Cauchy's formula in equation (13):

$$p^{\mathbf{n}}(t) = -(\boldsymbol{\sigma}(t) \cdot \mathbf{n}) \cdot \mathbf{v}(t) = (-\boldsymbol{\sigma}^{\mathrm{T}}(t) \cdot \mathbf{v}(t)) \cdot \mathbf{n} = \mathbf{p}(t) \cdot \mathbf{n} \tag{14}$$

where $\mathbf{p}(t)$ represents the instantaneous power flow density vector [44]. Equation (14) allows to determine the power flow through an arbitrary plane characterized by a unit outward normal vector $\mathbf{n}$ from the power flow through three mutually perpendicular planes.

The mean power flow density vector $\langle \hat{\mathbf{p}}(\omega) \rangle$ is the time average of $\mathbf{p}(t)$ over a period of vibration $2\pi/\omega$ and can be expressed in terms of the complex

quantities $\hat{\boldsymbol{\sigma}}(\omega)$ and $\hat{\mathbf{u}}(\omega)$ [42]:

$$\langle \hat{\mathbf{p}}(\omega) \rangle = -\frac{1}{2}\mathrm{Re}(\hat{\boldsymbol{\sigma}}^{\star}(\omega) \cdot \hat{\mathbf{v}}(\omega)) = -\frac{1}{2}\mathrm{Re}(i\omega\hat{\boldsymbol{\sigma}}^{\star}(\omega) \cdot \hat{\mathbf{u}}(\omega)) \tag{15}$$

where $\star$ indicates the complex conjugate. Equation (15) is valid for a continuum; expressions for the instantaneous and mean power flow density vector in a Timoshenko beam and a thin plate can be found in [45] and [46], respectively. The total mean power flow $\left\langle \hat{P}(\Gamma, \omega) \right\rangle$ through a surface Γ is finally calculated as:

$$\left\langle \hat{P}(\Gamma, \omega) \right\rangle = \int_{\Gamma} \langle \hat{p}^{\mathbf{n}}(\omega) \rangle \, d\Gamma = \int_{\Gamma} \langle \hat{\mathbf{p}}(\omega) \rangle \cdot \mathbf{n} \, d\Gamma \tag{16}$$

The power flow concept allows introducing power flow insertion gain $\widehat{\mathrm{PFIG}}(\omega)$ as a global indicator for source–receiver interaction:

$$\widehat{\mathrm{PFIG}}(\omega) = 10 \log_{10} \frac{\left\langle \hat{P}^{\mathrm{c}}(\Sigma_{\mathrm{b}}, \omega) \right\rangle}{\left\langle \hat{P}^{\mathrm{u}}(\Sigma_{\mathrm{b}}, \omega) \right\rangle} \tag{17}$$

where $\left\langle \hat{P}(\Sigma_{\mathrm{b}}, \omega) \right\rangle$ denotes the total mean power flowing into the building through the soil–building interface Σ_{b} (i.e. through the three soil–foundation interfaces indicated on figure 2). This provides a global measure to characterize the significance of through–soil coupling in numerical models, based on the mean vibrational energy entering a structure driving all internal structural vibrations and re–radiated noise [47]. A change of the amount of power flowing into the building caused by through–soil coupling is thus of main interest for the evaluation of source–receiver interaction. It must be emphasized, however, that the power flow approach is introduced here in order to make a global comparison of results obtained with two numerical methodologies (i.e. coupled vs. uncoupled).

In figure 6, the $\widehat{\mathrm{PFIG}}(\omega)$ is superimposed on the insertion gains $\widehat{\mathrm{IG}}_i(\mathbf{x}, \omega)$. The $\widehat{\mathrm{PFIG}}(\omega)$ varies around ± 2 dB in the lower frequency range, while the influence of source–receiver interaction seems to be negligible at higher frequencies. The spatial and directional variation are removed through this approach, as a single value per frequency is obtained.

Power flow provides additional insight in the physical behaviour, as it allows to identify the dominant vibration transmission paths. Figure 8 shows the mean power flow per unit length through the tunnel–soil interface as a function of the longitudinal coordinate and the frequency, where positive values correspond

to the transmission of energy from the tunnel into the soil (cfr. equation (13)). This figure clearly illustrates that the power flow distribution around the tunnel is not affected by the presence of the building in the frequency range of interest, as could be expected from figure 3.

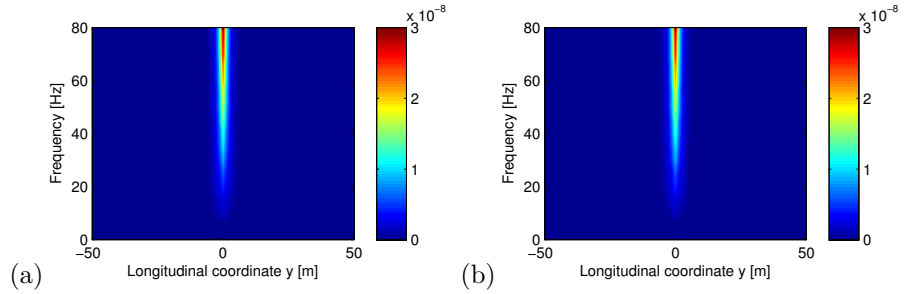

Figure 8: Mean power flow per unit length through the tunnel–soil interface due to vertical harmonic excitation in the tunnel at $\mathbf{x} = \{0\,\mathrm{m}, 0\,\mathrm{m}, -D_\mathrm{t} - d_\mathrm{t}/2 + t_\mathrm{t}\}^\mathrm{T}$, calculated with the (a) uncoupled and (b) coupled approach. The tunnel is embedded in a soft soil and situated at a depth $D_\mathrm{t} = 5\,\mathrm{m}$ below the free surface.

Figure 9 shows the mean power flow per unit length through the soil–foundation interface of the middle strip foundation as a function of the longitudinal coordinate and the frequency. Positive values indicate the transmission of energy from the soil into the foundations. Results obtained with the uncoupled and coupled approach are compared, revealing that through–soil coupling of source and receiver moderately affects the power flow distribution through the soil–foundation interfaces at low frequencies. Source–receiver interaction has only a minor influence at higher frequencies, however.

3.4 Parametric study

The power flow approach can now be employed to assess the significance of source–receiver interaction for different tunnel depths and soil types. Figure 10 shows the $\widehat{\mathrm{PFIG}}(\omega)$ in a frequency range from 0 Hz to 80 Hz for tunnel depths D_t varying from 5 m to 25 m, and for the three soil types outlined in table 1. The minimal distance between the tunnel roof and the strip foundations is denoted as $\mathscr{D} = D_\mathrm{t} - d_\mathrm{t}/2 - h_\mathrm{sf}$. It is often assumed in seismic engineering that source–receiver interaction can be neglected if the distance between source and receiver is sufficiently large compared to the wavelength of waves in the soil [15, 16]. This intuitive idea is assessed in figure 10 by

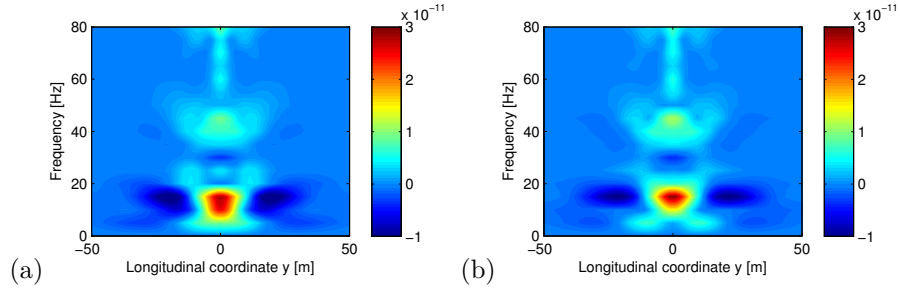

Figure 9: Mean power flow per unit length through the soil–foundation interface of the middle strip foundation due to vertical harmonic excitation in the tunnel at $\mathbf{x} = \{0\,\mathrm{m}, 0\,\mathrm{m}, -D_\mathrm{t} - d_\mathrm{t}/2 + t_\mathrm{t}\}^\mathrm{T}$, calculated with the (a) uncoupled and (b) coupled approach. The tunnel is embedded in a soft soil and situated at a depth $D_\mathrm{t} = 5\,\mathrm{m}$ below the free surface.

superimposing lines at which the distance $\mathscr{D}$ equals the dilatational wavelength λ_p in the soil, i.e. $\omega = 2\pi C_\mathrm{p}/\mathscr{D}$. The $\widehat{\mathrm{PFIG}}(\omega)$ tends to 0 dB above these lines, indicating that the uncoupled approach indeed yields the same result as the coupled approach if the distance $\mathscr{D}$ between source and receiver is larger than the dilatational wavelength λ_p. An increasing deviation up to ± 2 dB between the coupled and uncoupled approach can be observed below the lines, as the distance $\mathscr{D}$ is smaller than the wavelength λ_p. The uncoupling does, however, not systematically result in an under– or overestimation of the total mean power entering the building; this strongly depends on the tunnel depth, the soil type and the frequency considered. Although the different regions in the contour plots are not very sharply delimited, these results nevertheless suggest that the rule of thumb commonly applied in seismic engineering also applies to the prediction of railway induced vibrations.

The influence of source–receiver interaction is also investigated for an alternative foundation design. Figure 2b shows the four storey portal frame founded on a box foundation (subscript 'bf') with width $w_\mathrm{bf} = 12\,\mathrm{m}$, height $h_\mathrm{bf} = 1\,\mathrm{m}$ and thickness $t_\mathrm{bf} = 0.30\,\mathrm{m}$; the soil–foundation interface is thus larger than for the strip foundations previously considered. The same material properties as for the strip foundations are used. The total mean power flowing into the building in case of harmonic excitation at $\mathbf{x} = \{0\,\mathrm{m}, 0\,\mathrm{m}, -D_\mathrm{t} - d_\mathrm{t}/2 + t_\mathrm{t}\}^\mathrm{T}$ of a tunnel embedded in a soft soil situated at a depth $D_\mathrm{t} = 5\,\mathrm{m}$ is shown in figure 11b. The net power input is up to 8 dB higher than in the case where the building on embedded strip foundations is considered (figure 11a). Figure 11b indicates, however, that the significance of through–soil coupling also remains

limited to ±2 dB in the case of a box foundation, although the effect is slightly more pronounced than in case of embedded strip foundations.

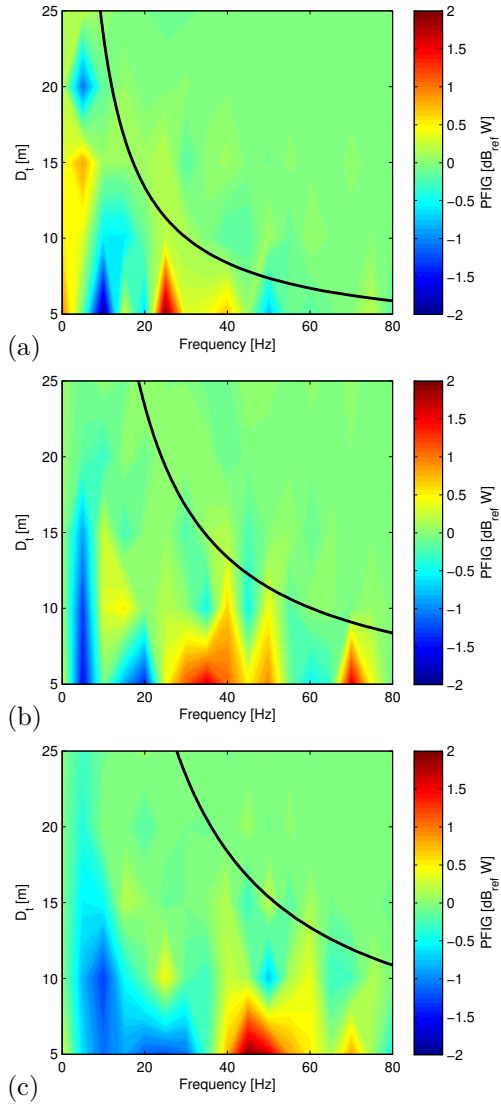

Figure 10: Power flow insertion gain $\widehat{\mathrm{PFIG}}(\omega)$ for a building founded on three embedded strip foundations in case of a (a) soft, (b) medium, and (c) stiff soil. The tunnel depth D_t varies from 5 m to 25 m.

The observed deviations of ± 2 dB are relatively small compared to other sources of uncertainty, such as small variations of soil characteristics [9, 10, 48], the interaction between neighbouring tunnels [13], or the presence of voids at the tunnel–soil interface [14]. This suggests that accounting for source–receiver interaction does not significantly improve the accuracy of vibration predictions. Nevertheless, if insertion gains $\widehat{\mathrm{IG}}_i(\mathbf{x}, \omega)$ at particular locations are considered, the source–receiver interaction effects can easily reach 10 dB in the frequency range of interest. This is of the same order of magnitude as other sources of uncertainty; this should be beared in mind when performing vibration predictions.

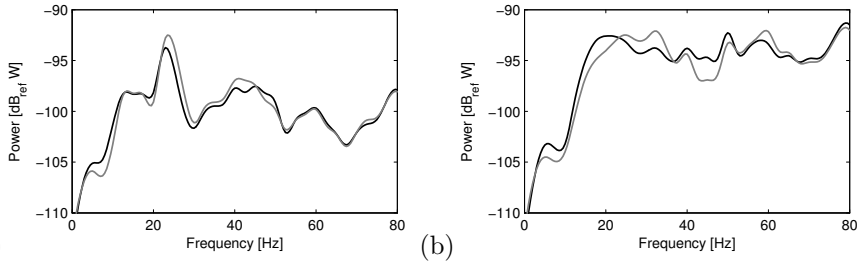

Figure 11: Total mean power flowing into the building founded (a) on three embedded strip foundations and (b) on a box foundation due to vertical harmonic excitation in the tunnel at $\mathbf{x} = \{0\,\mathrm{m}, 0\,\mathrm{m}, -D_\mathrm{t} - d_\mathrm{t}/2 + t_\mathrm{t}\}^\mathrm{T}$, calculated with the uncoupled (black line) and coupled (grey line) approach. The tunnel is embedded in a soft soil and situated at a depth $D_\mathrm{t} = 5\,\mathrm{m}$ below the free surface.

4 Dynamic interaction between a railway track at grade and a building

4.1 Case description

In this section, a conventional ballasted railway track at the surface of the halfspace is considered, as shown in figure 12. D_t indicates the distance between the centre of the track and the right wall of the building. The track consists of UIC 60 rails supported by rail pads on concrete sleepers, which are founded on a ballast layer. The rails are modelled as Euler-Bernoulli beams with a bending stiffness $E_\mathrm{r} I_\mathrm{r} = 6.4 \times 10^6$ Nm^2 and a mass per unit length $\rho_\mathrm{r} A_\mathrm{r} = 60\,\mathrm{kg/m}$ for each rail. A standard track gauge of 1.435 m is considered. The rail pads have

a stiffness $k_{\mathrm{rp}} = 300 \times 10^6\,\mathrm{N/m}$ and a damping coefficient $c_{\mathrm{rp}} = 3.5 \times 10^3\,\mathrm{Ns/m}$. The following sleeper characteristics are considered: a length $l_{\mathrm{sl}} = 2.60\,\mathrm{m}$, a width $b_{\mathrm{sl}} = 0.25\,\mathrm{m}$, a height $h_{\mathrm{sl}} = 0.20\,\mathrm{m}$ (under the rail), a sleeper distance $d_{\mathrm{sl}} = 0.60\,\mathrm{m}$ and a mass $m_{\mathrm{sl}} = 325\,\mathrm{kg}$. An equivalent continuous model is employed based on the equivalent rail pad stiffness $\overline{k}_{\mathrm{rp}} = k_{\mathrm{rp}}/d_{\mathrm{sl}}$, damping coefficient $\overline{c}_{\mathrm{rp}} = c_{\mathrm{rp}}/d_{\mathrm{sl}}$ and uniformly distributed sleeper mass $\overline{m}_{\mathrm{sl}} = m_{\mathrm{sl}}/d_{\mathrm{sl}}$ per unit length. The ballast layer has a thickness $t = 0.30\,\mathrm{m}$ and a width w_{t} varying linearly with depth from 3.60 m under the sleepers to 5.60 m at the track–soil interface. The ballast is characterized by a shear wave velocity $C_{\mathrm{s}} = 300\,\mathrm{m/s}$, a dilatational wave velocity $C_{\mathrm{p}} = 600\,\mathrm{m/s}$, a density $\rho = 2000\,\mathrm{kg/m^3}$ and a material damping ratio $\beta_{\mathrm{s}} = \beta_{\mathrm{p}} = 0.020$ in both deviatoric and volumetric deformation.

The same building as introduced in section 3 is considered at the receiver side (i.e. a four storey portal frame founded on embedded strip foundations), while all three soil types summarized in table 1 are investigated. The source consists of a unit harmonic vertical point load applied to the left rail at $y = 0\,\mathrm{m}$.

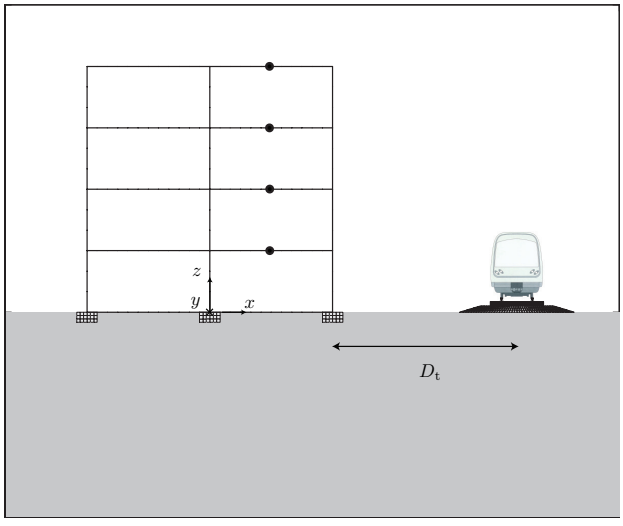

Figure 12: Railway track situated at a distance D_{t} from a four storey portal frame founded on three embedded strip foundations. Vibrations during the passage of a freight train are evaluated at the locations indicated by a dot.

4.2 Numerical results

It is first verified whether the track compliance $\hat{\mathbf{C}}^{\mathrm{tr}}(\omega)$ (and the generation of dynamic axle loads $\hat{\mathbf{g}}(\omega)$) is affected by source–receiver interaction. Figure 13 shows the rail receptance $\hat{u}_{\mathrm{r}}(y = 0\,\mathrm{m}, \omega)$ for a railway track on a soft soil (table 1) and aligned along $x = 15\,\mathrm{m}$ (figure 12); the distance D_{t} thus equals 9 m. It is clearly illustrated that the rail receptance is not modified by disregarding the presence of the building, suggesting that an uncoupled calculation suffices for the determination of the dynamic axle loads. Discretization of the track results in 1473 FE and 267 BE DOFs. An uncoupled calculation takes 4.6 min per frequency, while 11.5 min per frequency is required if source–receiver interaction is accounted for (after parallelization of the wavenumber domain computations).

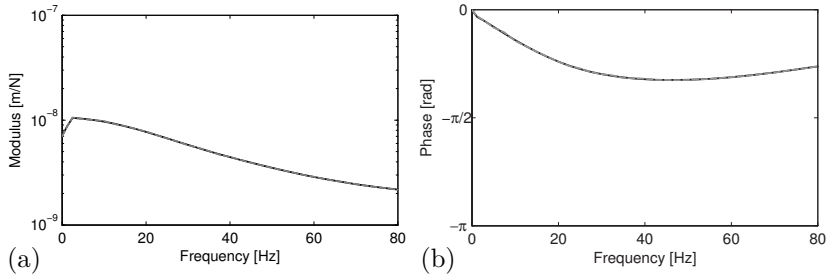

Figure 13: (a) Modulus and (b) phase of the rail receptance $\hat{u}_{\mathrm{r}}(y = 0\,\mathrm{m}, \omega)$ due to vertical harmonic excitation of the rail for a railway track on a soft soil situated at a distance $D_{\mathrm{t}} = 9\,\mathrm{m}$ from the building, calculated with the uncoupled (solid black line) and coupled (dashed grey line) approach.

Next, the transfer functions from track to building are investigated. Large spatial and directional variation is observed if source–receiver interaction is quantified through the insertion gain $\widehat{\mathrm{IG}}_i(\mathbf{x}, \omega)$ as defined in equation (12). This is illustrated in figure 14, which shows insertion gains $\widehat{\mathrm{IG}}_i(\mathbf{x}, \omega)$ for locations $\mathbf{x}$ corresponding to a grid of points located on the first floor of the four storey portal frame, within a range from $y = -10\,\mathrm{m}$ to $y = +10\,\mathrm{m}$. The power flow concept introduced in subsection 3.3 is applied to this case study as well in order to obtain a global assessment of the interaction effects.

Figure 15 shows the $\widehat{\mathrm{PFIG}}(\omega)$ in a frequency range from 0 Hz to 80 Hz for a distance D_{t} between the track and the building varying from 9 m to 29 m (i.e. for tracks aligned from $x = 15\,\mathrm{m}$ to $x = 35\,\mathrm{m}$), and for the three soil

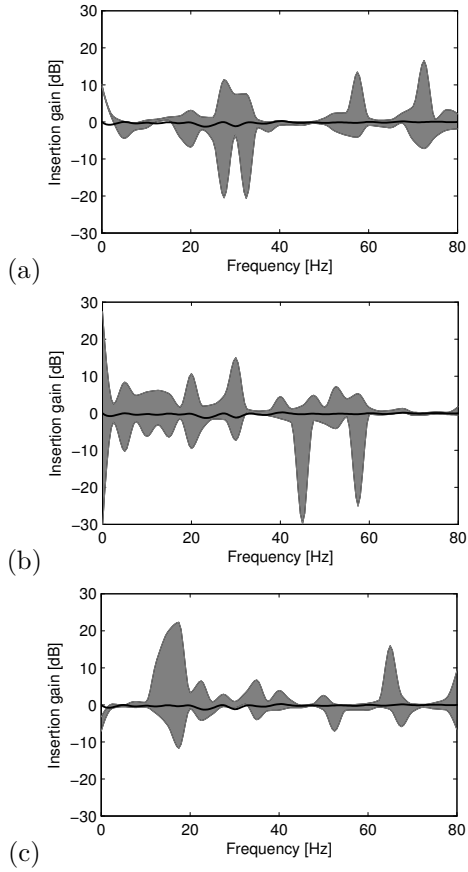

Figure 14: Vibration insertion gains (a) $\widehat{\mathrm{IG}}_x(\mathbf{x},\omega)$, (b) $\widehat{\mathrm{IG}}_y(\mathbf{x},\omega)$ and (c) $\widehat{\mathrm{IG}}_z(\mathbf{x},\omega)$ on the first floor of the four storey portal frame founded on three embedded strip foundations in a range $y \in [-10\,\mathrm{m}, 10\,\mathrm{m}]$ (grey patch). Superimposed is the power flow insertion gain $\widehat{\mathrm{PFIG}}(\omega)$ (black line).

types outlined in table 1. The minimal distance between the track and the strip foundations is denoted as $\mathscr{D} = D_\mathrm{t} - w_\mathrm{t}/2 - w_\mathrm{sf}/2$. It can be expected that source–receiver interaction is unimportant if the Rayleigh wavelength λ_R in the soil is very small compared to the source–receiver distance $\mathscr{D}$. Lines satisfying the relation $\omega = 6 \times 2\pi C_\mathrm{R}/\mathscr{D}$ (corresponding to frequencies at which the distance $\mathscr{D}$ is equal to six Rayleigh wavelengths λ_R) are superimposed on figure 15, and it can indeed be observed that the $\widehat{\mathrm{PFIG}}(\omega)$ tends to 0 dB outside the region bounded by these lines. Through–soil coupling of source and receiver affects the power flow input slightly if the Rayleigh wavelength is of the some order of magnitude as the distance $\mathscr{D}$. This differs from the observation in subsection 3.4 with a source located at depth, where interaction effects are observed if the dimensionless distance $\mathscr{D}/\lambda_\mathrm{p}$ becomes smaller than one. No clear trend in the deviation between the coupled and uncoupled approach is apparent in figure 15, however. Moreover, the overall influence of through–soil coupling remains situated between -1 dB and $+0.5$ dB, suggesting that source–receiver interaction only plays a negligible roll on the transfer from source to receiver.

4.3 Passage of a freight train

A comprehensive case study of the passage of a freight train on the railway track on the surface of a medium soil is finally considered; both the coupled and uncoupled models are employed. The distance D_t between the building and the track equals 9 m (figure 12). The freight train has a speed $v = 80$ km/h and is composed of two traction cars BB 22200, six Rilmms–R00 wagons, and 20 Sgss–S06 wagons [49]. The number of axles N_a, the carriage length L_t, the distance L_b between bogies, the axle distance L_a, and the unsprung axle mass M_u of the carriages are summarized in table 2. Only these unsprung masses are taken into account in the numerical model.

	N_a [−]	L_t [m]	L_b [m]	L_a [m]	M_u [kg]
Traction car BB 22200 (2)	4	17.48	9.69	2.80	3130
Rilmms–R00 wagon (6)	4	14.04	9.00	1.80	1225
Sgss–S06 wagon (20)	4	20.64	15.60	1.80	1225

Table 2: Characteristics of the freight train.

Dynamic axle loads $\hat{\mathbf{g}}(\omega)$ originating from the track unevenness $\hat{\mathbf{u}}_{\mathrm{w/r}}(\omega)$ are considered, assuming a track with an unevenness profile according to the FRA class 3 [50]; the latter corresponds to a track of moderate quality. The response

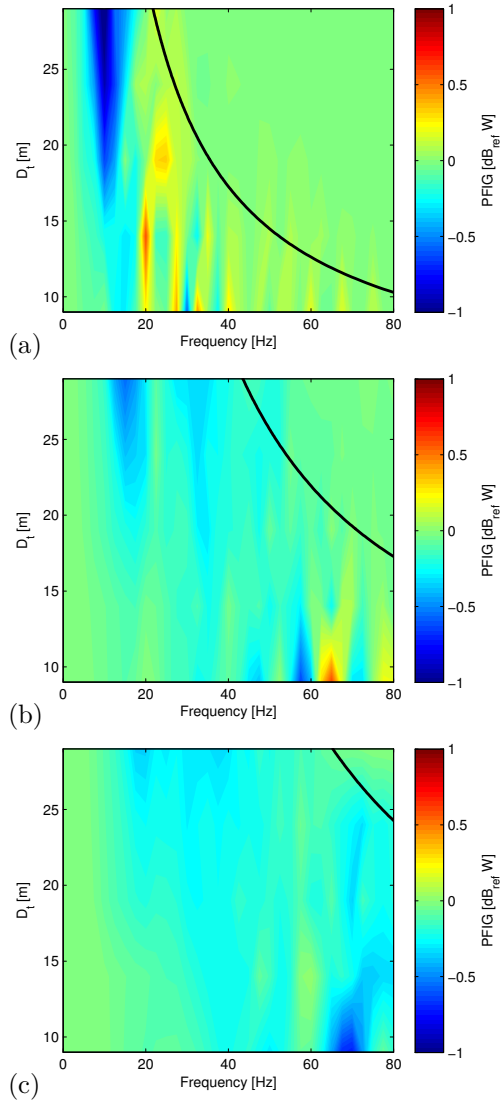

Figure 15: Power flow insertion gain $\widehat{\mathrm{PFIG}}(\omega)$ for a building founded on three embedded strip foundations in case of a (a) soft, (b) medium, and (c) stiff soil. The distance D_t between track and building varies from 9 m to 29 m.

due to a train passage is characterized by an increasing vibration level when the train is approaching, a nearly stationary vibration level during the passage of the train and a decreasing vibration level when the train moves away. It has been shown that the stationary part of the response can be well approximated assuming that the dynamic axle loads are applied at fixed positions [51]; this assumption is especially appropriate in case of long trains at a relatively low speed. This approach is therefore employed in this case study.

Figure 16 shows the one–third octave band RMS spectra of the first axle load $\hat{\mathbf{g}}_1(\omega)$ of the freight train, calculated with the uncoupled and coupled approach, respectively. Both curves coincide, indicating that the presence of the building can be disregarded for a correct estimation of the dynamic axle loads.

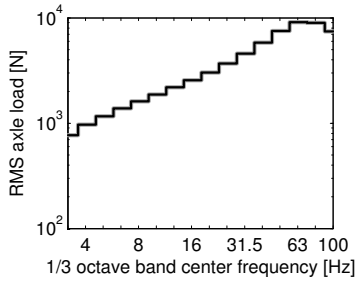

Figure 16: One–third octave band RMS spectra of the first axle load $\hat{\mathbf{g}}_1(\omega)$ of the freight train at a speed of 80 km/h, calculated with the uncoupled (black line) and coupled (grey line) approach. The railway track is situated at a distance $D_\mathrm{t} = 9\,\mathrm{m}$ from the building.

Figure 17 shows the one–third octave band RMS spectra of the horizontal and vertical vibration velocity at the mid–spans of the four floors on the right–hand side of the building (as indicated on figure 12). A reasonable agreement between the uncoupled and coupled approach is obtained up to $\pm 30\,\mathrm{Hz}$. This frequency approximately corresponds to the frequency at which the distance $\mathscr{D} = D_\mathrm{t} - w_\mathrm{t}/2 - w_\mathrm{sf}/2$ between the track and the strip foundations equals one Rayleigh wavelength λ_R in the soil, i.e. $f = C_\mathrm{R}/\mathscr{D} = 32.6\,\mathrm{Hz}$. The difference between the results is considerably larger at higher frequencies, however, indicating that discrepancies between the coupled and uncoupled approach mainly arise if the Rayleigh wavelength is comparable to the distance between source and receiver. As a train passage is considered (combining transfer functions from several axle positions to the building), the spatial variability of individual transfer functions due to source–receiver interaction is much less pronounced. Furthermore, small frequency shifts of these transfer functions are less apparent due to the presentation of the results in one–third

octave bands. As a result, the one–third octave band RMS spectra of the vibration velocities exhibit the same tendency as the power flow insertion gain $\widehat{\mathrm{PFIG}}(\omega)$ (figure 15).

5 Conclusions

The numerical prediction of vibrations in buildings due to railway traffic is a complicated problem where wave propagation in the soil couples the source and the receiver. In this paper, it has been investigated to which extent disregarding dynamic through–soil coupling of source and receiver affects the accuracy of numerical vibration predictions; the generation of the dynamic axle loads as well as the transfer from source to receiver have been considered. Two case studies have been addressed, considering a railway tunnel at depth and a ballasted track at the surface of a homogeneous halfspace, respectively.

It has been demonstrated that source–receiver interaction does not significantly affect the track compliance, which implies that the dynamic axle loads can be calculated with reasonable accuracy using an uncoupled strategy in which through–soil coupling is neglected. This has been explicitly verified for the passage of a freight train on a ballasted track. If the transfer functions from source to receiver are considered, however, significant local variations up to 10 dB in terms of pointwise vibration insertion gain are observed, showing a large spatial and directional variability. The overall wave field, however, is only modestly affected by the interaction as shown by a global comparison in terms of the mean vibrational energy entering a building. The case study involving a railway tunnel has illustrated that the interaction between a source at depth and a receiver only affects the power flow distribution if the dimensionless source–receiver distance $\mathscr{D}/\lambda_{\mathrm{p}}$ is smaller than one. This observation is in line with the rule of thumb commonly applied in seismic engineering. For a railway track at grade, interaction effects are observed for a dimensionless source–receiver distance $\mathscr{D}/\lambda_{\mathrm{R}}$ smaller than six. The identified global deviations of ± 2 dB (in terms of power flow insertion gain) represent a relatively small margin. A similar tendency is revealed if the passage of a freight train is considered, but the insertion gain at particular locations can easily reach 10 dB. This is of the same order of magnitude as other sources of uncertainty described in the literature; this should hence be taken into account when performing vibration predictions.

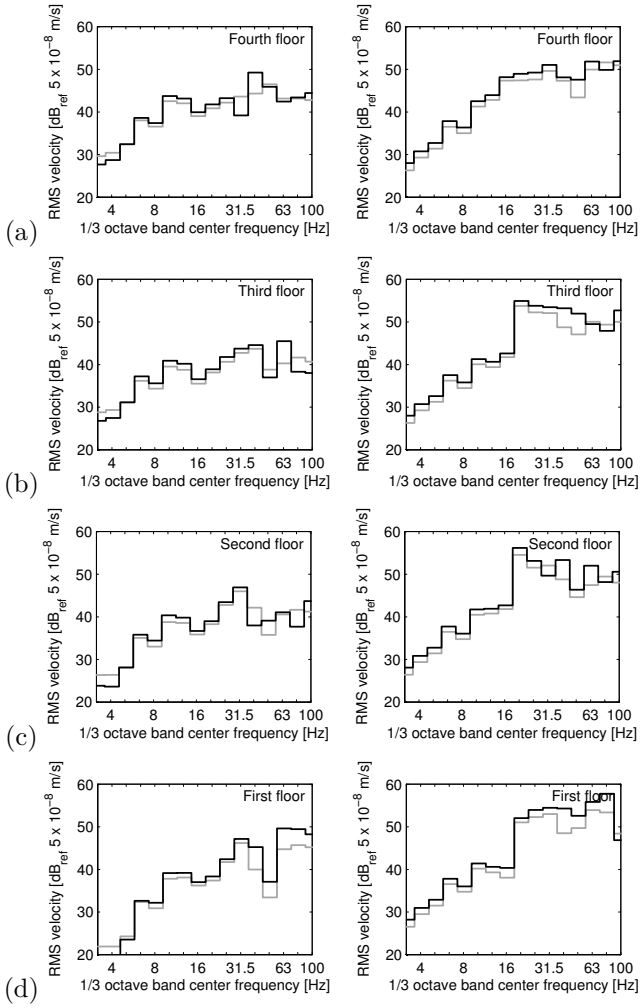

Figure 17: One–third octave band RMS spectra of the horizontal velocity $i\omega\hat{u}_x(\mathbf{x},\omega)$ (left) and the vertical velocity $i\omega\hat{u}_z(\mathbf{x},\omega)$ (right) at the (a) fourth, (b) third, (c) second, and (d) first floor of the four storey portal frame during to the passage of a freight train at a speed of 80 km/h, calculated with the uncoupled (black line) and coupled (grey line) approach. The railway track is situated at a distance $D_\mathrm{t} = 9\,\mathrm{m}$ from the building.

Acknowledgements

The first author is a doctoral fellow of the Research Foundation Flanders (FWO). The financial support is gratefully acknowledged.

References

[1] G. Lombaert, G. Degrande, J. Kogut, S. François, The experimental validation of a numerical model for the prediction of railway induced vibrations, Journal of Sound and Vibration 297 (3-5) (2006) 512–535.

[2] A. Kaynia, C. Madshus, P. Zackrisson, Ground vibration from high speed trains: prediction and countermeasure, Journal of Geotechnical and Geoenvironmental Engineering, Proceedings of the ASCE 126 (6) (2000) 531–537.

[3] L. Andersen, C. Jones, Coupled boundary and finite element analysis of vibration from railway tunnels – a comparison of two- and three-dimensional models, Journal of Sound and Vibration 293 (3-5) (2006) 611–625.

[4] J. Forrest, H. Hunt, A three-dimensional tunnel model for calculation of train-induced ground vibration, Journal of Sound and Vibration 294 (2006) 678–705.

[5] H. Hao, T. Ang, Analytical modelling of traffic-induced ground vibrations, Journal of the Engineering Mechanics Division, Proceedings of the ASCE 124 (8) (1998) 921–928.

[6] Y. Yang, H. Hung, Soil vibrations caused by underground moving trains, Journal of Geotechnical and Geoenvironmental Engineering, Proceedings of the ASCE 134 (11) (2008) 1633–1644.

[7] X. Sheng, C. Jones, D. Thompson, Modelling ground vibrations from railways using wavenumber finite- and boundary-element methods, Proceedings of the Royal Society A - Mathematical, Physical and Engineering Sciences 461 (2005) 2043–2070.

[8] S. François, M. Schevenels, G. Lombaert, P. Galvín, G. Degrande, A 2.5D coupled FE-BE methodology for the dynamic interaction between longitudinally invariant structures and a layered halfspace, Computer Methods in Applied Mechanics and Engineering 199 (23-24) (2010) 1536–1548.

[9] S. Jones, H. Hunt, The effect of inclined soil layers on surface vibration from underground railways using the thin layer method, ASCE Journal of Engineering Mechanics 137 (12) (2011) 887–900.

[10] S. Jones, H. Hunt, Predicting surface vibration from underground railways through inhomogeneous soil, Journal of Sound and Vibration 331 (9) (2012) 2055–2069.

[11] P. Costa, R. Calçada, A. Cardoso, A. Bodare, Influence of soil non-linearity on the dynamic response of high-speed railway tracks, Soil Dynamics and Earthquake Engineering 30 (4) (2010) 221–235.

[12] M. Esmaeili, J. Zakeri, S. Mosayebi, Effect of sand-fouled ballast on train-induced vibration, International Journal of Pavement Engineering. http://dx.doi.org/10.1080/10298436.2013.818146

[13] K. Kuo, H. Hunt, M. Hussein, The effect of a twin tunnel on the propagation of ground-borne vibration from an underground railway, Journal of Sound and Vibration 330 (25) (2011) 6203–6222.

[14] S. Jones, H. Hunt, Voids at the tunnel–soil interface for calculation of ground vibration from underground railways, Journal of Sound and Vibration 330 (2) (2011) 245–270.

[15] J. Bielak, K. Loukakis, Y. Hisada, C. Yoshimura, Domain reduction method for three-dimensional earthquake modeling in localized regions, Part I: Theory, Bulletin of the Seismological Society of America 93 (2) (2003) 817–824.

[16] C. Yoshimura, J. Bielak, Y. Hisada, A. Fernández, Domain reduction method for three-dimensional earthquake modeling in localized regions, Part II: Verification and applications, Bulletin of the Seismological Society of America 93 (2) (2003) 825–840.

[17] J. Qian, D. Beskos, Harmonic wave response of two 3-D rigid surface foundations, Soil Dynamics and Earthquake Engineering 15 (1996) 95–110.

[18] J. Mulliken, D. Karabalis, Discrete model for dynamic through-the-soil coupling of 3-D foundations and structures, Earthquake Engineering and Structural Dynamics 27 (7) (1998) 687–710.

[19] J. Qian, L. Tham, Y. Chueng, Dynamic cross-interaction between flexible surface footings by combined BEM and FEM, Soil Dynamics and Earthquake Engineering 25 (1996) 509–526.

[20] L. Tham, J. Qian, Y. Cheung, Dynamic response of a group of flexible foundations to incident seismic waves, Soil Dynamics and Earthquake Engineering 17 (1998) 127–137.

[21] L. Padrón, J. Aznárez, O. Maeso, 3-D boundary element – finite element method for the dynamic analysis of piled buildings, Engineering Analysis with Boundary Elements 35 (2011) 465–477.

[22] D. Clouteau, D. Aubry, Modification of the ground motion in dense urban areas, Journal of Computational Acoustics 9 (4) (2001) 1659–1675.

[23] M. Kham, J.-F. Semblat, P.-Y. Bard, P. Dangla, Seismic city-site interaction: main governing phemomena through simplified numerical models, Bulletin of the Seismological Society of America 96 (5) (2006) 1934–1951.

[24] G. Lombaert, D. Clouteau, The resonant multiple wave scattering in the seismic response of a city, Waves in Random and Complex Media 16 (3) (2006) 205–230.

[25] L. Menglin, W. Huaifeng, C. Xi, Z. Yongmei, Structure-soil-structure interaction: Literature review, Soil Dynamics and Earthquake Engineering 31 (12) (2011) 1724–1731.

[26] M. Stupazzini, R. Paolucci, Ground motion induced by train passage in urban area, in: P. Sas, B. Bergen (Eds.), Proceedings of ISMA2010 International Conference on Noise and Vibration Engineering, Leuven, Belgium, 2010, pp. 3547–3558.

[27] L. Schillemans, Impact of sound and vibration of the north-south high-speed railway connection through the city of Antwerp, Belgium, Journal of Sound and Vibration 267 (2003) 637–649.

[28] L. Shi, N. Zhang, The simulation analysis on vibration of a museum building nearby induced by urban subway transit, Advanced Materials Research 243-249 (2011) 3427–3431.

[29] X. Sheng, C. Jones, D. Thompson, A theoretical model for ground vibration from trains generated by vertical track irregularities, Journal of Sound and Vibration 272 (3-5) (2004) 937–965.

[30] S. Gupta, W. Liu, G. Degrande, G. Lombaert, W. Liu, Prediction of vibrations induced by underground railway traffic in Beijing, Journal of Sound and Vibration 310 (2008) 608–630.

[31] L. Filon, On a quadrature formula for trigonometric integrals, Proceedings of the Royal Society of Edinburgh 49 (1929) 38–47.

[32] M. Heckl, G. Hauck, R. Wettschureck, Structure-borne sound and vibration from rail traffic, Journal of Sound and Vibration 193 (1) (1996) 175–184.

[33] E. Kausel, J. Roësset, Stiffness matrices for layered soils, Bulletin of the Seismological Society of America 71 (6) (1981) 1743–1761.

[34] M. Schevenels, S. François, G. Degrande, EDT: An ElastoDynamics Toolbox for MATLAB, Computers & Geosciences 35 (8) (2009) 1752–1754.

[35] M. Bonnet, Boundary integral equation methods for solids and fluids, John Wiley and Sons, Chichester, United Kingdom, 1995.

[36] H. Schenck, Improved integral formulation for acoustic radiation problems, Journal of the Acoustical Society of America 44 (1968) 41–58.

[37] Z. Ozdemir, P. Coulier, M. Lak, S. François, G. Lombaert, G. Degrande, Numerical evaluation of the dynamic response of pipelines to vibrations induced by the operation of a pavement breaker, Soil Dynamics and Earthquake Engineering 44 (2013) 153–167.

[38] The MathWorks, MATLAB Parallel Computing Toolbox User's Guide (2013).

[39] C. Simmons, Measurement of sound pressure levels at low frequencies in rooms. Comparison of available methods and standards with respect to microphone positions, Acta Acustica united with Acustica 85 (1999) 88–100.

[40] R. Langley, Analysis of power flow in beams and frameworks using the direct-dynamic stiffness method, Journal of Sound and Vibration 136 (3) (1990) 439–452.

[41] M. Hussein, H. Hunt, A power flow method for evaluating vibration from underground railways, Journal of Sound and Vibration 293 (3-5) (2006) 667–679.

[42] H. Goyder, R. White, Vibrational power flow from machines into built-up structures, part I: Introduction and approximate analyses of beam and plate-like foundations, Journal of Sound and Vibration 68 (1) (1980) 59–75.

[43] H. Goyder, R. White, Vibrational power flow from machines into built-up structures, part II: Wave propagation and power flow in beam-stiffened plates, Journal of Sound and Vibration 68 (1) (1980) 77–96.

[44] J. Xing, W. Price, A power–flow analysis based on continuum dynamics, Philosophical Transactions of the Royal Society A - Mathematical, Physical and Engineering Sciences 455 (1999) 401–436.

[45] S. Hambric, Power flow and mechanical intensity calculations in structural finite element analysis, Journal of Vibration and Acoustics 112 (1990) 542–549.

[46] Z. Wang, J. Xing, W. Price, An investigation of power flow characteristics of L–shaped plates adopting a substructure approach, Journal of Sound and Vibration 250 (4) (2002) 627–648.

[47] J. Talbot, H. Hunt, A generic model for evaluating the performance of base-isolated buildings, Journal of Low Frequency Noise, Vibration and Active Control 22 (3) (2003) 149–160.

[48] H. Hunt, M. Hussein, Vibration from railways: can we achieve better than +/-10 dB prediction accuracy?, in: 14th International Congress on Sound and Vibration, Cairns, Australia, 2007.

[49] G. Lombaert, P. Galvín, G. Degrande, Prediction of railway induced vibrations at a site in Saint-Epain (France), Tech. Rep. BWM-2009-13, Department of Civil Engineering, KU Leuven (June 2009).

[50] V. Garg, R. Dukkipati, Dynamics of railway vehicle systems, Academic Press, Canada, 1984.

[51] H. Verbraken, G. Lombaert, G. Degrande, Verification of an empirical prediction method for railway induced vibrations by means of numerical simulations, Journal of Sound and Vibration 330 (8) (2011) 1692–1703.

Curriculum vitae

Pieter Coulier
°9 October 1987, Veurne, Belgium.

Education

2010 – 2014
PhD in Civil Engineering, Department of Civil Engineering, KU Leuven.

2008 – 2010
MSc in Civil Engineering, KU Leuven.

2005 – 2008
BSc in Civil Engineering, KU Leuven.

Professional experience

2010 – 2014
PhD fellow of the Research Foundation – Flanders (FWO),
Department of Civil Engineering, KU Leuven.

Publications

International journal papers

[1] P. Coulier, G. Lombaert, and G. Degrande. The influence of source–receiver interaction on the numerical prediction of railway induced vibrations. *Journal of Sound and Vibration*, 333(12):2520–2538, 2014.

[2] P. Coulier, A. Dijckmans, S. François, G. Degrande, and G. Lombaert. A spatial windowing technique to account for finite dimensions in 2.5D dynamic soil–structure interaction problems. *Soil Dynamics and Earthquake Engineering*, 59:51–67, 2014.

[3] P. Coulier, S. François, G. Lombaert, and G. Degrande. Coupled finite element – hierarchical boundary element methods for dynamic soil–structure interaction in the frequency domain. *International Journal for Numerical Methods in Engineering*, 97(7):505–530, 2014.

[4] P. Coulier, S. François, G. Lombaert, and G. Degrande. Application of hierarchical matrices to boundary element methods for elastodynamics based on Green's functions for a horizontally layered halfspace. *Engineering Analysis with Boundary Elements*, 37(12):1745–1758, 2013.

[5] P. Coulier, S. François, G. Degrande, and G. Lombaert. Subgrade stiffening next to the track as a wave impeding barrier for railway induced vibrations. *Soil Dynamics and Earthquake Engineering*, 48:119–131, 2013.

[6] Z. Ozdemir, P. Coulier, M.A. Lak, S. François, G. Lombaert, and G. Degrande. Numerical evaluation of the dynamic response of pipelines to vibrations induced by the operation of a pavement breaker. *Soil Dynamics and Earthquake Engineering*, 44:153–167, 2013.

Papers published in the proceedings of international conferences

[7] P. Coulier, S. François, V. Cuéllar, G. Degrande, and G. Lombaert. Design and performance of a stiff wave barrier in the soil. In *2nd International Symposium on Railway Geotechnical Engineering (GEORAIL 2014)*, Marne La Vallée, France, November 2014. Accepted for publication.

[8] P. Coulier, A. Dijckmans, V. Cuéllar, A. Ekblad, A. Smekal, G. Degrande, and G. Lombaert. Numerical and experimental study of stiff wave barriers for the mitigation of railway induced vibrations. In *Proceedings of ISMA 2014 International Conference on Noise and Vibration Engineering*, Leuven, Belgium, September 2014. Accepted for publication.

[9] P. Coulier, A. Cicirello, G. Lombaert, G. Degrande, and H.E.M. Hunt. Prediction of railway induced vibrations in an urban environment. In *Proceedings of the 11th World Congress on Computational Mechanics (WCCM XI)*, Barcelona, Spain, July 2014. Accepted for publication.

[10] P. Coulier, S. François, V. Cuéllar, G. Degrande, and G. Lombaert. Design and performance of a stiff wave barrier in the soil using 2.5D and 3D FE–BE models. In *Proceedings of the 11th World Congress on Computational Mechanics (WCCM XI)*, Barcelona, Spain, July 2014. Accepted for publication.

[11] M.G.R. Toward, J. Jiang, A. Dijckmans, P. Coulier, D.J. Thompson, G. Degrande, and G. Lombaert. Mitigation of railway induced vibration by using subgrade stiffening and wave impeding blocks. In *Proceedings of the 9th International Conference On Structural Dynamics, EURODYN 2014*, Porto, Portugal, 2014. Submitted for publication.

[12] A. Dijckmans, P. Coulier, J. Jiang, M.G.R. Toward, G. Degrande, G. Lombaert, and D.J. Thompson. Mitigation of railway induced vibrations by using heavy masses next to the track. In *Proceedings of the 9th International Conference On Structural Dynamics, EURODYN 2014*, Porto, Portugal, 2014. Submitted for publication.

[13] P. Coulier, A. Dijckmans, S. François, G. Degrande, and G. Lombaert. A spatial windowing technique to account for finite dimensions in 2.5D elastodynamic transmission and radiation problems. In *Proceedings of the 9th International Conference On Structural Dynamics, EURODYN 2014*, Porto, Portugal, 2014. Accepted for publication.

[14] P. Coulier, A. Dijckmans, J. Jiang, D.J. Thompson, G. Degrande, and G. Lombaert. Stiff wave barriers for the mitigation of railway induced vibrations. In J. Nielsen, D. Anderson, P. de Vos, P.-E. Gautier, M. Iida, J. Nelson, T. Tielkes, D. Thompson, and D. Towers, editors, *Proceedings of the 11th International Workshop on Railway Noise IWRN11*, pages 599–606, Uddevalla, Sweden, September 2013.

[15] P. Coulier, S. François, G. Degrande, and G. Lombaert. A numerical study of subgrade stiffening as a mitigation measure for railway induced vibrations through 2.5D and 3D FE-BE models. In M. Papadrakakis, V. Papadopoulos, and V. Plevris, editors, *Proceedings of the 4th International Conference On Computational Methods in Structural Dynamics and Earthquake Engineering, COMPDYN 2013*, Kos Island, Greece, June 2013. CD-ROM.

[16] P. Coulier, S. François, G. Lombaert, and G. Degrande. Coupling of finite elements and hierarchical boundary elements for dynamic soil-structure interaction problems. In M. Papadrakakis, V. Papadopoulos, and V. Plevris, editors, *Proceedings of the 4th International Conference On Computational Methods in Structural Dynamics and Earthquake*

Engineering, COMPDYN 2013, Kos Island, Greece, June 2013. CD-ROM.

[17] P. Coulier, S. François, G. Lombaert, and G. Degrande. A coupled finite element – hierarchical boundary element method based on Green's functions for a horizontally layered halfspace. In N. Heuer and C. Jerez-Hanckes, editors, *Proceedings of the Symposium of the International Association for Boundary Element Methods IABEM 2013*, pages 23–30, Santiago, Chile, January 2013.

[18] P. Coulier, S. François, G. Lombaert, and G. Degrande. Mitigation of railway induced vibrations by means of subgrade stiffening. In P. Sas, D. Moens, and S. Jonckheere, editors, *Proceedings of ISMA 2012 International Conference on Noise and Vibration Engineering*, pages 2837–2852, Leuven, Belgium, September 2012.

[19] P. Coulier, S. François, G. Lombaert, and G. Degrande. The numerical prediction of railway induced vibrations in an urban environment. In P.M. Pimenta and E.M.B. Campello, editors, *Proceedings of the 10th World Congress on Computational Mechanics WCCM 2012*, Sao Paulo, Brazil, 8–13 July 2012. CD-ROM.

[20] Z. Ozdemir, M.A. Lak, P. Coulier, S. François, G. Lombaert, and G. Degrande. Numerical evaluation of the dynamic response of pipelines to vibrations induced by the operation of a pavement breaker. In W. Zhai, H. Takemiya, G. De Roeck, and E. Tutumluer, editors, *Advances in Environmental Vibration. Proceedings of the 5th International Symposium on Environmental Vibration. ISEV 2011*, pages 808–815, Chengdu, China, October 2011. Science Press.

[21] P. Coulier, G. Degrande, and G. Lombaert. The influence of structure-soil-structure interaction on the numerical prediction of traffic induced vibrations. In W. Zhai, H. Takemiya, G. De Roeck, and E. Tutumluer, editors, *Advances in Environmental Vibration. Proceedings of the 5th International Symposium on Environmental Vibration. ISEV 2011*, pages 23–29, Chengdu, China, October 2011. Science Press, Beijing, China.

[22] P. Coulier, S. François, G. Degrande, and G. Lombaert. The influence of source-receiver interaction on the numerical prediction of traffic induced vibrations. *Proceedings of the Symposium of the International Association for Boundary Element Methods IABEM 2011*, pages 81–86, Brescia, Italy, September 2011.

[23] Z. Ozdemir, M.A. Lak, S. François, P. Coulier, G. Degrande, and G. Lombaert. A numerical model for the prediction of the response

of pipelines due to vibrations induced by the operation of a pavement breaker. In G. De Roeck, G. Degrande, G. Lombaert, and G. Müller, editors, *Proceedings of the 8th International Conference on Structural Dynamics EURODYN 2011*, pages 928–935, Leuven, Belgium, July 2011.

[24] P. Coulier, G. Degrande, K. Kuo, and H. Hunt. A comparison of two models for the vibration response of piled foundations to inertial and underground-railway-induced loadings. In *Proceedings of the 17th International Conference on Sound and Vibration*, Cairo, Egypt, July 2010. CD-ROM.

Papers published in the proceedings of local conferences

[25] P. Coulier, S. François, G. Degrande, and G. Lombaert. A numerical study of subgrade stiffening as a mitigation measure for railway induced vibrations. In W. Bosschaerts, B. Janssens, and B. Marinus, editors, *Proceedings of the 9th National Congress on Theoretical and Applied Mechanics NCTAM 2012*, Brussels, Belgium, May 2012.

Other contributions at international conferences or meetings

[26] G. Lombaert, P. Coulier, A. Dijckmans, and G. Degrande. Mitigation of railway induced vibration by measures in the transmission path. IBK Seminar, Institute of Structural Engineering ETH Zürich. Invited lecture, February 2014.

[27] A. Dijckmans and P. Coulier. Stiff wave barriers for railway induced ground vibration. RIVAS Final Conference. Vibrations – Ways out of the annoyance, Brussels, Belgium, November 2013.

[28] G. Degrande, P. Coulier, S. François, and G. Lombaert. Mitigation of railway induced vibrations using stiff wave barriers. 6th International Symposium on Environmental Vibration, ISEV 2013, Shanghai, China. Keynote lecture, November 2013.

[29] P. Coulier, S. François, G. Lombaert, and G. Degrande. Application of hierarchical matrices to elastodynamic FEM-BEM coupling in the frequency domain. 12th U.S. National Congress on Computational Mechanics USNCCM12, Raleigh, North Carolina, USA, July 2013.

[30] V. Cuéllar, P. Coulier, G. Degrande, and G. Lombaert. Mitigation of vibrations by stiff wave barriers: design of field test with a jet grouting wall. RIVAS Training Workshop: Reducing railway induced ground

vibration by interventions on the transmission path, Berlin, Germany, May 2013.

[31] P. Coulier, S. François, G. Degrande, and G. Lombaert. Mitigation of vibrations by stiff wave barriers: physical mechanisms. RIVAS Training Workshop: Reducing railway induced ground vibration by interventions on the transmission path, Berlin, Germany, May 2013.

[32] A. Dijckmans, P. Coulier, G. Lombaert, G. Degrande, J. Jiang, and D.J. Thompson. Transmission path mitigation measures for railway induced vibrations. RIVAS Mid Term Conference. Vibrations – The way ahead, Venice, Italy, October 2012.

[33] G. Lombaert, P. Coulier, A. Dijckmans, P. Fiala, S. François, S. Gupta, and G. Degrande. Excitation mechanisms and mitigation measures for ground-borne noise and vibration due to railway traffic. Fritz-Peter Müller award ceremony. Karlsruher Institut für Technologie, Karlsruhe. Invited lecture, October 2012.

[34] P. Coulier, S. François, G. Lombaert, and G. Degrande. The use of $\mathscr{H}$-matrices in the numerical prediction of railway induced vibrations and re-radiated noise. In *8th European Solid Mechanics Conference ESMC 2012*, Graz, Austria, July 2012.

[35] P. Coulier, S. François, G. Degrande, G. Lombaert, V. Cuéllar, and M. Rodriguez. A numerical study of subgrade stiffening as a mitigation measure for railway induced vibration. Workshop RIVAS WP4, Paris, France, January 2012.

[36] G. Lombaert, P. Coulier, J. Houbrechts, A. Dijckmans, S. François, and G. Degrande. Vibration mitigation measures for the propagation way from track to buildings. RIVAS seminar. Vibrations - Annoyance, Acceptance and Assuming the challenge to find solutions, September 2011.

[37] P. Coulier, M. Beckers, K. Kuo, M. Hussein, H. Hunt, and G. Degrande. Vibrational discomfort in buildings. Transport Research Arena Conference, June 2010.

Other contributions at local conferences or meetings

[38] G. Lombaert, M.A. Lak, Z. Ozdemir, P. Coulier, S. François, and G. Degrande. Trillingen ten gevolge van het beuken van wegen uit betonplaten. OCW-K.U.Leuven studiedag, Trillingsgecontroleerd stabiliseren van betonplaten voor duurzame asfaltverhardingen met scheurremmende lagen, December 2011.

[39] P. Coulier, G. Degrande, and G. Lombaert. Development of a coupled source and receiver model for vibrations due to urban railway traffic. ABAV studiedag, Wie-doet-wat in het Belgisch akoestisch onderzoek?, February 2011.

Internal reports and other publications

[40] G. Lombaert, A. Dijckmans, P. Coulier, G. Degrande, A. Smekal, A. Ekblad, D.J. Thompson, J. Jiang, M.G.R. Toward, W. Rücker, J. Keil, G. Vukotic, M. Rodríguez Plaza, Á. Andrés, V. Cuéllar, R. Garburg, and R. Müller. Design guide and technology assessment of the transmission mitigation measures. RIVAS project SCP0-GA-2010-265754, Deliverable D4.6, Report to the EC, December 2013.

[41] A. Dijckmans, P. Coulier, G. Degrande, G. Lombaert, A. Ekblad, A. Smekal, M. Rodríguez Plaza, Á. Andrés-Alguacil, V. Cuéllar, J. Keil, and G. Vukotic. Mitigation measures on the transmission path: results of field tests. RIVAS project SCP0-GA-2010-265754, Deliverable D4.5, Report to the EC, December 2013.

[42] P. Coulier, G. Degrande, A. Dijckmans, G. Lombaert, V. Cuéllar, M. Yuste, R. Müller, G. Vucotic, J. Keil, K. Auersch, E. Knothe, W. Rücker, S. Said, J. Jiang, D.J. Thompson, and M.G.R. Toward. Design of the mitigation measures at the test sites. RIVAS project SCP0-GA-2010-265754, Deliverable D4.3, Report to the EC, January 2013.

[43] H. Verbraken, P. Coulier, G. Lombaert, and G. Degrande. Measurement of free field vibration during impact tests on a pile at a site in Loon-Plage (France). Report BWM-2012-09, Department of Civil Engineering, KU Leuven, September 2012.

[44] P. Coulier, H. Verbraken, G. Lombaert, and G. Degrande. Determination of the dynamic soil properties by surface wave characterization at a site in Loon-Plage (France). Report BWM-2012-08, Department of Civil Engineering, KU Leuven, September 2012.

[45] P. Coulier, A. Dijckmans, G. Degrande, G. Lombaert, J. Jiang, and D. Thompson. Optimum test conditions for field tests of vibration mitigation measures in the transmission path. RIVAS project SCP0-GA-2010-265754, Deliverable D4.2, Report to the EC, August 2012.

[46] H. Verbraken, P. Coulier, G. Lombaert, and G. Degrande. Measurement of transfer functions at a site in Lincent. Report BWM-2012-07, Department of Civil Engineering, KU Leuven, July 2012.

[47] H. Verbraken, P. Coulier, G. Lombaert, and G. Degrande. Measurement of train passages and transfer functions at a site in Lincent. Report BWM-2012-05, Department of Civil Engineering, KU Leuven, June 2012.

[48] P. Coulier, H. Verbraken, G. Lombaert, and G. Degrande. Trillingsmetingen in het postsorteercentrum te Hasselt: fase 1. Report BWM-2012-04, Department of Civil Engineering, KU Leuven, March 2012.

[49] P. Coulier, G. Degrande, A. Dijckmans, J. Houbrechts, G. Lombaert, W. Rücker, L. Auersch, M.R. Plaza, V. Cuéllar, D. Thompson, A. Ekblad, and A. Smekal. Scope of the parametric study on mitigation measures on the transmission path. RIVAS project SCP0-GA-2010-265754, Deliverable D4.1, Report to the EC, October 2011.

[50] Z. Ozdemir, M.A. Lak, P. Coulier, S. François, G. Lombaert, and G. Degrande. Numerical evaluation of the dynamic response of pipelines to vibrations induced by the operation of a pavement breaker. Report BWM-2011-04, Department of Civil Engineering, KU Leuven, June 2011.

[51] P. Coulier, M. Schevenels, and G. Degrande. Trillingsmetingen in een woning in de Brasschaatsesteenweg te Kalmthout. Report BWM-2011-06, Department of Civil Engineering, KU Leuven, April 2011.

Master's thesis

[52] P. Coulier. The vibration response of piled foundations to inertial and underground railway induced vibrations. Master's thesis, Department of Civil Engineering, KU Leuven & Cambridge University, United Kingdom, 2010.

FACULTY OF ENGINEERING SCIENCE
DEPARTMENT OF CIVIL ENGINEERING
STRUCTURAL MECHANICS
Kasteelpark Arenberg 40 box 2448
B–3001 Leuven